



**HAL**  
open science

# Contrôles géologiques, structuraux, minéralogiques et géochimiques sur la formation des minerais riches dans le district minéralisé de Streltsovsky, Russie

Alexei Aleshin

► **To cite this version:**

Alexei Aleshin. Contrôles géologiques, structuraux, minéralogiques et géochimiques sur la formation des minerais riches dans le district minéralisé de Streltsovsky, Russie. Earth Sciences. Université Henri Poincaré - Nancy 1, 2008. English. NNT : 2008NAN10152 . tel-01746149

**HAL Id: tel-01746149**

**<https://hal.univ-lorraine.fr/tel-01746149v1>**

Submitted on 29 Mar 2018

**HAL** is a multi-disciplinary open access archive for the deposit and dissemination of scientific research documents, whether they are published or not. The documents may come from teaching and research institutions in France or abroad, or from public or private research centers.

L'archive ouverte pluridisciplinaire **HAL**, est destinée au dépôt et à la diffusion de documents scientifiques de niveau recherche, publiés ou non, émanant des établissements d'enseignement et de recherche français ou étrangers, des laboratoires publics ou privés.



## AVERTISSEMENT

Ce document est le fruit d'un long travail approuvé par le jury de soutenance et mis à disposition de l'ensemble de la communauté universitaire élargie.

Il est soumis à la propriété intellectuelle de l'auteur. Ceci implique une obligation de citation et de référencement lors de l'utilisation de ce document.

D'autre part, toute contrefaçon, plagiat, reproduction illicite encourt une poursuite pénale.

Contact : [ddoc-theses-contact@univ-lorraine.fr](mailto:ddoc-theses-contact@univ-lorraine.fr)

## LIENS

Code de la Propriété Intellectuelle. articles L 122. 4

Code de la Propriété Intellectuelle. articles L 335.2- L 335.10

[http://www.cfcopies.com/V2/leg/leg\\_droi.php](http://www.cfcopies.com/V2/leg/leg_droi.php)

<http://www.culture.gouv.fr/culture/infos-pratiques/droits/protection.htm>



Faculté des Sciences & Techniques UMR CNRS 7566  
U.F.R.S.T.M.P.  
Ecole Doctorale  
RP2E (Ressources, Produits, Procédés et Environnements)

## Thèse

---

présentée pour l'obtention de titre de

**Docteur de l'Université Henry Poincaré, Nancy-I**

en Sciences de la Terre et de l'Univers

par

**Alexei ALESHIN**

**Geological, structural, mineralogical and geochemical controls of  
the formation of the uranium-rich ores in the Streltsovsky ore  
field, Russia.**

**Membres du jury:**

**M. Michel CUNEY** Directeur de Recherche, CNRS, UMR G2R, Nancy

**M. Vasilii VELICHKIN** Corresponding Member of RAS, IGEM,  
Moscow, Russia

**M. Maurice PAGEL** Professeur, Université d'Orsay Paris Sud  
**M. Reimar SELTMANN** Director of CERCAMS, Natural History  
Museum, London, UK

**M. Claude CAILLAT** Ingénieur géologue, AREVA, Vélizy

**M. Michel CATHELIN** Directeur de Recherche, CNRS, UMR  
G2R, Nancy





## Table of contents

TABLE OF CONTENTS.....	3
TABLE OF CAPTIONS.....	7
LIST OF TABLES .....	17
ACKNOWLEDGMENTS .....	19
RÉSUMÉ.....	21
ABSTRACT .....	23
РЕЗЮМЕ .....	25
RÉSUMÉ ÉTENDU .....	27
EXTENDED ABSTRACT.....	29
РАСШИРЕННОЕ РЕЗЮМЕ .....	31
GENERAL INTRODUCTION .....	35
<i>Objectives and topical problems of the study</i> .....	36
<i>Methods of investigation and factual material</i> .....	37
<i>Thesis structure</i> .....	39
<b>PART I. GEOLOGY OF THE STRELTSOVSKY ORE FIELD</b> .....	<b>41</b>
1. LOCATION OF THE STRELTSOVSKY ORE FIELD IN THE REGIONAL STRUCTURES OF EASTERN TRANSBAIKALIA .....	43
2. GEOLOGICAL SETTINGS OF THE STRELTSOVSKY ORE FIELD .....	49
2.1. Structural stages and magmatism .....	49
2.2. Tectonics .....	53
2.3. Ore body controls.....	57
3. 3D GIS-MODELING OF GEOLOGICAL STRUCTURE AND AN ORE BODY IN THE OKTYABRSKY DEPOSIT .....	61
3.1. Approaches of modeling .....	61
3.2. Geological model of the central part of the Oktyabrsy deposit .....	62
3.3. Numerical model of the ore body and geological controls of high-grade uranium mineralization .....	65
3.4. Conclusions.....	70
<b>PART II. MINERALOGY OF THE DEPOSITS AND GEOCHEMICAL BEHAVIOUR OF ELEMENTS IN MAGMATIC AND HYDROTHERMAL PROCESSES</b> .....	<b>71</b>
1. URANIUM AND FLUORINE BEHAVIOUR IN THE LATE MESOZOIC VOLCANIC ROCKS OF THE STRELTSOVSKY CALDERA.....	73
<i>Conclusions</i> .....	78
2. MINERALOGY OF THE DEPOSITS.....	81
2.1. Stages of the Late Mesozoic hydrothermal process.....	82
2.1.1. The preore stage .....	82
2.1.2. The uranium ore stage .....	89
2.1.3. The 1 <sup>st</sup> postore stage .....	90
2.1.4. The 2 <sup>nd</sup> postore stage .....	97
2.2. Mineral parageneses.....	101
2.2.1. Mineral assemblages of the preore stage .....	102
2.2.2. Mineral assemblages of the uranium ore stage .....	103
2.2.3. Mineral assemblages of the 1 <sup>st</sup> postore stage.....	112

# Table of contents

2.2.4. Mineral assemblages of the 2 <sup>nd</sup> postore stage .....	130
2.3. <i>Typomorphism of minerals</i> .....	135
2.3.1. Pitchblende .....	135
2.3.2. U-Si metagel .....	141
2.3.3. Micas .....	144
2.3.4. Chlorites .....	148
2.3.5. Fluorite .....	148
3. BEHAVIOR OF ELEMENTS DURING THE LATE MESOZOIC HYDROTHERMAL PROCESS .....	156
3.1. <i>Uranium and other elements behavior during the preore and postore metasomatic alteration of the host rocks</i> .....	156
3.1.1. Whole-rock geochemistry .....	157
3.1.2. Dispersion halos of uranium around ore bodies .....	162
3.1.3. Conclusions .....	166
3.2. <i>Geochemistry of episyenitization</i> .....	167
4. REE IN PITCHBLENDE AND HOST ROCKS .....	170
<b>PART III. PHYSICOCHEMICAL CONDITIONS OF MINERALIZATION</b> .....	<b>177</b>
1. FLUID INCLUSIONS STUDY .....	179
1.1. <i>Preore stage</i> .....	179
1.2. <i>Fluid inclusions in quartz of the ore stage</i> .....	180
1.3. <i>Fluid inclusions in quartz of the 1<sup>st</sup> postore stage</i> .....	184
2. PHYSICOCHEMICAL CONDITIONS OF LATE MESOZOIC MINERALIZATION: THERMOBAROGEOCHEMICAL AND MINERALOGICAL EVIDENCES	187
<b>PART IV. GENETIC MODEL OF THE URANIUM ORE FORMATION</b> .....	<b>191</b>
1. CRITICAL REVIEW OF EXISTING GENETIC MODELS .....	193
2. ASSESSMENT OF CRYSTALLIZATION TIMING OF THE UPPER CRUSTAL MAGMA CHAMBER BY FINITE DIFFERENCE METHOD .....	197
2.1. <i>Introduction</i> .....	197
2.2. <i>Statement of the problem</i> .....	198
2.3. <i>Modeling results and discussion</i> .....	200
3. MAGMATOGENEOUS (POST-MAGMATIC) MODEL OF THE URANIUM ORE FORMATION IN THE STRELTSOVSKY ORE FIELD .....	205
3.1. <i>The ore forming process – from the source to the deposits</i> .....	205
3.1.1. The area of ore-bearing fluid generation. ....	205
3.1.2. The area of U transportation.....	207
3.1.3. The area of ore deposition. ....	207
3.2. <i>Relationships between the uranium ore formation and pre– and postore hydrothermal processes</i> .....	209
<b>GENERAL CONCLUSIONS</b> .....	<b>213</b>
BIBLIOGRAPHY .....	217
ANNEXES .....	225
Annex I. <i>Main statistical parameters of samplings on host rocks subjected to illitization with associated alteration of different intensity</i> .....	225
ELECTRONIC ANNEXES .....	233

## Table of contents

---

<i>E-annex I. 3D GIS model of the central part of the Oktyabrsky deposit, with the installation of Acrobat Reader 3D.....</i>	<i>233</i>
<i>E-annex II. Results of microprobe analyses .....</i>	<i>233</i>
<i>E-annex III. Results of ICP-MS analyses of mineral separations of fluorite and carbonate.....</i>	<i>233</i>
<i>E-annex IV. Results of whole-rock analyses (ICP-AES, -MS, XRF, INAA).....</i>	<i>233</i>



## Table of captions

Fig. 1.1. Location of the SOF in the regional structures of the Eastern Transbaikalia. ....	44
Fig. 1.2. Structure of the Earth's crust and regional gravity field in the Transbaikal region.....	45
Fig. 1.3. Geological structure of the Urulunghuevsky local uplift and position of the Streltovsky caldera (in deep green) (after Ishchukova, 1998, with modifications) .....	46
Fig. 1.4. Gravity field of the Urulunghuevsky uplift (after Dukhovskii, 1998, with modifications). ....	48
Fig. 1.5. Stratigraphic column of the Streltsovsky caldera. After (Geology, formation conditions..., 1981, with modifications).....	50
Fig. 1.6. Geological map of the Streltsovsky ore field, after Ishchukova et al. (1998).. ....	52
Fig. 1.7. 3D block-diagram of the Earth's crust under the Streltsovsky caldera and surroundings created on the base of 3D GIS model (built in GeoSpline) with invoking geophysics data (Menaker, 1970, 1972, 1990; Dukhovskii, 1998).....	55
Fig. 1.8. 3D GIS model of the upper part of the Earth's crust built in GeoSpline ARX-module under AutoCAD based on geologic maps and geophysics data. ....	56
Fig. 1.9. Geological section through the Antei and the Streltsovsky deposits (after Ishchukova et al., 1998, with modifications).....	58
Fig. 1.10. Cross-section along the 209 <sup>th</sup> prospecting line in the Oktyabrsky deposit (after Ishchukova et al., 1998, with modifications). Pinky – Lower Paleozoic and Variscan granites of the basement, green – trachybasalts of the Priargunsky suit (two lower thick flows) and the Turginsky suite (two upper thin sheets), brown – trachydacites of the Priargunsky suite. White – tuffaceous conglomerates and sandstones. Black – uranium ore bodies. Numbers in circles – fault numbers.....	63
Fig. 1.11. Scanned images of three transversal cross-sections along prospecting lines 209, 210+50 and 213, one longitudinal cross-section and geological map of mine horizon +362 m which were used as a graphical base for 3D GIS model of the Oktyabrsky deposit. Images are positioned in real coordinates in 3D space of AutoCAD Map 2008.....	64
Fig. 1.12. 3D model of geological structure of the Oktyabrsky deposit built in AutoCAD Map 2008 with the use of GeoSpline module. Layered structure of sedimentary-volcanogene stratum intersected by numerous steeply dipping longitudinal faults of the Malo-Tulukuevsky shear zone is noticeable. Box with blue-cyan lines – sampling of 9 mine slices prepared for database. The height of the model box – 625 m. ....	65
Fig. 1.13. 3D model of geological structure of the Oktyabrsky deposit imported into Gocad with the raster image of the cross-section on prospecting line 209. Three red cross-sections in the box – 3D model of the ore body built in Gocad.....	67
Fig. 1.14. Generalized intervals of gamma-sampling on 9 mining slices digitized in AutoCAD Map. Blue – commercial intervals, cyan – barren intervals. Y axis points to the north, X axis – to the east. The length of the model box – 200 m, the height – 30 m. ....	67
Fig. 1.15. Numerical model of the ore body in the Oktyabrsky deposit built in Gocad with surfaces of the 2 <sup>nd</sup> fault (transparent crimson surface) and the 7 <sup>th</sup> fault (transparent brownish-green). Surfaces of isoconcentration of uranium (isosurfaces) 0.1% (transparent green) and 1% (red). It is visible that the richest part of the ore body is constrained by the 2 <sup>nd</sup> fault at its joint with the 7 <sup>th</sup> fault (red dashed line) and is located below the surface of the 2 <sup>nd</sup> fault. Lesser grade mineralization is controlled by the NW faults (blue dashed line) and screened by the longitudinal 2 <sup>nd</sup> fault. Geological and numerical models of the ore body were combined in GeoSpline and then exported in PDF3D format. ....	68
Fig. 1.16. Misinterpretation of primary sampling in cases of low-density and highly anisotropic data: erroneous elongation of uranium isosurfaces along boreholes (pointed by white arrows) and breaks of isosurfaces (white zigzags) along the 2 <sup>nd</sup> fault (magenta dashed line) and NW	

## Table of captions

faults (yellow dashed lines). Long cyan and blue lines – gamma-sampling of boreholes. Northern part of the ore body model. ....	ERREUR ! SIGNET NON DEFINI.
Fig. 2.1. Basalts altered with different intensity and uranium distribution in the rocks: (a) – the freshest basalt with olivine (olv) partly replaced with carbonate (crb) and unaltered matrix; (b) – tracks of uranium are evenly distributed in matrix and are practically absent in olivine phenocryst; (c) – basalt overprinted by carbonatization, chloritization and illitization, Ti-accessories are completely replaced with leucoxene (lcx); (d) – superimposed uranium is concentrated in leucoxenized accessories and in a thin seam of leucoxene. Photomicrographs of thin-polished section St-138 in transmitted plane-polarized light (a) and section St-111 in transmitted and reflected plane-polarized light, black field (c); (b), (d) – lavsan detectors of corresponding sections. The long side of photomicrographs is 1.1 mm (a,b) and 3.9 mm (c,d).	74
Fig. 2.2. Location of samples of basalts (1-3) and rhyolites (4) in the sedimentary-volcanogeneous sequence of the Streltsovsky caldera. 1 – basalts of the lower flow of the Priargunsky suite, 2 – basalts of the upper flow of the Priargunsky suite, 3 – basalts of the Turginsky suite. ....	76
Fig. 2.3. (a) Uranium and thorium contents in basalts and (b) fluorine content in biotite from basalts plotted against Fe/(Fe+Mg) ratio of biotite. Data on the y axis in figure (a) correspond to samples where U was not analyzed.....	77
Fig. 2.4. Evolution of U content in volcanic rocks and the uranium ores in the Late Mesozoic regarding depths of magma generation and ore deposition. Uranium and fluorine were depleted in basic magma with time while they were progressively accumulated in more acidic magmas towards the surface. ....	79
Fig. 2.5. Paragenetic mineral succession of the Late Mesozoic hydrothermal process in the SOF deposits. Compiled using the data of Ishchukova et al. (1998), and Andreeva and Golovin (1998). (1–6) Minerals: (1) metasomatic, (2) veined, (3) highly abundant, (4) abundant, (5) not abundant, (6) rare. ....	83
Fig. 2.6. Halos of preore and postore alteration in trachydacites in the west-northern wall of the Tulukui open pit. Weak preore alteration is presented by brownish-red dacites while postore alteration is manifested as intensively bleached light greenish-grey and orange dacites. Rectangles with numbers – areas of detailing: 1 – Fig. 2.7 and 2.8, 2 - Fig. 2.9, 3 - Fig. 2.10.	84
Fig. 2.7. Relics of slightly altered brownish-red dacites in the central parts of fractured blocks and narrow zones of more intensive alteration with distinct boundaries (brownish-grey dacites) along cleavage fissures. The boundaries in the lower left corner of the photograph are more diffuse. Detail of area No.1 in the Fig. 2.6. ....	85
Fig. 2.8. Zone of intensive post-ore bleaching of light-orange color (Fe oxides leaching) with narrow conjugate rim of green color (intensive illitization) along vertical fracture. The length of the GPS box is 5 cm. Detail of area No.1 in the Fig. 2.6. ....	85
Fig. 2.9. Intensively hematized dark brownish-red dacites (synore hematitization) with superimposed bleached zones of intensive postore alteration (light-orange areas along fissures) and calcite veinlets (white). Light-green zones of intensive illitization are also noticeable along a dense network of cleavage fractures (pointed with an arrow). Detail of area No.2 in the Fig. 2.6. ....	86
Fig. 2.10. Typical “background” dacites slightly altered during the preore stage with vague diffusive boundaries between less altered brownish-red and more altered brownish-grey varieties of rocks. The length of the GPS box – 5 cm. Detail of area No. 3 in the Fig. 2.6.	
Fig. 2.11. Large fractured grain of low-Fe sphalerite (sph) is intersected by an albite streak (alb) and later quartz-pitchblende veinlets (ptb) which, in turn, are crossed by an illite-quartz stringer (Q) of the 1 <sup>st</sup> postore stage. The Antei deposit, horizon +134 m. Photomicrograph of thin-polished section St-362a in plane-polarized transmitted light. ....	88

## Table of captions

- Fig.2.12. Fragments of breccia with jordisite cement (jrd) and cleophane(sph)-jordisite intergrowth are cemented with synore albite (alb) impregnated with fine-dispersed Fe oxides. The Antei deposit. Thin-polished section St-511. Photomicrograph in transmitted plane light.88
- Fig. 2.13. Individual fractures with uranium mineralization accompanied by hematitization halos in basalts. Dark-grey blocks of slightly altered basalts are noticeable in the upper central and right parts of the photograph. A wide aureole of postore bleaching is present in the left part. Hematite dispersion in the bleached zone produced light-orange to yellow color of the rock. Fault No.40, Western site of the Streltsovsky deposit, horizon +384 m.....91
- Fig. 2.14. Mineralized fault No.160 being the main ore body of the Antei deposit. Quartz-pitchblende mineralization in the linear breccia zone (black) is accompanied by hematitization of illitized granites. White – kaolinization of the 2<sup>nd</sup> postore stage along the fracture. Horizon +134 m. ....91
- Fig. 2.15. Stockwork type of streaky-disseminated uranium mineralization in trachydacites. Hematitization along thin veinlets merged into a single halo. Dark-green – chlorite films on fracture surfaces, light-grey – carbonate veins and films in fractures. Rich ore body in a cataclase zone in the Oktyabrsky deposit. Horizon +309 m.....92
- Fig. 2.16. Steeply dipping ore body with disseminated uranium mineralization and relatively wide halo of hematitization in tuff-conglomerates. Light-grey – intensively argillized conglomerates, dark brownish-red in the lower right corner – weakly altered conglomerates. Luchisty deposit, horizon +590 m.....92
- Fig. 2.17. Local bleached zones developed along fissures and cryptocrystalline quartz veinlets are superimposed on a hematitization halo in the peripheral part of the uranium ore body in basalts. Hematite is completely dissolved in areas of light-grey color of the bleaching zones while orange color indicates incomplete removal of the Fe oxides. Streltsovsky deposit, Western site, horizon + 375 m. 1 unit on the cord – 10 cm. .... **ERREUR ! SIGNET NON DEFINI.**
- Fig. 2.18. Hematite from the peripheral area of uranium mineralization is diffused along halos of intensive postore bleaching of basalts. Postore alteration develops from vertical fractured zone with chlorite mineralization (dark-grey in the left part of the photograph). Gradual transition from orange to light-yellow and light-grey tints reflects decrease of Fe oxide content in bleaching zones. The absence of Fe oxides outside the bleaching zones in slightly altered green basalts evidences that hematite diffusion occurred during the 1<sup>st</sup> postore stage. Streltsovsky deposit, Western site, horizon +384 m..... **ERREUR ! SIGNET NON DEFINI.**
- Fig. 2.19. Episyenitization zone and uranium ore body in the Antei deposit. Panorama of the the gallery wall across the Fault no. 160 with a sample location scheme. Antei deposit, horizon +84 m.....96
- Fig. 2.20. Hematized granite intersected by a linear brecciation zone with synore albite-2 cement and intensive quartz dissolution. Some pores are opened both in granite and breccia but most of them are filled by white ankerite, dark-grey calcite and pyrite of the 1<sup>st</sup> postore mineral complex. Polished sample St-620 (see Fig. 2.17 for location). Area in a rectangle is present in Fig. 2.19 as a photomicrograph.....98
- Fig. 2.21. Breccia with fine-grained albite-2 cement and pores after quartz dissolution. The pores are partly filled by ankerite. Unaltered fragment of K-feldspar of granite is noticeable in the upper part of the figure. Thin-polished section St-620 (detailed area from Fig. 2.18) in transmitted polarized light. ....98
- Fig. 2.22. Brecciated relics of outer zones of pitchblende spherulites (ptb) are cemented by quartz of the 1<sup>st</sup> postore stage (Q). Light-grey phase – U-Si metagel. Its thin stringers in quartz (for example, beneath a relic of large pitchblende spherulite in the upper part of the figure) testify to its later formation regarding quartz. Central part of the pitchblende relic mentioned in brackets is dissolved and replaced by quartz and two phases of U-Si metagel – common light-



## Table of captions

---

- grey and fine-grained white, close in intensity to pitchblende. BSE image of thin-polished section St-143d, Western site of the Streltsovsky deposit in basalts, horizon +375 m. ....100
- Fig. 2.23. Aggregate of short-prismatic synore albite is intersected and corroded by fine flakes of Ca-zeolite (light-yellow). Dark-brown in the right part – Fe oxides. Photomicrograph of thin-polished section St-630a, with analyzer. Antei deposit, ore body at the horizon +84 m. ....100
- Fig. 2.24. A zoned plagioclase crystal in a slightly altered “background” granites: the central more basic zone is completely replaced by illite and Fe-Mg carbonate while the outer more acidic zone remains practically unaltered. Antei deposit. Thin-polished section St-531, transmitted light, crossed polarizers. ....104
- Fig. 2.25. Dissemination of native copper (Cu, orange in reflected light) in quartz of the 1<sup>st</sup> generation (Q<sub>1</sub>) in a thin veinlet in basalts. Q<sub>2</sub> – cryptocrystalline quartz of the 2<sup>nd</sup> generation, clc – calcite, Q+Fe – cryptocrystalline quartz impregnated with Fe oxides. Tulukuevsky deposit. Thin-polished section St-540a, in both reflected and transmitted light, semi-crossed polarizers. Scale bar - 100 μm. ....104
- Fig. 2.26. Large pyrite crystals of the 1<sup>st</sup> generation and disseminated pyrite crystals of the 2<sup>nd</sup> generation (pyr) partly replaced by jordisite (jrd) along specific zones of pyrite. Black – cryptocrystalline quartz of the 1<sup>st</sup> preore mineral complex. Antei deposit, thin-polished section St-551c. BSE image. ....105
- Fig. 2.27. Thin veinlet of albite-2 of the uranium ore stage impregnated with Fe oxides crosscut two grains of illitized plagioclase in granites. Orientation of polysynthetic twins of albite-2 strictly coincides with that of plagioclase grains (NE in the left grain and NW in the right grain). Between these two grains, small isometric albite grains develop reflecting orientation change (epitaxial junction). Antei deposit, thin-polished section St-516-2b. Transmitted light, crossed polarizers. ....105
- Fig. 2.28. Inner part of a plagioclase grain in granites is intensively replaced with tabular albite-2 crystals with Fe oxides and fine-flake illite. Albite-2 crystals orientation coincide with plagioclase prism (epitaxy) testifies to their pre-illite formation (otherwise, aggregate of disoriented illite flakes could not provide epitaxy). The outer more acid rim of plagioclase (generally oligoclase 11-17) remained unaltered. Only hair-like stringers of illite and hematized albite-2 intersecting the rim are noticeable in the lower left corner of the photomicrograph. Antei deposit, thin-polished section St-516-2b. Transmitted light, crossed polarizers. ....107
- Fig. 2.29. Pitchblende spherulites (ptb), xenomorphic to long-prismatic Ti oxide crystals (Ti-ox) which later were intensively replaced by U-Si metagel (U-Si). Western site of the Streltsovsky deposit, ore body in basalts. Thin-polished section St-396a. Reflected plane light. ....107
- Fig. 2.30. Two first generations of quartz of the uranium ore stage. Micrograin quartz of the first generation Q<sub>1</sub> in intersected by a veinlet of coarser grained quartz of the 2<sup>nd</sup> generation Q<sub>2</sub> (a). The Western site of the Streltsovsky deposit. Photomicrograph of thin-polished section St-406 in transmitted light with crossed polarizers. Idiomorphic bipyramidal quartz crystals of the 2<sup>nd</sup> generation are overgrown by pitchblende spherulites (ptb) with partial join growth (b). Antei deposit. Photomicrograph of thin-polished section St-520 in reflected plain light. ....108
- Fig. 2.31. Idiomorphic crystal of quartz Q<sub>2</sub> is overgrown by microgranular aggregate of quartz of the 3<sup>rd</sup> generation Q<sub>3</sub> and pitchblende spherulites (light-grey). Typical ore of the Antei deposit. Photomicrograph of thin-polished section St-602 in plane reflected light. ....108
- Fig. 2.32. Pitchblende spherulites (ptb) overgrew prismatic brannerite crystals (brn) which, in turn, overgrew quartz crystals of the 2<sup>nd</sup> generation (Q<sub>2</sub>). Fluorite (flr) and calcite (crb) of the 1<sup>st</sup> postore stage grew on the pitchblende surface. Western site of the Streltsovsky deposit, ore body in basalts. Photomicrograph of thin-polished section St-406 in plane reflected light. ....109



## Table of captions

- Fig. 2.33. Tight intergrowth of prismatic brannerite crystals (grey) and pitchblende (light-grey, white) in pseudomorphs over Ti-magnetite in basalts. Western site of the Streltsovsky deposit. BSE images of thin-polished section St-112..... 109
- Fig. 2.34. Pitchblende of the early fine-spherulitic generation (ptb-f1) cements dacite fragments (dac) and is overgrown by pitchblende of the coarse-spherulitic generation (ptb-c). Calcite of the 1<sup>st</sup> postore stage (crb) cements fragments of the latter. U-Si metagel (U-Si) intensively replaces dacite fragments and thin pitchblende veinlets in dacite. Quartz of the 1<sup>st</sup> postore stage forms complete pseudomorphs (Q<sub>flr</sub>) after octahedral crystals of fluorite of the 1<sup>st</sup> generation (rhombs and triangles in the section plane) paragenic with pitchblende ptb-f1. Oktyabrsky deposit. Photomicrograph of thin-polished section St-220d in plane reflected light. .... 111
- Fig. 2.35. Three generations of anisotropic pitchblende with fluorite. Coarse-spherulitic pitchblende (ptb-c) overgrows large octahedral fluorite crystals of the 2<sup>nd</sup> generation (flr-2) and massive aggregate of the early fine-spherulitic pitchblende (ptb-f1). Fragments of ptb-f1 and ptb-c pitchblende are cemented by a fine aggregate of the late fine-spherulitic pitchblende (ptb-f2) and small octahedral crystals of the 3<sup>rd</sup> fluorite generation (flr-3) saturating pitchblende aggregate. Fluorite of both generations is partly replaced by galena (small white segregations). Central site of the Streltsovsky deposit, a rich ore body in dacites. Photomicrograph of thin-polished section St-77c in reflected light with crossed polarizers... 111
- Fig. 2.36. The medium-spherulitic pitchblende generation (ptb-m) formed after the coarse-spherulitic generation (ptb-c) and before the late fine-spherulitic one (ptb-f2). Central site of the Streltsovsky deposit, a rich ore body in dacites. BSE image of thin-polished section St-77b. .... 113
- Fig. 2.37. Octahedral crystals of fluorite of the 2<sup>nd</sup> generation (flr-2) are overgrown by large spherulites of anisotropic pitchblende ptb-c. Q – quartz of the 1<sup>st</sup> postore stage. Steps on the faces of fluorite octahedrons (pointed with arrows) indicate complementary growth of fluorite when small nuclei of pitchblende spherulites temporarily stopped their growth. Thus, partial joint growth of the 2<sup>nd</sup> fluorite generation and pitchblende ptb-c is established. Central site of the Streltsovsky deposit. Photomicrograph of thin-polished section St-77c in both transmitted and reflected light with semi-crossed polarizers. .... 113
- Fig. 2.38. A pore in episyenitized zone in granites is partly filled with ankerite (ank) and quartz (Q) grown on ankerite. E.R. – epoxy resin (pore), K-fsp and Pl – consequently microcline and plagioclase of granite. Antei deposit. Photomicrograph of thin-polished section St-617 in transmitted light with crossed polarizers ..... 115
- Fig. 2.39. Albite of the 1<sup>st</sup> postore stage (alb) grown on microcline grains of granite (K-fsp) in a pore (E.R. – epoxy resin) in the episyenitized zone. Antei deposit. Photomicrograph of thin-polished section St-621 in transmitted light with crossed polarizers. .... 115
- Fig. 2.40. Pitchblende spherulites (ptb) are replaced by leucoxene (lcx) along fractures and inductive surfaces, and later – by U-Si metagel (U-Si). Western site of the Streltsovsky deposit. Photomicrograph of thin-polished section St-396a in plane reflected light, with water immersion. .... 117
- Fig. 2.41. Quartz of the 1<sup>st</sup> postore stage with inlayers of fine flakes of illite (ilt) in inner growth zones. After these zones quartz was splitted on sub-domains (pointed with arrows). Antei deposit. Photomicrograph of thin-polished section St-21b in transmitted light with crossed polarizers. .... 117
- Fig. 2.42. Pitchblende (ptb) is intensively replaced by becquerelite (bcq). The latter is overgrown by yellow variety of U-Si metagel (U-Si). Oktyabrsky deposit. Photomicrograph of thin-polished section St-211a in plane transmitted light. .... 118
- Fig. 2.43. Pitchblende relics (small white phases) in becquerelite pseudomorphs (light-grey phase). The latter is cemented by yellow U-Si metagel (dark-grey phase), intersected by its

## Table of captions

- thin veinlets and partly replaced. Black – aluminosilicate matrix of dacite. Oktyabrsky deposit. BSE image of thin-polished section St-211a. .... 118
- Fig. 2.44. Fluorite crystals (flr) grew on thin quartz comb and then grew simultaneously with quartz (Q) forming inductive surfaces of joint growth. A cubic surface of fluorite was overgrown by the late quartz generation. After fluorite, late carbonate (crb) and chlorite (chl) were deposited. Centralny site of the Streltsovsky deposit. Photomicrograph of thin-polished section St-77 in transmitted light with crossed polarizers..... 119
- Fig. 2.45. Quartz-pyrite-carbonate association of the 1<sup>st</sup> postore stage. Pyrite (pyr) is xenomorphic relative to quartz (Q) and corrodes the latter (indicated with arrows). Mn-calcite (clc) is xenomorphic to quartz and pyrite. It dissolved pyrite almost completely (in the lower right corner of the figure). Antei deposit. Photomicrograph of thin-polished section St-510 in reflected plane light. .... 119
- Fig. 2.46. Quartz of the 1<sup>st</sup> postore stage (Q) is overgrown by 3 chlorite generations (chl-1, chl-2, and chl-3). Central part of the veinlet is filled by calcite (crb). Western site of the Streltsovsky deposit. Photomicrograph of thin-polished section St-120 in plane transmitted light..... 120
- Fig. 2.47. Illite (ilt) fills the central part of a veinlet growing on quartz of the 1<sup>st</sup> postore stage (Q), early ankerite (crb) and albite of the uranium ore stage (alb). Intensive corrosion of quartz and albite by illite is noticeable. Antei deposit. Photomicrograph of thin-polished section St-551d in transmitted light with crossed polarizers..... 120
- Fig. 2.48. Paragenetic association of polyphase U-Si metagel with chlorite (a) and native antimony (b). Panel (a): more uranium phase of U-Si metagel (white) deposited on the walls of a pore in postore quartz (black) while its central part is filled with more siliceous U-Si metagel (grey) with chlorite flakes (dark-grey). Panel (b): skeleton crystals of native antimony (white) in U-Si metagel (grey); black – quartz of the 1<sup>st</sup> postore stage. Central site of the Streltsovsky deposit. BSE images of thin-polished section St-77a. .... 121
- Fig. 2.49. Walls of a pore in dacites are covered by a U-Si metagel (U-Si, white) which is overgrown by a complex gel of variable composition (Si-Fe-Na-Al-Ca, grey) with segregations of a lighter Mo-Fe-Si gel. Central part of the pore is filled by calcite (clc) impregnated with small prismatic coffinite crystals (cfn). Thin light-grey rim in the base of calcite filling is also composed of coffinite crystals. Oktyabrsky deposit. BSE image of thin-polished section St-220-1..... 121
- Fig. 2.50. Polyphase U-Si metagel (different shades of grey) in a veinlet in basalts (black at the top) with a relic of pitchblende spherulite (ptb, white). Linear cracks in U-rich phase (light grey) along which diffusion of Si-rich phase (dark grey) occurred are indicated with arrows. Central pore in Si-rich phase and numerous fissures of shrinkage are noticeable. Western site of the Streltsovsky deposit. BSE image of thin-polished section St-396a. .... 122
- Fig. 2.51. A colloform rhythmically zonal segregation of polyphase U-Si metagel grown on pyrite grain (pyr) in a veinlet of quartz of the 1<sup>st</sup> postore stage. More uranium phases are brighter and more siliceous – darker. Antei deposit. BSE image of thin-polished section St-501..... 122
- Fig. 2.52. Fluorite crystals that were overgrown by pitchblende (ptb) was completely replaced by quartz (Q) and carbonate (crb) of the 1<sup>st</sup> postore stage. Fluorite presence may be induced only from the shape of protocrytals decorated by pitchblende. Western site of the Streltsovsky deposit. Photomicrograph of thin-polished section St-125 in plane reflected light. 123
- Fig. 2.53. Coarse-spherulitic pitchblende (ptb-1) grew on presumably fluorite crystals (former contours are shown by magenta dashed line). After complete dissolution of fluorite and conceivably some part of pitchblende during episyenitization (?), redeposited pitchblende (ptb-2) precipitated on the cavity walls (growth directions are indicated by red arrows). The rest of the vug was filled by quartz (Q<sub>flr</sub>). Besides, some part of coarse-spherulitic pitchblende (ptb-1) and redeposited pitchblende (ptb-2) was metasomatically replaced by quartz (Q<sub>ptb</sub>).

## Table of captions

- Directions of metasomatic quartz development are pointed by blue arrows. Centralny site of the Streltsovsky deposit. BSE image of thin-polished section St-77b.....123
- Fig. 2.54. Different forms of pitchblende replacement by U-Si metagel – diffusive (a) and corrosive (b). Panel (a): Two U-Si metagel phases developed after pitchblende (ptb): early more uranium (light-grey, U-Si<sub>1</sub>) and late more siliceous (dark-grey, U-Si<sub>2</sub>). Gal – galena segregations. Fuzzy areas of incomplete diffusive replacement of pitchblende are indicated by arrows. Pane (b): Core parts of pitchblende spherulites (light-grey) are corroded by two phases of U-Si metagel (grey, dark-grey). The latter also corrosively replaces intermediate spherulite zone along pitchblende fibers. Oktyabrsky deposit. BSE image of thin-polished section St-220.....126
- Fig. 2.55. A pitchblende spherulite (ptb) resorbed during episyenitization (?) and cemented by quartz of the 1<sup>st</sup> postore stage (Q). The latter was replaced by U metagel (U) in close intergrowth with fine chlorite (?) flakes (chl) and later – by siliceous U-Si metagel (U-Si). Area outlined by a violet rectangle in the left part of the figure is exhibited in the right part. A fragment from Fig. 2.20. Western site of the Streltsovsky deposit. BSE image of thin-polished section St-143d. ....126
- Fig. 2.56. Pitchblende (ptb) is intensively corroded by jordisite (jrd) containing globular (ring-shaped) and flaky segregations of lead sulfide (Pb). Streltsovsky deposit. BSE image of thin-polished section St-85/67a (the sample was kindly presented by Dr. Igor V. Mel'nikov). .....129
- Fig. 2.57. Polyphase Mo-S metagel. Early light-grey phase (Mo-1) covers the walls of the pore. It is overgrown by intermediate grey phase (Mo-2), and the central part of the pore is filled by late light-grey phase (Mo-3). Shrinkage fissures are the most marked and abundant in the 2<sup>nd</sup> grey phase. Ptb – fine pitchblende spherulites. Antei deposit. Photomicrograph of thin-polished section St-366b in plane reflected light. ....129
- Fig. 2.58. Polychrome (blue, violet and yellow) fluorite of the 2<sup>nd</sup> postore stage. Porcelain-like variety of fluorite (light-pinky) is the latest generation filling the cavity between crusts of yellow fluorite and “garbage” aggregate of rock debris and blue fluorite. Central site of the Streltsovsky deposit. Sample St-176. ....132
- Fig. 2.59. A fragment of hematized dacite is overgrown by rhythmical crusts of dark-violet fluorite and pyrite (pyr). This aggregate was later cemented by “garbage” dark-blue fluorite interlaid with porcelain-like light-blue fluorite. Then that all was overgrown by thin dark-violet fluorite crust and calcite (clc). Mineralogical levels composed of porcelain-like fluorite are shown by red arrows. Central site of the Streltsovsky deposit. Sample St-176. ....132
- Fig. 2.60. Porcelain-like fluorite composed of grains of colorless, blue and pinky fluorite intensively impregnated by fine kaolinite flakes. Density of the latter is higher in outer parts of crystals and in intergranular space. Central site of the Streltsovsky deposit. Photomicrograph of thin-polished section St-176 in plane transmitted light. Scale bar – 20 μm. ....133
- Fig. 2.61. Chlorite-fluorite aggregate with jordisite (jrd) segregations. Two chlorite generations are noticeable in fluorite (flr): more Fe-rich (chamosite, chl-Fe in the figure) and less Fe, more Mg (Fe-prochlorite, chl-Mg). Kaolinite (kaol) forms close intergrowth with quartz (Q). Central cite of the Streltsovsky deposit. BSE image of thin-polished section St-176. Points of EDS analysis are shown. ....133
- Fig. 2.62. Idiomorphic quartz crystals of the 2<sup>nd</sup> postore stage (grey) are partly resorbed and overgrown by fine chlorite-kaolinite aggregate. Chlorite (small white dots and flakes) is in tight even intergrowth with synchronous kaolinite individuals (fine grey phases) that testifies to their paragenesis. Antei deposit. BSE image of thin-polished section St-517a. ....134
- Fig. 2.63. Large flakes of molybdenite (mlb) are located in colorless, light-violet and pinky fluorite (flr). Similar fine molybdenite flakes occur in intergranular space of fine-grained fluorite in the upper left corner of the figure. Kaolinite segregations (kaol) are saturated with

## Table of captions

Fe oxides (Fe). Central site of the Streltsovsky deposit. Photomicrograph of thin-polished section St-176 in both transmitted and reflected plane light. Scale bar – 20 $\mu\text{m}$ . .....	134
Fig. 2.64. The average contents of Ca, Zr, and Fe in pitchblende located in different rocks (basalts, dacites, granites). From the data of electron microprobe analysis (in wt.%).....	138
Fig. 2.65. The average contents of Ca, Zr, and Fe in the least altered host rocks of the SOF deposits (basalts, dacites, granites). From the data of ICP-AES and XRF analyses (in ox.%).....	138
Fig. 2.66. Aggregate of the zonal coarse-spherulitic pitchblende (different shades of grey) overgrown fluorite crystals and fragments of dacites (black). Magenta line – a profile of electron microprobe analysis presented in Fig. 2.67 and 2.68. Central site of the Streltsovsky deposit. BSE image of thin-polished section St-77c. SEM Hitachi S-2500. ....	139
Fig. 2.67. Contents of Ca, Pb, and Zr (in wt.%) along the profile of electron microprobe analysis shown in Fig. 2.66. The detailed BSE image along the profile is shown in the low part of the figure. The direction of the pitchblende growth is indicated by an arrow.....	140
Fig. 2.68. Contents of Fe, Ti, and As (in wt.%) along the profile of electron microprobe analysis shown in Fig. 2.66. The detailed BSE image along the profile is shown in the low part of the figure. The direction of the pitchblende growth is indicated by an arrow.....	140
Fig. 2.69. Ternary diagram of U, Si, and Ca contents in the U-Si metagel (from the data of the electron microprobe analysis, in at.%).....	143
Fig. 2.70. Thin crust of the U-Si metagel grown on the pyrite grain (black). Alternating of brown and green zones in the metagel is noticed. Antei deposit. Photomicrograph of thin-polished section St-501 in plane transmitted light.....	143
Fig. 2.71. Different colors of the U-Si metagel (U-Si) – light-yellow, light-brown and dark-brown – in neighbour segregations. Exocontact zone of the pitchblende veinlet (ptb) with calcite (crb) and former fluorite ([flr]). The latter was completely replaced by chlorite-carbonate aggregate during the 1 <sup>st</sup> postore stage. High-grade ore body in the Oktyabrsky deposit. Photomicrograph of thin-polished section St-220-3 in plane transmitted light.....	145
Fig. 2.72. Amorphous particles of the U-Si metagel with diffused microdiffraction halos. HRTEM image in bright field. ....	145
Fig. 2.73. A particle of the U-Si metagel saturated with fine (3-5 nm) crystallites of uraninite (ring reflexes in the left insertion) and a larger crystallite of possibly coffinite (point reflexes in the right insertion). HRTEM image in dark field (crystalline phases are bright). ....	146
Fig. 2.74. Composition of light micas located in different rocks (from electron microprobe data, in at.%). Figurative points of normative composition of smectite and kaolinite are indicated by yellow crosses, and illite – by an oval. Trends of the composition change are shown by arrows. ....	146
Fig. 2.75. Composition of light micas in the quartz veinlet, bleached basalts and background basalts (from the data of electron microprobe analysis, in wt.%). Western site of the Streltsovsky deposit, sample St-139. ....	149
Fig. 2.76. Composition of chlorites developed in the SOF deposits in different rocks (from the electron microprobe analyses, calculated from at.%) plotted on the Winchell-Tröger diagram (Tröger, 1959). Large symbols denote the average compositions of chlorites located in the appropriate rocks. ....	149
Fig. 2.77. Chondrite normalized REE patterns in fluorite of the 1 <sup>st</sup> postore stage (a) and the 2 <sup>nd</sup> postore stage (b) of the Streltsovsky deposit, Gozogor (c) and Abagaityi (d) deposits (from the data of ICP-MS analysis).....	152
Fig. 2.78. Spectra of X-ray (a-h), cryophoto (i) and laser-excited (j) luminescence of fluorite: a – sample St-77 before ignition, b – sample St-77 after ignition, c-e – fluorite of the 1 <sup>st</sup> postore stage from sites with different U content from the Streltsovsky deposit after ignition, f – fluorite of the 2 <sup>nd</sup> postore stage from the Streltsovsky deposit, g – fluorite from the Gozogor	



## Table of captions

deposit after ignition; h – fluorite from the Abagaityi deposit; i-j – CPL and LEL spectra of fluorite of the 1 <sup>st</sup> postore stage from the Streltsovsky deposit.....	153
Fig.2.79. Dependence between intensities of REE in luminescence spectra of fluorite and U content in host rocks: a – relation between $I(\text{Eu}^{2+}, \text{XRL})$ (1), $I(\text{Gd}^{3+}, \text{XRL})$ (2), $I(\text{Eu}^{2+}, \text{CPL})$ , (3) and U in dacites; b – relation between ratios of $\text{Eu}^{2+}/\text{Yb}^{2+}$ (CPL) (1), $\text{Gd}^{3+}/\text{Er}^{3+}$ (XRL) (2), $(\text{Sm}_{604}^{3+}/\text{Er}^{3+})$ (XRL) (3) and U in dacites.....	154
Fig. 2.80. Diagram of the ranged $R_{\text{element}}$ ratios in basalts, dacites, and granites reflected the gain (if > 1) and the loss (if < 1) of elements during intensive illitization of host rocks. ....	159
Fig. 2.81. U and Th contents in basalts, granites and dacites subjected to moderate and intensive postore alteration (from ICP-MS and INAA data). Data with high U contents in the dacites (up to 396 ppm U) and in the granites (up to 274 ppm U) are trimmed.....	161
Fig. 2.82. U and Th contents in background basalts, granites and dacites subjected to weak preore alteration (from ICP-MS and INAA data).....	161
Fig. 2.83. An ore body in basalts with associated albitization and hematitization, and superimposed bleached zones along fissures. The ore body is crosscut by a vein of the postore calcite. Samples of differently altered rocks are shown in the lower part of the figure. The northern wall of the gallery in the Western site of the Streltsovsky deposit, horizon +383 m.....	163
Fig. 2.84. Diagram of U contents in groundmass (in ppm), phenocrysts and leucoxene aggregates in basalts subjected to alteration of different type and intensity. ....	166
Fig. 2.85. Chemical composition of episyenitized granites on the Le Bas diagram indicating relative alkali gain against the silica loss. Numbers near points on the diagram correspond to sample numbers. Background granites have been sampled outside the considered cross-section.....	168
Fig. 2.86. Chondrite-normalized REE patterns of pitchblende.(a) Hosted in dacite, (1, 2) sample St-220h, (3–8) sample 85-67a from the collection of I.V. Mel'nikov; (b) hosted in granite, (1, 2) sample St-602, and basalt, (3, 4) sample St-391. (I–IV) Tetrads; $t_1$ and $t_3$ are the values of the tetrad effect in tetrads I and III, respectively. ....	171
Fig. 2.87. Chondrite-normalized REE patterns of (a) basalt, (b) dacite, (c) Variscan granite, and (d) rhyolite in the SOF from ICP-MS data. ....	171
Fig. 2.88. LREE/HREE ratio of pitchblende hosted in granite, dacite, and basalt and of host rocks. (1) Pitchblende, (2) rocks.....	172
Fig. 3.1. (a, b) $T_{\text{hom}}$ vs. $T_{\text{m.eut}}$ and (c, d) $T_{\text{hom}}$ vs. C for FIs for the (a, c) Antei and (b, d) Streltsovsky deposits. (1) Quartz $Q_1$ and (2) quartz $Q_2$ of the uranium ore stage; (3) quartz of the 1 <sup>st</sup> postore stage. The dashed line separates the fields of sodium chloride and sodium bicarbonate–chloride solutions.....	181
Fig. 3.2. $T_{\text{hom}}$ vs. $T_{\text{m.eut}}$ (a) and $T_{\text{hom}}$ vs. C (b) for FIs in quartz of the ore stage in the Streltsovsky and the Antei deposits. High-temperature quartz of the 1 <sup>st</sup> generation ( $Q_1$ ) is marked with the dashed area.....	182
Fig. 3.3. $T_{\text{hom}}$ vs. $T_{\text{m.eut}}$ (a) and $T_{\text{hom}}$ vs. C (b) for FIs in quartz of the 1 <sup>st</sup> postore stage in the Streltsovsky and the Antei deposits located in ore bodies of different grade.....	182
Fig. 4.1. Initial temperature distribution after emplacement of the intrusion (hatched rectangle).....	202
Fig. 4.2. Variation of temperature distribution during crystallization of the intrusion. (1) $t = 3.25$ ka (region of melt has been reduced by 25%); (2) $t = 13.7$ ka (region of melt has been reduced by 50%); (3) $t = 31.4$ ka (region of melt has been reduced by 75%); (4) $t = 56.3$ ka (intrusion has completely solidified); (5) $t = 75$ ka (the temperature of the entire intrusion is lower than the temperature of melt crystallization and continues to fall due to thermal conduction to the country rocks). The intrusion is hatched. ....	202
Fig. 4.3. Variation of temperature distribution after complete crystallization of melt. $t =$ (1) 100 ka, (2) 200 ka, (3) 500 ka, (4) 1 Ma, and (5) 3 Ma. The intrusion is hatched. The dashed line	

## Table of captions

---

indicates an unperturbed temperature distribution that corresponds to the accepted geothermal gradient.....	203
Fig. 4.4. Variation of the main physicochemical parameters of hydrothermal fluids at the preore, uranium ore, and first postore stages and geochemical specialization of the respective mineral complexes. (1–3) Isotopic age of hydromica (Andreeva et al., 1996) and pitchblende (Chernyshev and Golubev, 1996): (1) K–Ar age of hydromica, (2) Rb–Sr age of hydromica and ankerite, (3) U–Pb age of pitchblende. ....	210

## List of tables

Table 2.1. Isotopic ages of hydromica metasomatites in the SOF (Andreeva et al., 1996)	89
Table 2.2. Statistical parameters of brannerite composition from microprobe data (SX-50, SX-100, UHP), in wt.%.	109
Table 2.3. Average composition of polyphase Mo-S metagel (average from 2 analyses for each phase, from SX-100 microprobe data, in wt.%).	128
Table 2.4. The average contents of elements and the main statistical parameters of their distribution in the pitchblende (from the data of electron microprobe SX-50 and SX-100, in wt.%).	136
Table 2.5. The average contents of elements and the main statistical parameters of their distribution in the pitchblende grouped by the host rocks (from the data of electron microprobe SX-50 and SX-100, in wt.%).	137
Table 2.6. Average composition of the U-Si metagel from the data of electron microprobe analysis (in wt.%).	141
Table 2.7. Composition of samplings on geochemical analyses of host rocks affected by the preore and the postore alteration.	157
Table 2.8. Statistical results of U quantification in different components of basalts by fission track radiography (in ppm).	164
Table 3.1. Main physicochemical parameters of hydrothermal fluids in the Streltsovsky and Antei deposits, from fluid inclusion studies in quartz.	184
Table 3.2. Temperature, salinity and gas composition in comb-like quartz of the 1 <sup>st</sup> postore stage regarding the grade of uranium mineralization in the Streltsovsky deposit.	186
Table 3.3. Temperature, salinity and gas composition in comb-like quartz of the 1 <sup>st</sup> postore stage regarding the grade of uranium mineralization in the Antei deposit.	186





## Acknowledgments

This work has been done as a logical continuation of long lasting joint studies of specialists from CREGU and from IGEM (Moscow, Russia) aimed on investigation of formation conditions of Mo-U mineralization of the Streltsovsky ore field (SOF) accumulated in unique a geological setting. By such a way the studies provided by the author performed in close cooperation with numerous geologists from CREGU and COGEMA have been facilitated tremendously.

Firstly, I would like to express my endless heart appreciation to my French chief **Michel CUNEY** who made efforts to initiate my work in a new status, organized full access to sophisticated equipment being available at G2R and UHP, showed unlimited patience with such a disorganized person like me during all these years, and shared with me his encyclopaedic knowledge on various aspects of uranium mineralization in numerous discussions. Separately, I am grateful to him and his wife **Liliane** who heartly received me at their house during my stay in France and let me discover their beautiful country “from inside”.

I am also exceedingly thankful to my Russian chief, professor **Vasilii VELICHKIN** who guided this work from the Russian side and provided all necessary support starting with field works and finishing with discussion of the results obtained. His extensive experience in uranium behavior in magmatic processes and related hydrothermal activity helped me greatly in elaborating of the final genetic model of uranium mineralization in the SOF deposits.

I feel sincere gratitude to **Michel CATHELIN** and **Jean DUBESSY** for their brief but very effective advices concerning uranium geochemistry and about the inner world of fluid inclusions. The latter have been investigated with the priceless help of **Tatiana KRYLOVA** – a good deal of the genetic model is based on her data obtained with the support of a “fairy of Raman spectroscopy” – **Thérèse LHOMME**. I am obliged to you so much.

Invaluable help in 3D modeling of ore bodies in one of the SOF deposits was rendered by an indisputable authority in the gOCAD software **Christian LE-CARLIER** and his assistant **Claire VERMET**. I heartly appreciate the efforts they made despite overloading by their own work.

I am also very grateful to **Jessica BONHOURE** for her help in getting data on REE distribution in pitchblende from the SOF deposits. It occurred to be one of the key factors for constraining the genetic model of uranium mineralization.

## Acknowledgments

---

Special thanks I should express to **Marc BROUAND** who permanently supported me in providing microprobe and scanning electron microscope studies, selflessly helping in terrible organization problems.

Thin sections are “the eyes” of a mineralogist and **Cedric DEMEURIE** helped “my eyes” to get opened finishing my sections which I had no time to finish in Moscow, giving me his equipment for my needs, and teaching his techniques. It is difficult to overestimate your help Cedric, now I make one of the best sections in Moscow in many respects due to your tricks!

All former and present staff of **G2R, CREGU, UHP** (Service Commun) (Nancy, France) and in particular: Bernard POTY (thank you so much for your participation in my fate), Mr. SCHUHMACHER and the secretary team: Marie Odile, Laurence, Christine, Patrick LAGRANGE, Roland MAIRET (Magnificent Administrator), Marc LESPINASSE, Alain KOHLER, Laurent RICHARD (the Russian-Belgian Friendship Voluntary Society of the BEER LOVERS), Cedric CARPENTIER, Laurent DESINDES, Remy CHEMILLAC, Greg ANDRE, Donatienne DEROME - you greatly supported me during the first year and so on...

From the Russian part, I would like to express my kind regards to **Lidiya ISHCHUKOVA** who gave me first lessons of geological mapping and uranium survey in NW China in 1993 and later shared with me her tremendous knowledge on the SOF deposits. I also extremely thankful to all geologists of the Priargunsky enterprise (PPGKhO) who helped me greatly in providing my field works, supplying with geological maps and other materials, especially to **Sergei SHCUKIN, Victor TOLSTOBROV, Boris PROSEKIN** and many other geologists at mines. My special thanks to **Ludmila SERDYUK** – the only mineralogist in the SOF – for her help and support all these years.

I heartily appreciate the help of **Yury DYMKOV** – the greatest specialist in genetic mineralogy and my teacher since dozens of years. The most what I achieved in mineralogy I am obliged to you.

I also thank many people who participated in this work by discussions, hot debates, corrections, criticism, approval, and just by friendly words...

## Résumé

Les nouveaux travaux que nous avons réalisés nous ont permis d'établir que U et F ont été progressivement enrichis depuis les volcanites basiques (170 Ma), jusqu'aux volcanites acides (140 Ma). L'épisode hydrothermal post-magmatique Crétacé (140-125 Ma) a été subdivisé en stades: préminéralisation, synminéralisation et les premier et deuxième stades post-minéralisation. La minéralisation primaire à brannérite-pechblende est associée avec la fluorite. Lors du premier stade postminéralisation les minéraux d'U ont été remplacés par des méta-gels U-Si antérieurement identifiés comme de la coffinite. L'altération anté-minéralisation et la minéralisation U ont été formées par des fluides chlorurés et bicarbonatés sodiques entre 250 et 300°C. La minéralisation U a commencé avec une albitisation et une hématisation de l'encaissant lors de la percolation d'un fluide supercritique à 530-500°C. Brannérite et pechblende ont précipité vers 350-300°C. Les spectres des éléments des terres rares (ETR) de la pechblende localisée dans les trachybasaltes, trachydacites et granites ont une forte anomalie positive en Sm et Nd et un effet tétrade W marqué, caractéristiques différentes de celles des rhyolites dérivées d'une chambre magmatique localisée dans la croûte supérieure. Ces données et l'intervalle de 5 Ma séparant le magmatisme siliceux de la formation de la minéralisation U ne permet pas de proposer que l'U dérive de cette chambre. Nous proposons qu'un magma acide riche en Li et F est la source de l'U. U(IV) ainsi que les ETR ont été fractionnés dans les fluides comme complexes fluorés. La minéralisation U a été déposée au niveau d'une barrière



## Abstract

The ambiguity in the genetic interpretations of uranium ore formation for the Mo–U deposits of the Streltsovsky ore field led us to perform additional geochemical, mineralogical, and thermobarogeochemical studies. As a result, it has been established that closely associated U and F were progressively gained in the Late Mesozoic volcanic rocks from the older basic volcanics (170 Ma) to the younger silicic igneous rocks (140 Ma). The Early Cretaceous postmagmatic hydrothermal epoch (140–125 Ma) is subdivided into preore, uranium ore, and first and second postore stages. The primary brannerite–pitchblende ore was formed in association with fluorite. During the first postore stage, this assemblage was replaced by a U–Si metagel, which was previously identified as coffinite. The metagel shows a wide compositional variation; its fine structure has been studied. The preore metasomatic alteration and related veined mineralization were formed under the effect of sodium (bicarbonate)–chloride solution at temperatures of 250–200°C. Uranium ore formation began with albitization and hematization of rocks affected by a supercritical fluid at 530–500°C; brannerite and pitchblende precipitated at 350–300°C. The chondrite-normalized REE patterns of pitchblende hosted in trachybasalt, trachydacite, and granite demonstrate a pronounced Sm–Nd discontinuity and a statistically significant tetrad effect of W type. These attributes were not established in REE patterns of rhyolites derived from the upper crustal magma chamber. These data and the chronological gap of 5 Ma between silicic volcanism and ore formation do not allow us to suggest that uranium was derived from this magma chamber. According to the proposed model, an evolved silicic Li–F magma was a source of uranium.  $U^{4+}$ , together with REE, were fractionated into the fluid phase as complex fluoride compounds. The uranium mineralization was deposited at a temperature barrier. It is suggested that hydromica alteration and the formation of molybdenum mineralization were genetically unrelated to the uranium ore formation.



## Резюме

Неоднозначность генетических интерпретаций процесса уранового рудообразования на Mo-U-месторождениях Стрельцовского рудного поля обусловила необходимость проведения дополнительных комплексных геохимических, минералогических и термобарогеохимических исследований. В результате выявлен "геохимический парагенезис" U и F, которые закономерно накапливались в позднемезозойских вулканических породах: от ранних основных (170 млн. лет) до поздних кислых (140 млн. лет). В постмагматическом раннемеловом гидротермальном этапе (140–125 млн. лет) выделены четыре стадии: дорудная, урановорудная, первая и вторая пострудные. Первичные браннерит-настурановые руды отлагались в парагенезисе с флюоритом, а в 1-ю пострудную стадию они были интенсивно замещены U-Si метагелем, который ранее считался коффинитом. Приведены данные о коллоидной природе U-Si метагеля, показаны широкие вариации его состава, изучена тонкая структура.

Метасоматические изменения и образование жильной минерализации в дорудную стадию происходило из натрово-(бикарбонатно)-хлоридных растворов при температуре от 250 до 200°C. Процесс уранового рудообразования начинался с альбитизации и гематитизации пород при 530–500°C при воздействии на них окологритического флюида, а отложение браннерита и настурана происходило при понижении температуры до 350–300°C.

Изучение распределения редкоземельных элементов (РЗЭ) в настуране, локализованном в трахибазальтах, трахидацитах и гранитах, выявило резко выраженный Sm-Nd разрыв в нормированных кривых и статистически значимый тетрадный эффект W-типа. Данные признаки отсутствуют в распределении РЗЭ в риолитах, которые образованы при излиянии кислой магмы из верхнекорового очага. Это обстоятельство, а также значительный (5 млн. лет) временной разрыв между кислым вулканизмом и рудообразованием, не позволяют считать данный очаг потенциальным источником урана.

Согласно предлагаемой авторами гипотезе, источником урана была эволюционировавшая кислая Li-F магма, от которой  $U^{4+}$  вместе с РЗЭ отделялся во флюидную фазу в виде комплексных фторидных соединений. Отложение урановой минерализации происходило на температурном барьере. Предполагается, что

## Резюме

---

гидрофлюидизация пород и образование молибденовой минерализации генетически не связаны с урановорудным процессом.



## Résumé étendu

Dix neuf gisements à Mo-U avec des réserves totales en uranium de 250 000 tonnes U sont localisées dans une caldera s'étendant sur 140 km<sup>2</sup>. Non seulement les réserves importantes en U mais aussi ses relations avec magmatisme contrasté tardi-mésozoïque avec basalte-dacite-rhyolite font de Streltsovsky un champ minéralisé en uranium de classe mondiale, sans équivalent du point de vue de la signification économique par rapport aux autres gisements à Mo-U associés à des roches volcaniques. L'ambiguïté sur les interprétations génétiques de la formation des minéralisations en uranium a conduit l'auteur à développer ses propres travaux de recherche afin de tenter de clarifier certains des aspects génétiques sur la formation des minerais, et d'élaborer sur cette base des guides pour l'exploration de minéralisations du même type.

Une tendance générale a été établie pour les roches volcaniques et consiste en leur enrichissement en U et F depuis les roches les plus anciennes (170 Ma) et les plus basiques (2.0- 2.5 ppm U and 0.3 wt. % F) à travers des roches intermédiaires et modérément siliceuses (10 ppm U et ? F) jusqu'aux plus jeunes (140 Ma) et les plus siliceuses (15-25 ppm U et ~3 wt. % F). Ainsi, nous avons à faire à une association géochimique U-F progressivement accumulée dans les roches ignées pendant le tardi-mésozoïque, qui témoigne indirectement ses relations avec la paragenèse à pechblende-fluorite des minéralisations postmagmatiques.

Le système hydrothermal postmagmatique éocène (140-125 Ma) est subdivisé en stades: pré-minéralisation, syn-minéralisation, et les premiers et seconds stades post-minéralisation. Pendant le stade pré-minéralisation, les roches du socle et de la pile sédimentaire-volcanique de la caldera ont toutes deux été soumises à une altération argileuse pervasive mais peu intense avec chloritisation, carbonatation et silicification. L'altération métasomatique a été accompagnée par la formation de filonnets de quartz cryptocristallins avec pyrite et des sulfures de Mo et Zn. Le minerai primaire à brannérite-pechblende a été formé en association avec de la fluorite et du quartz pendant le stade de la minéralisation à uranium. Il a été suivi par de l'albitisation et de l'hématite dans des zones étroites. A la fin du premier stade postminéralisation, cet assemblage a été intensivement remplacé par un métagel à U-Si, qui avait été antérieurement identifié comme de la coffinite. Une altération plus locale mais plus intense et similaire à celle du stade pré-minéralisation s'est développée le long de fissures et de filonnets à quartz-fluorite-carbonate associés à de la pyrite et des sulfures de Mo, Zn, Cu et autres chalcophiles. Des filonnets de fluorite polychrome avec du

## Resume etendu

---

quartz et de la calcite suivis par des zones étroites de kaolinisation ont été développés durant le second stade post-minéralisation en quantité subordonnée relativement aux stades antérieurs.

L'étude détaillée de la phase à U-Si a révélé qu'elle était polyphasée avec une large variation des rapports U/Si (2/1-1/2 en % at.), que sa structure était zonaire et métacolloïdale lors de son dépôt, qu'elle renfermait de nombreuses fissures de retrait, et qu'elle était généralement amorphe. De même l'absence de faces cristallines dans ces ségrégations, montre de manière non ambiguë la nature colloïdale de cette phase. Des cristallites d'uraninite et de coffinite de 3-15 nm ont été détectés dans certaines des phases à U-Si riches en U indiquant le début de la cristallisation de ces métagels.

L'étude des inclusions fluides révèle que l'altération métasomatique pré-minéralisation et les minéralisations filoniennes associées se sont formées à partir de solutions chlorurées sodiques-(bicarbonatées) à une température de 210°C. La minéralisation d'uranium débute avec l'albitisation et l'hématisation des roches associées avec un fluide supercritique à 530-500°C. Brannérite et pechblende précipitent à 350-300°C à partir de solutions essentiellement à Na-Cl avec des salinités variées. La minéralisation en uranium primaire et les roches encaissantes ont été altérées de manière intense par des fluides à Na-HCO<sub>3</sub>-Cl à des températures de 365 à 170°C. Les  $T_{\text{hom}}$  des inclusions fluides décroissent régulièrement depuis les failles jusqu'à leurs exocontacts et les zones de stockwork avec une décroissance de la teneur en U du minerai. De l'oxygène et de l'hydrogène moléculaires sont les seuls constituants gazeux des inclusions fluides dans le quartz syn-minéralisation et sont les composants prédominant dans les inclusions du quartz post-minéralisation localisé dans les minerais riches. La phase gazeuse est enrichie en CO<sub>2</sub> en dehors des failles et dans les minerais riches. La radiolyse de l'eau est à l'origine de la production d'O<sub>2</sub> et d'H<sub>2</sub>.

Les spectres ETR de la pechblende dans les trachybasaltes, trachydacites, et granites montrent une anomalie en Sm-Nd marquée and un effet tétrade de type W qui n'ont pas été observés dans les rhyolites qui dérivent d'une chambre magmatique de la croûte supérieure.

Ces données et l'intervalle chronologique de 5 Ma entre le volcanisme siliceux et la formation de la minéralisation ne montrent pas que l'uranium dérive de cette chambre magmatique. Selon le modèle proposé, un magma Li-F siliceux très fractionné a été la source de l'uranium. L'uranium tétravalent et les ETR ont fractionné dans la phase fluide sous forme de complexes fluorés. La minéralisation à uranium s'est déposée à une barrière de température. Il est proposé que l'altération prolongée à hydromicas et la formation de la minéralisation à Mo et Zn ne sont pas génétiquement liées à la formation du minerai d'uranium qui représente un événement relativement court (~500 ka).

## Extended abstract

Nineteen Mo-U deposits with total uranium reserves of 250 000 tonnes are located within a caldera extending over 140 km<sup>2</sup>. Not only the huge U reserves but also its relation to a contrasted Late Mesozoic basalt-dacite-rhyolite series make the Streltsovsky ore field a world-class uranium object, unrivalled in economic significance among other Mo-U deposits related to volcanic rocks. The ambiguity of the genetic interpretations of uranium ore formation led the author to provide his own investigations in an attempt to clarify some of the genetic aspects of the ore formation, and to elaborate on this base criteria for the exploration of similar mineralization.

A general trend has been established for the volcanic rocks consisting of their enrichment in U and F from the oldest (170 Ma) basic rocks (2.0- 2.5 ppm U and 0.3 wt. % F) through the intermediate and moderately silicic rocks (10 ppm U and ? F) to the youngest (140 Ma) highly silicic rocks (15-25 ppm U and ~3 wt. % F). Thus, we are dealing with a U-F geochemical association progressively accumulated during Late Mesozoic within igneous rocks, which indirectly testifies its relation with the postmagmatic pitchblende-fluorite mineral assemblage of the ore.

The Early Cretaceous postmagmatic hydrothermal epoch (140-125 Ma) is subdivided into preore, uranium ore, and first and second postore stages. During the preore stage, both basement rocks and the sedimentary-volcanogenic pile of the caldera were subjected to pervasive but not intensive clay alteration with chloritization, carbonatization and silicification. Metasomatic alteration was accompanied by the formation of cryptocrystalline quartz veins with pyrite and Mo-Zn sulfides. The primary brannerite-pitchblende ore was formed in association with fluorite and quartz during the uranium ore stage. It was followed by narrow zones of albitization and hematization. At the first postore stage, this assemblage was intensively replaced by a U-Si metagel, which was previously identified as coffinite. More local but more intensive alteration similar to that of the preore stage was developed along fissures and quartz-fluorite-carbonate veins with pyrite, sulfides of Mo, Zn, Cu and other chalcophile elements. Veins of polychrome fluorite with quartz and calcite followed by narrow zones of kaolinization were developed during the second postore stage in subordinate amounts relatively to previous stages.

Detailed study of the U-Si phase revealed its polyphase composition with a wide variation of U:Si ratios (2:1-1:2 in at.%), primary metacolloidal zonal texture of its

## Extended abstract

---

deposition, numerous fissures of shrinkage, and the amorphous state of the majority of the phases. Along with the absence of crystal faces in the segregations, it unambiguously testifies to the colloidal nature of the phase. Uraninite and coffinite crystallites of 3-15 nm size were detected in some of U-rich varieties of U-Si phase indicating the beginning of metagel crystallization.

Fluid inclusion study revealed that the preore metasomatic alteration and related veined mineralization were formed under the effect of sodium-(bicarbonate)-chloride solution at a temperature of 210°C. The uranium ore formation began with albitization and hematization of rocks associated with a transcritical fluid at 530-500°C. Brannerite and pitchblende precipitated at 350-300°C from essentially Na-Cl solution of various salinities. Primary uranium mineralization and host rocks were intensively altered under the influence of Na-HCO<sub>3</sub>-Cl fluids at temperatures of 365 to 170°C.  $T_{\text{hom}}$  of FIs regularly decreases from faults to their exocontact and stockwork zones and with the decrease of uranium ore grade. Molecular oxygen and lesser hydrogen are in fact the only constituents of the gas phase of FIs in synore quartz and predominant components in inclusions of postore quartz located in the high-grade ore. The gas phase is enriched in CO<sub>2</sub> outside the faults and the rich ore bodies. Water radiolysis is the reason for O<sub>2</sub> and H<sub>2</sub> production.

The chondrite-normalized REE patterns of pitchblende hosted in trachybasalt, trachydacite, and granite demonstrate a pronounced Sm-Nd discontinuity and a statistically significant tetrad effect of W type. These attributes have not been established in the REE patterns of the rhyolites derived from the upper crustal magma chamber.

These data and a chronological gap of 5 Ma between silicic volcanism and ore formation do not allow us to suggest that uranium was derived from this magma chamber. According to the proposed model, an evolved silicic Li-F magma was a source of uranium. Quadrivalent uranium, together with REE, was fractionated into the fluid phase as complex fluoride compounds. The uranium mineralization was deposited at a temperature barrier. It is suggested that long-lasting hydromica alteration and the formation of molybdenum and zinc mineralization were genetically unrelated to the uranium ore formation which occurred as a relatively short (~500 ka) event against this background.

## Расширенное резюме

Девятнадцать Мо-U месторождений с общими запасами 250 000 тонн расположены в кальдере площадью 140 км<sup>2</sup>. Не только огромные запасы месторождений, но также их связь с контрастными позднемезозойскими базальт-дацит-риолитовыми сериями сделали Стрельцовское рудное поле уникальным объектом, не имеющим аналогов среди других Мо-U месторождений, связанных с вулканизмом. Неоднозначность генетических интерпретаций уранового рудообразования заставило автора провести собственные исследования для уточнения генетических вопросов с одной стороны и для выработки на этой основе поисково-оценочных критериев аналогичного оруденения, с другой.

Выявлена общая закономерность для вулканических пород, заключающаяся в их обогащении ураном и фтором от наиболее поздних (170 млн. лет) пород основного состава (2-2.5 г/т U и 0.3 мас.% F) через средние и умеренно кислые (10 г/т U и ? F) к наиболее молодым кислым породам (15-25 г/т U и ~3 мас.% F). Таким образом, выявлена U-F геохимическая ассоциация, прогрессивно накапливающаяся в магматических породах в течение позднего мезозоя, которая косвенно свидетельствует о постмагматической природе настуран-флюоритового парагенезиса в рудах.

В раннемеловом постмагматическом гидротермальном этапе выделены дорудная, урановорудная, первая и вторая пострудные стадии. В течение дорудной стадии как породы фундамента, так и осадочно-вулканогенного выполнения кальдеры подверглись обширным, но неинтенсивным глинистым изменениям, сопровождаемым хлоритизацией, карбонатизацией и окварцеванием. Метасоматические изменения сопровождались образованием жил криптокристаллического кварца с пиритом и сульфидами Mo и Zn. Первичные браннерит-настурановые руды были образованы в парагенезисе с флюоритом и кварцем в течение урановорудной стадии. Они сопровождались узкими ореолами альбитизации и гематитизации. В течение первой пострудной стадии, эта ассоциация была интенсивно замещена U-Si метателуром, который изначально идентифицировался как коффинит. Более локальные, но и более интенсивные изменения, сходные с таковыми в дорудную стадию, были развиты вдоль трещин и кварц-флюорит-карбонатных жил с пиритом, сульфидами Mo, Zn, Cu и других халькофильных элементов. Жилы полихромного флюорита с кварцем и кальцитом, сопровождаемые узкими зонами каолинизации, были развиты в течение

## Расширенное резюме

---

второй пострудной стадии в подчиненном количестве по сравнению с предшествующими стадиями.

Детальное исследование U-Si фазы позволило выявить ее полифазное строение с широкими вариациями U:Si отношения (2:1-1:2 в ат.%), первично метаколлоидную зональную текстуру ее отложения, многочисленные трещины усыхания и аморфное состояние подавляющего числа фаз. Наряду с отсутствием гранных форм, это однозначно свидетельствует о коллоидной природе этой фазы. В некоторых разновидностях U-Si метатея, обогащенного ураном, обнаружены кристаллиты уранинита и коффинита размером 3-15 нм, что указывает на начало кристаллизации метатея.

Изучение флюидных включений выявило, что дорудные метасоматические изменения и сопутствующая жильная минерализация образованы из натрово-(бикарбонатно)-хлоридных растворов при температуре 210°C. Образование урановых руд началось с альбитизации и гематитизации пород под воздействием окологритических флюидов при 530-510°C. Браннерит и настуран отложились при 350-300°C из существенно Na-Cl растворов различной солености. Первичная урановая минерализация и вмещающие породы были интенсивно изменены под воздействием Na-HCO<sub>3</sub>-Cl растворов при температуре 365-170°C. Температура гомогенизации флюидных включений закономерно снижается от разломов к их экзоконтактам и штокверковым зонам, и по мере уменьшения содержания урана в руде. Молекулярный кислород и, в меньшей степени, водород являются фактически единственными компонентами газовой фазы флюидных включений в синрудном кварце и преобладающими компонентами включений в пострудном кварце, локализованном в богатых рудах. Газовая фаза включений обогащена углекислотой вне зон разломов и богатых рудных тел. Причиной образования O<sub>2</sub> и H<sub>2</sub> является радиолиз воды.

Нормализованные кривые распределения РЗЭ в настуране, локализованном в трахибазальтах, трахидацитах и гранитах, характеризуются ярко выраженным Sm-Nd разрывом и статистически устойчивым тетрадным эффектом W-типа. Эти признаки отсутствуют в распределении РЗЭ в риолитах, излившихся из верхнекоровой магматической камеры.

Эти данные, а также хронологический разрыв в 5 млн. лет между кислым вулканизмом и рудообразованием, не позволяют считать, что уран был отщеплен от этой верхнекоровой магматической камеры. В соответствии с предлагаемой моделью, источником урана явилась эволюционировавшая кислая Li-F магма. Четырехвалентный

## Расширенное резюме

---

уран вместе с РЗЭ фракционировал во флюидную фазу в виде фторидного комплекса. Урановая минерализация отложилась на температурном барьере. Предполагается, что длительная гидрослюдизация и образование Мо-Zn минерализации генетически не связаны с урановым рудообразованием, которое проявилось как относительно короткое (~500 тыс.лет) событие на этом фоне.





## General introduction

Nineteen Mo-U deposits with total uranium reserves of 250 000 tonnes are located within a caldera extending over 140 km<sup>2</sup>. Not only the huge U reserves but also its relation to a contrasting Late Mesozoic basalt-dacite-rhyolite series make the Streltsovsky ore field a world-class uranium object, unrivalled in economic significance among other Mo-U deposits related to volcanic rocks. Up to now, only a few smaller and ordinary deposits of this type are known worldwide.

The Streltsovsky deposit – the first one in the ore field – was discovered by Lydia Ishchukova in 1963 after several years of intensive but unsuccessful prospecting. Since more than 30 years the geology of the ore field, the geological and structural conditions of ore localization, the mineral composition of ore, wall-rock metasomatic alteration, and the physicochemical conditions of ore and wall rock formation were subjects of investigations by territorial, industry-related, and academic institutions, including the Geological Exploration Expedition no. 324 of Sosnovgeologiya Enterprise, PPGKhO JSC, the Transbaikal Research Institute, the All-Russia Research Institute of Geology (VSEGEI), the All-Russia Research Institute of Mineral Resources (VIMS), the All-Russia Research Institute of Chemical Technology (VNIKhT), the Institute of Geochemistry and Analytical Chemistry (GEOKhI), and the Institute of Geology of Ore Deposits, Petrography, Mineralogy, and Geochemistry (IGEM), Russian Academy of Sciences (RAS). An extensive set of factual data was collected and analyzed.

The team of the First Expedition of IGEM RAS, headed by Professor Wolfson, provided important insights into the uranium ore formation within the Streltsovsky ore field (SOF). A wide series of problems were studied, from the evolution of magmatism and localization of ore mineralization in the ore field to the mineral assemblages and fluid inclusions (FIs) in minerals. On the basis of this knowledge, a genetic model of these unique deposits was proposed.

The results obtained by different research teams have much in common concerning the geology of the ore district and ore field and their evolution, the localization of orebodies, the distribution of uranium and associated elements in host rocks, the staged hydrothermal activity, the physicochemical conditions of ore formation, the species of uranium transport, and the factors that controlled the deposition of uranium ore.

However, the treatments of some features are ambiguous and in some cases alternative. In particular, there are divergent views concerning the sequence of veined and

## General introduction

---

metasomatic mineral formation and interpretation of isotopic ages of igneous rocks and hydrothermal mineralization. The difference in opinions is caused by the complex, multistage character of magmatism and hydrothermal activity.

There are at least three competing genetic models for the economic uranium mineralization known to date, differing in the inferred source of uranium. The adherents of one of the hypotheses suppose that the main mass of uranium concentrated in orebodies was leached from host rocks during intense preore metasomatic alteration (Modnikov et al., 1984; Naumov et al., 1985; Ishchukova et al., 1991; Chabiron et al., 2003). According to another concept (Ishchukova et al., 1998), the upper mantle was the main source of uranium and leaching of uranium from the host rocks is regarded as a local phenomenon that does not affect the formation of economic ore. The hypothesis developed by Wolfson and his team considered an upper crustal source of silicic magma as the most probable initial reservoir of uranium ore. Since many aspects of the mineral formation sequence, dating of igneous rocks and hydrothermal processes, the behavior of uranium in these processes, and the genetic interpretations remain questionable, it was necessary to perform additional investigations using more modern methods.

### **Objectives and topical problems of the study**

The main objective outlined at the beginning of the work appears in the thesis title “Geological, structural, mineralogical and geochemical controls of the formation of the uranium-rich ores in the Streltsovsky ore field”. It implies the resolution of the main questions of ore formation – understanding of the spatial location of the major blocks of different rocks and the structural “skeleton” of faults which are fluid conductors and define the pathways of ore transportation, elaboration of a refined paragenetic scheme as the main basis for further special studies, constraints on the physicochemical condition of ore formation based on typomorphic features of minerals and fluid inclusion study to understand the main factors having caused the precipitation of uranium minerals.

Of course, it would be extremely difficult to provide all these investigations by one person. That is why the author concentrated mainly on mineralogical and geochemical studies as the most important and still ambiguous topics. Geological settings have been well refined during more than 30 years of exploration so this part was compiled from publications and numerous unpublished reports.

## General introduction

---

Specific studies helping to image spatial correlation of different structural elements with ore bodies and even the structure of the upper part of the earth crust were performed using 3D modeling of geological surfaces and internal structure of ore bodies. The latter task was solved in the gOCAD software with the help of Christian Le-CARLIER (CRPG).

Another important and time-consuming part is fluid inclusion studies. This work has been done in close collaboration with a specialist from IGEM, Dr. Tatiana KRYLOVA. The author provided sampling of quartz veins in the SOF, making thin sections to determine quartz generation, and making double-polished sections for FI studies. Tatiana KRYLOVA fulfilled microthermometry of the inclusions in IGEM and Raman microspectroscopy with the help of Thérèse LHOMME in G2R (Nancy).

During the work on the thesis, unexpected results on REE behavior in pitchblende and volcanic rocks have been obtained which allowed the extension of the framework of the thesis and the proposition of a genetic model of uranium mineralization in the SOF. As several genetic models already existed, differently interpreting actual material and offering different ideas on the triad: source of uranium → pathways of transportation → factors and mechanism of deposition, the author ought to resolve some key questions and examine the appropriateness of their postulates. Two the most important questions – timing of the uppercrustal magma chamber solidification and the possibility of the evolved acid Li-F magma to derive ore-forming fluids with significant U concentrations, were studied with the priceless help of Victor MAL'KOVSKY and Alexander PEK (IGEM) in the first case, and Alexander RED'KIN (IEM) – in the second case. The author's role consisted of general target setting and boundary conditions elaboration for mathematical modeling and experimental runs, as well as the discussion of the results obtained.

### **Methods of investigation and factual material**

In the course of fieldwork at the Streltsovsky, Antei, Oktyabrsky, Luchisty, Tulukui, and Krasny Kamen deposits and elsewhere in the ore field, about a thousand specimens and core samples of Mo–U ore, metasomatic rocks, and unaltered host rocks were collected and about 1500 thin sections were examined in transmitted and reflected light under an optical microscope.

To determine the chemical compositions of uranium minerals, sulfides, silicates, and carbonates, more than 3000 analyses were made on Cameca SX-50 and SX-100 microprobes at the Henri Poincaré University, Nancy, France, and a few hundred analyses, on a Hitachi S-

## General introduction

---

2500 SEM equipped with a KeveX EDS (analyst A. Koehler, Henri Poincaré University) and a Jeol JSM-5300 SEM equipped with a Link ISIS EDS (analyst O.A. Doinikova, IGEM RAS). The fine structure of a U–Si metagel previously identified as coffinite was studied on a Philips CM-20 high-resolution TEM with microdiffraction and a Princeton PGT EDS (analyst J. Ghanbaja, Henri Poincaré University). The REE contents in pitchblende were determined on a Cameca IMS-3f ion microprobe (CRPG, Nancy) (analyst J. Bonhoure, UMR G2R).

The FIs in quartz of several generations, fluorite, and calcite were studied at IGEM RAS with microthermometric methods (freezing study and homogenization) on a Linkam THMS600 heating and freezing stage, which works within a temperature range from  $-196$  to  $+600^{\circ}\text{C}$ . The compositions of gas and solid phases in the inclusions were determined with Raman microspectroscopy on a DILOR XY device (analyst T. Lhomme, Henri Poincaré University). Four hundred and twenty inclusions from 30 samples were studied with various methods.

Geochemical studies were based on results of whole-rock analyses obtained by ICP-AES and -MS spectroscopy and, to a lesser extent, by XRF and INAA methods. The majority of ICP analyses were produced in CRPG (Nancy), and smaller part – in the Institute of Experimental Mineralogy (IEM, Chernogolovka, Russia) and in the Institute of Mineralogy, Geochemistry and Crystallochemistry of Rare Elements (IMGRE, Moscow). XRF and INAA analyses were produced in IGEM. 240 samples were analyzed. More than 100 samples were analyzed with XRF and INAA.

Local uranium distribution in mineral phases and mineral aggregates of rocks with quantitative determination of uranium content have been studied by fission track radiography in IGEM. Sample irradiation was provided in the nuclear reactor (IRT) in Moscow Engineering Physics Institute (MEPhI). Calculation of uranium content was fulfilled by making digital photomicrographs of tracks on lavalan detectors after etching in KOH solution at  $40^{\circ}\text{C}$ , and then further treatment using special techniques. The technique was developed by the author and consisted of obtaining numeric data on track density in photomicrographs using the Corel PhotoPaint raster editor, and calculations in the FoxPro Data Base Management System (DBMS) using a set of specially written programs.

Statistical treatment of the geochemical results generally included calculation of the main parameters of statistical distribution (mean, standard deviation, skewness, kurtosis, coefficient of variation), and anomalous values (outliers) were considered by the winsorization procedure. Estimation of a distribution law was based on the formal rule implying that standardized kurtosis and skewness have to fit the range of  $[-3;3]$ . Only normal and

## General introduction

---

logarithmically normal laws have been considered, if both of them did not satisfy the rule, the best one has been chosen. Rough mistakes in distribution law evaluation were controlled by the coefficient of variation (standard deviation normalized on the mean) and visually by observing histograms.

GIS modeling was used for the 3D analysis of the spatial relations between the main structural elements of the upper crust near the SOF and the localization of uranium ore at the Antei and Oktyabrsky deposits. 3D geological models were created with the GeoSpline module, specially developed at IGEM RAS and functioning under the AutoCAD Map GIS editor. 3D numerical models of orebodies were created in the gOcad program (C. Le-Carlier, CRPG, France) and afterward were imported into AutoCAD Map for analysis.

### **Thesis structure**

The thesis is divided into four parts.

The first part “Geology of the Streltsovsky ore field” is mostly descriptive. Regional geological settings of large crustal domains of the Eastern Transbaikal region, as well as geological structure of the SOF are described there. The results of 3D GIS modeling of the central part of the Oktyabrsky deposit are included in this part as a separate chapter because it helps to understand the geological structure of the deposit and structural controls on the ore bodies.

The second part “Mineralogy of the deposits and geochemical behavior of elements in magmatic and hydrothermal processes” contains main results obtained by the author. It is subdivided into four chapters – (1) “Uranium and fluorine behavior in the Late Mesozoic volcanic rocks of the Streltsovsky caldera”; (2) “Mineralogy of the deposits”, describing vein and metasomatic bodies, mineral parageneses, typomorphic features of the most important minerals and substantiating the paragenic scheme; (3) “Behavior of elements during the Late Mesozoic hydrothermal process”, where the results of geochemical studies are exhibited; and (4) “REE in pitchblende and host rocks”, where specific studies of REE behavior are considered separately because of their novelty, complexity and importance for the genetic model.

The third part “Physicochemical conditions of mineralization” deals with the results of fluid inclusion studies provided by Tatiana KRYLOVA in cooperation with Thérèse LHOMME, and constrains physicochemical conditions of hydrothermal processes on the basis of FIs, mineralogical and geological evidences.

## General introduction

---

The fourth part “Genetic model of the uranium ore formation” is a synthesis of all previously examined studies. With additional results provided by mathematical modeling and experimental investigations, a new genetic model of uranium formation is considered in this part.

Primary raw data on the results of geochemical whole-rock analyses and electron microprobe results are placed in the electronic annexes written on a CD-ROM as Excel files because they occupy too much space if printed. Along with these, the 3D GIS model of the Oktyabrsky deposit in PDF3D format with an installation of Acrobat Reader 3D software is contained in the electronic annexes. Keys for databases along with notes and explanations are placed in the appropriate annexes.

# Part I. Geology of the Streltsovsky ore field





## **1. Location of the Streltsovsky ore field in the regional structures of Eastern Transbaikalia**

The Streltsovsky caldera is located within the Variscan Mongol-Okhotsky foldbelt and, in its limits, in the Amur-Bureya terrain (microcontinent). Several blocks have been revealed in the western part of the terrain - two uplifts of Proterozoic-Paleozoic basement (northern Urumkan-Urovsky and southern Urulunghuevsky blocks) separated by the Gazimursky block which underwent moderate stable sinking from Precambrian to Late Mesozoic (Fig. 1.1).

From the seismic data (Menaker, 1990), the lowest Moho depth of approximately 42 km occurs in the central part of the Gazimursky block while the Urumkan-Urovsky and especially the Urulunghuevsky blocks are characterized by elevated Moho depth (up to 36-37 km). The same tendency is observed for the roof of the basaltic layer: the Conrad discontinuity depth varies from 21 km in the center of the Gazimursky block to 14-15 km within the uplifted blocks (Fig. 1.2). The regional gravity field reflects the thickness of the Earth's crust of the area. As the Gazimursky block possesses relatively important thickness, it is characterized as regional gravity minimum in comparison with the Urulunghuevsky and Urumkan-Urovsky blocks.

Basement of the uplifts is composed of Archean (?)–Middle Proterozoic metamorphic rocks and granitoids with small intrusives and dikes of Mesozoic polyphased granitoids – from quartz diorites and granodiorites to leucocratic alkaline granites and pegmatites. Magmatic rocks prevail in the basement (Ishchukova et al., 1998).

The most ancient rocks are Archean (?) crystalline schists and plagiogneisses and Lower Proterozoic amphibolites, gneisses, schists, sandstones and conglomerates, as well as dolomites and marbles. Granite gneisses, granodiorites and plagiogranites were formed during the Early Paleozoic as the result of metamorphic rock migmatization in the early stages of the local uplift. Furthermore during the Late Paleozoic, large bodies of granites and granodiorites were formed mainly in the central parts of the domes.

Widespread Late Mesozoic intracraftonic tectonomagmatic activation occurred both on the territory of the Mongol-Okhotsky foldbelt and the Siberian platform, forming the Mongol-Priargunsky volcanic belt. Several stages of Mesozoic magmatism occurred in the Urulunghuevsky uplift from Late Triassic to Early Cretaceous. The first stage (Late Triassic–

## 1. Location of the SOF in the regional structures

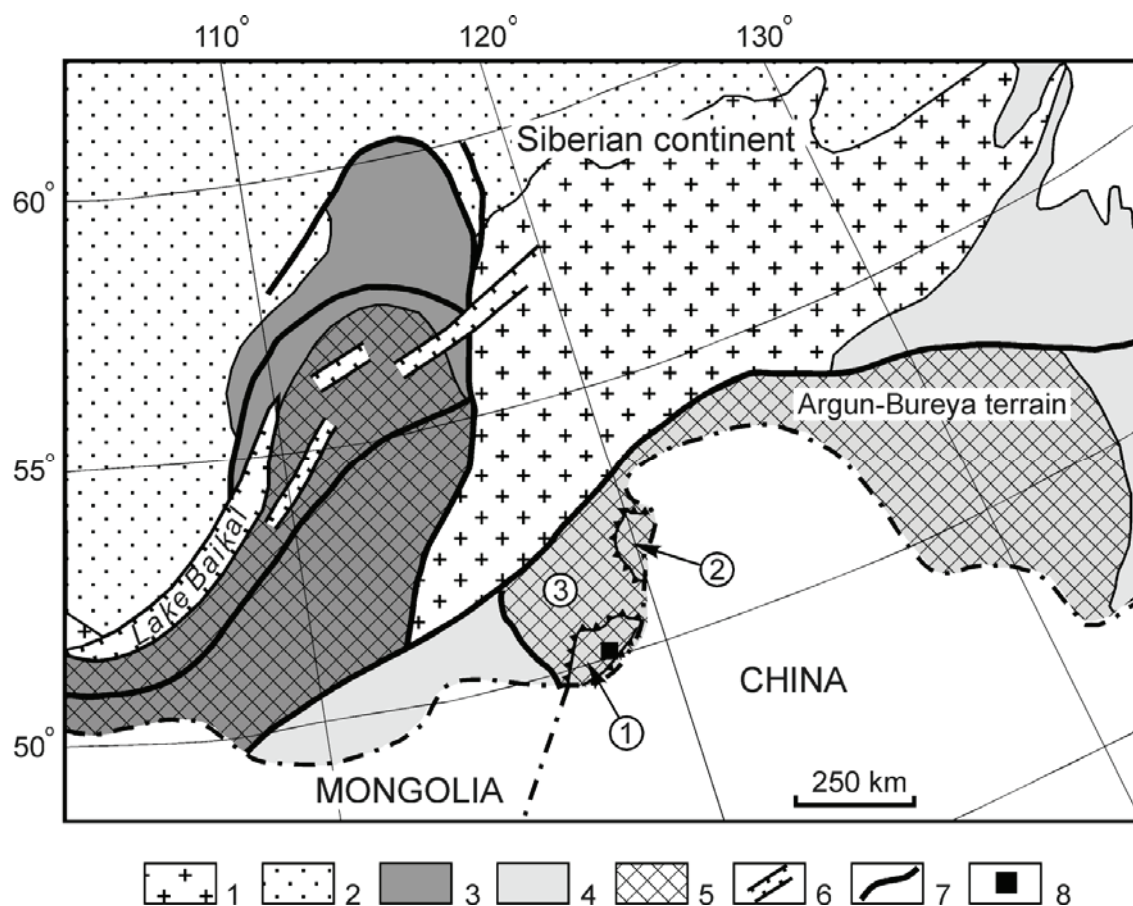


Fig. 1.1. Location of the SOF in the regional structures of the Eastern Transbaikalia.  
 1-2 – Siberian continent: 1 – Pre-Riphean basement (Aldan shield), 2 – sedimentary cover;  
 3-4 – foldbelts: 3 – Late Precambrian and Paleozoic (Transbaikalien foldbelt), 4 – Mesozoic (Mongol-  
 Okhotsky foldbelt); 5 – terrains (microcontinents); 6 – present continental rifts;  
 7 – sutures; 8 – the Strel'tsovsky ore field. Numbers in circles: 1 – Urumkan-Urovsky block,  
 2 – Urumkan-Urovsky block, 3 – Gazimursky block

Early Jurassic) was essentially depressed and only few intrusive bodies of melanocratic granites and granodiorites with an age of 208-196 Ma (from K-Ar dating) were developed in the Gazimursky and Urumkan-Urovsky blocks (Andreeva et al., 1996).

The most intensive magmatic processes took place in Middle-Late Jurassic and Late Jurassic-Early Cretaceous differently in various blocks. Polyphased Middle-Late Jurassic intrusives of the Shakhtaminsky complex (quartz diorites and monzonites → granites, granodiorites and granosyenites → leucogranites → acidic and basic dikes) and granites with granodiorites of the Sretensky complex were formed mainly in the downfaulted Gazimursky block (166-153 Ma from K-Ar and Rb-Sr dating). On the contrary, volcanic processes simultaneous with the intrusions mentioned above were

## 1. Location of the SOF in the regional structures

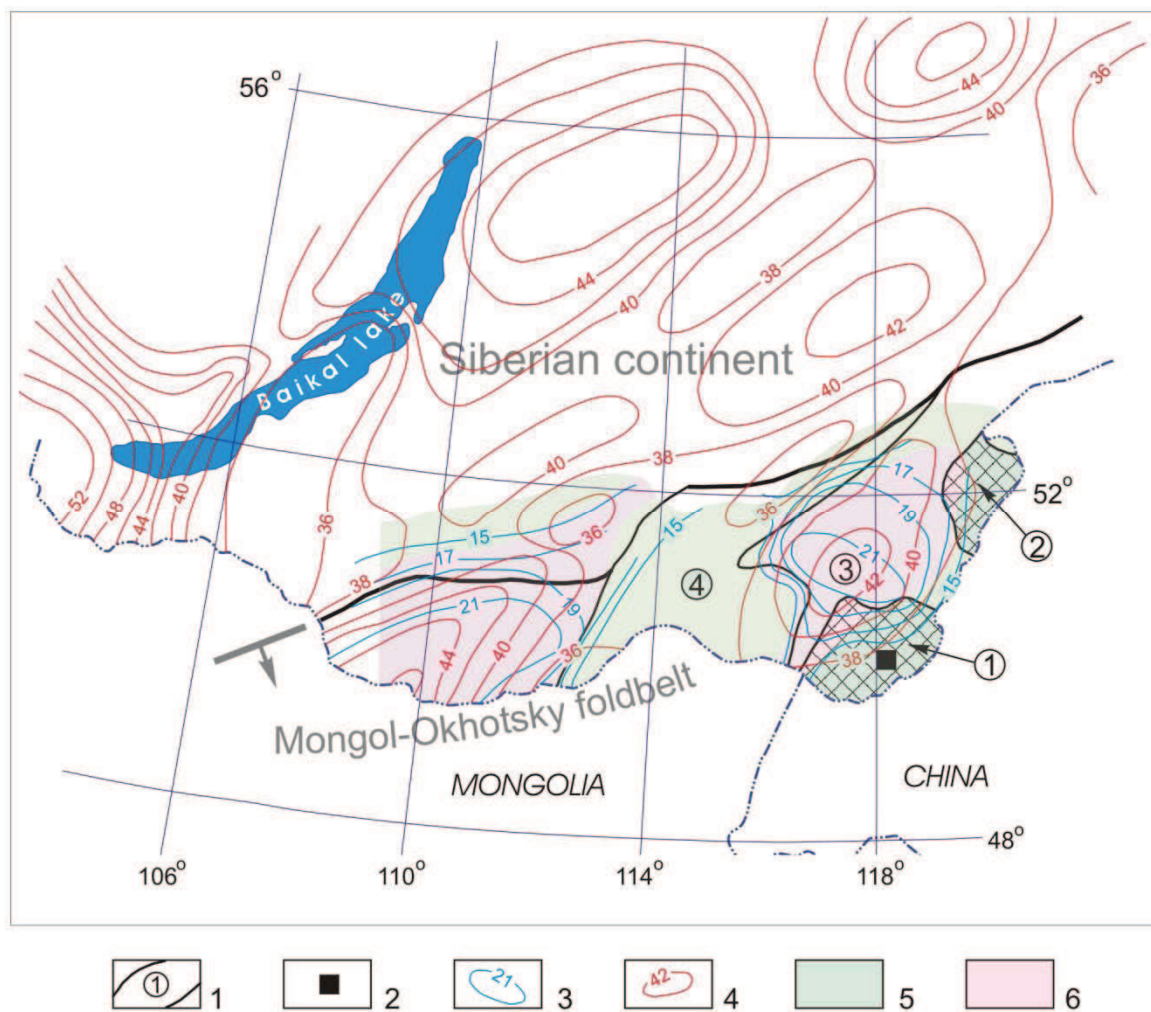


Fig. 1.2. Structure of the Earth's crust and regional gravity field in the Transbaikal region  
 1 – major geological blocks of the Mongol-Okhotsky foldbelt: 1 – Urulekhuevsky uplift, 2 – Urumkan-Urovsky uplift, 3 – Gazimursky block, 4 – Aginsky block; 2 – location of the SOF; 3 – depth of the Conrad's discontinuity (after Menaker, 1970); 4 – Moho depth (after Menaker, 1990); 5 – regional gravity maximum; 6 – regional gravity minimum (after Menaker, 1972).

predominant in the uplifted Urulekhuevsky and Urumkan-Urovsky domes. Volcanism began with trachybasalt effusion at 170-176 Ma and the latest trachydacites were formed at approximately 155 Ma (Andreeva et al., 1996<sub>2</sub>). Trachybasalts and trachydacites formed the lower Priargunsky suite of the Streltsovsky caldera.

The 3<sup>rd</sup> Late Jurassic–Early Cretaceous stage is characterized mainly by subalkaline acid magmatism. Similar to the previous stage, hypabyssal bodies of subalkaline leucocratic monzonite granites of the Kukulbei complex were formed mainly in the Gazimursky block 146-135 Ma in accordance with K-Ar and Rb-Sr dating (Andreeva et al., 1996<sub>2</sub>). In the same period of time (150-138 Ma), sheets of subalkaline rhyolites erupted within uplifted blocks

## 1. Location of the SOF in the regional structures

---

interlayered with sandstones, tuffs and rare basalt sheets. The upper Turginsky suite of predominantly rhyolite composition was formed in the Streltsovsky caldera. Subvolcanic facies are presented by extrusions and dikes of fine-porphyries rhyolites, quartz syenite-porphyries and granosyenite-porphyries.

The latest 4<sup>th</sup> stage of Mesozoic magmatic activity (Early Cretaceous) was poorly developed in Eastern Transbaikalia. Small bodies of biotite granites and leucogranites with ages of 125-120 Ma were formed in the southern part of the Gazimursky block and in the northern part of the Urulunghuevsky block. Rhyolite ignimbrites (120-118 Ma) were spread mainly in the Urumkan-Urovsky block while only sandstone strata with lignites of the Kutinsky Lower Cretaceous suite were formed in the Urulunghuevsky uplift.

The question of the existence of the 4<sup>th</sup> stage in the Streltsovsky caldera is still a matter of discussion. Ishchukova et al. (1998) believes that the uppermost sheets of rhyolites and basalts were formed at approximately 120 Ma. The youngest age has been obtained for the upper basalts at 108 Ma (the only data obtained by K-Ar dating is unfortunately from 1964, Bocharov et al., 1978). However, these rocks host the uranium mineralization of the Bezrechnoye deposit with an age of 135 Ma (Chernyshev & Golubev, 1996). To solve the problem, samples of fresh sanidine rhyolites were taken during field work in 2007 for future K-Ar dating in IGEM.

Thus, Mesozoic intracratonic magmatic activation occurred within the Mongol-Priargunsky volcanic belt from 208 to 120 Ma, i.e. approximately 90 Ma in total.

The SOF is situated in the Urulunghuevsky uplift which is elongated in a north-eastern direction conformable to the general strike of the Mongol-Okhotsky foldbelt (Fig. 1.3). This block consists of four local uplifts of 2<sup>nd</sup> order separated by large troughs striking north-east, and deeply rooted meridional fault zones. The Argunsky uplift which hosts the Streltsovsky and the larger Kuitunsky calderas is separated from the Kuladzhinsky uplift westward by the meridional Chindachinsky shear zone which is the west boundary of larger Dalainor-Gazimursky shear zone. These two uplifts are separated from the Margutsek-Klichkinsky uplift north-westward by the Vostochno-Urulunghuevsky trough striking north-east. The last uplift, in turn, is bounded from the north-west by the Zapadno-Urulunghuevsky trough which developed along the deeply seated north-eastern Burkinsky shear zone. The Tsagan-Oluevsky uplift is a marginal one and is located on the other side of the Zapadno-Urulunghuevsky trough to the north-west.



## 1. Location of the SOF in the regional structures

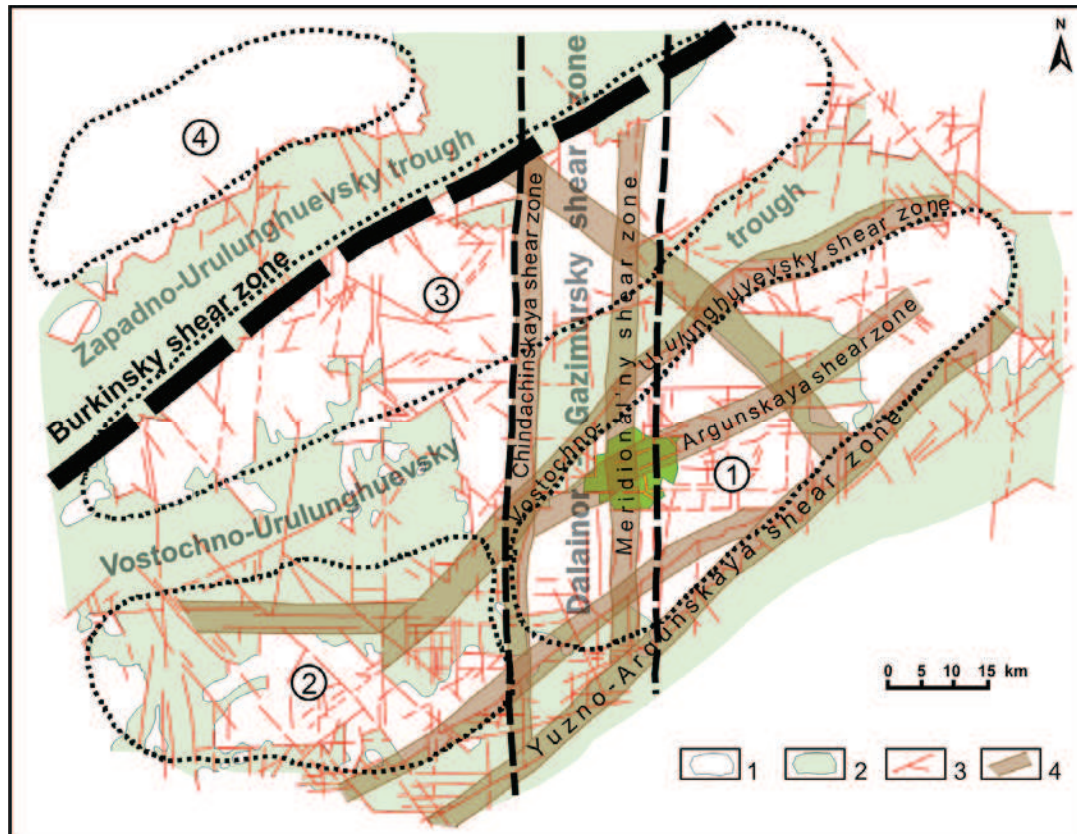


Fig. 1.3. Geological structure of the Urulunghuevsky uplift and position of the Streltovsky caldera (in deep green) (after Ishchukova, 1998, with modifications)  
 1 - basement uplifts, 2 - superimposed depressions, 3 - faults and shear zones, 4 - deeply rooted shear zones; numbers in circles – local uplifts (areas in dashed lines): 1 - Argunsky, 2- Kuladzhinsky, 3 - Margutsek-Klichkinsky, 4 - Tsagan-Oluevsky.

As mentioned above, the Urulunghuevsky uplift differs from the Gazimursky downfaulted block by elevated gravity field (regional gravity maximum). The Burkinsky fault is a gravity step which separates these two megablocks. The gravity field of the Urulunghuevsky block is also heterogeneous. The Argunsky uplift appears as a local gravity minimum which is sharply bounded westward from the elevated field of the Kuladzhinsky uplift by the marginal Chindachinsky fault of the Dalainor-Gazimursky meridional shear zone. In contrast to the Argunsky local uplift, the central part of the Margutsek-Klichkinsky uplift is a gravity maximum in a background of an elevated gravity field in the Urulunghuevsky block (Fig. 1.4).

A regional meridional seismic profile performed along the Dalainor-Gazimursky shear zone, by “common depth point – converted wave” method, allowed Dukhovskiy et al. to conclude (1998; Fig. 1.4) that there is a maximum concentration of linear subvertical and gently sloping S-discontinuities in the crystalline basement beneath the Streltsovsky caldera

## 1. Location of the SOF in the regional structures

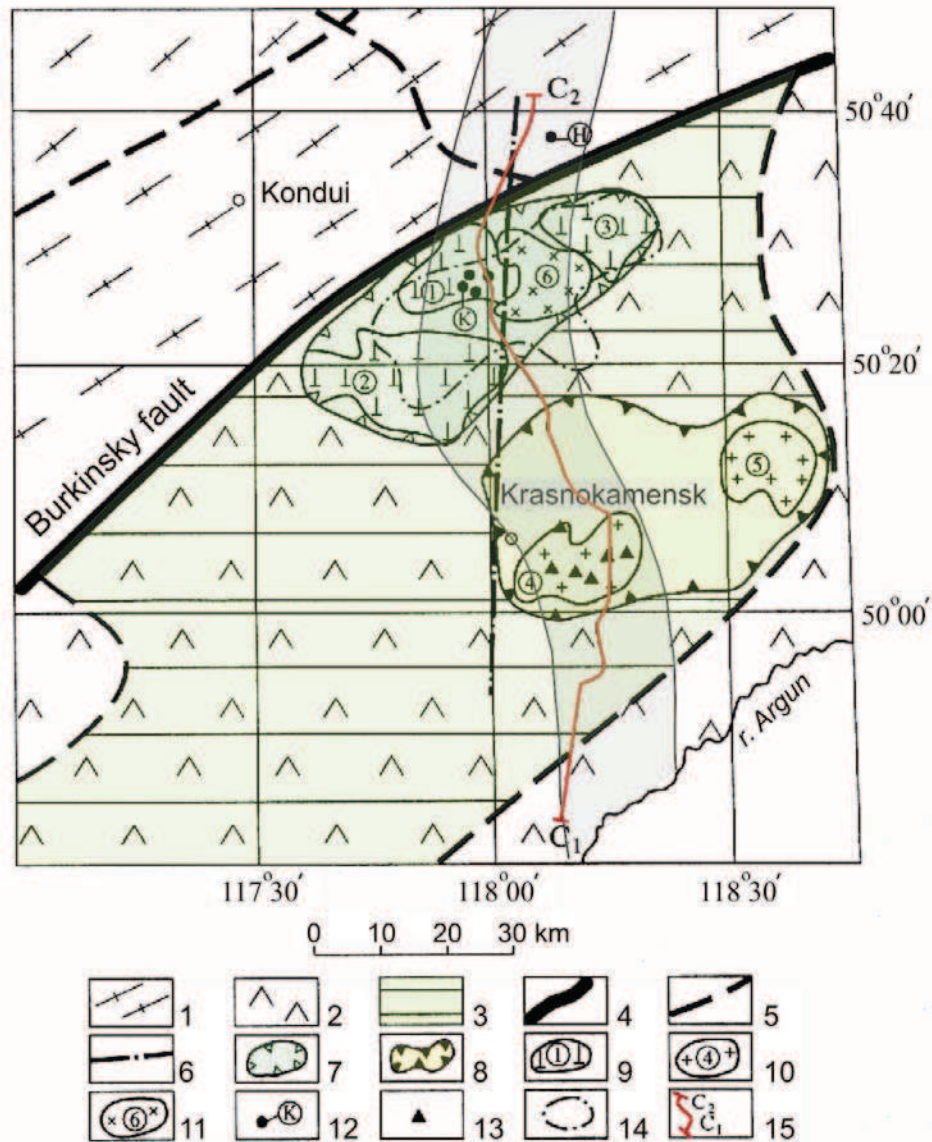


Fig. 1.4. Gravity field of the Uralunghuevsky uplift (after Dukhovskiy, 1998, with modifications).

1-3 – regional fields of the 1<sup>st</sup> and 2<sup>nd</sup> orders: 1 – regional minimum, 2 – regional maximum, 3 – Uralunghuevsky minimum of the 2<sup>nd</sup> order; 4 – regional gravity step of the 1<sup>st</sup> order; 5 – regional gravity step of the 2<sup>nd</sup> order; 6 – large gravity discontinuities; 7 – local gravity maximum of the 1<sup>st</sup> order (Klichkinsky ore district); 8 – local gravity minimum of the 1<sup>st</sup> order (Yuzhno-Argunsky ore district); 9 – local gravity maximum of the 2<sup>nd</sup> order; 10 – local gravity minimum of the 2<sup>nd</sup> order (ore fields: 4 – Streltsovsky, 5 – Kuitunsky); 11 – local gravity minimum of the 2<sup>nd</sup> order corresponding to the Kir-Kirinsky granite massive; 12 – polymetallic deposits; 13 – uranium deposits; 14 – area of polymetallic showings and deposits distribution; 15 – seismic profile. Grey meridional belt – deeply rooted Dalainor-Gazimursky shear zone.

traced down to depths of more than 12 km. This column, made of highly permeable Earth's crust, is obviously controlled by the intersection of the meridional Dalainor-Gazimursky and north-eastern Argunsky deeply seated shear zones (Fig. 1.3; Ishchukova et al., 1998).

## **2. Geological settings of the Streltsovsky ore field**

The geological structure of the Streltsovsky caldera and its surroundings has been reported in numerous publications and reports (Ishchukova et al., 1966; Bocharov et al., 1978; Wolfson, 1981; Dukhovskiy et al., 1998; Ishchukova et al., 1998). Most of the geological features of the SOF have been well-studied since the discovery of the first deposit more than 40 years ago.

### **2.1. Structural stages and magmatism**

Two structural stages are distinguished in the SOF composition which are similar to the Urulunghuevsky uplift in general: Archean–Middle Paleozoic metamorphic-granitoid basement and Middle Jurassic–Lower Cretaceous sedimentary-volcanogeneous strata of the caldera and adjacent Eastern-Urulunghuevsky trough (Fig. 1.5). The most ancient Archean–Middle Proterozoic metamorphic rocks (plagiogranites, orthoamphibolites, crystalline schists, marbles) and Lower Paleozoic granite gneisses are spread mostly across north-western, north-eastern and south-western parts of the caldera frame (Fig. 1.6). Early Paleozoic gneisses were developed upon Archean–Proterozoic metamorphic rocks forming a dome-like structure elongated in the north-eastern direction. This structure is remarkable for the foliation and schistosity of metamorphic rocks which are distinctly observed in the wings of the dome. On the periphery of the wings, blocks of metamorphic rocks can reach up to several kilometers in size, then their size decreases towards the center of the dome and they are found as small xenoliths and skialiths in the Lower Paleozoic granite gneisses (Ishchukova et al., 1998).

Variscan granites are developed mainly in the central and south-eastern parts of the caldera basement, as well as in the south-eastern frame designating central part of the dome. Towards the margins of the dome and to greater depths (down to 2.8 km from data of deep drilling), normal biotite granites are gradually changed to granodiorites and even diorites. They also contain xenoliths of partly reworked amphibolites and other metamorphic rocks.

Mesozoic granites are not exposed in the vicinity of the caldera. The Kibirevsko-Idanginsky leucocratic granites have been discovered 10 km north-east from the caldera by drilling. Besides these, large fragments of morion granites similar to the Mesozoic Kir-Kirinsky



## 2. Geological settings of the SOF

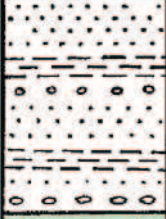
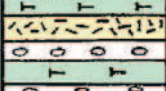
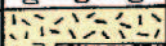

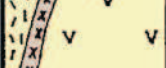



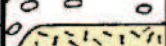
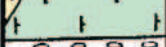
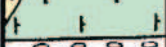
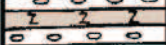

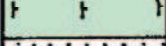



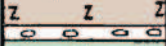


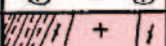

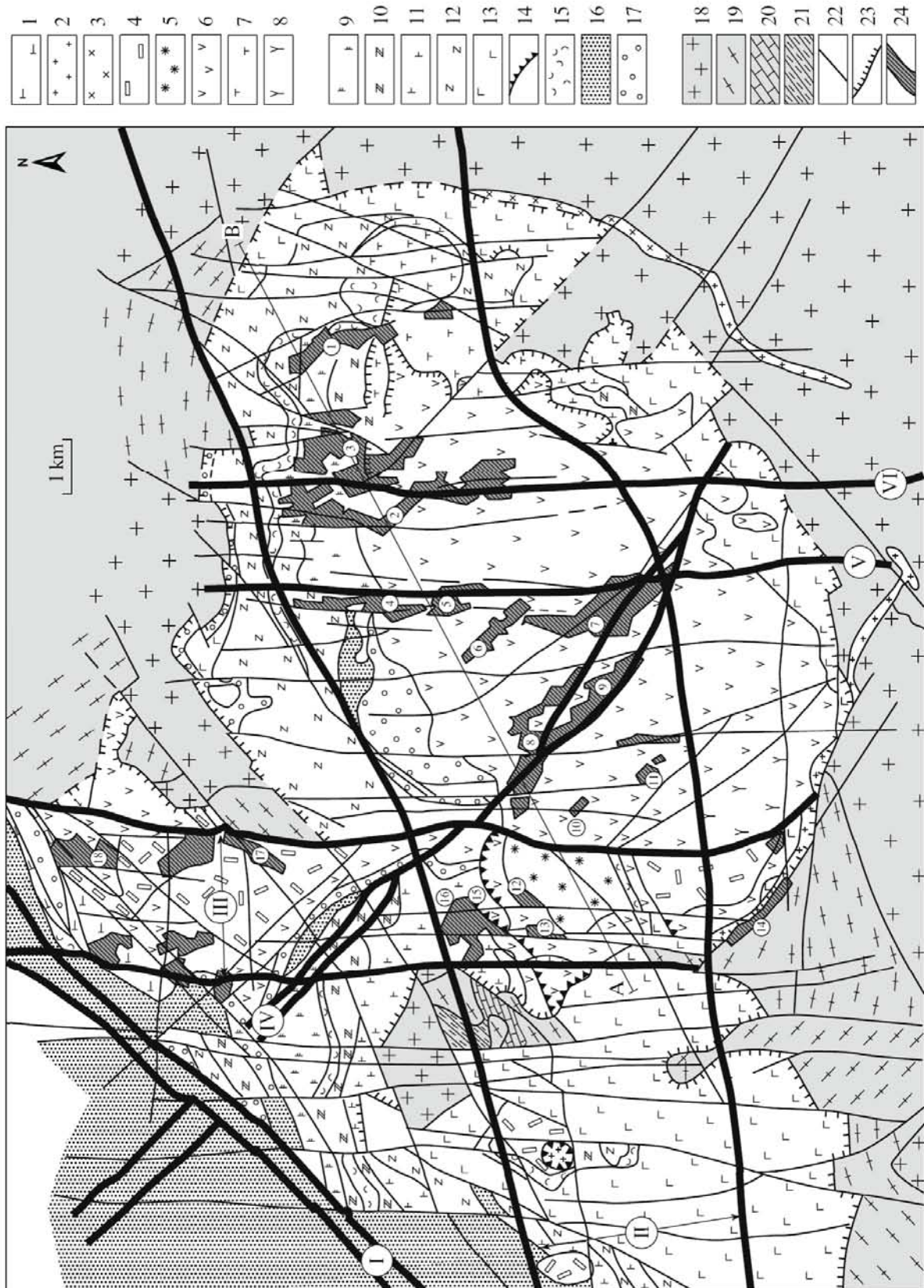
Suites	Series	Stratigraphic column	Thickness, m	Rock description
Turginsky (J.-K.)	Upper		400	Sandstones, siltstones, gravelites and conglomerates with thin coal interlayers
			190	Trachybasalts, rhyolite tuffs with thin conglomerates and volcanic glass sheets
	Medium		400	Liparite sheets and their lava breccias
			50	Conglomerates
			450	Rhyolite sheets and their eruptive breccias in neck facies, dikes of syenite-porphyry
			20	Conglomerates
			20	Trachybasalts
			150	Conglomerates
			130	Trachybasalts
	Lwr		170	Conglomerates
		80	Rhyolites	
Priargunsky (J)			150	Trachybasalts
			40	Conglomerates
			100	Trachydacites
			50	Conglomerates
			150	Trachybasalts
			40	Sandstones
			400	Trachydacites
			80	Conglomerates
		400	Trachybasalts	
		150	Basal conglomerates	
AR-PZ				Basement granites, gneiss granites, crystalline shists, amphibolites and marmorized limestones

Fig. 1.5. Stratigraphic column of the Streltsovsky caldera. After Wolfson (1981, with modifications).



## 2. Geological settings of the SOF



See caption overleaf

Fig. 1.6 (previous page). Geological map of the Streltsovsky ore field, after Ishchukova et al. (1998). (1–13) Upper Jurassic–Lower Cretaceous volcanic sequence filling the caldera: (1) basalt, (2) dikes and subvolcanic bodies of rhyolite with small phenocrysts, (3) syenite and syenite and granosyenite porphyries, (4) upper flow of rhyolites with small and large phenocrysts, (5) cream-colored spherulitic rhyolite, (6) massive and fluidal felsite and quartz porphyry, (7) andesite, (8) lower flow of spherulitic and thin fluidal glassy rhyolite, (9) upper flow of basalt and basaltic andesite, (10) upper flow of trachydacite, (11) middle flow of basalt, (12) lower flow of trachydacite, (13) lower flow of basaltic andesite; (14) paleovolcanoes; (15–17) tuffaceous and sedimentary rocks: (15) tuff, (16) sandstone with siltstone interbeds, (17) conglomerate and gravelstone; (18–21) Paleozoic basement of the caldera: (18) Variscan coarse- and medium-grained granites, (19) Caledonian gneissose granite, (20) marble, (21) siltstone, phyllite, quartz–sericite schist, and quartzite; (22) steeply dipping faults; (23) gently dipping faults; (24) contours of deposits (numbers in circles): 1. Shirondukui, 2. Streltsovsky, 3. Antei, 4. Oktyabrsky, 5. Luchisty, 6. Martovsky, 7. Maly Tulukui, 8. Tulukui, 9. Yubileiny, 10. Vesenny, 11. Novogodny, 12. Pyatiletny, 13. Krasny Kamen, 14. Yugo-Zapadny, 15. Zherlovny, 16. Argunsky, 17. Bezrechny, 18. Dal'ny; Fault zones (numbers in circles): I. Vostochno-Urulyunguiskey, II. Argunsky, III. Meridionalny, IV. Tulukuevsky, V. Malo-Tulukuevsky, VI. Central.

granites in the Margutsek-Klichkinsky local uplift, were found in drillings in the latest dikes of granosyenite-porphyries in the western part of the Streltsovsky caldera (Wolfson, 1981). However, in contrast to the granites of the Kukulbei complex, these morion granites possess trace elements and accessory minerals typical of usual Variscian granites of the caldera basement.

Total thickness of the Mesozoic sedimentary-volcanogeneous cover of the caldera amounts to 1000–1200 m in the deepest parts. Bedding is usually gentle, steep pitch (up to 45°) is observed only near marginal faults bounding the caldera and on the slopes of paleovalleys in the basement surface.

Two suites are revealed in the caldera stratas. The lower Priargunsky suite is composed of three trachybasalt sheets separated by two layers of trachydacites and siltstone-sandstone-conglomerate beds with admixture of tuffaceous material (Fig. 1.5). The suite occurs on the eroded surface of basement rocks and is underlain by a horizon of basal conglomerates. K-Ar and Rb-Sr ages of volcanic rocks of the Priargunsky suite are 170–154 Ma indicating Middle–Late Jurassic ages (Andreeva et al., 1996<sub>2</sub>).

The upper Turginsky suite is composed mainly of peralkaline rhyolites interlayered with tuffaceous-sedimentary rocks containing organic matter and thin rare coal beds. Rocks enriched with carbonaceous matter are mostly found in the northern part of the caldera and in adjacent Eastern-Urulunghuevsky trough north-westward. The K-Ar age of rhyolites is determined as 153–143 Ma (Ishchukova et al., 1998). The upper part of the Turginsky suite is represented by rhyolite tuffs, basalts and sandstones. The age of upper basalts and rhyolites remains unknown (Bocharov et al., 1978). Only a few K-Ar dates were obtained for upper basalts and rhyolites in the northern part of the Streltsovsky caldera at 108–124 Ma but they are not enough reliable. From one side, similar volcanites in other locations demonstrate more

## 2. Geological settings of the SOF

---

ancient ages – 140-154 Ma. From the other side, acidic volcanism of similar age (120-125 Ma) was widely developed in the Severno-Argunsky depression 100 km north-east from the Streltsovsky caldera and in the Yuzhno-Argunsky trough 20 km to the south. So the total duration of the Turginsky suite formation is Late Jurassic–Early Cretaceous.

Several volcanic events producing lavas of different compositions filled the Streltsovsky caldera and Urulunghuevsky trough during separate pulses. The earliest effusions of basaltic lava took place from fissure volcanoes located in the Urulinghuevsky shear zone which separates the Streltsovsky caldera from the Eastern-Urulunghuevsky trough (Fig. 1.7). Their activity alternated with trachydacite volcanoes located eastward, outside the caldera.

Acidic volcanism was produced by three volcanoes – two of them are located in the Meridional shear zone (Yugo-Zapadny volcano at the cross of the Meridionalny zone and southern fault bounded the caldera, and Krasnokamensky volcano north of Yugo-Zapadny) and Zapadno-Tulukuevsky volcano to the west of caldera. After the bulk of acidic magma was erupted from the upper crustal chamber situated approximately 5 km below the caldera (from geophysical data), collapse occurred and resulted in the caldera formation. The latest portions of acidic magma have formed complex extrusive bodies of felsite lava breccias and granosyenite-porphyry dikes. Volcanic activity finished with basalt effusion from renewed volcanoes located in the Vostochno-Urulunghuevsky shear zone.

### 2.2. Tectonics

Brittle structures of various scales – from deeply seated shear zones in the Earth's crust to contraction (cooling) fracturing in volcanic sheets – are extensively manifested in the SOF. Actually, the entire caldera is situated within the meridional Dalainor-Gazimursky shear zone which caused widespread development of meridional faults inside the caldera. The largest among them are the Chindachinsky fault zone which limited the Dalainor-Gazimursky shear zone from the west (Fig. 1.3) as well as the Meridional and parallel Fluoritovy faults which occur in the western part of the caldera, forming the Meridional shear zone. The Malo-Tulukuevsky and Central shear zones are the principal ones in the eastern part of the SOF (Fig. 1.6).

The Argunsky shear zone, with a north-eastern strike (NE60-70), is not distinctly revealed in the caldera filling but it is one of the most important structures in the basement. It consists of numerous steeply dipping faults of east-north-eastern, sometimes latitudinal strike,

## 2. Geological settings of the SOF

---

intensively altered with high-temperature feldspathization, greisenization and other metasomatic processes. It is reflected in linear zones of gravity minima traced to depths of several kilometers, with the most contrasted gravity minimum observed at depths of 3-6 km. Total thickness of the Argunsky shear zone is 3-5 km. It dips gently north-west intersecting with the Vostochno-Urulunghuevsky shear zone at depths of 12-15 km (Fig. 1.7, 1.8).

All large faults and shear zones mentioned above are long-lived ones, they began during folding in the Proterozoic, and were renewed during all younger stages of deformation including Mesozoic intracraton activation.



## 2. Geological settings of the SOF

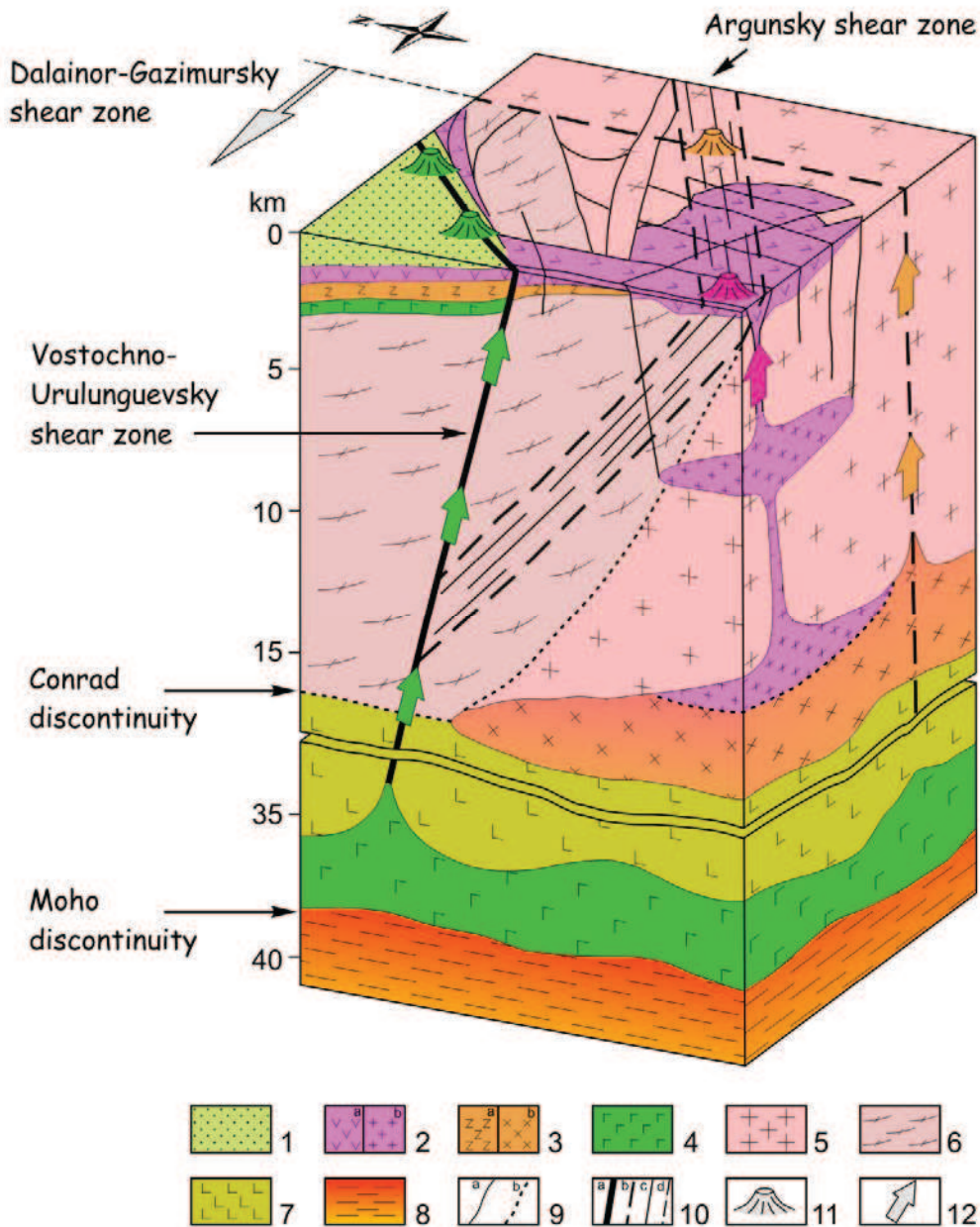


Fig. 1.7. 3D block-diagram of the Earth's crust under the Streltsovsky caldera and surroundings created on the base of 3D GIS model (built in GeoSpline) with invoking geophysical data (Menaker, 1970, 1972, 1990; Dukhovskiy et al., 1998).

1 – sandstones and siltstones filled the Vostochno-Urulunguevsky trough, 2 – rhyolites (a) and leucocratic granites (b); 3 – trachydacites (a) and granodiorites (b); 4 – trachybasalts (a) and “basaltic layer” of the Earth's crust (after Menaker, 1990) (b); 5 – Variscian granites, 6 – Proterozoic – Lower Paleozoic gneiss granites, 7 – basic-metamorphic layer of the Earth's crust (after Menaker, 1990), 8 – upper mantle, 9 – rock boundaries: distinct (a), and gradient (b); 10 - tectonic dislocations: large shear zones (a), implicit shear zones (b), fault zones (c), implicit fracturing zones (d); 11 – paleovolcanoes: rhyolitic (pink), dacitic (brown), basaltic (green); 12 – directions of magma uplift: acidic (pink), intermediate-acidic (brown), and basic (green).

## 2. Geological settings of the SOF

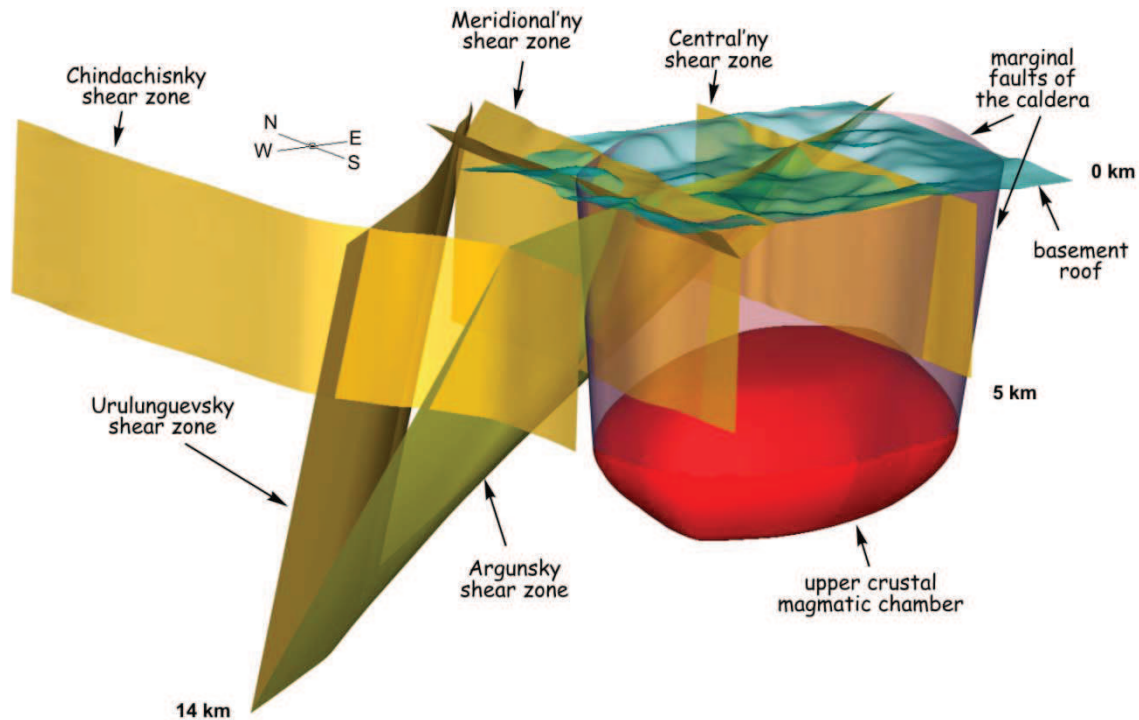


Fig. 1.8. 3D GIS model of the upper part of the Earth's crust built in GeoSpline ARX-module under AutoCAD based on geologic maps and geophysical data.

Besides meridional and north-eastern faults, faults of north-western strike occur both in the basement rocks and volcanic strata. Streltsovsky and Tulukuevsky faults are the largest ones. The Streltsovsky fault hosts thick post-uranium fluorite veins in the Streltsovsky deposit and can be traced to the south-east. The Tulukuevsky fault controls a group of deposits in the central part of the caldera, crosses the Meridional fault and continues further north-west. Vertical displacement along the fault reaches 200 m.

The caldera is bounded by marginal faults with steep dip (up to  $80^\circ$ ) towards the center and with fault throw reaching up to several hundred meters. Dikes of rhyolite and granosyenite-porhyry are often located in the marginal faults.

Faults developed differently in basement rocks and caldera filling. North-eastern (NE20-30 and NE60-70) and latitudinal faults are more typical in the basement rocks. Faults striking NE20-30 host the uranium mineralization in the Antei and Shirondukui deposits in

## 2. Geological settings of the SOF

---

basement granites. Meridional and NW330-340 faults occur mainly in volcanics of the caldera, where they control the majority of the deposits.

Gently pitching faults and overthrusts were developed at the contacts of layers of volcanic and sedimentary rocks with different physical-mechanical properties, mainly between different structural levels. Thickness of such faults varies from several to 30 meters increasing at the intersection with steeply dipping faults and shear zones. These gentle faults usually are filled by tectonic clay and served as screens for intrastratal steep faults and ascending flows of hydrothermal solutions.

Brittle volcanic rocks (trachydacites, rhyolites) are favourable for contraction fracturing which produced horizontal fluid permeability along the layers.

Thus, extensive development of long-lived steeply dipping shear zones of different strike and gentle faults induced complicated block structure of the basement and sedimentary-volcanogeneous stratas of the Streltsovsky caldera.

### 2.3. Ore body controls

Nineteen molybdenum-uranium deposits are located within the caldera extending over 140 km<sup>2</sup>. Because of the high density of uranium deposits in a limited region, it is often difficult to separate one deposit from another. In fact, it is one huge knot of uranium mineralization (Fig. 1.6).

A distinctive feature of the SOF uranium deposits which distinguishes them from other deposits of the Mo-U formation is their location in all varieties of basement rocks and filling of the caldera. Two large deposits (Antei and Argunsky) with a quarter of the total uranium reserves are located in basement rocks (Variscan granites and Proterozoic marbles respectively). The other 17 deposits are hosted by various sedimentary-volcanogeneous rocks of the Streltsovsky caldera. Four of them are situated in neck facies of volcanites confined to the Meridional shear zone (Zherlovy, Pyatiletny, Krasny Kamen, Yugo-Zapadny) and represent only 5% of total U reserves. The other 13 deposits (70% of the reserves) are spread in the stratified filling of the caldera. The most productive lithological-structural units of uranium mineralization are the rhyolites of the Turginsky suite (Tulukuevsky, Novogodny and Yubileiny deposits located in NW Tulukuevsky shear zone) and trachydacites of the Priargunsky suite (Streltsovsky, Oktyabrsky and Malo-Tulukuevsky deposits controlled by the Central and Malo-Tulukuevsky meridional shear zones). Typical location of ore bodies in

## 2. Geological settings of the SOF

basement granites and stratified sedimentary-volcanogeneous rocks is shown on the example of the Antei and Streltsovsky deposits (Fig. 1.9).

Ore bodies are not exposed at the surface. The highest parts of the ore bodies occur at depths of 100-150 m. Vertical stretch of mineralization in the volcanic strata is 200-600 m below the surface; the interval of commercial mineralization located in the basement is 400-900 m. The deepest location of uranium mineralization was discovered by deep drilling in granites at a depth of 2500 m.

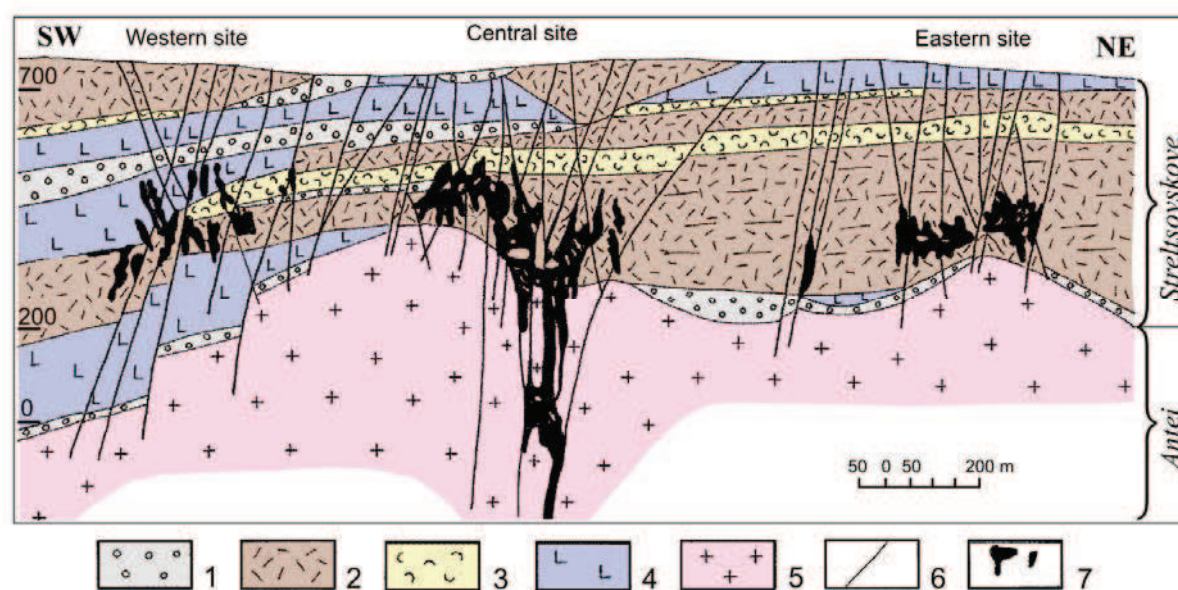


Fig. 1.9. Geological section through the Antei and the Streltsovskoye deposits (after Ishchukova et al., 1998, with modifications).

1-4 – sedimentary-volcanogenic filling of the caldera: 1 – conglomerates, 2 – trachydacites, 3 – trachydacite tuffs, 4 – trachybasalts; 5 – Variscan granites, 6 – faults and shear zones, 7 – ore bodies

All the deposits are disposed within the two largest shear zones - Argunsky and Meridional, moreover, only three small deposits (Yugo-Zapadny, Bezrechny and Dal'ny) are not controlled by the Argunsky zone. Within the limits of the Argunsky shear zone, the deposits are controlled by meridional and north-western faults. Many deposits in the eastern part of the caldera (Shirondukyiy, Streltsovskoye, Oktyabrskoye, Luchistoye) are controlled by meridional shear zones – Shirondukuisky, Central and Malo-Tulukuevskoye, the other (Tulukuevskoye, Malo-Tulukuevskoye, Yubileiny, Martovskoye) are controlled by the north-western Tulukuevskoye shear zone and some smaller parallel faults.

The Meridional shear zone is also very important in the location of uranium deposits. One of the largest Argunsky deposit, along with the small Krasny Kamen', Pyatiletny, and



## 2. Geological settings of the SOF

---

Zherlovy deposits, and the Krasnokamensky volcano are located at the intersection of the Meridional and Argunsky shear zones. The Yugo-Zapadny deposit is situated at the intersection of the Meridional shear zone with a marginal caldera fault in the south of the SOF while the Bezrechny and Dal'ny deposits occur in the northern extension of the Meridional zone.

At the scale of the deposits, ore bodies are often controlled by intersections of faults of different strike, and their joints and flexures. A special role is played by gently pitching interstratal faults and overthrusts as they served as screens for ascending flows of uranium bearing solutions. Ore bodies are often located beneath or above such screening faults particularly at their intersections with steeply dipping faults. The basement roof is also an important screen surface which determined the splitting of the main ore-hosting fault of the Antei deposit and increasing ore body thickness and grade beneath basal conglomerates of the caldera pile (Ishchukova et al., 1998).

Swell-like uplifts of the caldera basement also constrain location of some ore bodies and entire deposits such as, for example, the Eastern site of the Streltsovsky deposit (Fig. 1.9), the Shirondukyi, Oktyabrsky deposits and others. They focused ascending flows of ore-forming fluids as erosional windows among weakly permeable basalt sheets (Wolfson, 1981).

Three major morphological types of ore bodies have been recognized – (1) single and complex veins, (2) flat and vertical linear stockworks, and (3) tabular, sheet ore bodies. Transition varieties are also observed.

Vein-type ore bodies are mostly typical of rocks with high strength and elastic properties (granites, subvolcanic facies of granosyenite-porphyry, basalts) which caused development of single faults or localized shear zones. The Antei deposit, situated in granites, is the best example of vein-type ore body (Fig. 1.9). Stockwork-like ore bodies are characteristic in brittle rocks (trachydacites, rhyolites) which underwent tectonic deformation leading to dense fracture networks. Elevated porosity of these rocks also facilitated fluid penetration not only along fissures but through the rock mass, forming streaky-disseminated mineralization in stockworks. Sheet ore bodies often occur in layers of porous rocks (argillized tuffaceous siltstones, sandstones and conglomerates) with high permeability along the beds, with permeability further improved by gently pitching interstratal faults.

Complicated ore bodies were formed at the intersection of different structures and in neck facies of volcanic rocks in the Krasnokamensky volcano (Zherlovy, Pyatiletny, Krasny Kamen' deposits). Particular breccia-type ore bodies were formed in the Argunsky deposit in

## 2. Geological settings of the SOF

---

marbles. A breccia zone 100-150 m thick controls high-grade uranium ore body and was formed presumably due to impact of pressurized gas-saturated hydrothermal fluid (Ishchukova et al., 1998).

Thus, uranium mineralization in the SOF deposits occurs in all varieties of rocks regardless of their chemical composition or mechanical properties. These latter determined different types of fracture development and, in such a manner, different morphologies of the ore bodies.

### **3. 3D GIS-modeling of geological structure and an ore body in the Oktyabrsky deposit**

Two objectives have been followed in this work: (1) elaboration of a methodology of 3D modeling of complex geological structure in ore deposits, and (2) revealing ore body controls on the example of uranium deposits in the Streltsovsky ore field.

#### **3.1. Approaches of modeling**

3D modeling of complex geological objects such as block-layered geological structure of deposits disturbed by numerous faults of different strike and pitch is not routine work. Presently, there is a large family of computer programs on the market designed for 3D modeling of the geological structure of deposits and numerical modeling of ore bodies – from relatively simple solutions (Rockworks, Earthworks Exploration Office, SurvCADD, MineFrame, Micromodel, Samara+FataMorgana, MineScape, Surpack and others) with the price varying from first ths. US\$ to \$10 000, to complex multi-module programs such as Datamine, Micromine, FracSIS, and Gemcom with the price ranging from \$10 000 and above. Many of programs of the first group can create only simple layered geological models and as a consequence are not suitable for our purposes. Powerful programs of the second group suit the needs of mining companies for the development of deposit exploration models. They are rather expensive, require significant effort to master and can be only partly used for scientific application.

Separately, there is a group of programs which may be used for 3D modeling of complex irregular surfaces (ArcGIS family, AutoCAD) or especially designed programs for the modeling of 3D geological structures and ore bodies (Gocad). However, ArcGIS software is designed mostly for 2D GIS, but despite this real 3D models can be also constructed by this software. AutoCAD was initially created for the purposes of the engineering industry and architecture and because of this deals mostly with regular surfaces.

Gocad could satisfy our requirements except that it is not really GIS software. This means it is impossible to attach and keep any attributive information to objects in Gocad which is necessary for the construction of numerical models of ore bodies (for example, attaching the number of ore concentration to the sample object). So another additive program is required for preliminary building of a database of samples by digitizing and attaching attributive information to objects, and verifying the database. Only then it is possible to import the database into Gocad.

### 3. 3D GIS modeling

---

This brief review demonstrates that to date there is no single ready-to-use program suitable for the problem (at least, the author isn't aware of such a program). After deliberation of all "pro et contra" a decision was made to design a special module operating under AutoCAD to diminish the disadvantages of the latter in construction of complex irregular surfaces. This work was entrusted to the group of programmers under the leadership of Prof. Alexander ALEXANDROVICH (Computing Center of the Russian Academy of Sciences).

Requirements specification compiled by the author included such features as construction of B-spline surfaces based on digitized 2D-polylines converted to splines, trimming of one surface by another, combining of surfaces on joint lines, exploding (disassembling) of the surfaces, selection of point objects at given distances from the surface, calculation of surface area, data import and export, and other abilities. The program was realized as an ARX-module executed under AutoCAD Map 2000-2008 and was named GeoSpline. Thus, we developed a way to use all the facilities of the well-designed powerful AutoCAD software on one hand and the ability of 3D GIS-modeling from the very first steps (combining of scanned images of geological maps and cross-sections, their positioning in 3D and digitizing) to building the final 3D model in the same environment, on the other hand.

#### **3.2. Geological model of the central part of the Oktyabrsy deposit**

The Oktyabrsky deposit located in the eastern part of the SOF (Fig. 1.6) has been chosen as an example object for 3D GIS modeling because the most complete dataset on the geological structure and ore bodies sampling is available for this deposit. The deposit is hosted by layered sedimentary-volcanogeneous filling of the caldera and is controlled by the meridional Malo-Tulukuevsky shear zone. The latter consists of a series of subparallel steeply dipping faults with smaller feathering faults of predominantly NW strike. The richest ore body of the deposit is situated above the dome-like uplift of granite basement in the lower basalt sheet and in the thick dacite sheet over it (Fig. 1.10). Initial graphic materials for a geological model included three transversal latitudinal cross-sections (prospecting lines 209, 210+50 and 213), one longitudinal cross-section and a geological plan of mine horizon +362 m located at the depth of 370 m below the day surface (Fig. 1.11). Dimensions of the modelled volume are 470×400×625 m (latitude×longitude×height respectively).

Main faults and contacts of the rocks on these cross-sections and plan were digitized with 2D polylines. The position of the polylines was further corrected to bring the skeleton of the model to mutual agreement among all the sections and the plan. Subsequently, 2D

### 3. 3D GIS modeling

polylines were converted to splines and 3D-mesh surfaces were constructed (Fig. 1.12). In cases of coupling of fault surfaces, trimming procedures were performed to cut one surface by another.

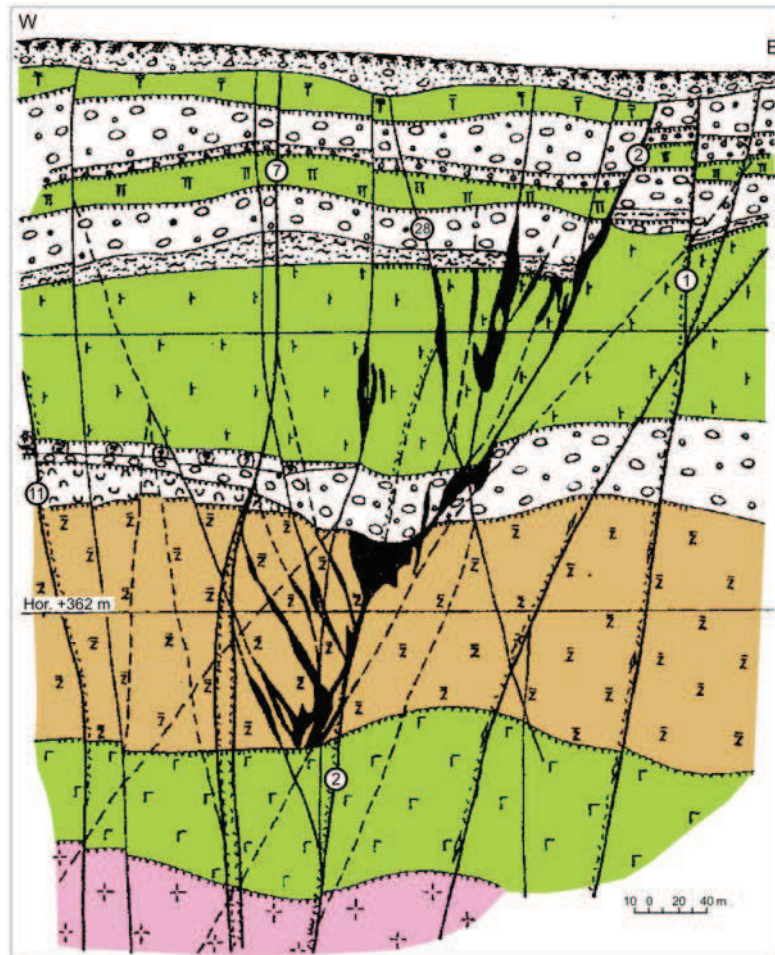


Fig. 1.10. Cross-section along the 209<sup>th</sup> prospecting line in the Oktyabrsky deposit (after Ishchukova et al., 1998, with modifications). Pink – Lower Paleozoic and Variscan granites of the basement, green – trachybasalts of the Priargunsky suite (two lower thick flows) and the Turginsky suite (two upper thin sheets), brown – trachydacites of the Priargunsky suite. White – tuffaceous conglomerates and sandstones. Black – uranium ore bodies. Numbers in circles – numbers of main faults.

After construction of the 3D geological model in GeoSpline, surfaces of faults and rock contacts were successfully exported into Gocad through the DXF exchange format along with raster images (Fig. 1.13).



### 3. 3D GIS modeling

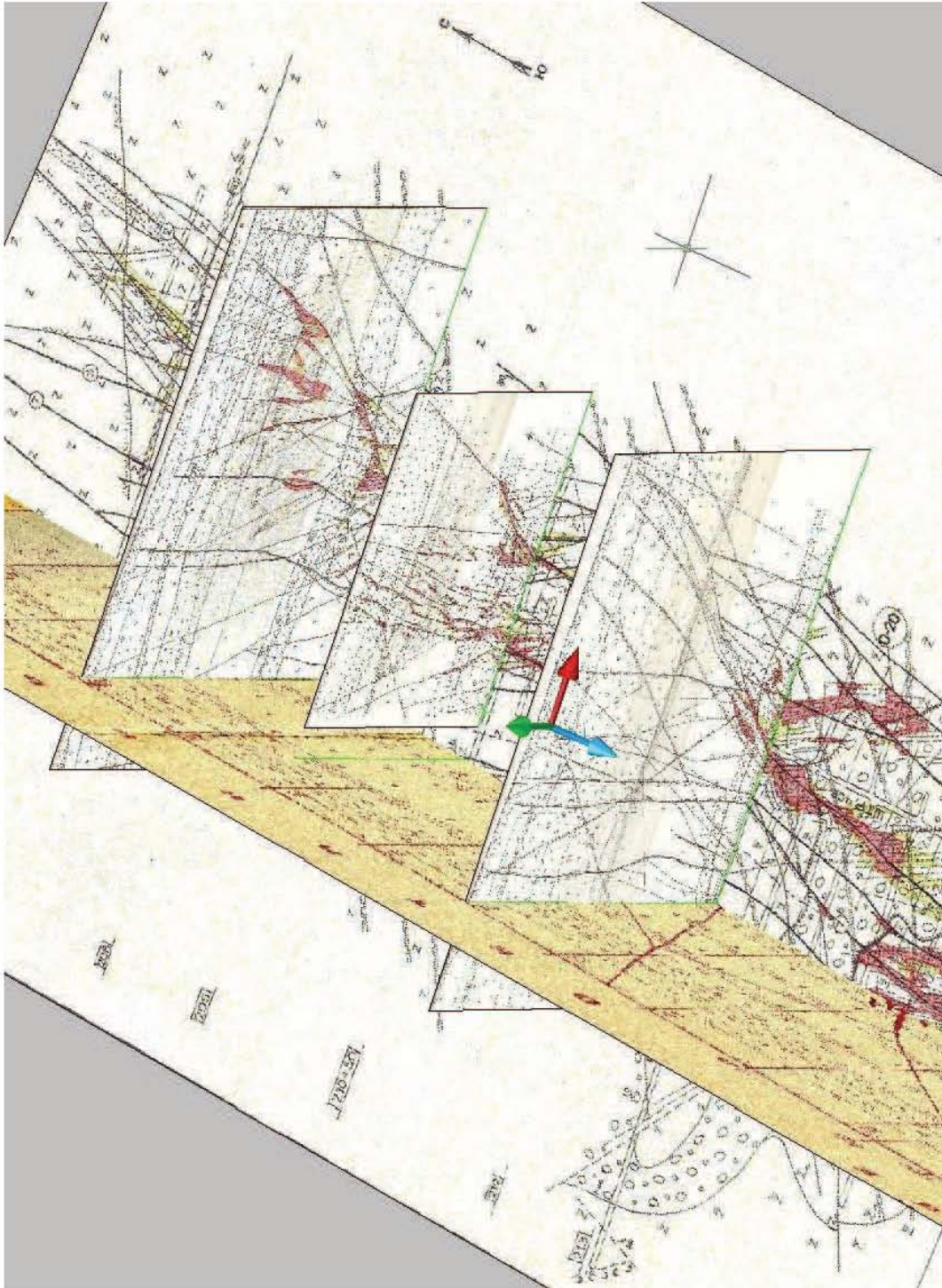


Fig. 1.11. Scanned images of three transversal cross-sections along prospecting lines 209, 210+50 and 213, one longitudinal cross-section and geological map of mine horizon +362 m which were used as a graphical base for 3D GIS model of the Oktyabrsky deposit. Images are positioned in real coordinates in 3D space of AutoCAD Map 2008.

## 3. 3D GIS modeling

### 3.3. Numerical model of the ore body and geological controls of high-grade U ore

An ore body model was constructed on the basis of sampling schemes on 9 mining slices above the horizon +302 m in the area of the geological modeling. Mines in the SOF are explored by descending slicing with solidifying backfill (concrete). The height of a slice is 3 m, so total height of the modelled volume of 9 slices comprises 27 m. Faces of mine galleries are sampled by radiometry through 20 cm, then the samples in each profile are averaged with calculation of generalized balance (commercial) intervals and barren rocks. Underground drillings and blastholes are sampled by gamma-logging which are generalized in the same way.

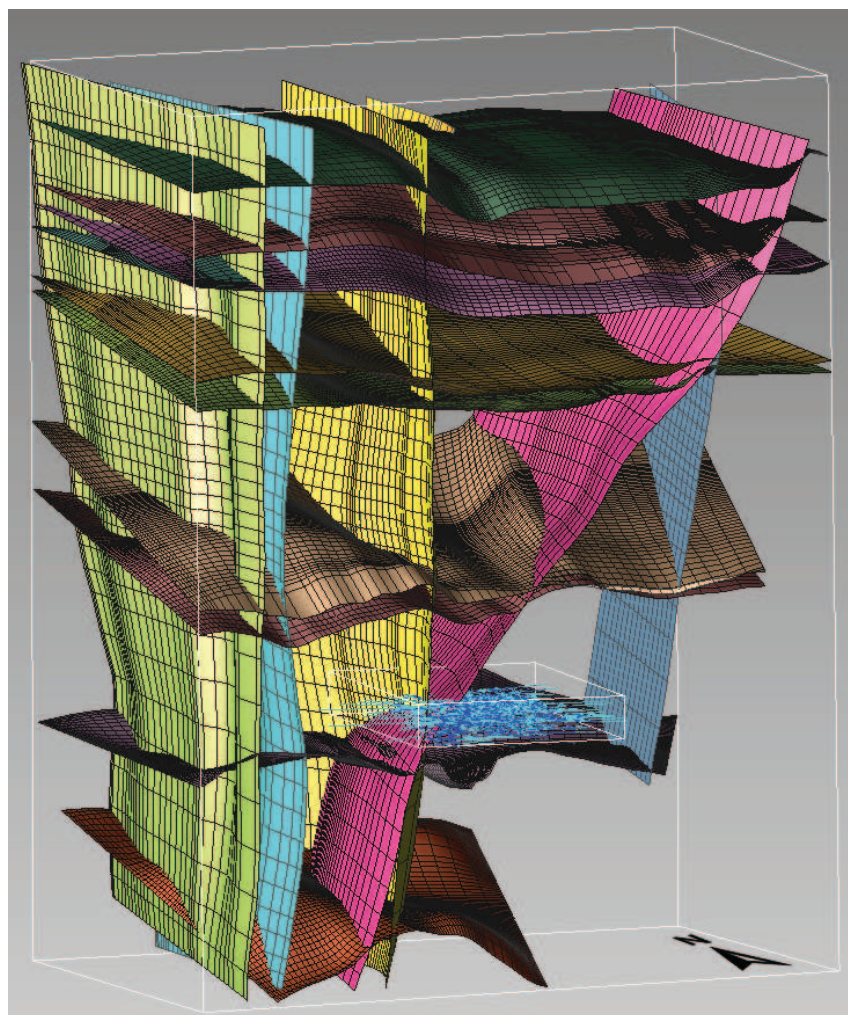


Fig. 1.12. 3D model of geological structure of the Oktyabrsky deposit built in AutoCAD Map 2008 with the use of GeoSpline module. Layered structure of sedimentary-volcanogeneous stratum intersected by numerous steeply dipping longitudinal faults of the Malo-Tulukuevsky shear zone is noticeable. Box with blue-cyan lines – sampling of 9 mine slices prepared for database. The height of the model box – 625 m.



### 3. 3D GIS modeling

---

These generalized intervals with their numbers were plotted on slice maps of 1:500 scale. Tables containing sample numbers, generalized sample lengths, average uranium contents and grade×thickness parameters were plotted on the same maps. These maps were scanned during field work. Unfortunately, no primary data on gamma-sampling of both face galleries and holes were available.

The procedure of 3D modeling of the ore body consisted of merging the parts of the scanned slice maps into single rasters for each slice, their correction with affine transformation (“rubbersheet” procedure in AutoCAD Map) and positioning into real 3D coordinates in AutoCAD Map. Sample intervals on raster maps were digitized by segments, and numbers of samples were attached to each segment (Fig. 1.14).

Scanned tables of generalized gamma-sampling results were typed in Excel with the help of a student of Henri Poincaré University Claire Vermet. Coordinates of the beginning and the end of sample segments along with their numbers were exported to CSV text file format using the data export facility of GeoSpline. Then the text file was converted to DBF format as well as the Excel table of gamma-sampling results. Joining of sample coordinates with gamma-sampling results was performed in one of the most advanced relational DataBase Management Systems – Visual FoxPro version 5.0. Two DBF files (sample coordinates and sample data) were merged with their key fields – sample numbers. Verification of the database with the use of set of programs written by the author disclosed some disagreements among the data and allowed correction. Total volume of the database amounted to 4150 samples.

After verification, the database was converted back to Excel format and imported into Gocad. Construction of the numerical model of the ore body was performed by Christian le-Carlier (CRPG, Nancy). The model consisted of voxels – minimal cubic volumes containing information on uranium concentration. Voxel size amounted to 1×1×1 m, and total volume of the ore body model constituted 160×250×28 m. Irregular primary data were brought to the regular 3D network by simple interpolation method.

The 3D numerical model built in Gocad was visualized in two ways – as a system of three orthogonal sections in the box of model space (Fig. 1.13), or as surfaces of equal uranium concentration, termed isosurfaces. Surfaces of uranium isoconcentration of 0.1% and 1% were built in Gocad and then exported through DXF exchange format to AutoCAD Map for its combination with the 3D geological model. Unfortunately, during this export, single triangulated isosurfaces (TIN-surfaces) were exploded into myriads of 3D Face objects in AutoCAD, so that it required huge computer resources to manipulate the model. To solve the



### 3. 3D GIS modeling

problem, both geological model and numerical model of the ore body were exported through PDF3D software into PDF format with maintenance of layered structure and all 3D properties of the models (electronic annex 1).

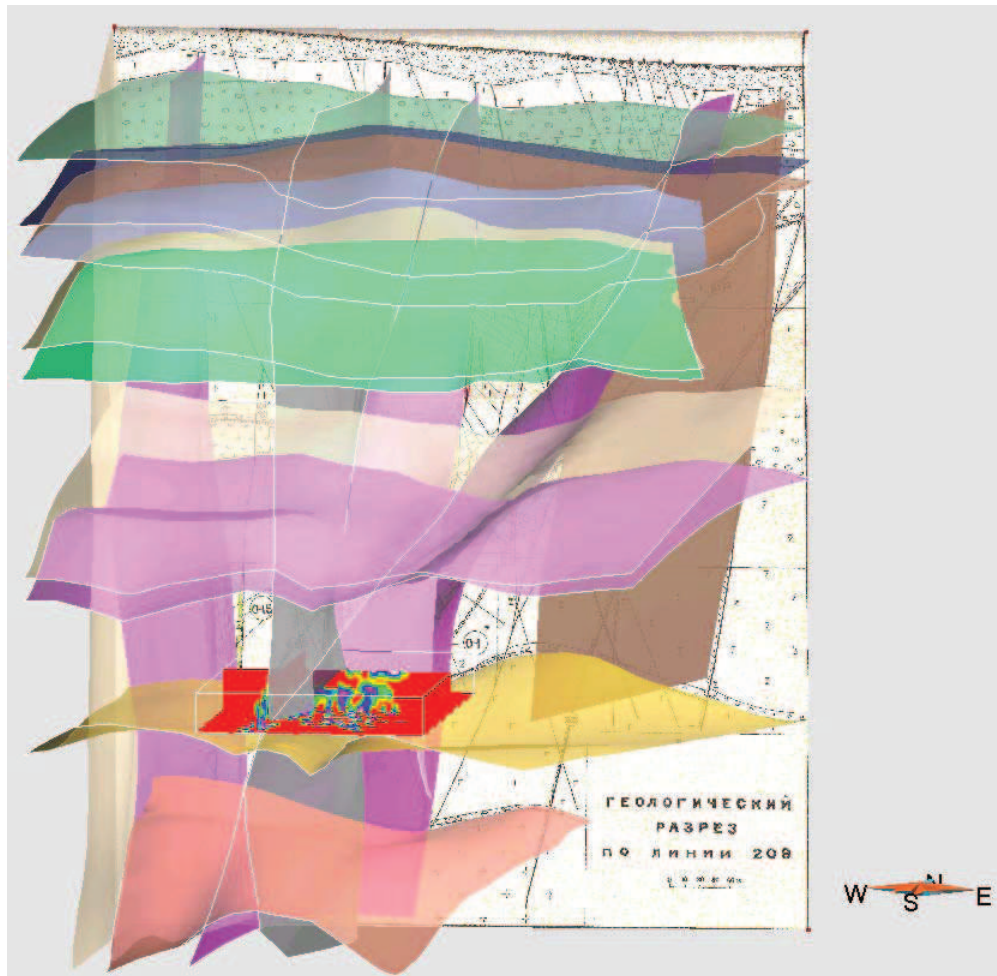


Fig. 1.13. 3D model of geological structure of the Oktyabrsky deposit imported into Gocad with the raster image of the cross-section on prospecting line 209. Three red cross-sections in the box – 3D model of the ore body built in Gocad.

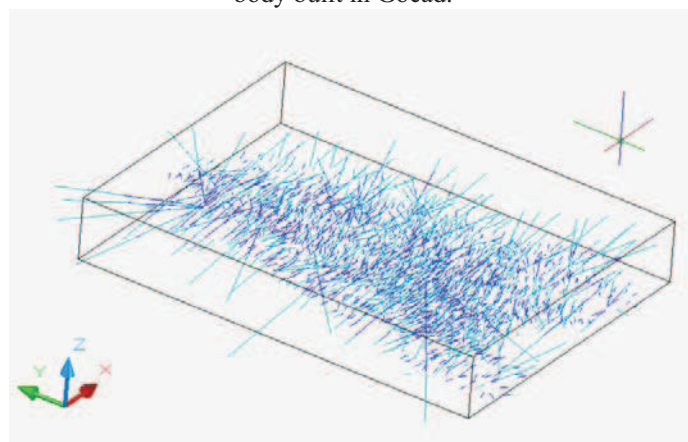


Fig. 1.14. Generalized intervals of gamma-sampling on 9 mining slices digitized in AutoCAD Map. Blue – commercial intervals, cyan – barren intervals. Y axis points to the north, X axis – to the east. The length of the model box – 200 m, the height – 30 m.

### 3. 3D GIS modeling

Analysis of the internal structure of the ore body and its spatial relation with the geological structure of the Oktyabrsky deposit revealed that the highest-grade part of uranium mineralization is controlled by the meridional 2<sup>nd</sup> fault at its joint with the meridional but more steep 7<sup>th</sup> fault (Fig. 1.15). The main part of the ore body occurs in the footwall of the 2<sup>nd</sup> fault, and only a few mineralized zones are located in the top wall of the fault. This indicates the screening of ascending fluid flows, which penetrated along the series of steeply dipping NW faults (blue in Fig. 1.15), to the 2<sup>nd</sup> fault. As a result, the rich uranium mineralization is controlled by these NW faults south-east of the 2<sup>nd</sup> fault, and by the footwall of the latter.

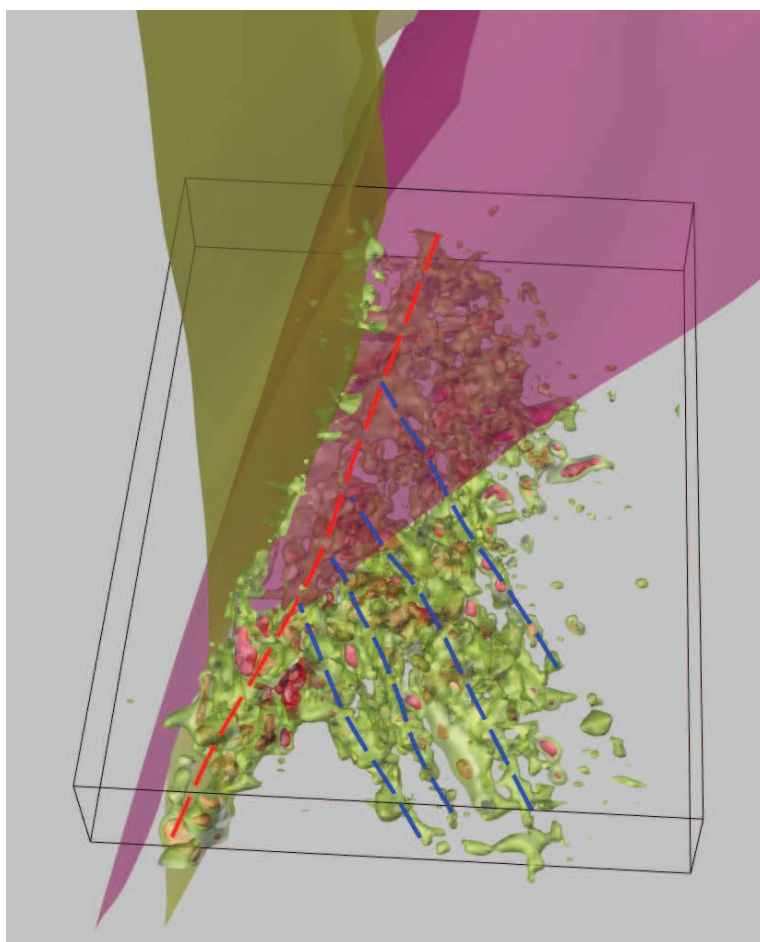


Fig. 1.15. Numerical model of the ore body in the Oktyabrsky deposit built in Gocad with surfaces of the 2<sup>nd</sup> fault (transparent crimson surface) and the 7<sup>th</sup> fault (transparent brownish-green). Surfaces of isoconcentration of uranium (isosurfaces) 0.1% (transparent green) and 1% (red). It is apparent that the richest part of the ore body is constrained by the 2<sup>nd</sup> fault at its joint with the 7<sup>th</sup> fault (red dashed line) and is located below the surface of the 2<sup>nd</sup> fault. Lesser grade mineralization is controlled by the NW faults (blue dashed line) and screened by the longitudinal 2<sup>nd</sup> fault. Geological and numerical models of the ore body were combined in GeoSpline and then exported in PDF3D format.

The internal structure of the ore body is highly heterogeneous. Relatively small ore knots with uranium content exceeding 1% are randomly distributed along the faults

### 3. 3D GIS modeling

(Fig.1.15). They are controlled mostly by joints of faults of different strike, as well as splitting zones and flexures, based on observations in mining galleries in the Oktyabrsky deposit.

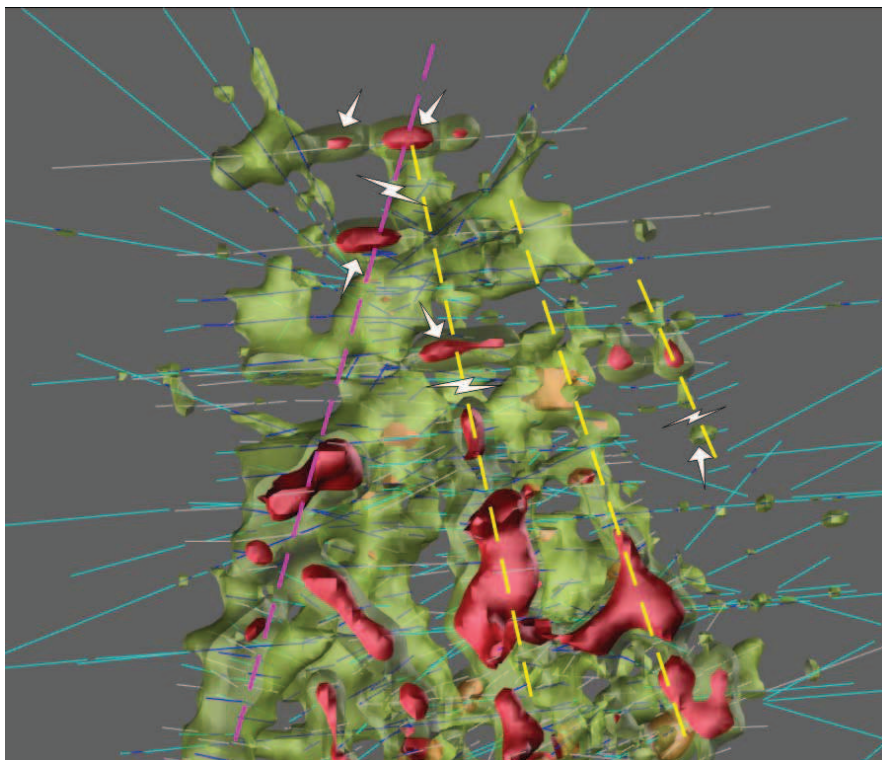


Fig. 1.16. Misinterpretation of primary sampling in cases of low-density and highly anisotropic data: erroneous elongation of uranium isosurfaces along boreholes (pointed by white arrows) and breaks of isosurfaces (white zigzags) along the 2<sup>nd</sup> fault (magenta dashed line) and NW faults (yellow dashed lines). Long cyan and blue lines – gamma-sampling of boreholes. Northern part of the ore body model.

Morphology of some high-grade clusters in the northern part of the model cannot be explained from a geological point of view. Elongated disconnected clusters are oriented in transversal direction regarding to the strike of NE or NW faults (Fig. 1.16). Analysis of sample locations reveal a low-density data network in this part of the ore body on one hand, and the predominance of borehole gamma-logging over face galleries on the other. It means that in the central and southern parts of the model, isosurfaces were built on the basis of relatively short and more or less dense, evenly distributed samples of mining galleries while in the northern part rare borehole data prevail. These latter are characterized by a high anisotropy of the sampling because the distance between samples along one drilling is essentially shorter than the distance between neighbour drillings. It usually causes the

### 3. 3D GIS modeling

---

phenomena of “bull-eye” shape of the isolines on contour maps, induced by small isolated isometric maxima of concentrations along a borehole.

In our case, clusters elongated in transversal directions were influenced by isolated anomalies along single boreholes oriented perpendicular to the strike of the main ore controlling faults, i.e. latitudinally. The absence of barren samples between anomalies has not caused a combination of the anomalies because of the long distances between them.

The problem is rather common and is not solved in a general case yet. Kriging procedure can reduce it significantly but only in the case of isotropic data distribution or anisotropic distribution with one predominant direction of anisotropy for correct variogram orientation. In the case of our model, there are at least two directions of natural anisotropy – NE20 and NW340 (the 2<sup>nd</sup> fault and feathering NW faults respectively). Choosing one of them will distort the results of interpolation for the other. So the best solution, from the author’s viewpoint, is the use of a simple interpolation method with subsequent analysis of the results keeping in mind that it is not “the ultimate truth” but preliminarily generalized data and further interpretation with geological experience is necessary.

#### 3.4. Conclusions

The analysis of existing software for 3D modeling of a geological structure of deposits and an internal structure of ore bodies demonstrated the absence of ready-to-use solutions for our purposes. Careful selection of computer programs optimal in their possibilities and price is necessary.

The use of numeric modeling of both the geological structure of the Oktyabrsky deposit and the ore body exhibited the exceptional value of such an approach. Its goal is clear presentation of complex geological structures on one hand and revealing their role in the control of rich clusters of ore bodies on the other.

However, it must be noted that direct mechanistic utilization of statistical treatment of complex, unevenly distributed data may lead to misinterpretation of the spatial structure of an ore body and to mistakes in exploration of a deposit. The experience of a geologist in such an interpretation is highly desirable to obtain correct results.

## Part II. Mineralogy of the deposits and geochemical behaviour of elements in magmatic and hydrothermal processes





## **1. Uranium and fluorine behaviour in the Late Mesozoic volcanic rocks of the Streltsovsky caldera**

Because many researchers suggest genetic links between uranium ore mineralization in the SOF and magmatism, the distribution of uranium and associated elements in igneous rocks of different ages is of interest. The available information on U contents in igneous rock is rather extensive (Ishchukova et al., 1998; Andreeva et al., 1990, 1996<sub>1</sub>). However, these results were obtained with radiometric methods or XRF, with a detection limit of 1.2 ppm, which is twice as high as the average U content in basalts. Besides this, uranium contents in trachybasalts published for some statistical samples (e.g., Ishchukova, 1998, p.118) are abnormally high (above 7 ppm) with very low Th/U ratios (0.8-0.9) which unambiguously indicates superimposed uranium concentrations.

Additional study of the behaviour of uranium in the magmatic rocks was carried out by the author using more precise analytical methods (inductively coupled plasma mass spectrometry (ICP-MS) and instrumental neutron activation analysis (INAA)). The intensity and type of metasomatic alteration was studied in thin-polished sections under an optical microscope. The syngenetic or epigenetic character of uranium distribution in samples was determined with fission-track radiography (Fig. 2.1).

Four epochs of Late Mesozoic magmatism are recognized in the eastern Transbaikal region (Andreeva et al., 1996<sub>2</sub>). The first epoch (208–187 Ma) was not intense and did not affect the SOF.

During the second epoch (178–154 Ma), granodiorite–granite–leucogranite plutons were emplaced a few hundred kilometers north of the SOF. They contain ordinary uranium concentration with respect to the average uranium abundance for these rocks (2.7-4.8 ppm after Taylor & Mc Lennan, 1985). At the same time, trachybasalts and trachydacites of the Priargunsky suite were erupted at the site of the future Streltsovsky caldera. Uranium and fluorine distribution in these rocks is the main focus of the current study.

The third epoch of magmatism (150–138 Ma) is the most important in terms of uranium ore formation because the SOF was formed after crystallization of intrusive and volcanic rocks pertaining to this epoch. These rocks are distinctly enriched in Ta, Nb, W, Be, and U. Minor hypabyssal intrusions of Li–F leucogranite and subvolcanic ongonite intrusions were emplaced in this epoch in the eastern Transbaikal region. Most of these intrusions were formed 144–138 Ma ago (Badanina et al., 2004, 2006; Kuznetsov et al., 2004;



# 1. U and F behavior in volcanic rocks

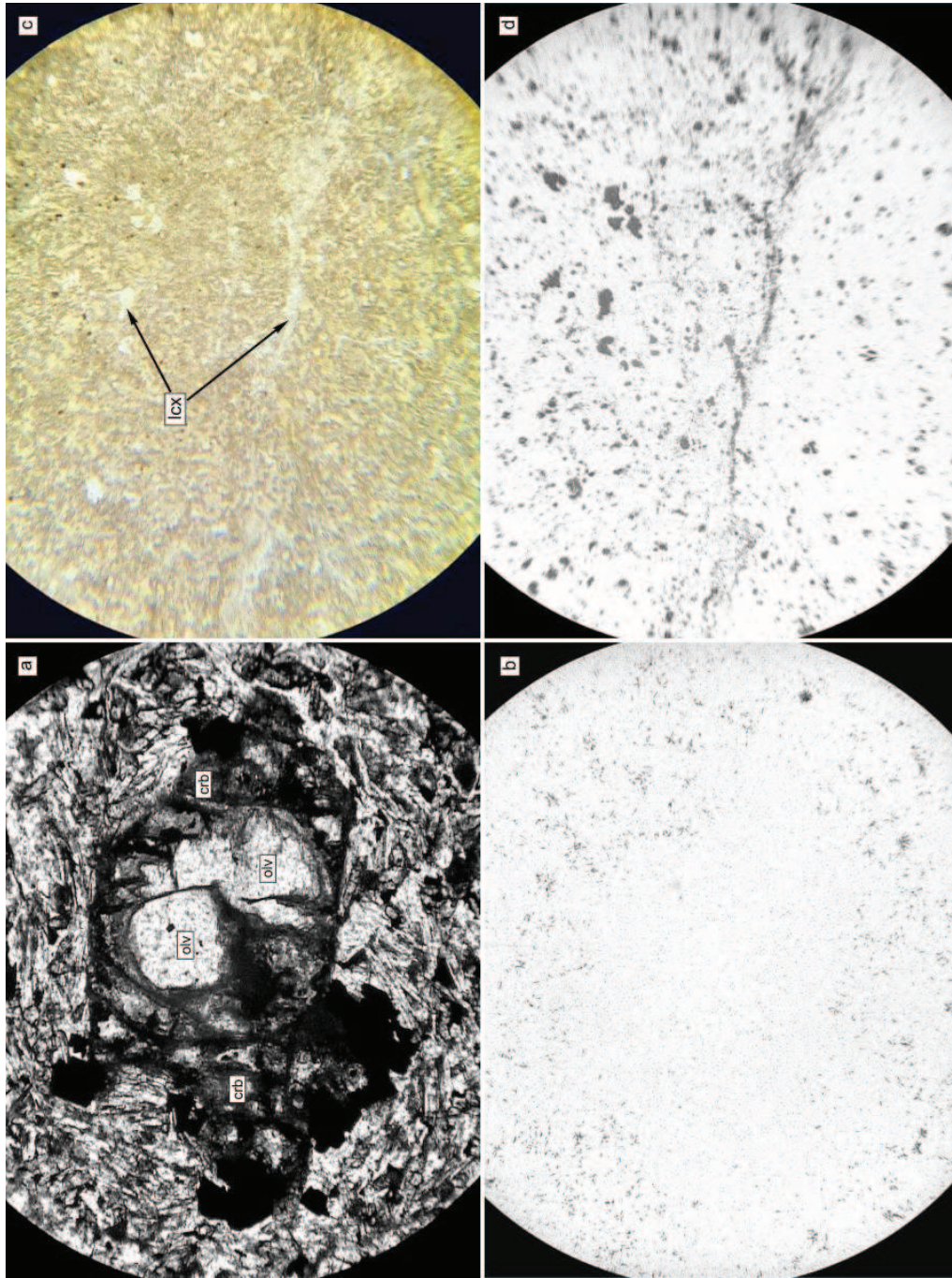


Fig. 2.1. Basalts altered with different intensity and uranium distribution in the rocks: (a) – the freshest basalt with olivine (olv) partly replaced with carbonate (crb) and unaltered matrix; (b) – tracks of uranium are evenly distributed in the matrix and are practically absent in the olivine phenocryst; (c) – basalt overprinted by carbonatization, chloritization and illitization, Ti-accessories are completely replaced with leucoxene (lcx); (d) – superimposed uranium is concentrated in leucoxenized accessories and in a thin seam of leucoxene. Photomicrographs of thin-polished section St-138 in transmitted plane-polarized light (a) and section St-111 in transmitted and reflected plane-polarized light, black field (c); (b), (d) – lvsan detectors of corresponding sections. The long side of photomicrographs is 1.1 mm (a,b) and 3.9 mm (c, d)

## 1. U and F behavior in volcanic rocks

---

Andreeva et al., 1996<sub>2</sub>). Silicic volcanics of the Turginsky suite enriched in U (15–25 ppm) were erupted in the Streltsovsky caldera. According to the data of P.S. Kozlova and colleagues (unpublished IGEM data), similar U contents were established in the rare-metal leucogranite of the Kir-Kirinsky pluton (12–30 ppm U), located 50 km north of the SOF; the Suktui pluton (9.6–28 ppm U), 130 km northwest of the SOF; and the Khangilai pluton (10.8 ppm U, on average), 250 km northwest of the SOF.

The fourth epoch (126–117 Ma) is characterized by decreasing magmatic activity. At that time, the Konduisky pluton, a morion-bearing leucogranite, dated at 125–120 Ma (Andreeva et al., 1996<sub>2</sub>), was emplaced 50 km northwest of the SOF and silicic lavas were erupted 100 km to the northeast and 20 km to the southeast between 120–118 Ma ago. Both intrusive and volcanic rocks possess moderate uranium concentrations compared to the average content of silicic igneous rocks or even lower.

The distribution of U and other elements in the trachybasalts from the Streltsovsky caldera was studied at several stratigraphic levels (Fig. 2.2). The lower trachybasalt flows of the Priargunsky suite were sampled in underground galleries at the Streltsovsky deposit (samples St-110, St-124, St-131, St-136, St-138, St-139, St-146-458, appendix 1). The upper flows of the same suite were sampled in the open pit at the Tulukui deposit (samples St-357, St-539, St-540). The younger flows of the overlying Turginsky suite were sampled at the surface near the Dal'ny deposit (samples T05-50, T05-51, T05-53).

It has been established that trachybasalts of the lower flow of the Argunsky suite is characterized by the high U content for these types of rocks (1.8–2.5 ppm, 2.37 ppm in average; Fig. 2.3a). The overlying trachybasalt flows from the Argunsky and Turginsky formations contain 1.0–1.8 ppm U. These results are broadly consistent with the range of U contents in basalts of the Streltsovsky caldera obtained from radiometric analysis and fission track radiography (1.2–2.8 ppm, according to data of P.S. Kozlova, B.M. Sel'tsov, V.V. Viktorov, and other authors from IGEM, unpublished data).

Some slightly altered samples from the lower flow are marked by elevated superimposed U contents (3–6 ppm), which deviate from the average crustal Th/U ratio of 3–4 and are not shown in Fig. 2.3a. Therefore, the radioelement content of these samples was estimated from Th content as a less mobile element. It can be seen from Fig. 2.3a, that the Th content in basalts of the lower flow (8.0–9.5 ppm) is higher than in basalts of the upper flows (5.2–6.0 ppm) and these two groups do not overlap in Th content. These results raise the statistical significance of the elevated U content in the lower basalts.



# 1. U and F behavior in volcanic rocks

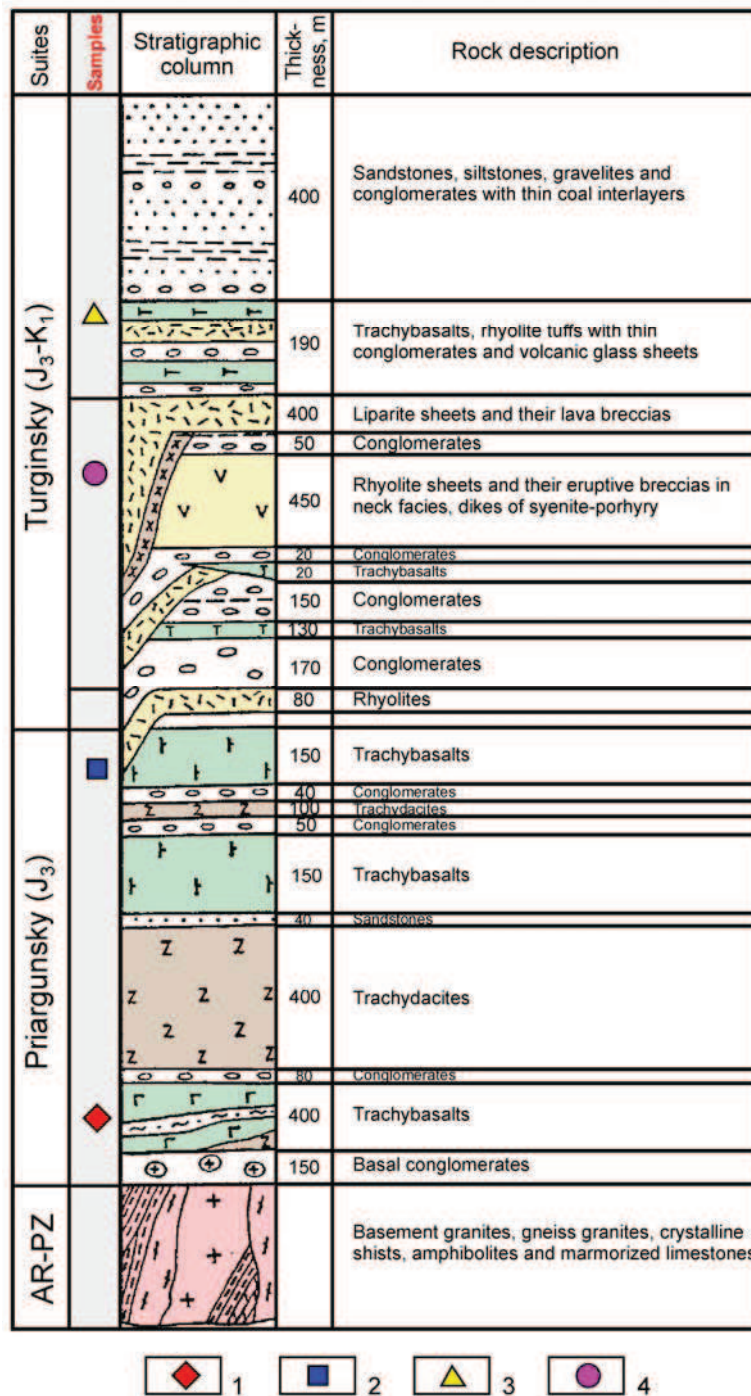


Fig. 2.2. Location of samples of basalts (1-3) and rhyolites (4) in the sedimentary-volcanogeneous sequence of the Streltsovsky caldera. 1 – basalts of the lower flow of the Priargunsky suite, 2 – basalts of the upper flow of the Priargunsky suite, 3 – basalts of the Turginsky suite.

The close association of uranium with fluorite in many uranium deposits led us to determine F contents in igneous rocks of the SOF. Fluorine concentration in rocks is supposed to be proportional to its content in biotite determined by electron microprobe analysis (SX-100, UHP), and in melt inclusions from rhyolites (Chabiron et al., 2001).

# 1. U and F behavior in volcanic rocks

Fluorine contents in SOF biotite are rather stable features, and even in metasomatically altered varieties of basalts it remained at the same level as in the freshest rocks.

Fluorine shows the same trend in basalts as for uranium. Biotite from the lower flow of the Priargunsky suite is characterized by the highest F content, up to 5.7 wt. % (6.6 at %). It is one of the highest values for biotite from various genetic types of rocks from the literature. The F content in biotite is inversely correlated with the Fe mole fraction (*Reviews...*, 1984), as is clearly seen from Fig. 2.3b. Due to this fact, different groups of biotite are better distinguished by correlating F with the Fe/(Fe+Mg) ratio of biotite rather than only on F concentration. The F content in biotites from the upper flows in the Priargunsky and Turginsky formations is lower than in biotite from the lower flow of the

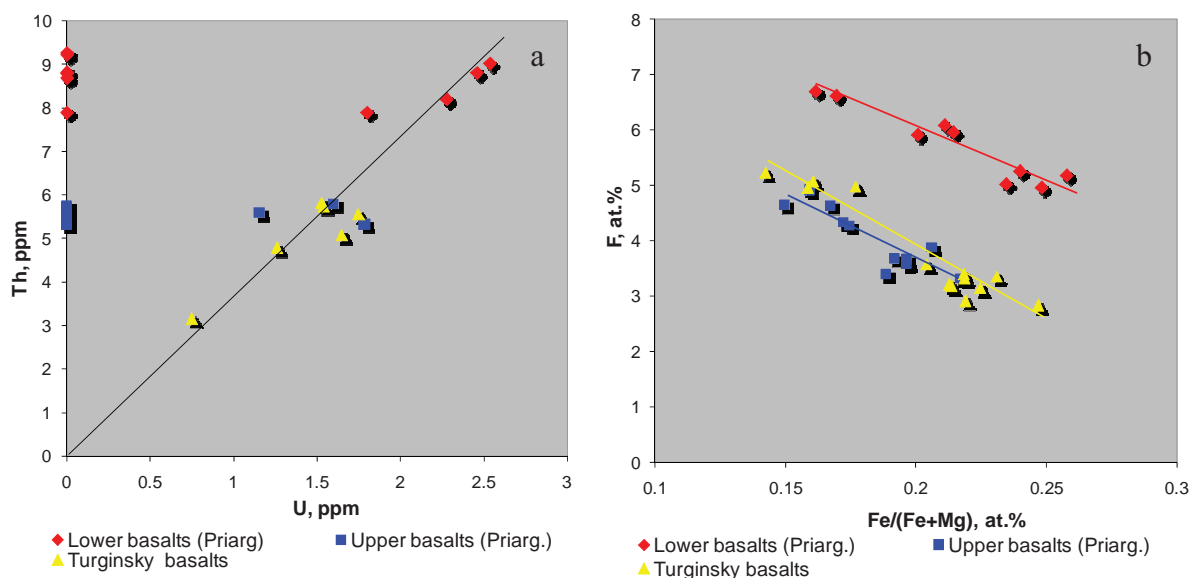


Fig. 2.3. (a) Uranium and thorium contents in basalts and (b) fluorine content in biotite from basalts plotted against Fe/(Fe+Mg) ratio of biotite. Data on the y axis in figure (a) correspond to samples where U was not analyzed.

Priargunsky suite and they form two distinct groups (Fig. 2.3b).

The F content in the initial basic magma forming the lower basalt flow estimated on the assumption that this element mostly concentrates in biotite and apatite. As the F concentration in biotite inversely depends on its Fe/(Fe+Mg) ratio, the maximum fluorine content should be in Mg-biotite at 8.34 wt. % (calculated from linear trend equation). Assuming average biotite concentration in basalt as 3%, the estimation of the F content in parental basic magma is  $8.34 \times 0.03 = 0.25$  wt. %. Additive fluorine from apatite is negligible

## 1. U and F behavior in volcanic rocks

---

relative to biotite because the average apatite content in basalt is around 0.1 % (from ICP-ES data) and the F concentration in apatite is 0.2 wt. % (from microprobe data), so the F concentration in magma from apatite is 0.02 wt. %. The total fluorine content in the initial basic magmas is approximately 0.27 wt. %.

The average F content in parental magma forming the upper flows of the Priargunsky and Turginsky suites is estimated as 0.19 wt. %. This evaluation is based on the difference between the F content in biotite from the lower basalt flows of the Priargunsky suite and the upper basalt flows.

Similar average F content (0.299 wt. %) in basalt with >1.3 wt. % K<sub>2</sub>O was calculated by Naumov et al. (1998) from F concentrations in melt inclusions and quenched basaltic glasses worldwide.

The U and F contents in silicic melt from the upper crustal magma chamber as a source of rhyolite of the Turginsky suite were estimated from data on melt inclusions (Chabiron et al., 2001). It has been established that the melt contained 14–23 ppm U and 1.4–3.2 wt. % F. These results support previously obtained data on high U contents in silicic volcanic glasses in the SOF (Andreeva et al., 1996<sub>2</sub>).

Unfortunately we failed to find unaltered biotite grains or melt inclusions in quartz phenocrysts from trachydacite, which could be used for estimation of U and F contents. According to Andreeva et al. (1990), the average U content in the least altered trachydacites is 9.8 ppm; the primary character of the U distribution in this rock was corroborated by fission-track radiography. Our unpublished data coincide with this estimate and indicate that the concentration of U in trachydacite and other volcanic rocks in the Streltsovsky caldera is three to four times higher than the average uranium content in the same type of rocks.

Thus, the revealed general trend is the enrichment of volcanic rocks in U and F from the oldest basic rocks (2.0–2.5 ppm U and 0.3 wt. % F) through the intermediate and moderately silicic rocks (10 ppm U and ? F) to the youngest highly silicic rocks (15–25 ppm U and ~3 wt. % F).

### Conclusions

Geochemical studies revealed close association of U and F which progressively increased in Late Mesozoic rocks from the oldest basic volcanics through the intermediate and moderately silicic rocks to the youngest highly silicic rocks.

# 1. U and F behavior in volcanic rocks

The tendency of U and F accumulation may be traced not only in time (from the oldest rocks to the youngest ones) but also in space when considering magma sources. In this respect, accumulation occurred upwards – from the mantle produced basic magmas (basalts) through intermediate space and composition magmas (dacites) to uppercrustal derived acidic magmas (rhyolites).

If this tendency is applied to the area of the uranium ore deposition, it logically comes to the end in time (170 Ma → 160-150 Ma → 140 Ma → **135 Ma**) and space (40 km → ~15 km → **0-1.5 km**) with the maximum concentration of these elements in the ores (2 ppm U, 0.3% F → 10 ppm U, ? F → 20 ppm U, 3% F → **~2000 ppm U, ? F**) (Fig. 2.4). Consequently, we are dealing with a Late Mesozoic U–F geochemical association which indirectly testifies to the postmagmatic nature of the pitchblende–fluorite mineral paragenesis found in the ores.

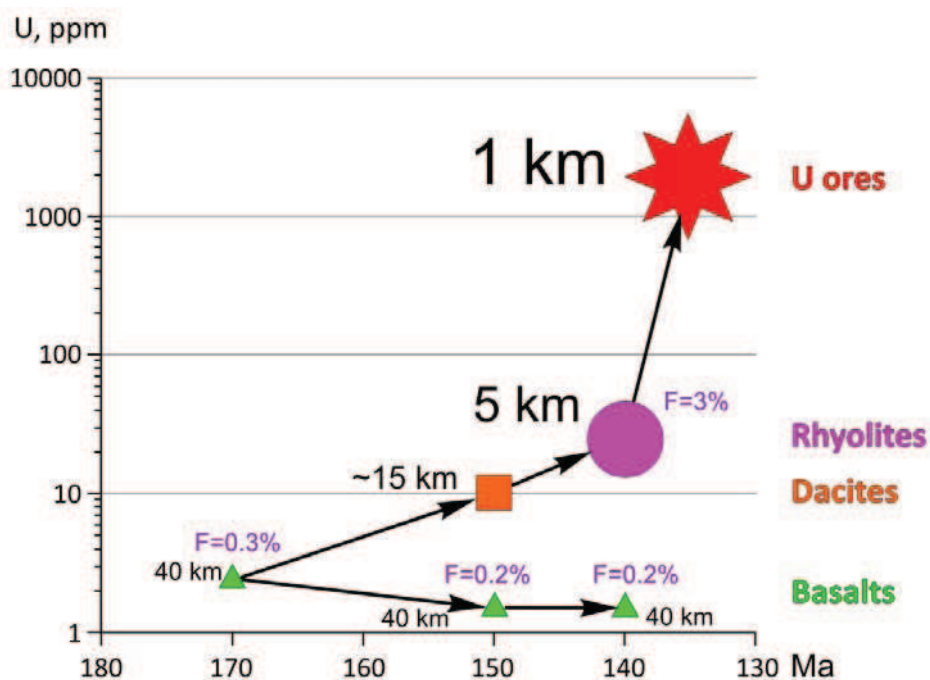


Fig. 2.4. Evolution of U content in volcanic rocks and the uranium ores in the Late Mesozoic regarding depths of magma generation and ore deposition. Uranium and fluorine were depleted in basic magma with time while they were progressively accumulated in more acidic magmas towards the surface.





## 2. Mineralogy of the deposits

Mineralogical studies of the SOF deposits begun in the early 1960s and interest has lasted over 40 years of prospecting and mining of this unique ore field. Numerous mineralogists and research teams studied different aspects of mineralization – from the Early Paleozoic high-temperature feldspatization to the contemporary hypogene processes that occur in underground mines and open pits. Their results were set forth in unpublished reports and in closed transactions devoted to uranium deposits of the USSR. Some of the researchers studied specific questions such as the types of metasomatic alteration (O.V.Andreeva, V.A.Golovin, G.T.Volostnukh), carbonate mineralization (V.I.Vorontsov), or K-feldspar investigations (N.A.Peretz). Other researches (V.P. Rogova, M.V. Vampilov, I.V. Mel'nikov, I.V. Chernykh, K.V. Skvortsova, N.S. Trofimov) investigated various mineral associations and their temporal and spatial relations which led them to substantiate paragenetic schemes of staged hydrothermal mineralization.

Comparisons of different succession schemes demonstrates the absence of any generally recognized view on mineralogy of the SOF deposits. Only rough tendencies in the sequence of mineral formation during the Late Mesozoic epoch could be outlined: (1) widespread preore argillic alteration with the subsequent formation of sulfide-bearing cryptocrystalline quartz veins; (2) uranium ore formation expressed by the deposition of a brannerite–coffinite–pitchblende mineralization and molybdenite along with development of wall-rock albitization and hematization; (3) formation of a postore quartz–fluorite–molybdenite assemblage; and (4) formation of the youngest quartz carbonate–fluorite veins with kaolinization in exocontact zones.

However, the number of stages and details of mineral assemblages within each stage remained a matter of discussion. It may be explained by the complexity of the multistage sustained hydrothermal processes which occurred in the SOF. This disagreement even forced one of the researchers to make an appeal to mineralogists to bring their views into coincidence (Wolfson et al., 1981). It necessitated provision of the author's own mineralogical studies as a background for further complex investigations.

The author tried to pay equal attention to metasomatic and veined mineralization as both of them are the result of an indivisible hydrothermal process. But whereas establishment of mineral succession in veins is based on numerous ontogenic criteria (including intersection, overgrowth, cementation, etc.), in metasomatic rocks it is limited only by the replacement of one mineral by another. From the author's experience, the sequence of

## 2. Mineralogy of the deposits

---

metasomatic replacement in wall-rocks and mineral deposition in veins within a stage is the same reflecting the evolution of a fluid composition from the beginning of the stage to its end. Therefore, if no other direct or indirect evidences existed, mineral succession in veins was spread on metasomatic mineralization when compiling the paragenetic scheme.

Commercial uranium mineralization was formed in the Late Mesozoic epoch, after contrasted basalt-dacite-rhyolite volcanism and widespread quartz-illite-chlorite-carbonate metasomatic alteration of the rocks. However, scarce uraninite mineralization is known related to Late Paleozoic and Early Mesozoic greisenization (Ishchukova et al., 1998). According to U-Pb dating of disseminated uraninite in Precambrian basement rocks (Chernushev and Golubev, 1996) its isotopic is 457-459 Ma. The oldest dated uraninite was formed at approximately 770 Ma (Golubev, personal communication, 2008). Nevertheless, the author believes that this polychronic disseminated uraninite mineralization did not play any significant role in the formation of the giant reserves of the SOF deposits. Therefore, the processes preceding the Late Mesozoic tectonic-magmatic activization of the Transbaikal region are not considered here.

### 2.1. Stages of the Late Mesozoic hydrothermal process

According to newly obtained data, four stages of the Late Mesozoic hydrothermal process have been recognized: (1) preore, (2) uranium ore, (3) 1<sup>st</sup> postore, and (4) 2<sup>nd</sup> postore (Fig. 2.5).

#### 2.1.1. *The preore stage*

During the preore stage metasomatic alteration of basement rocks and sedimentary-volcanogeneous filling of the caldera occurred with simultaneous formation of veined mineralization. This postvolcanic pervasive alteration (illitization, carbonatization, chloritization and silicification) was not intense but affected the entire body of host rocks from the basement and volcanic pile. In contrast to the postore alteration, which as a rule is intense and controlled by faults, the halos of preore metasomatic alteration are visually vague.

Areas of weak alteration developed with different intensities have been observed in mines and open pits (Fig. 2.6). Alteration is expressed in rock bleaching of different intensities. Most distinctly alteration is revealed in basalts and dacites: their color changes from black to dark grey and greenish grey for basalts and from brownish red to brown and brownish grey for rhyolites and dacites (Fig. 2.7, 2.10). The boundaries between areas of

## 2. Mineralogy of the deposits

rocks affected by alteration of different intensity are as a rule diffuse and do not exhibit any evident structural

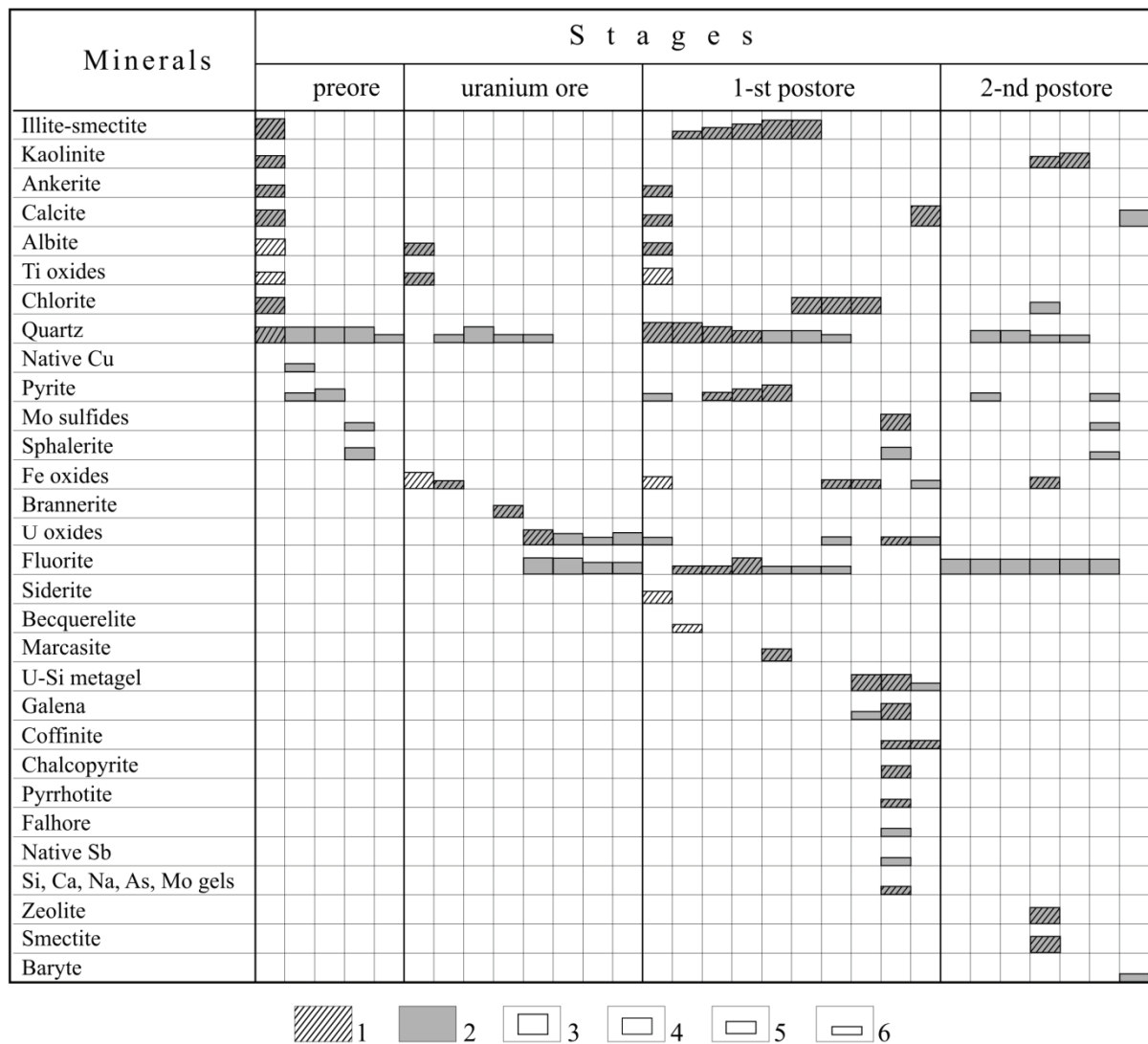


Fig. 2.5. Paragenetic mineral succession of the Late Mesozoic hydrothermal process in the SOF deposits. Compiled using the data of Ishchukova et al. (1998), and Andreeva and Golovin (1998). (1–6) Minerals: (1) metasomatic, (2) veined, (3) highly abundant, (4) abundant, (5) not abundant, (6) rare.

## 2. Mineralogy of the deposits



Fig. 2.6. Halos of preore and postore alteration in trachydacites in the west-northern wall of the Tulukui open pit. Weak preore alteration is presented by brownish-red dacites while postore alteration is manifested as intensively bleached light greenish-grey and orange dacites. Rectangles with numbers – areas of detailing: 1 – Fig. 2.7 and 2.8, 2 – Fig. 2.9, 3 – Fig. 2.10.



## 2. Mineralogy of the deposits

---



Fig. 2.7. Relics of slightly altered brownish-red dacites in the central parts of fractured blocks and narrow zones of more intensive alteration with distinct boundaries (brownish-grey dacites) along cleavage fissures. The boundaries in the lower left corner of the photograph are more diffuse. Detail of area No.1 in the Fig. 2.6.



Fig. 2.8. Zone of intensive post-ore bleaching of light-orange color (Fe oxides leaching) with narrow conjugate rim of green color (intensive illitization) along vertical fracture. The length of the GPS box is 5 cm. Detail of area No.1 in Fig. 2.6.



## 2. Mineralogy of the deposits

---



Fig. 2.9. Intensively hematized dark brownish-red dacites (synore hematization) with superimposed bleached zones of intensive postore alteration (light-orange areas along fissures) and calcite veinlets (white). Light-green zones of intensive illitization are also noticeable along a dense network of cleavage fractures (pointed with an arrow). Detail of area No.2 in Fig. 2.6.



Fig. 2.10. Typical “background” dacites slightly altered during the preore stage with vague diffusive boundaries between less altered brownish-red and more altered brownish-grey varieties of rocks. The length of the GPS box – 5 cm. Detail of area No. 3 in Fig. 2.6.

## 2. Mineralogy of the deposits

---

control by large faults (Fig. 2.10). However, sometimes distinct halos of more intense bleaching are observed along cleavage fissures (Fig. 2.7). Granite as a coarse-grained rock does not show the weak preore alteration, its color remains pinky-grey and boundaries between areas of different intensity of alteration are always vague. Marbles are the only variety of rocks where preore alteration was not developed.

Not only metasomatic processes occurred during the preore stage. All the rocks also contain abundant thin veinlets filled with the same minerals as newly formed minerals of altered rocks – illite-smectite, carbonate, quartz, chlorite and sulfides of Fe, Zn, Mo. Carbonate and chlorite predominate in basalts while quartz is a prevalent mineral in granites, rhyolites and dacites. The thickness of the veinlets varies from fractions of a millimeter to several centimeters. Some rare quartz and carbonate veins several decimeters thick also belong to the preore mineral complex<sup>1</sup>.

Establishing the preore stage as a separate stage is difficult in comparison with the younger stages. Difficulties result from low intensity metasomatic alteration, similarity of mineral composition with the 1<sup>st</sup> postore stage, and from superimposition of the later stage hydrothermal fluids which obscure features of the preore complex. However, clear intersection of cryptocrystalline quartz veinlets with pyrite, low-Fe sphalerite (cleophane) and amorphous Mo sulfide (jordisite) by quartz-pitchblende stringers evidence earlier formation of a quartz-polymetallic mineralization comparable to the uranium one (Fig. 2.11, 2.12). No macroscopic-scale substantiation of the preore stage were obtained due to the dispersed character of the thin stringers in host rocks.

Arguments in favor of the preore age of metasomatic alteration of rocks are even more obscure. The most reliable facts are the K-Ar isotope data on illite which demonstrate wide ranges of ages from 139 to 129 Ma (Table 2.1, after Andreeva et al., 1996<sub>2</sub>) covering both preore and postore time spans. The only definitive fact about illitization with associated carbonatization, chloritization and silicification is that halos of high-intensity alteration controlled by fractures are superimposed on the uranium ore mineral complex (Fig. 2.9, 2.17). Areas of low-intensity alteration might be peripheric zones of postore metasomatites as well as preore ones (according to isotopic data). Similarly, timing of moderate alteration is not clear (Fig. 2.7). Relationships between mineral assemblages of low-intensity alteration and uranium assemblages cannot clear up the question because the latter (albite, quartz, pitchblende,

---

<sup>1</sup> Mineral complex is a set of minerals formed during one stage of hydrothermal process.



## 2. Mineralogy of the deposits

---

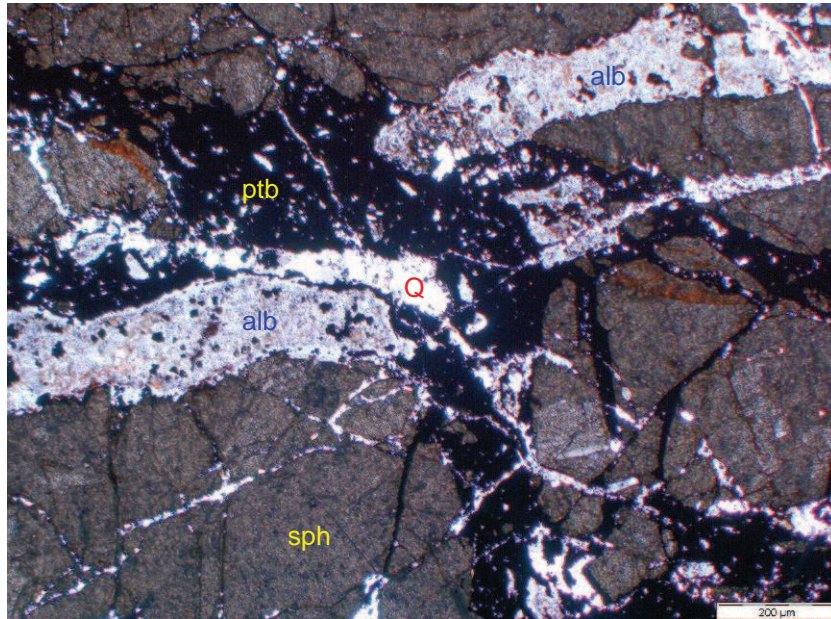


Fig. 2.11. Large fractured grain of low-Fe sphalerite (sph) is intersected by an albite streak (alb) and later quartz-pitchblende veinlets (ptb) which, in turn, are crossed by an illite-quartz stringer (Q) of the 1<sup>st</sup> postore stage. The Antei deposit, horizon +134 m. Photomicrograph of thin-polished section St-362a in plane-polarized transmitted light.

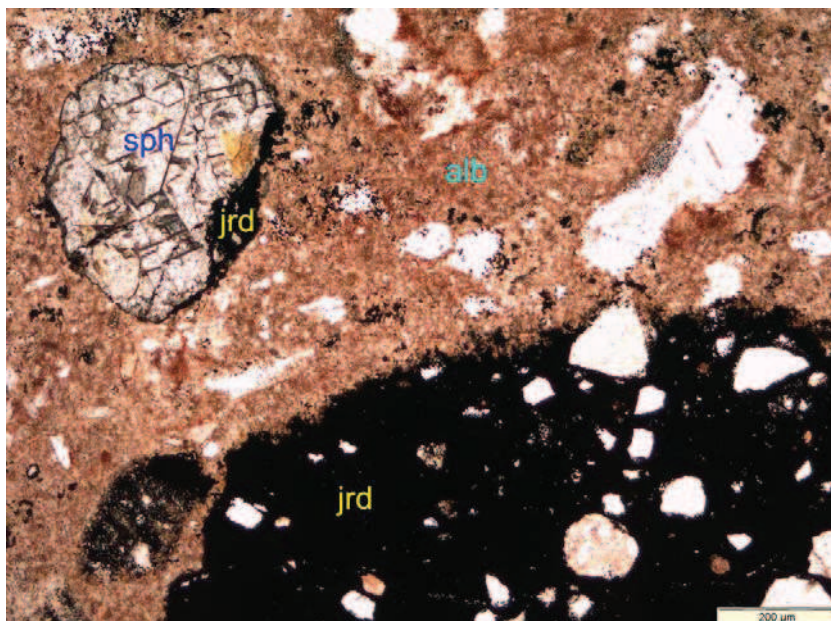


Fig. 2.12. Fragments of breccia with jordisite cement (jrd) and cleophane (sph)-jordisite intergrowth are cemented with synore albite (alb) impregnated with fine-dispersed Fe oxides. The Antei deposit. Thin-polished section St-511. Photomicrograph in transmitted plane light.

## 2. Mineralogy of the deposits

brannerite) are resistant to weak illitization. So in both cases (preore or postore age of weak alteration) the relationships should be the same.

Table 2.1. Isotopic ages of hydromica metasomatites in the SOF (Andreeva et al., 1996<sub>2</sub>)

NN	Deposit	Mineral	K-Ar age, Ma	Rb-Sr age, Ma
1	Yubileiny	illite	139±8	
2	Streltsovsky	illite	138±5	
3	Argunsky	illite	138±5	
4	Streltsovsky	illite	136±5	
5	Streltsovsky	illite	135±5	
6	Streltsovsky	illite+ankerite	135±5	131±2
7	Streltsovsky	illite	134±5	
8	Streltsovsky	illite	134±5	
9	Argunsky	illite	134±5	
10	Streltsovsky	illite	134±5	
11	Streltsovsky	illite	133±5	
12	Streltsovsky	illite+ankerite	133±5	133±2
13	Streltsovsky	illite	130±5	
14	Streltsovsky	illite	129±5	

Summarizing, the preore hydrothermal stage lasted from the end of the 3<sup>rd</sup> stage of Late Mesozoic magmatism (approximately 140 Ma) until the uranium ore stage (135 Ma). It was an extensive metasomatic alteration of relatively low intensity, generally not controlled distinctly by faults and fractures. It therefore follows that the hydrothermal solution penetrated gradually through interstitial and pore channels of rocks.

### *2.1.2. The uranium ore stage*

The minerals of the uranium ore stage occur locally compared to other stages. As it is strictly controlled by fractures, all the morphological varieties of ore bodies are determined mostly by the physicochemical properties of enclosing rocks.

The ore mineral complex occurs in veins accompanied by relatively narrow aureoles of hematization and albitization. Quartz and dark-violet fluorite are the only gangue minerals developed in veins and stringers. Uranium minerals (pitchblende and, in lesser amounts,

## 2. Mineralogy of the deposits

---

brannerite and uraninite) occur in veinlets as well as in the host rocks as dissemination. Alteration zones are not extensive, they develop at a distance of not more than a few decimeters from individual mineralized faults and fractures. In stockworks, disconnected aureoles of hematization and albitization along fractures merge into one large halo. Halo width may reach up to tens of meters depending on the thickness of the stockwork zone.

Basalts and granites possess the highest strength properties (the Young's modulus) and they release deformation tension mostly as single fractures. Uranium ore mineral complex is developed in these rocks usually as veins and linear breccia zones with conjugate narrow zones of hematization (Fig. 2.13, 2.14).

Trachydacites and rhyolites are more brittle. This property caused preferential development of cataclased zones and, consequently, stockwork type streaky-disseminated uranium mineralization with large halos of hematization (Fig. 2.15). Tuffaceous sandstones, gritstones and conglomerates are characterized by the lowest Young's modulus among all the rocks which has determined the prevailing development of dispersed fractures. Even fault zones consist of numerous separated fissures. This feature along with high porosity of sedimentary rocks gave rise to disseminated uranium mineralization in fault zones (Fig. 2.16) and wide development of bedded ore bodies controlled by layers of tuff-sandstones and conglomerates.

The age of pitchblende, as the main uranium mineral in the SOF, was determined by U-Pb dating at  $135 \pm 2$  Ma (Chernyshev and Golubev, 1996). Its later formation regarding the preore mineral complex is constrained mainly by microscopic observations (Fig. 2.11) rather than by structural studies because of the poor structural controls of the preore complex. Also, isotopic ages of some of the hydromicas point on their formation before the uranium ore stage (Table 2.1).

### *2.1.3. The 1<sup>st</sup> postore stage*

During the 1<sup>st</sup> postore stage widespread veined mineralization accompanied by halos of intensive alteration was formed. This mineral complex is more widespread than the uranium ore one but also more locally comparable to the mineral complex of the preore stage. Quartz, carbonate, chlorite and illite-smectite with sulfides are the main minerals both in veins and altered rocks, as they are in the preore mineral complex. The main difference of



## 2. Mineralogy of the deposits

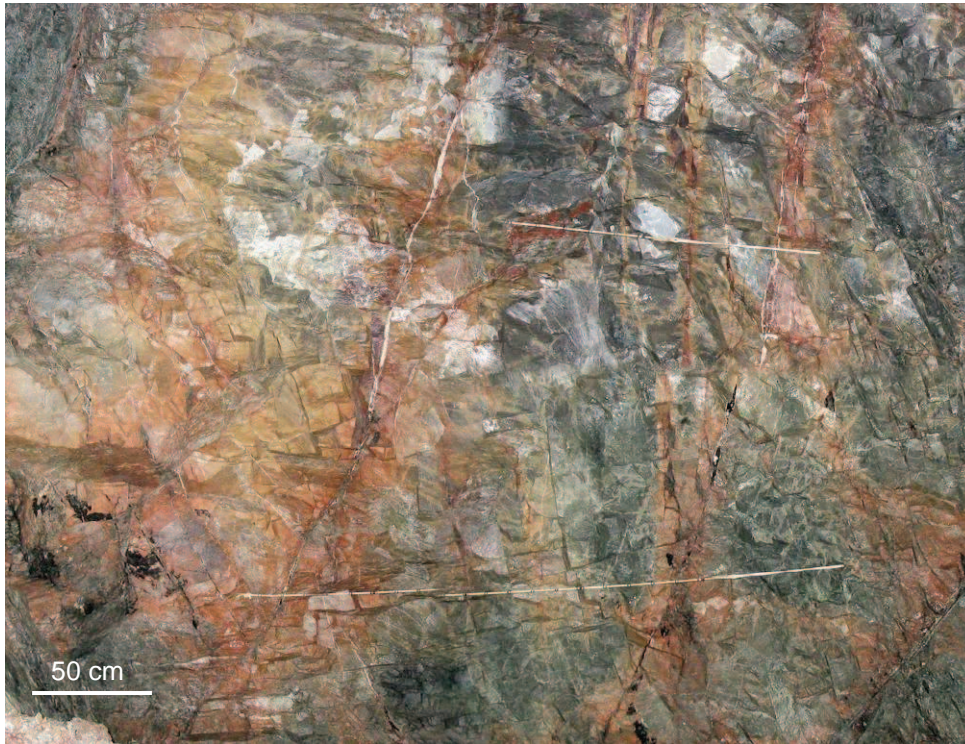


Fig. 2.13. Individual fractures with uranium mineralization accompanied by hematization halos in basalts. Dark-grey blocks of slightly altered basalts are noticeable in the upper central and right parts of the photograph. A wide aureole of postore bleaching is present in the left part. Hematite dispersion in the bleached zone produced light-orange to yellow color of the rock. Fault No.40, Western site of the Streltsovsky deposit, horizon +384 m.



Fig. 2.14. Mineralized fault No.160 being the main ore body of the Antei deposit. Quartz-pitchblende mineralization in the linear breccia zone (black) is accompanied by hematization of illitized granites. White – kaolinization of the 2<sup>nd</sup> postore stage along the fracture. Horizon +134 m.



## 2. Mineralogy of the deposits

---



Fig. 2.15. Stockwork type of streaky-disseminated uranium mineralization in trachydacites. Hematization along thin veinlets merged into a single halo. Dark-green – chlorite films on fracture surfaces, light-grey – carbonate veins and films in fractures. Rich ore body in a cataclase zone in the Oktyabrsky deposit. Horizon +309 m.



Fig. 2.16. Steeply dipping ore body with disseminated uranium mineralization and relatively wide halo of hematization in tuff-conglomerates. Light-grey – intensively argillized conglomerates, dark brownish-red in the lower right corner – weakly altered conglomerates. Luchisty deposit, horizon +590 m.

## 2. Mineralogy of the deposits

---

composition between them is the presence of fluorite and U-Si metagel in the 1<sup>st</sup> postore mineral complex.

Alteration of the host rocks also occurs differently. For the 1<sup>st</sup> postore stage, relatively local and intensive aureoles distinctly controlled by faults and fractures are typical. Evident cases of superimposition of bleaching zones on synore hematization halos were observed in basalts (Fig. 2.17), dacites (Fig. 2.9) and granites in various deposits. It unambiguously indicates a later formation of the intensive alteration with respect to the uranium mineral complex.

*Bleaching.* A typical feature of the postore bleaching is Fe oxide dissolution. It concerns syngenetic Fe oxides in the rhyolites and dacites (Fig. 2.7) or hematization aureoles around ore bodies (Fig. 2.9, 2.17). If bleaching is intensive enough or if the amount of Fe oxide is moderate, the latter are completely removed, giving a light-grey color to the bleached zones. Otherwise, some Fe oxide remains in halos of postore alteration and the rock color changes from orange to light-yellow depending on the amount of remaining Fe oxide (Fig. 2.8, 2.9, 2.13, 2.17, 2.18).

*Illite rims.* Aureoles of bleaching are often accompanied by relatively narrow light-green rims caused by intense illite development in the rock matrix (Fig. 2.8). Illite develops broadly within the bleaching halos but its amount in the light-green rims is appreciably higher than in the bleached zones. Strict coincidence of the light-green rims with the bleaching zones testifies their genetic link, in other words, it is a typical metasomatic zonation.

The amount of rocks subjected to the intensive alteration of the 1<sup>st</sup> postore stage varies from 10% to 70-80% in different parts of the SOF. The mean is approximately 20-30% according to the author's estimation. In fault zones and ore bodies, the intensity of development of the bleaching halos is higher (Fig. 2.9, 2.13, 2.18). One of the largest bleaching zones was observed in the north-western wall of the Tulukui open pit where it is controlled by the NW striking ore-bearing fault zone no.1 (Fig. 2.6). Its width reaches up to 100-150 m.

*Episyenites.* Another type of alteration was observed in the granites of the Antei deposit. Quartz leaching of different intensity (episyenitization or dequartzification) occurred along the main ore-controlling fault no.160 at a different depth from the highest horizons to the lowest ones (more than 250 m downdip on the fault). O.V. Andreeva mentioned about "porous granites" in a report (Andreeva and Golovin, 1979) where she presumably related this process to post-uranium kaolinization.



## 2. Mineralogy of the deposits



Fig. 2.17. Local bleached zones developed along fissures and cryptocrystalline quartz veinlets are superimposed on a hematization halo in the peripheral part of the uranium ore body in basalts. Hematite is completely dissolved in areas of light-grey color of the bleaching zones while orange color indicates incomplete removal of the Fe oxides. Streltsovsky deposit, Western site, horizon + 375 m. 1 unit on the cord – 10 cm.



Fig. 2.18. Hematite from the peripheral area of uranium mineralization is diffused along halos of intensive postore bleaching of basalts. Postore alteration develops from vertical fractured zone with chlorite mineralization (dark-grey in the left part of the photograph). Gradual transition from orange to light-yellow and light-grey tints reflects decrease of Fe oxide content in bleaching zones. The absence of Fe oxides outside the bleaching zones in slightly altered green basalts evidences that hematite diffusion occurred during the 1<sup>st</sup> postore stage. Streltsovsky deposit, Western site, horizon +384 m.

## 2. Mineralogy of the deposits

---

Structural control of episyenites by fault no.160 is not always evident, sometimes the leached zone deviates from the fault at the distance of 5 to 15 meters (Fig. 2.19). The zone has fuzzy boundaries because it is reflected mainly by an increased porosity without significant color change in illitized granites. The width of the zones reaches up to 10 meters and more. If vugs are filled with minerals of the 1<sup>st</sup> postore stage (quartz, carbonate, fluorite), episyenitization zones become difficult to recognize.

The position of episyenites in the paragenetic scheme results from their development after synore albite (Fig. 2.20, 2.21) and pitchblende (Fig. 2.22) on one hand, and before quartz and other minerals of the 1<sup>st</sup> postore stage (Fig 2.21, 2.22), on the other. In other words, episyenitization starts at the beginning of the 1<sup>st</sup> postore stage when the quartz of the granites and some part of the pitchblende mineralization were leached out.

*Quartz-carbonate-fluorite veining.* Veins and veinlets with thicknesses from several millimeters to 1 m are widespread as well as bleaching zones. They develop inside and far beyond ore bodies. Crystalline and cryptocrystalline quartz, and carbonate are the main minerals of the veins; dark-violet fluorite occurs in subordinate amounts. Similar to the preore complex, quartz prevails in granites, less in dacites, while carbonate predominates in basalts. Chlorite is also a widespread mineral but it develops mainly as breccia cement and thin films in fractures of cataclastic zones (Fig. 2.15, 2.18).

*Relative chronology.* The formation of the 1<sup>st</sup> postore complex after the uranium ore stage is proved by the superposition of bleaching zones on hematization halos accompanying the uranium ore bodies, and by intersections of quartz-pitchblende aggregates by illite-quartz-carbonate stringers. Post-uranium ore K-Ar ages obtained on illite (<135 Ma) determined by Andreeva et al. (1996<sub>2</sub>) predominate in the isotopic data on illite. The most reliable determinations provided by K-Ar and Rb-Sr methods on a paragenetic pair illite-ankerite demonstrate its post-uranium formation (Table 2.1).

Distinction of the mineral assemblages of the 1<sup>st</sup> postore complex into an individual stage from the uranium ore stage is based on the following facts:

- Mineral assemblages of the 1<sup>st</sup> postore stage (both veined and metasomatic ones) are spread over a much wider domain than the uranium associations. No regular spatial coincidence between them has been established. It is clearly observed from the predominant spatial separation of the molybdenum ore bodies composed of postore jordisite from the uranium ore bodies at the Argunsky deposit (Ishchukova et al., 1998).



## 2. Mineralogy of the deposits

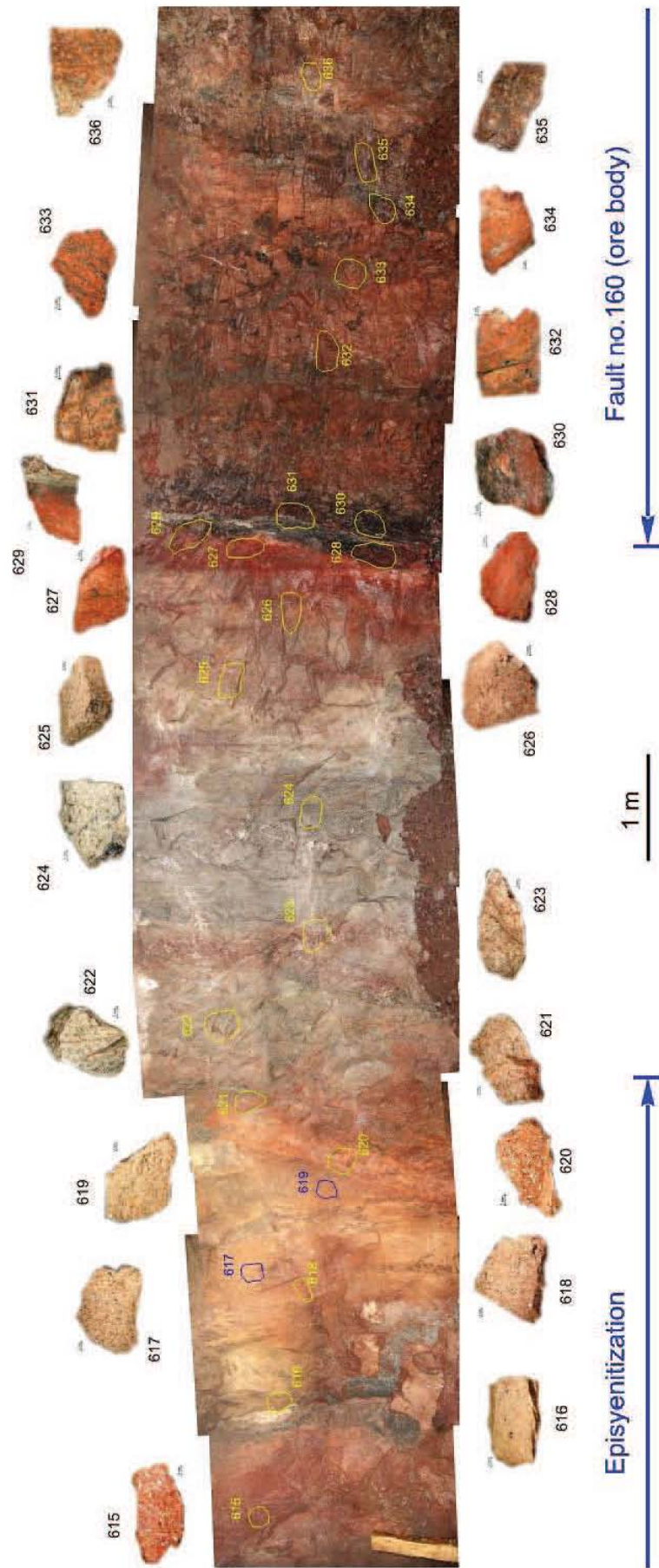


Fig. 2.19. Episyenitization zone and uranium ore body in the Antei deposit. Panorama of the the gallery wall across the Fault no. 160 with a sample location scheme. Antei deposit, horizon +84 m.

## 2. Mineralogy of the deposits

---

- These two mineral complexes are also different in composition: no sulfides nor carbonates or illite-smectite are present in the uranium ore association, similarly, the only uranium mineral (U-Si metagel) of the postore complex occurs exclusively within the uranium ore bodies (areas of primary uranium mineralization), indicating the absence of an independent uranium specialization of the postore assemblage;
- These two associations were formed under essentially different physicochemical conditions ( $T$  and  $pH$  above all) as will be demonstrated below. Episyenites which are aggressive to uranium mineralization indicate such a difference in physicochemical conditions at the beginning of the 1<sup>st</sup> postore stage.

The total time span of the 1<sup>st</sup> postore stage could be evaluated as 135-130 Ma based on isotopic dating of pitchblende and illite.

### *2.1.4. The 2<sup>nd</sup> postore stage*

The 2<sup>nd</sup> postore stage is characterized by a decrease of hydrothermal activity. Mineralization is presented by quartz-carbonate-fluorite veins with scarce sulfides accompanied by narrow halos of kaolinization and wider aureoles of smectite alteration with zeolite. Veins of polychrome fluorite may reach up to a few meters thick, for example the Streltsovsky fluorite vein which outcrops on the surface. This vein initiated prospecting in the area for fluorite and led to the subsequent discovery of uranium deposits.

Kaolinization occurred insignificantly as relatively narrow rims (up to several centimeters thick) along quartz-carbonate-fluorite veinlets and fractures in the eastern part of the Streltsovsky caldera (Fig. 2.14). In the western part of the SOF within the Meridional fault zone, kaolinite spreads essentially wider, and it is a predominant mineral in wall-rock alteration. It develops mostly at the upper horizons in this area and changes into illite below the depth of 900 m (Ishchukova et al., 1998; Andreeva and Golovin, 1998). This vertical zonality may be explained in two ways: (1) zonality of a single process caused by a temperature drop in an open structure of the Meridional fault zone (Ishchukova et al., 1998), and (2) superposition of metasomatic alteration of different stages. Many researchers (O.V.Andreeva, V.A.Golovin, L.P.Ishchukova and others) believe that kaolinization in the western part of the caldera occurred during the preore stage although no distinct evidence for this point of view has been presented. Along with this, facts of the latest formation of kaolinite in the eastern part of the SOF are numerous and well-known. Thus, the question of timing of kaolinization and,



## 2. Mineralogy of the deposits

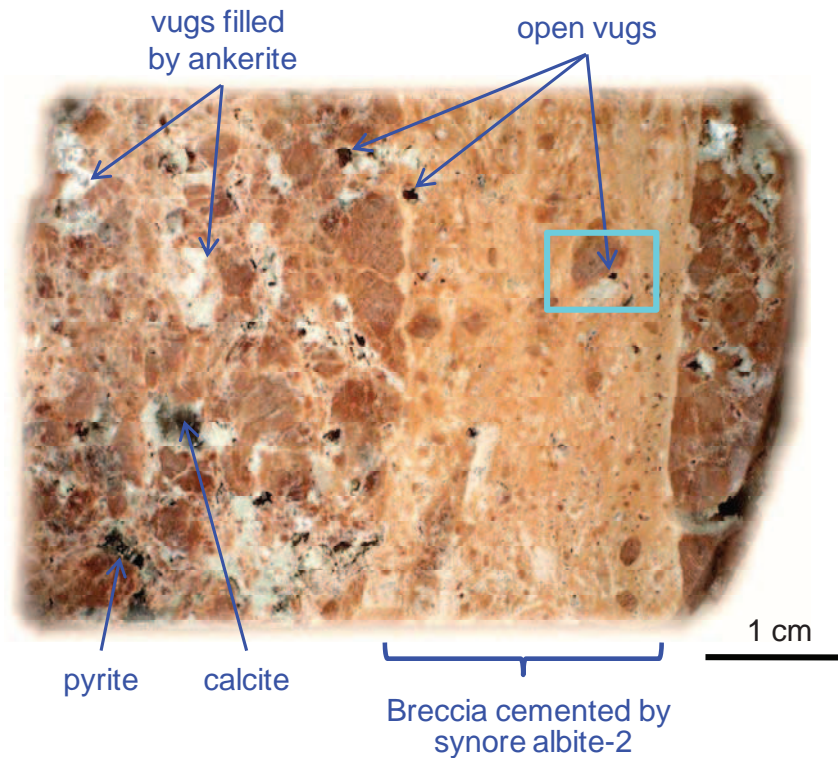


Fig. 2.20. Hematized granite intersected by a linear brecciation zone with synore albite-2 cement and intensive quartz dissolution. Some pores are open both in granite and breccia but most of them are filled by white ankerite, dark-grey calcite and pyrite of the 1<sup>st</sup> postore mineral complex. Polished sample St-620 (see Fig. 2.17 for location). Area in a rectangle is present in Fig. 2.19 as a photomicrograph.

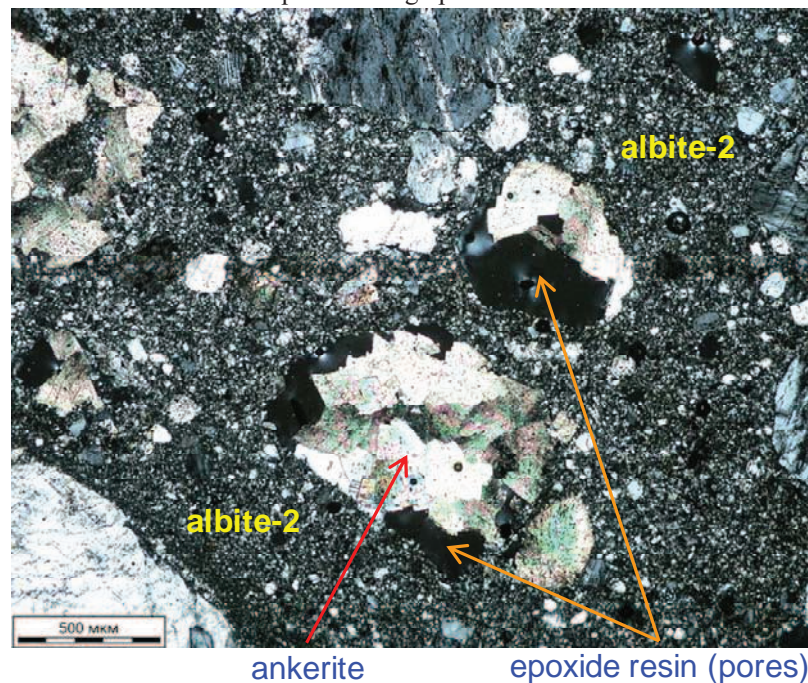


Fig. 2.21. Breccia with fine-grained albite-2 cement and pores after quartz dissolution. The pores are partly filled by ankerite. Unaltered fragment of K-feldspar of granite is noticeable in the upper part of the figure. Thin-polished section St-620 (detailed area from Fig. 2.18) in transmitted polarized light.

## 2. Mineralogy of the deposits

---

hence, metasomatic zonation in the western part of the caldera still remains a matter of discussion. Taking into account clear evidence of affiliation of kaolinite with the 2<sup>nd</sup> postore stage, the author is inclined towards the version of multistage zonation.

Predominant development of kaolinite in the western part of the caldera and illite in its eastern part, O.V.Andreeva and V.A.Golovin explain as follows: after Late Mesozoic magmatism, kaolinite developed above illite in the section reflecting vertical zonation of a single process. Later, the western block separated from the eastern one by the Meridional fault was dropped down with a dip throw of about 700 m. After that the upper part of the eastern block where kaolinite developed was eroded and illitized rocks were exposed on the surface.

The kaolinized part of the western dropped block was preserved from erosion (Andreeva and Golovin, 1998). This model contradicts the following facts:

1. From the analysis of the caldera basement surface, its altitude is approximately the same both for the western and the eastern parts of the caldera. Its deepest parts in the west of caldera are related to funnel-shaped root parts of two rhyolite volcanoes. All the caldera collapsed with a throw up to 700-1000 m relatively to the enclosing rocks.
2. Not only the sedimentary-volcanogenic sequence of the caldera but also the granitic and metamorphic rocks of the western frame were kaolinized as observed in cross-sections (Andreeva and Golovin, 1998, p.208).
3. Only 100-200 m of rocks were eroded after Late Mesozoic magmatism (Ishchukova et al., 1998, p.497). This was not sufficient for the destruction of the upper kaolinized part of the sequence in the eastern part of the caldera (according to Andreeva and Golovin, 1998).

All these facts are evidence against the hypothesis of Andreeva and Golovin (1998). It is most likely that kaolinization occurred during the 2<sup>nd</sup> postore stage everywhere in the caldera but was developed more intensively in the western part of it due to an abrupt temperature and pressure drop in the relatively open structure of the Meridional fault zone (according to Ishchukova's personal communication).

Smectite-zeolite alteration developed predominantly in the northern part (the Dal'ny deposit) and in the western part of the SOF. Andreeva and Golovin (1998) propose their postore formation. Evident intersections of synore albite by zeolite stringers were observed by the author in an ore body from deep horizons of the Antei deposit (Fig. 2.23). Besides, smectite as the marginal member of the smectite-illite series is widespread in the metasomatites of the 1<sup>st</sup> postore stage. Its post-uranium timing is well constrained. Smectite-zeolite wall-rock alteration in the surroundings of the Dal'ny deposit is different from the



## 2. Mineralogy of the deposits

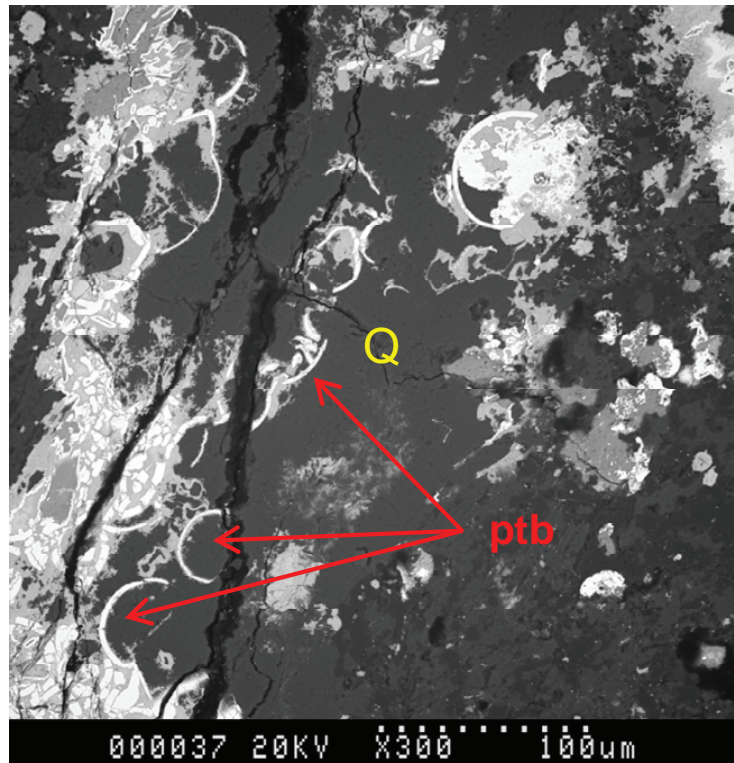


Fig. 2.22. Brecciated relics of outer zones of pitchblende spherulites (ptb) are cemented by quartz of the 1<sup>st</sup> postore stage (Q). Light-grey phase – U-Si metagel. Its thin stringers in quartz (for example, beneath a relic of large pitchblende spherulite in the upper part of the figure) testify to its later formation regarding quartz. Central part of the pitchblende relic mentioned in brackets is dissolved and replaced by quartz and two phases of U-Si metagel – common light-grey and fine-grained white, close in intensity to pitchblende. BSE image of thin-polished section St-143d, Western site of the Streltsovsky deposit in basalts, horizon +375 m.

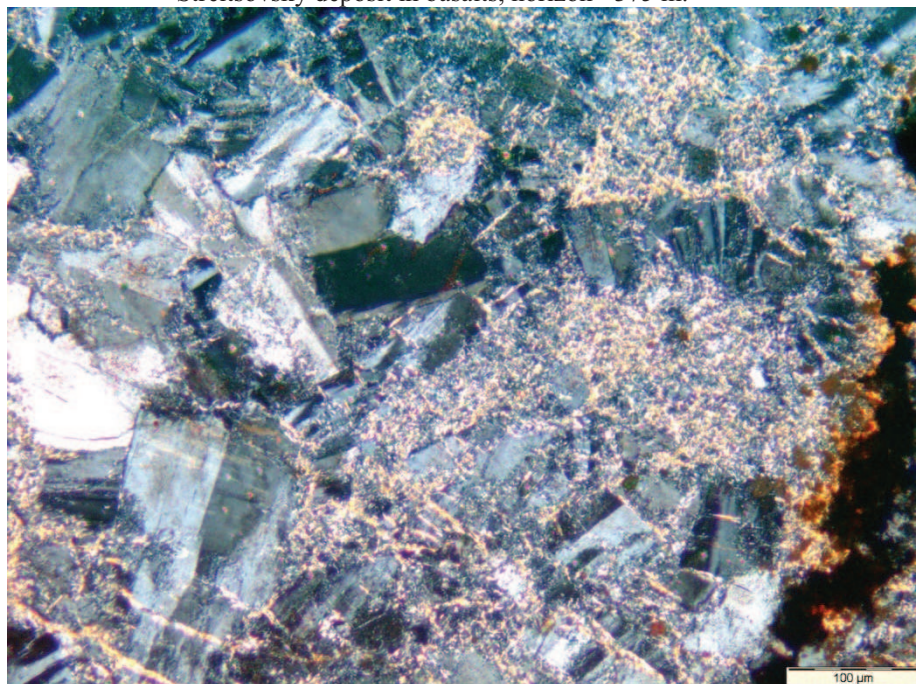


Fig. 2.23. Aggregate of short-prismatic synore albite is intersected and corroded by fine flakes of Ca-zeolite (light-yellow). Dark-brown in the right part – Fe oxides. Photomicrograph of thin-polished section St-630a, with analyzer. Antei deposit, ore body at the horizon +84 m.

## 2. Mineralogy of the deposits

---

typical illite-smectite metasomatites of the SOF (Andreeva and Golovin, 1998) which allows them to be affiliated with the 2<sup>nd</sup> postore mineral complex.

Distinction of the above mentioned mineral assemblages into a separate 2<sup>nd</sup> postore stage is based on the following facts:

- polychrome fluorite was formed after dark-violet fluorite of the 1<sup>st</sup> postore mineral complex;
- smectite-zeolite alteration in the northern part of the SOF developed differently from illite-smectite alteration of the 1<sup>st</sup> postore stage;
- the age of similar polychrome fluorite mineralization associated with adularia, kaolinite and zeolite developed in the south Priargun region at the Urtui deposit (20 km south of the SOF) and at the Garsonui deposit (40 km north of the SOF) was determined by K-Ar method at  $123 \pm 5$  Ma (Kotov and Kotova, 1995; Anferov et al., 1995), indicating a noticeable temporal break with the 1<sup>st</sup> postore stage in the SOF.

### 2.2. Mineral parageneses

A brief description of mineral parageneses and determination of their paragenetic position in the Late Mesozoic hydrothermal process will be covered by this section. A few preliminary remarks should be given. The paragenetic scheme (Fig. 2.5) reflects the general sequence of mineralization – both veined and metasomatic – which occurred in different deposits and in different rocks. Therefore, some mineral associations shown as synchronous may develop separately in different rocks (simultaneously or not) and it doesn't mean that it corresponds to an observed paragenesis. In some cases, especially for metasomatic rocks, it is difficult if not impossible to establish a mineral succession. In that instance all the minerals of the association are shown as simultaneous but it is a “conditional paragenesis” resulting from the impossibility to determine an exact succession.

Besides this, mutually exclusive minerals may develop in different parts of the deposits at the same time – for example,  $U^{6+}$  minerals in areas of local oxidation in rich ore bodies and  $U^{4+}$  minerals outside such zones. They should be shown as synchronous minerals despite the fact that they do not represent a paragenetic association.

## 2. Mineralogy of the deposits

---

### *2.2.1. Mineral assemblages of the preore stage*

Mineral associations of the preore stage developed as veinlets and as larger, metasomatic zones in the host rocks. Rocks that macroscopically look unaltered, may present metasomatic alteration under the microscope. Basalts are the least altered rocks. The freshest sample of dark grey to black basalt (St-138) exhibits olivine moderately replaced by calcite (Fig. 2.1) and less altered phenocrysts of pyroxene. Groundmass and phenocrysts of plagioclase are slightly replaced by fine-flaked illite-smectite and calcite. Biotite and titanium accessory minerals (Ti-magnetite  $[\text{Fe}(\text{Fe},\text{Ti},\text{Cr})_2\text{O}_4]$ , ilmenite  $[\text{FeTiO}_3]$ , ulvospinel  $[\text{TiFe}_2\text{O}_4]$ ) are stable. Slightly altered basalts of greenish-grey color which also could be considered as the result of preore alteration, show more intense carbonatization of olivine (up to complete replacement by calcite) and pyroxene as well as illitization and carbonatization of plagioclase. Cryptocrystalline quartz and chalcedony begin to develop in minor amounts as thin streaks and metasomatic segregations. Ti-magnetite is partly altered to leucoxene while other Ti accessories and biotite are preserved.

Dacites, even the least altered varieties of dark brownish-red color, are characterized by stronger alteration when compared to basalts. Phenocrysts of plagioclase are replaced by calcite and illite up to 50%, biotite is completely replaced by illite, Fe and Ti oxides, and rarely by carbonates. Fine-grained quartz develops over phenocrysts and in the groundmass. Accessory magnetite is partly substituted by hematite. Finely dispersed Fe-oxides in the rock matrix are preserved during alteration which causes the brownish-red color of the rock. Insignificantly bleached brownish-grey dacites exhibit higher rates of carbonatization, illitization and silicification of plagioclase phenocrysts and partial removal of Fe-oxides dispersed in the matrix. Calcite is the only metasomatic carbonate detected in dacites.

Weakly altered granites display the sporadic development of fine-flake illite in plagioclase followed by carbonate (ankerite, siderite or calcite). As plagioclase is often zoned in granites, core, more basic zones (oligoclase 18-24, according to electron microprobe analyses) are replaced by illite more intensively than outer acidic zones (oligoclase 11-17) which sometimes are not altered at all (Fig. 2.24). During illitization, oligoclase is transformed to albite 4-6. Biotite may be partially replaced by chlorite, and titanite – by leucoxene.

The composition of the veins and veinlets belonging to the 1<sup>st</sup> preore complex is similar to the mineral assemblages of newly formed minerals in altered rocks. Sometimes it is



## 2. Mineralogy of the deposits

---

difficult to separate these two forms of mineralization – vein and metasomatic – when microscopic stringers of some tenths of a millimeter thick have the same composition as metasomatically developed cryptocrystalline quartz, carbonate, illite-smectite, etc. For example, native copper in hair-like veinlets of cryptocrystalline quartz and calcedony with calcite, chlorite and illite-smectite located in basalts (Fig. 2.25) are similar in composition and structure to cryptocrystalline quartz veins several decimeters thick, with jordisite, cleophane and pyrite in granites (Fig. 2.26) if their thickness is not taken into account.

Two pyrite generations were established in granites – relatively coarse-grained and later fine-grained (Fig. 2.26). Jordisite was formed after pyrite of both generations because it replaces pyrite along specific less resistant zones and overgrows grains of the 2<sup>nd</sup> generation. Cleophane segregations in some cases reach 1 cm (Fig. 2.11). It was seemingly deposited after pyrite which is implicitly indicated by the cementation of pyrite by sphalerite. Its synchronous position with jordisite in the paragenetic scheme is a matter of convention.

Light mica in slightly altered basalts belongs mostly to the illite-smectite series with a potassium content varying from 0 (smectite) to 7.5 wt.% (from microprobe data<sup>2</sup>). Some illite flakes from basalts possess abnormal Fe concentration from several to 13.6 wt.%, in this case illite features strong pleochroism in deep bright-green color. Mixed-layered mica occurred in slightly altered granites and dacites (regarded as alteration product of the 1<sup>st</sup> preore stage) and is essentially more potassic. It corresponds to pure illite with K contents from 6.1 to 8.8 wt.%.

Kaolinite has been attributed to the 1<sup>st</sup> preore stage by Andreeva and Golovin (1998), and Ishchukova et al., (1998). They concluded that kaolinite was widely developed before uranium mineralization in the western part of the ore field (the Yugo-Zapadny, Krasny Kamen, Zherlovy, Pyatiletny deposits). Preore kaolinite formation has not been established in this work, nevertheless kaolinite was included in the 1<sup>st</sup> preore stage due to a lack of own observations in the western part of the SOF.

### ***2.2.2. Mineral assemblages of the uranium ore stage***

The uranium ore formation began with wall-rock hematization and albitization. Albite impregnated with finely dispersed Fe oxides (albite-2 according to Ishchukova et al., 1998) developed in two approximately equivalent ways – metasomatically in host rocks and in thin microscopic-scale veinlets. It forms small prismatic crystals from 0.05 to 1 mm long. In

---

<sup>2</sup> Here and below the conclusion on mixed-layered mica composition is inferred only from microprobe data. No X-ray studies were provided.

## 2. Mineralogy of the deposits

veinlets, it often exhibits epitaxy with plagioclase in the granites and dacites (Fig. 2.27) or grows perpendicular to the veinlet walls with usual zones of geometric selection (natural

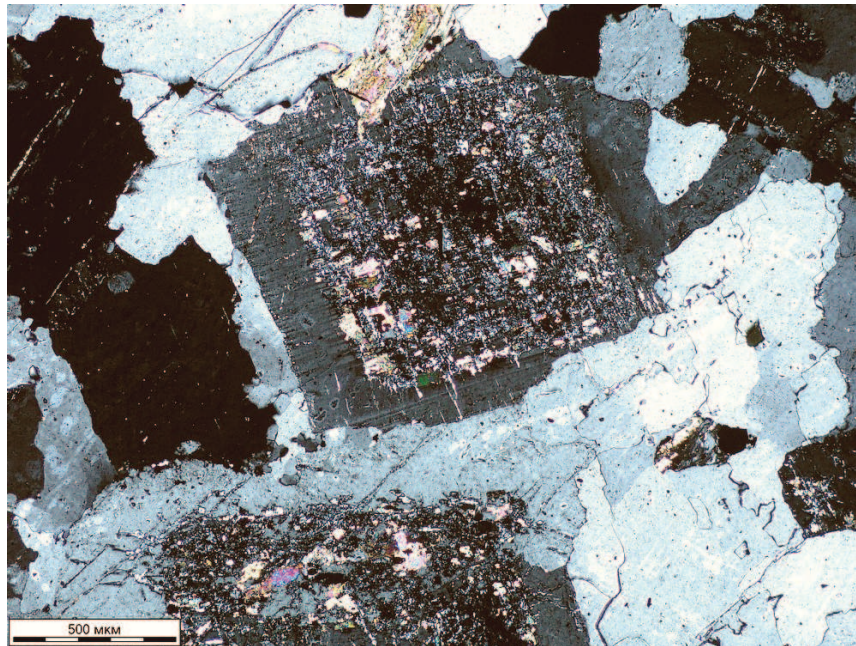


Fig. 2.24. A zoned plagioclase crystal in a slightly altered “background” granite matrix: the central more basic zone is completely replaced by illite and Fe-Mg carbonate while the outer more acidic zone remains practically unaltered. Antei deposit. Thin-polished section St-531, transmitted light, crossed polarizers.

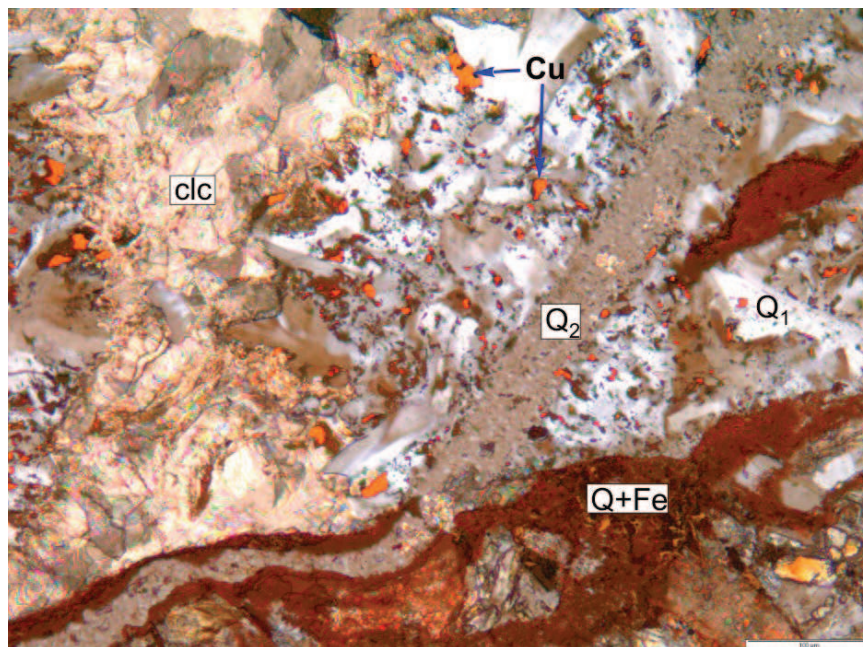


Fig. 2.25. Dissemination of native copper (Cu, orange in reflected light) in quartz of the 1<sup>st</sup> generation (Q<sub>1</sub>) in a thin veinlet in basalts. Q<sub>2</sub> – cryptocrystalline quartz of the 2<sup>nd</sup> generation, clc – calcite, Q+Fe – cryptocrystalline quartz impregnated with Fe oxides. Tulukuevsky deposit. Thin-polished section St-540a, in both reflected and transmitted light, semi-crossed polarizers. Scale bar - 100 μm.



## 2. Mineralogy of the deposits

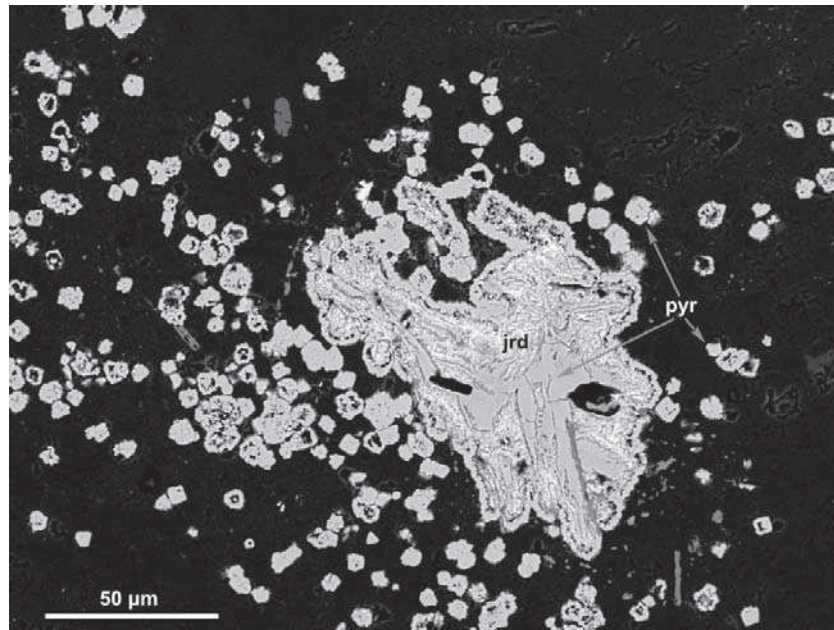


Fig. 2.26. Large pyrite crystals of the 1<sup>st</sup> generation and disseminated pyrite crystals of the 2<sup>nd</sup> generation (pyr) partly replaced by jordisite (jrd) along specific zones of pyrite. Black – cryptocrystalline quartz of the 1<sup>st</sup> preore mineral complex. Antei deposit, thin-polished section St-551c. BSE image.

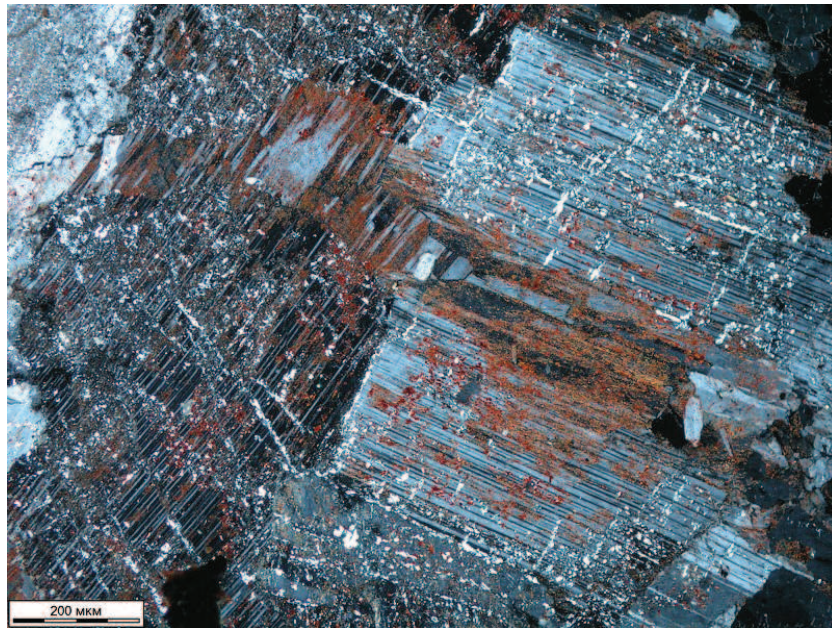


Fig. 2.27. Thin veinlet of albite-2 of the uranium ore stage impregnated with Fe oxides crosscuts two grains of illitized plagioclase in granite. Orientation of polysynthetic twins of albite-2 strictly coincides with that of plagioclase grains (NE in the left grain and NW in the right grain). Between these two grains, small isometric albite grains develop reflecting orientation change (epitaxial junction). Antei deposit, thin-polished section St-516-2b. Transmitted light, crossed polarizers.

## 2. Mineralogy of the deposits

---

selection of minerals growing more perpendicular than their neighbours). Cementation of fragments of preore sulfides (Fig. 2.12) and host rocks is usual for synore albite. In the rock matrix, it replaces plagioclase (Fig. 2.28) and K-feldspar in granites as well as rock groundmass and feldspar phenocrysts in volcanic rocks. Ti-oxides were formed before brannerite and pitchblende during the uranium ore stage. Largely developed prismatic crystals of Ti-oxide (presumably rutile from its habitus) are often idiomorphic to pitchblende spherulites (Fig. 2.29) indicating their earlier formation concerning uranium oxide.

Quartz was formed next to albite as shown by intersections of albite by quartz-pitchblende veinlets (Fig. 2.11). Three quartz generations have been distinguished. Quartz of the first generation ( $Q_1$ ) was observed only once in a rich ore body hosted by basalts in the Streltsovsky deposit (the Western site). It comprises micrograin (50-100  $\mu\text{m}$ ) aggregates of isometric crystals (Fig. 2.30a) impregnated by finely-dispersed Fe-oxides similar to albite-2 giving a pink color to the quartz. Quartz of the 2<sup>nd</sup> generation is coarser grained (0.05-1 mm) and its veinlets intersect quartz  $Q_1$  aggregates. Pitchblende was formed directly after  $Q_2$  as indicated texturally. As seen in Fig. 2.30b, pitchblende spherulites inlay outer zones of quartz crystal forming inductive surfaces. The latter are the symmetric parabolic surfaces formed during joint precipitation at the decrease of growth rate of the quartz and at the increase of that of the pitchblende.

Further on, micrograin aggregates of pitchblende of the 1<sup>st</sup> generation and quartz of the 3<sup>rd</sup> generation ( $Q_3$ ) were deposited, cementing relatively large crystals of quartz  $Q_2$  (Fig. 2.31). This is typical for the Antei deposit. In this aggregate, quartz  $Q_3$  may be both idiomorphic and xenomorphic to pitchblende spherulites. The size of  $Q_3$  crystals varies from 5 to 15-20  $\mu\text{m}$ . The sharp difference in grain size between  $Q_2$  and  $Q_3$  along with clear paragenetic association of the latter with pitchblende testify to an abrupt change of physicochemical conditions and the beginning of uranium precipitation.

Brannerite is the first uranium mineral in the SOF deposits. It was formed slightly earlier than pitchblende which is evidenced by overgrowth of brannerite crystals by pitchblende spherulites (Fig. 2.32). However, no signs of tectonic movements between these minerals, corrosion of brannerite by pitchblende or any other minerals between them have been observed. In pseudomorphs over Ti-magnetite and other Ti accessories brannerite and pitchblende constitute a paragenetic association (Fig. 2.33). All this testifies against the point of view of M.V.Vampilov, I.V.Mel'nilov and other mineralogists which believed that



## 2. Mineralogy of the deposits

brannerite was formed in a separate preceding stage before pitchblende (Ishchukova et al., 1998). The composition of unaltered brannerite is stable and generally corresponds to the

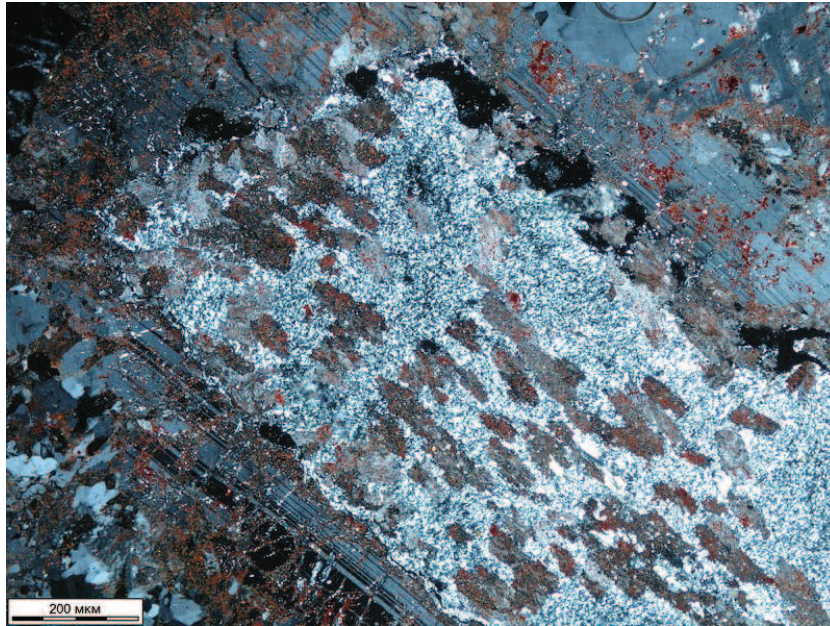


Fig. 2.28. Inner part of a plagioclase grain in granite is intensively replaced with tabular albite-2 crystals with Fe oxides and fine-flake illite. Albite-2 crystal orientations coincide with plagioclase prism (epitaxy) which testifies to their pre-illite formation (otherwise, aggregate of disoriented illite flakes could not provide epitaxy). The outer more acid rim of plagioclase (generally oligoclase 11-17) remained unaltered. Only hair-like stringers of illite and hematized albite-2 intersecting the rim are noticeable in the lower left corner of the photomicrograph. Antei deposit, thin-polished section St-516-2b. Transmitted light, crossed polarizers.

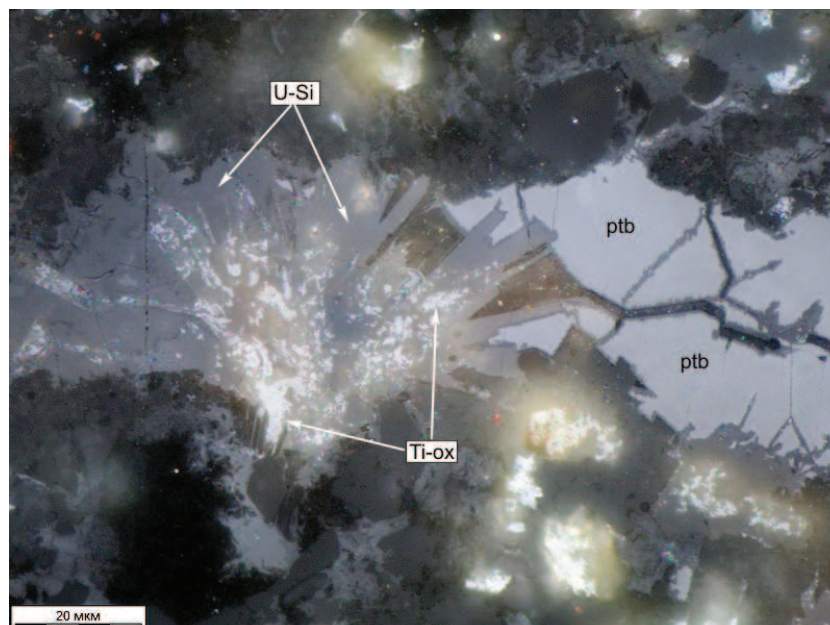


Fig. 2.29. Pitchblende spherulites (ptb) are xenomorphic to long-prismatic Ti oxide crystals (Ti-ox), which later were intensively replaced by U-Si metagel (U-Si). Western site of the Streltsovsky deposit, ore body in basalts. Thin-polished section St-396a. Reflected plane light.



## 2. Mineralogy of the deposits

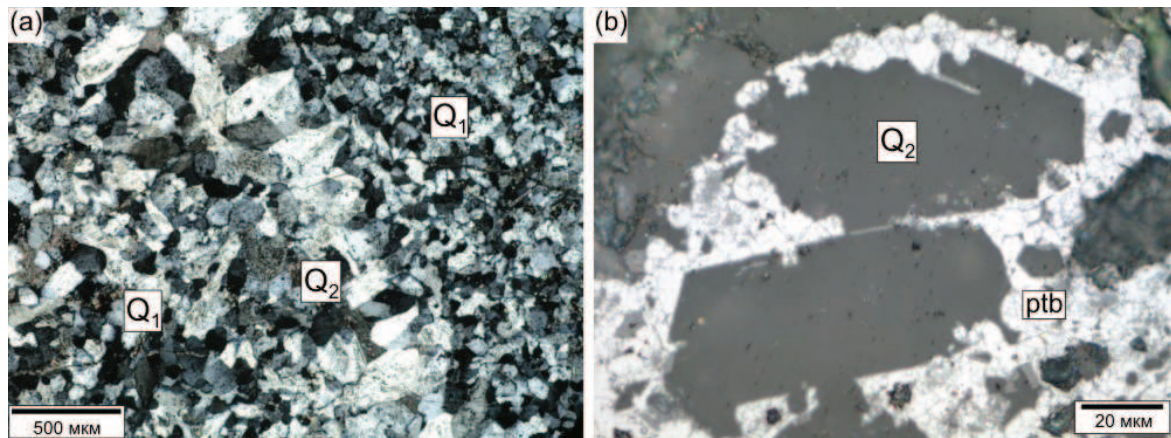


Fig. 2.30. Two first generations of quartz of the uranium ore stage. Micrograin quartz of the first generation  $Q_1$  is intersected by a veinlet of coarser grained quartz of the 2<sup>nd</sup> generation  $Q_2$  (a). The Western site of the Streltsovsky deposit. Photomicrograph of thin-polished section St-406 in transmitted light with crossed polarizers. Idiomorphic bipyramidal quartz crystals of the 2<sup>nd</sup> generation are overgrown by pitchblende spherulites (ptb) with partial join growth (b). Antei deposit. Photomicrograph of thin-polished section St-520 in reflected plain light.

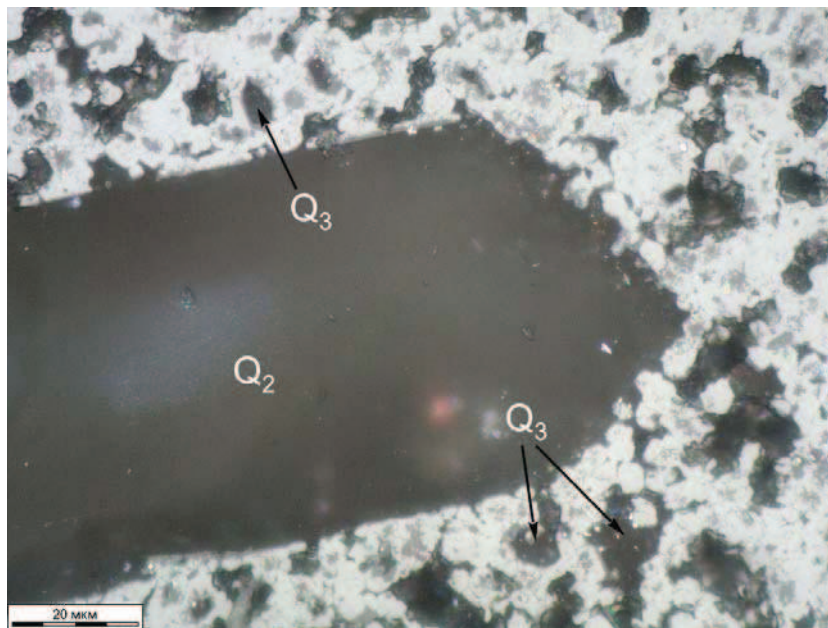


Fig. 2.31. Idiomorphic crystal of quartz  $Q_2$  is overgrown by microgranular aggregate of quartz of the 3<sup>rd</sup> generation  $Q_3$  and pitchblende spherulites (light-grey). Typical ore of the Antei deposit. Photomicrograph of thin-polished section St-602 in plane reflected light.

## 2. Mineralogy of the deposits

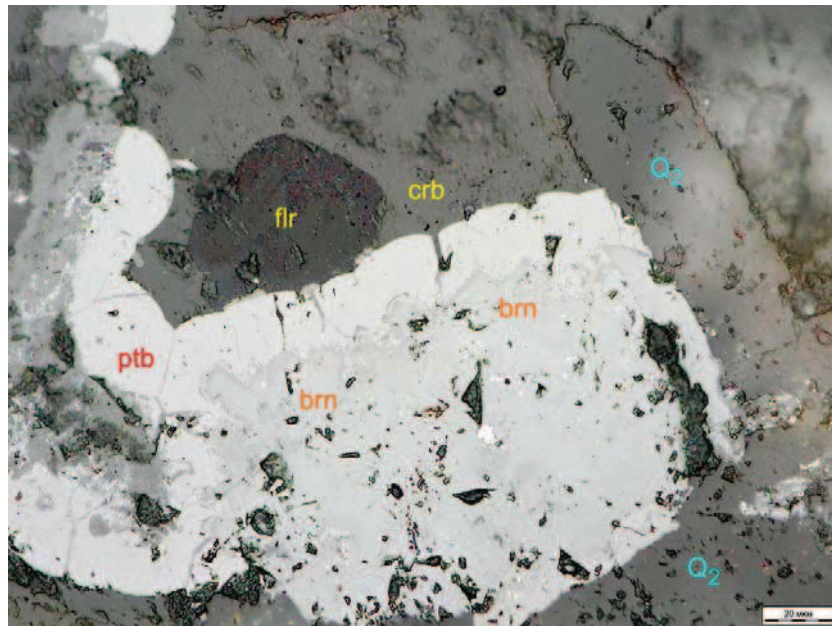


Fig. 2.32. Pitchblende spherulites (ptb) overgrew prismatic brannerite crystals (brn) which, in turn, overgrew quartz crystals of the 2<sup>nd</sup> generation (Q<sub>2</sub>). Fluorite (flr) and calcite (crb) of the 1<sup>st</sup> postore stage grew on the pitchblende surface. Western site of the Streltsovsky deposit, ore body in basalts. Photomicrograph of thin-polished section St-406 in plane reflected light.

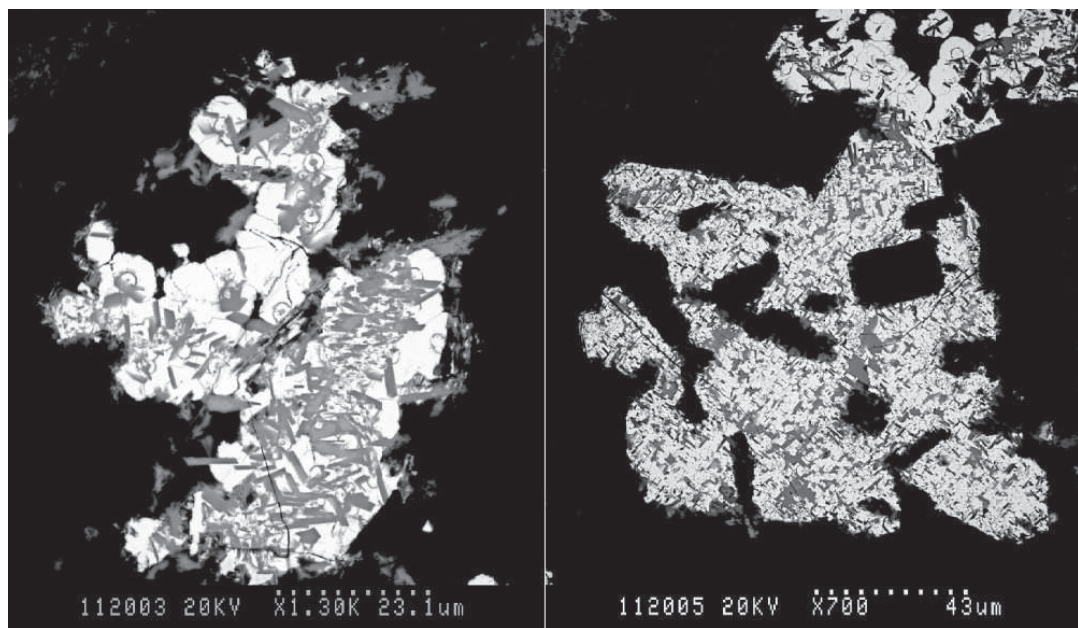


Fig. 2.33. Tight intergrowth of prismatic brannerite crystals (grey) and pitchblende (light-grey, white) in pseudomorphs over Ti-magnetite in basalts. Western site of the Streltsovsky deposit. BSE images of thin-polished section St-112.

stoichiometry of this mineral  $[(U_{0.91}Ca_{0.17})_{1.08}(Ti_{1.97}Fe_{0.08})_{2.05}O_6]$  (average of 29 microprobe analyses). The main statistical characteristics of brannerite composition are presented in Table 2.2. Brannerite is less abundant than pitchblende (5–10% of the volume of pitchblende).

## 2. Mineralogy of the deposits

Table 2.2. Statistical parameters of brannerite composition from microprobe data (SX-50 & -100, UHP) (wt.%)

Elem	Vol	Dstrb	Min	Max	Avr	Stand
U	56	norm.	42.2	48.2	45.4	1.29
Ti	56	norm.	18.0	23.8	19.7	0.77
O	56	norm.	20.5	23.3	21.6	0.49
Fe	56	log.	0.3	2.5	0.98	0.48
Si	56	norm.	0.0	1.7	0.81	0.38
Zr	56	log.	0.1	2.5	0.63	0.41
Pb	56	norm.	0.0	1.3	0.52	0.26
Mn	25	log.	0.1	0.4	0.15	0.09
Al	56	norm.	0.0	0.8	0.14	0.08
Total	56	log.	88.6	95.5	91.9	1.84

Note: Vol – sampling volume, Dstrb – distribution law (norm. – normal, log. – logarithmically normal), Avr – average according to the distribution law (simple mean for normal distribution and geometric mean for logarithmically normal one), Stand – standard deviation.

Three main generations of pitchblende have been distinguished. The first, early fine-spherulitic generation (ptb-f1) is represented by pitchblende spherulites from 5 to 30  $\mu\text{m}$  large. It forms fine dissemination in wall rocks, cement of breccia (Fig. 2.34) and thin veinlets. It is widely developed: virtually all the ore bodies of the Antei deposit are composed of this generation.

The second, coarse-spherulitic generation (ptb-c) occurs as large spherulites up to a few centimeters in size and thick crusts mainly in rich ore bodies. It grows distinctly on fragments of ptb-f1 pitchblende aggregates (Fig. 2.34) which indicates tectonic movements between these generations. Up to 3-4 rhythms of large spherulites may be observed in the crusts. In a strict sense, all these rhythms are separate generations so ptb-c pitchblende is a “breed” of similar generations (after Yu.M.Dymkov, 1985).

The third, late fine-spherulitic generation of pitchblende (ptb-f2) is identical to ptb-f1 generation but the only feature – it was found exclusively as crusts covering coarse-spherulitic pitchblende and breccia cement (Fig. 2.35). These two fine-spherulitic generations could be distinguished only by the presence of the coarse-spherulitic generation or in the case of metasomatic dissemination in wall rocks which is only typical of the ptb-f1 pitchblende.



## 2. Mineralogy of the deposits

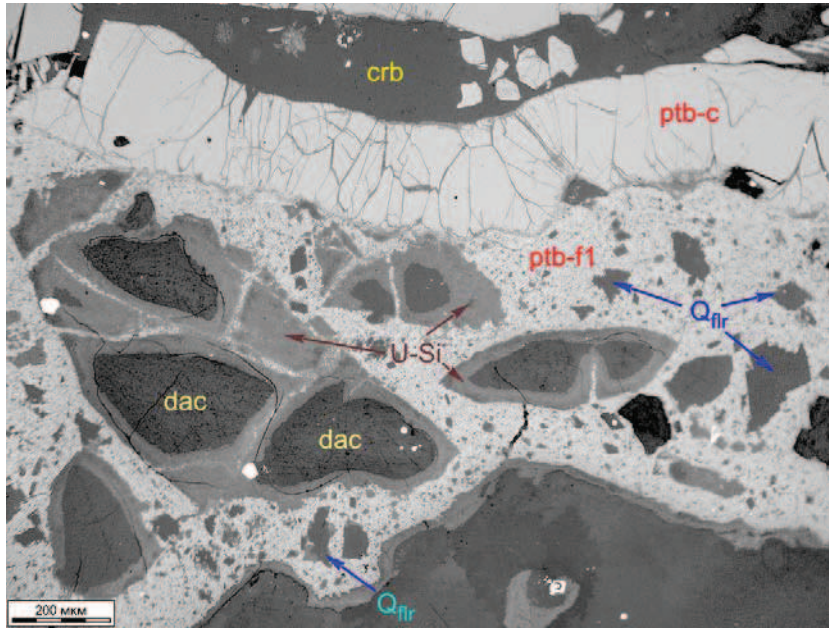


Fig. 2.34. Pitchblende of the early fine-spherulitic generation (ptb-f1) cements dacite fragments (dac) and is overgrown by pitchblende of the coarse-spherulitic generation (ptb-c). Calcite of the 1<sup>st</sup> postore stage (crb) cements fragments of the latter. U-Si metagel (U-Si) intensively replaces dacite fragments and thin pitchblende veinlets in dacite. Quartz of the 1<sup>st</sup> postore stage forms complete pseudomorphs (Q<sub>flr</sub>) after octahedral crystals of fluorite of the 1<sup>st</sup> generation (rhombs and triangles in the section plane) paragenetic with pitchblende ptb-f1. Oktyabrsky deposit. Photomicrograph of thin-polished section St-220d in plane reflected light.

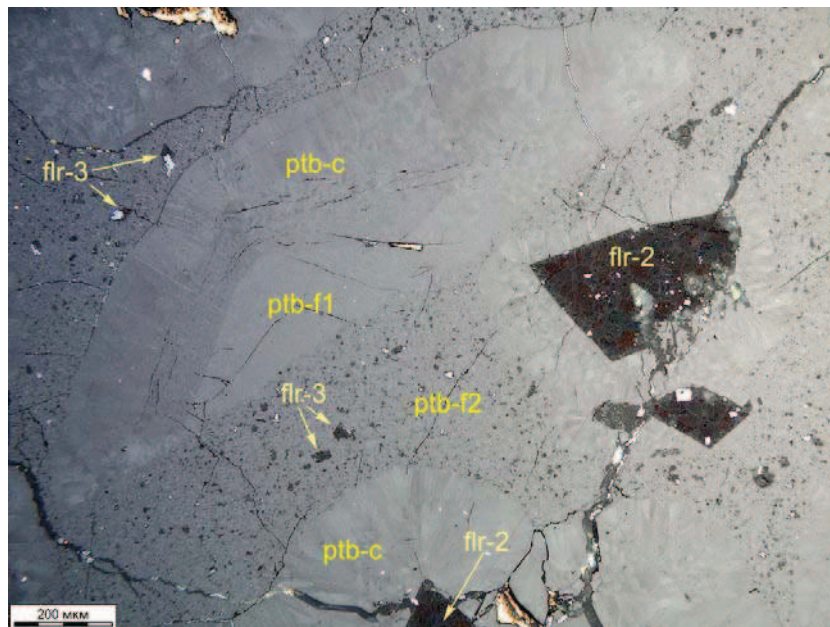


Fig. 2.35. Three generations of anisotropic pitchblende with fluorite. Coarse-spherulitic pitchblende (ptb-c) overgrows large octahedral fluorite crystals of the 2<sup>nd</sup> generation (flr-2) and massive aggregate of the early fine-spherulitic pitchblende (ptb-f1). Fragments of ptb-f1 and ptb-c pitchblende are cemented by a fine aggregate of the late fine-spherulitic pitchblende (ptb-f2) and small octahedral crystals of the 3<sup>rd</sup> fluorite generation (flr-3) saturating pitchblende aggregate. Fluorite of both generations is partly replaced by galena (small white segregations). Central site of the Streltsovsky deposit, a rich ore body in dacites. Photomicrograph of thin-polished section St-77c in reflected light with crossed polarizers.



## 2. Mineralogy of the deposits

---

In rare cases, medium-spherulitic pitchblende generation (ptb-m) has been observed between coarse- and late fine-spherulitic ones (Fig. 2.36). Presumably, it signifies intermediate composition uraniferous fluid circulated in the background of a general tendency of decreasing pitchblende growth time and/or uranium concentration in the fluid.

Dark-violet, dark-brown fluorite is a typical mineral accompanying pitchblende universally. It was formed in paragenesis with all pitchblende generations – from the early fine-spherulitic to the late fine-spherulitic. As could be seen from Fig. 2.34, fine aggregate of ptb-f1 pitchblende is impregnated with octahedral fluorite crystals of different size which later were completely replaced by quartz. The size of former fluorite crystal varies from relatively large (up to 0.2 mm) to small, similar to pitchblende spherulites (several tens of a micron). It means that the growth of some fluorite crystals began before pitchblende ptb-f1 and its octahedrons were overgrown by fine pitchblende and fluorite forming a paragenic association.

Relatively large crystals of fluorite of the 2<sup>nd</sup> generation (flr-2) preceded coarse-spherulitic pitchblende ptb-c with their partial joint grows (Fig. 2.37). It indicates a paragenetic association of pitchblende and fluorite. The last pitchblende generation ptb-f2 is also accompanied by fluorite of the 3<sup>rd</sup> generation (flr-3). As is shown in Fig. 2.35, fluorite flr-3 matches pitchblende ptb-f2 in size. In such a way, a clear relation in size of pitchblende and synchronous fluorite is established.

Octahedral habitus predominates for all fluorite generations of the uranium ore stage. In some cases, square shapes of fluorite crystals are observed in sections. It may mean cubic habitus but it is also possible for octahedrons in a section.

Wide development of synore fluorite of different generations in the SOF deposits has been revealed by the author for the first time. The fact is that synore fluorite was intensively replaced by quartz, illite, chlorite, U-Si metagel and other minerals during the 1<sup>st</sup> postore stage (Fig. 2.34). Its relics were preserved only in a few places while numerous complete pseudomorphs could be hardly recognized as former fluorite, and only by their unusual shape for replacement minerals. It caused omission of these “ghosts” of synore fluorite by other mineralogists and by the author in the early stages of his mineralogical studies in the SOF.

### *2.2.3. Mineral assemblages of the 1<sup>st</sup> postore stage*

The first revealed process of the 1<sup>st</sup> postore stage is episyenitization (or dequartzification). It was observed in the granites of the Antei deposit at different levels.

## 2. Mineralogy of the deposits

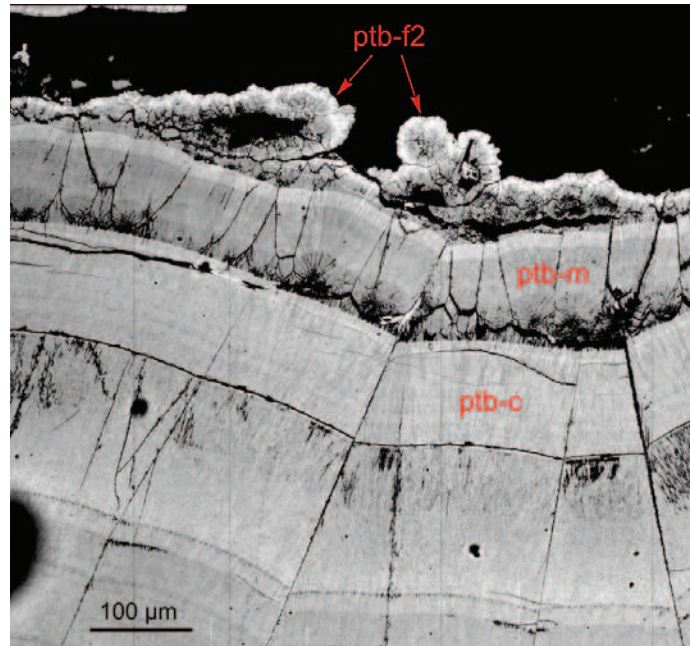


Fig. 2.36. The medium-spherulitic pitchblende generation (ptb-m) formed after the coarse-spherulitic generation (ptb-c) and before the late fine-spherulitic one (ptb-f2). Central site of the Streltsovsky deposit, a rich ore body in dacites. BSE image of thin-polished section St-77b.

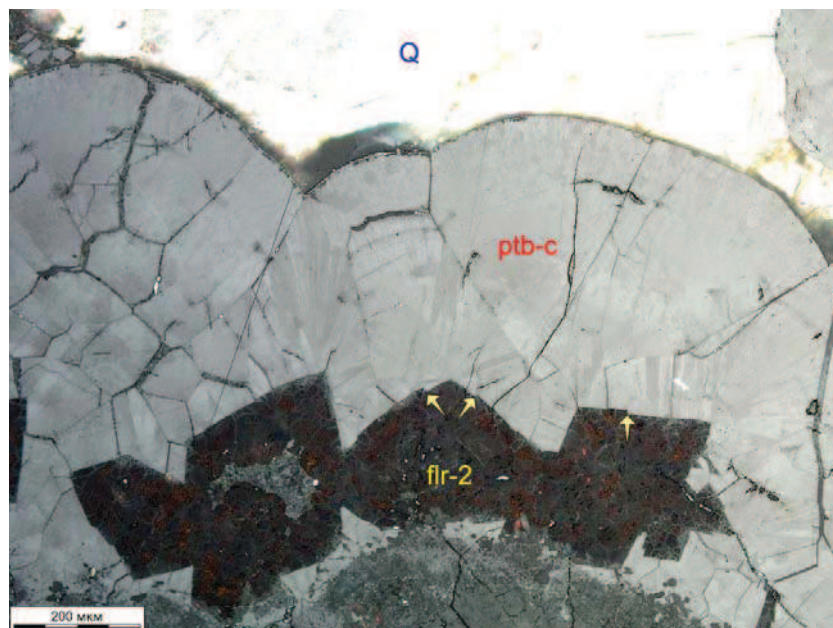


Fig. 2.37. Octahedral crystals of fluorite of the 2<sup>nd</sup> generation (flr-2) are overgrown by large spherulites of anisotropic pitchblende ptb-c. Q – quartz of the 1<sup>st</sup> postore stage. Steps on the faces of fluorite octahedrons (pointed with arrows) indicate complementary growth of fluorite when small nuclei of pitchblende spherulites temporarily stopped their growth. Thus, partial joint growth of the 2<sup>nd</sup> fluorite generation and pitchblende ptb-c is established. Central site of the Streltsovsky deposit. Photomicrograph of thin-polished section St-77c in both transmitted and reflected light with semi-crossed polarizers.

## 2. Mineralogy of the deposits

---

Since no minerals were deposited during this process, it was not represented in the paragenetic scheme (Fig. 2.5). Evidently, episyenitizing fluids circulated not only in granites. In a rich ore body in basalts of the Western site (the Streltsovsky deposit), numerous pitchblende relics were found cemented by quartz of the 1<sup>st</sup> postore stage (Fig. 2.22). As the only known mineral replacing pitchblende – U-Si metagel – was formed far after quartz, episyenitization is the most likely process to have caused pitchblende dissolution. Similar resorbed pitchblende spherulites cemented by pyrite and quartz of the 1<sup>st</sup> postore stage were found in different parts of the Antei deposit.

After quartz dissolution in granites, the vugs were partly or completely filled with quartz, ankerite, calcite, fluorite and pyrite (Fig. 2.20, 2.21, 2.38). Possibly, quartz precipitated on pore walls and in veinlets was previously leached out during episyenitization. If that is the case, it is a conjugate deposition of dissolved silica. Small albite crystals were also observed in the cavities grown epitaxially on K-feldspar and plagioclase of granites (Fig. 2.39). Albite was identified optically by the small angle of extinction between polysynthetic twins. L.P.Ishchukova (personal communication) found postore albite as well. The observed succession of mineralization in vugs is the same as in veins and veinlets in the different deposits of the SOF located in different host rocks.

Wall-rock alteration during the 1<sup>st</sup> postore stage is very similar to that of the preore stage. The difference is noticeable mainly macroscopically by intensive rock bleaching along fractures, veins and veinlets typical of the 1<sup>st</sup> postore stage (Fig. 2.8, 2.9, 2.17, 2.18). Under the microscope, a more intense development of silicification, carbonatization, illitization and chloritization can be established in such zones. Formation of fluorite, sulfides and U-Si metagel in altered rocks may be pointed out for the 1<sup>st</sup> postore stage as another difference from the preore stage. All Ti accessories become unstable in zones of intensive bleaching. Not only Ti-magnetite and titanite but ilmenite as well are replaced by leucoxene and Fe oxides. Titanium was widely redistributed in altered rocks as leucoxene along fissures and in intergranular space. Replacement of pitchblende spherulites by leucoxene has been established in basalts (Fig. 2.40).

Also at variance with the preore stage, intensive bleaching in rocks enriched in Fe<sup>3+</sup> (dacites, tuff-sandstones, gritstones and conglomerates, all the varieties of hematized rocks) led to complete or partial removal of Fe<sup>3+</sup>. In the last case (Fig. 2.8, 2.9, 2.18), Fe oxides have been redistributed in bleaching zones in microfissures and intergranular space against the background of their decomposition.



## 2. Mineralogy of the deposits

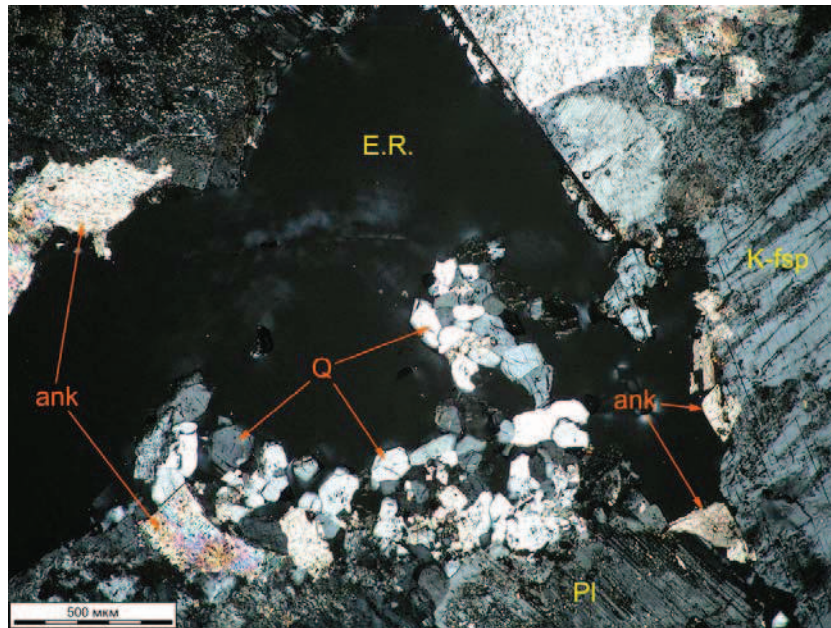


Fig. 2.38. A pore in episyenitized zone in granites is partly filled with ankerite (ank) and quartz (Q) grown on ankerite. E.R. – epoxy resin (pore), K-fsp and Pl – consequently microcline and plagioclase of granite. Antei deposit. Photomicrograph of thin-polished section St-617 in transmitted light with crossed polarizers

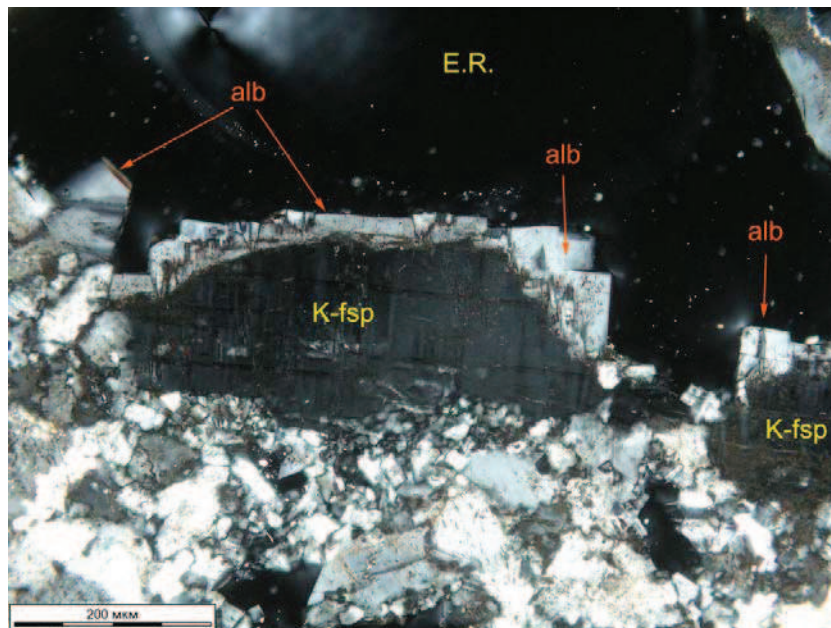


Fig. 2.39. Albite of the 1<sup>st</sup> postore stage (alb) grown on microcline grains of granite (K-fsp) in a pore (E.R. – epoxy resin) in the episyenitized zone. Antei deposit. Photomicrograph of thin-polished section St-621 in transmitted light with crossed polarizers.



## 2. Mineralogy of the deposits

---

Carbonate of the 1<sup>st</sup> generation is one of the earliest mineral in the 1<sup>st</sup> postore mineral complex. It is usually ankerite or siderite in granites and basalts but in dacites it is represented only by calcite. Carbonate grows on walls of veinlets or cements rock fragments (in ore bodies – hematized, albitized rocks with uranium mineralization) and is overgrown by quartz, fluorite and later calcite. Early carbonate predominates in basalts while it is subordinate to quartz in granites.

Quartz grows on the carbonate (Fig. 2.38). The crystals have a comb-like shape of crystals caused by the splitting of their peripheral parts into sub-domains (Fig. 2.41). Numerous generations of quartz develop in thick veins. In some cases crystalline quartz is periodically intergrown with cryptocrystalline and calcedony-like quartz of different grain sizes, up to 20 rhythms may occur in such zoned veins.

Quartz of the 1<sup>st</sup> postore stage along with chlorite and carbonate intensively replaces fluorite of the uranium ore stage (Fig. 2.52). According to the author's estimation, most of synore fluorite was destroyed during metasomatism of the 1<sup>st</sup> postore stage. In rare cases, weak replacement of pitchblende by postore quartz was noticed as fine-grained granular aggregates and larger metasomatic quartz crystals in pitchblende (Fig. 2.53).

Fluorite was formed after quartz with their partial joint growth (Fig. 2.44). Similar to fluorite of the uranium ore stage, it is characterized by a dark-violet, rarely – dark-brown color. Sometimes thin zones of fluorite crystals have blue to light-blue color. Differently to syn-uranium fluorite, only cubic habitus is seen in postore fluorite crystals.

Two generations of pyrite have been distinguished. The first generation was observed in single cases as fine dissemination (from several tens to several hundreds of microns) in growth zones of the early calcite generation. The second generation of pyrite dominates essentially among sulfides of the 1<sup>st</sup> postore stage. It was formed after the bulk of quartz, partly synchronously with fluorite but before chlorite and calcite of the late generation (Fig. 2.45). Pyrite is also replaced by U-Si metagel and cemented by galena, low-Fe sphalerite, fahlore (tennantite-tetrahedrite series), and chalcopyrite. Marcasite was deposited simultaneously with pyrite. It often forms close intergrowths with cubic iron sulfide of similar grain size.

Chlorite was formed after pyrite and after the bulk of fluorite. It overgrows quartz and fluorite crystals (Fig. 2.44). However, sometimes chlorite is overgrown by fluorite which is evidence for sustained deposition of fluorite. Up to three chlorite generations has been observed in narrow chlorite rims in basalts (Fig. 2.46). These generations are distinguished by

## 2. Mineralogy of the deposits

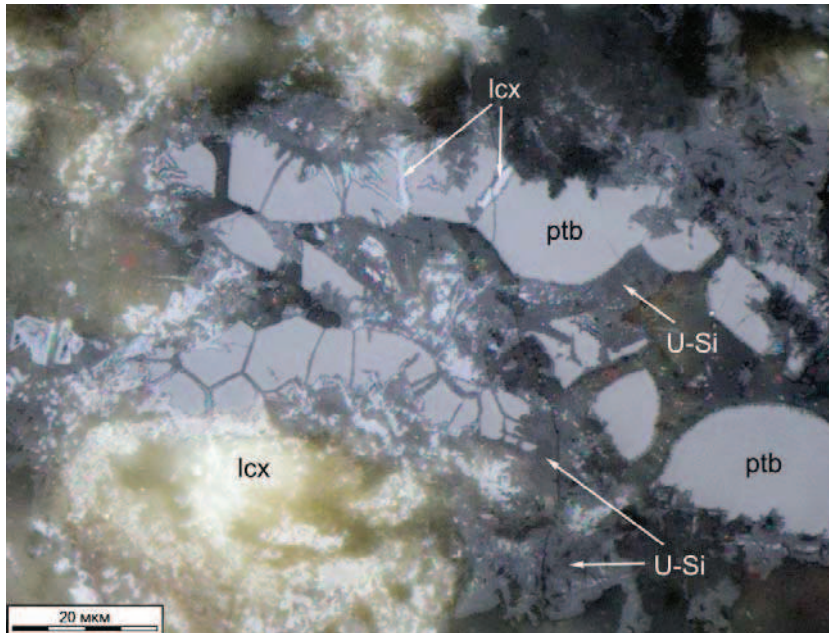


Fig. 2.40. Pitchblende spherulites (ptb) are replaced by leucoxene (lcx) along fractures and inductive surfaces, and later – by U-Si metagel (U-Si). Western site of the Streltsovsky deposit. Photomicrograph of thin-polished section St-396a in plane reflected light, with water immersion.

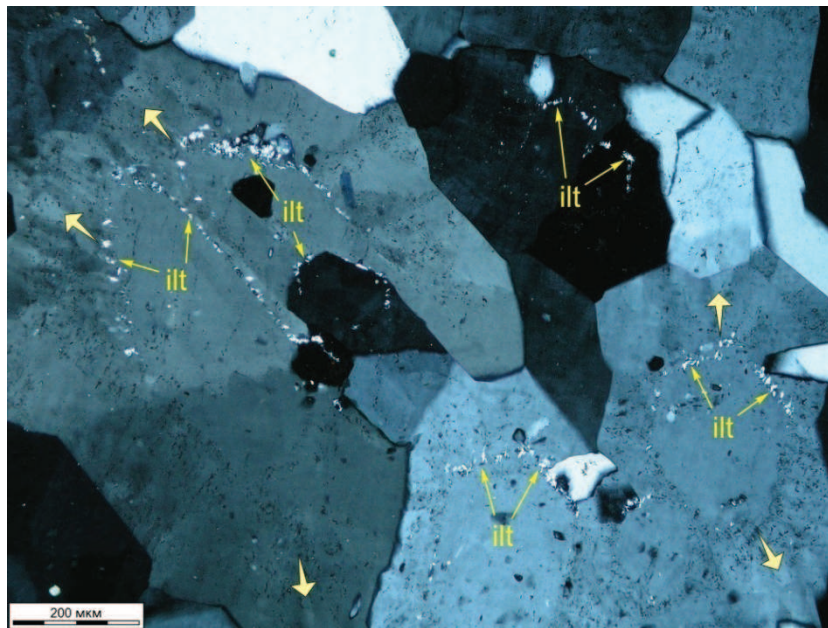


Fig. 2.41. Quartz of the 1<sup>st</sup> postore stage with inlayers of fine flakes of illite (ilt) in inner growth zones. After these zones quartz was split into sub-domains (pointed out with arrows). Antei deposit. Photomicrograph of thin-polished section St-21b in transmitted light with crossed polarizers.

## 2. Mineralogy of the deposits

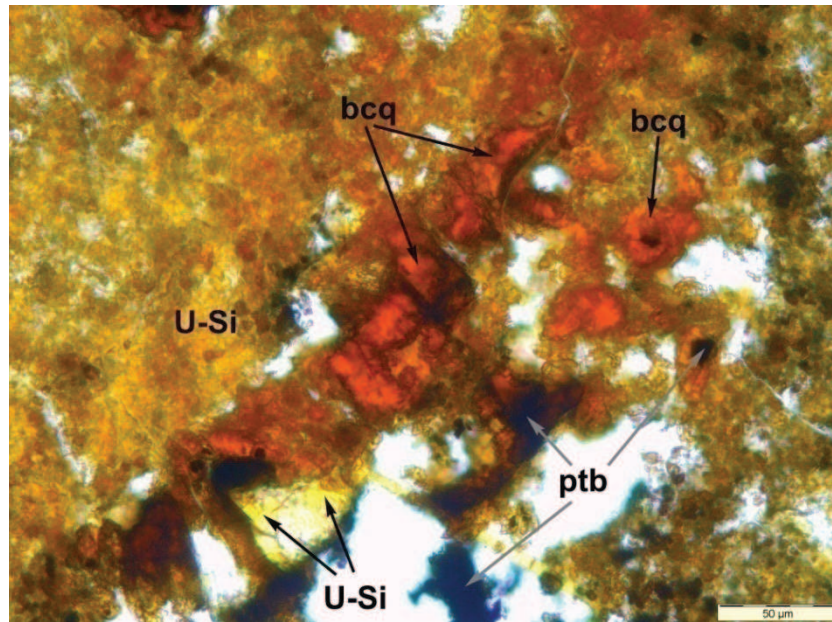


Fig. 2.42. Pitchblende (ptb) is intensively replaced by becquerelite (bcq). The latter is overgrown by a yellow variety of U-Si metagel (U-Si). Oktyabrsky deposit. Photomicrograph of thin-polished section St-211a in plane transmitted light.

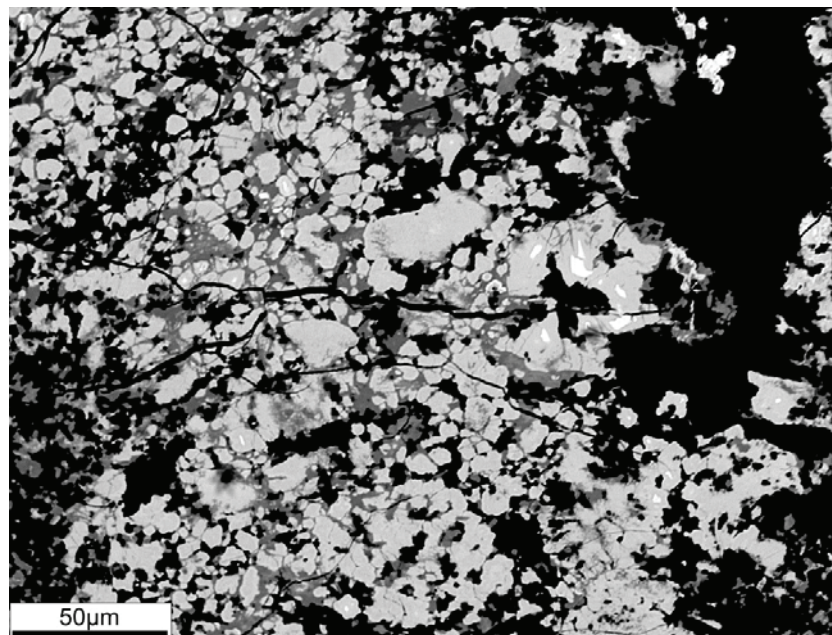


Fig. 2.43. Pitchblende relics (small white phases) in becquerelite pseudomorphs (light-grey phase). The latter is cemented by yellow U-Si metagel (dark-grey phase), intersected by its thin veinlets and partly replaced. Black – aluminosilicate matrix of dacite. Oktyabrsky deposit. BSE image of thin-polished section St-211a.



## 2. Mineralogy of the deposits

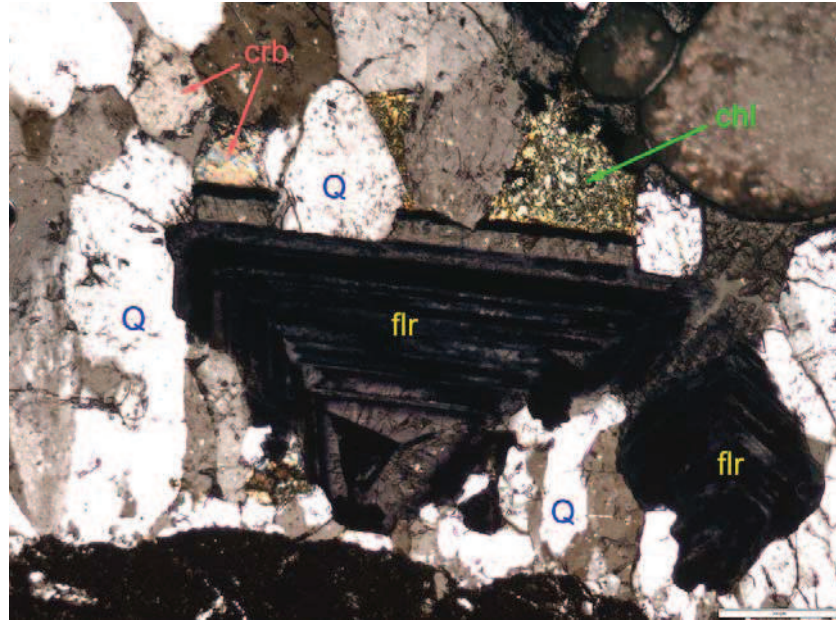


Fig. 2.44. Fluorite crystals (flr) grew on thin quartz comb and then grew simultaneously with quartz (Q) forming inductive surfaces of joint growth. A cubic surface of fluorite was overgrown by the late quartz generation. After fluorite, late carbonate (crb) and chlorite (chl) were deposited. Centralny site of the Streltsovsky deposit. Photomicrograph of thin-polished section St-77 in transmitted light with crossed polarizers.

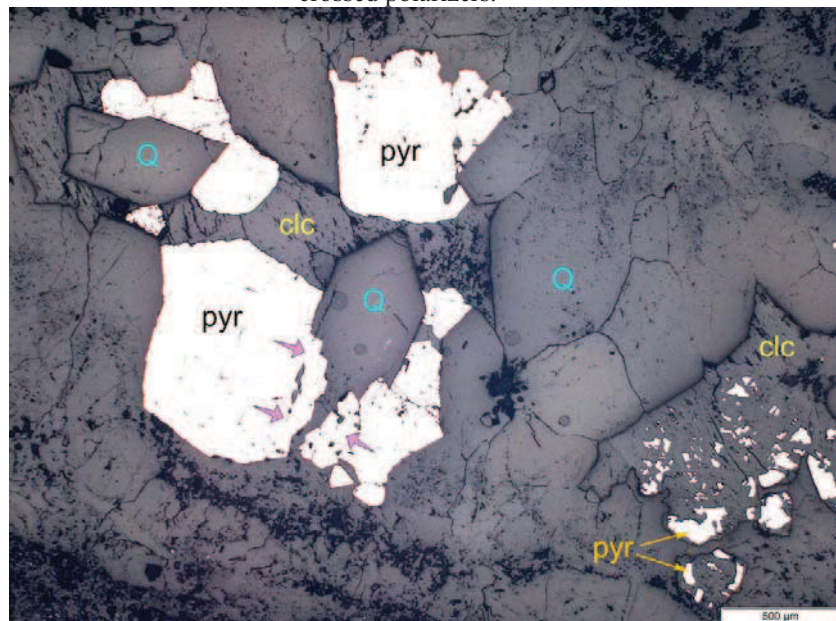


Fig. 2.45. Quartz-pyrite-carbonate association of the 1<sup>st</sup> postore stage. Pyrite (pyr) is xenomorphic relative to quartz (Q) and corrodes the latter (indicated with arrows). Mn-calcite (clc) is xenomorphic to quartz and pyrite. It dissolved pyrite almost completely (in the lower right corner of the figure). Antei deposit. Photomicrograph of thin-polished section St-510 in reflected plane light.



## 2. Mineralogy of the deposits

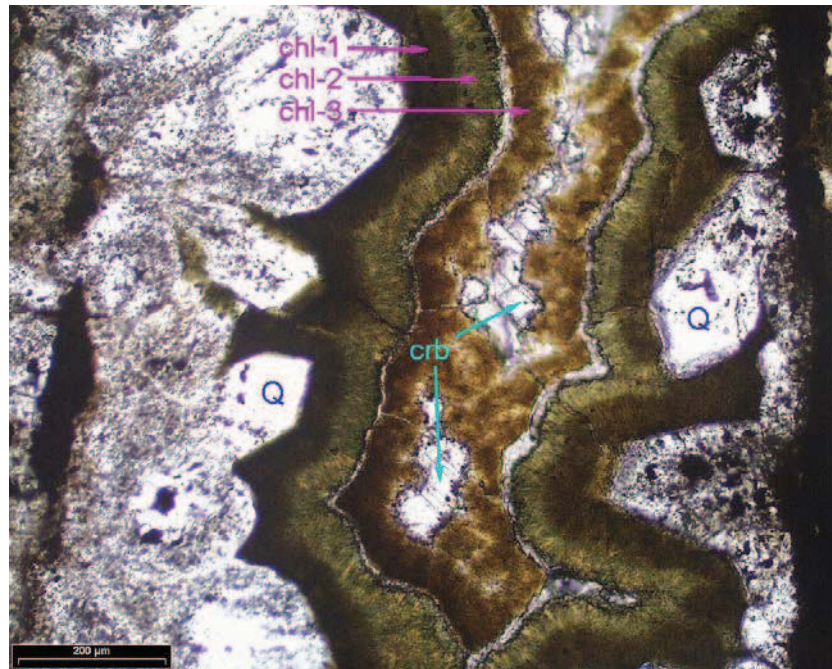


Fig. 2.46. Quartz of the 1<sup>st</sup> postore stage (Q) is overgrown by 3 chlorite generations (chl-1, chl-2, and chl-3). Central part of the veinlet is filled by calcite (crb). Western site of the Streltsovsky deposit. Photomicrograph of thin-polished section St-120 in plane transmitted light.

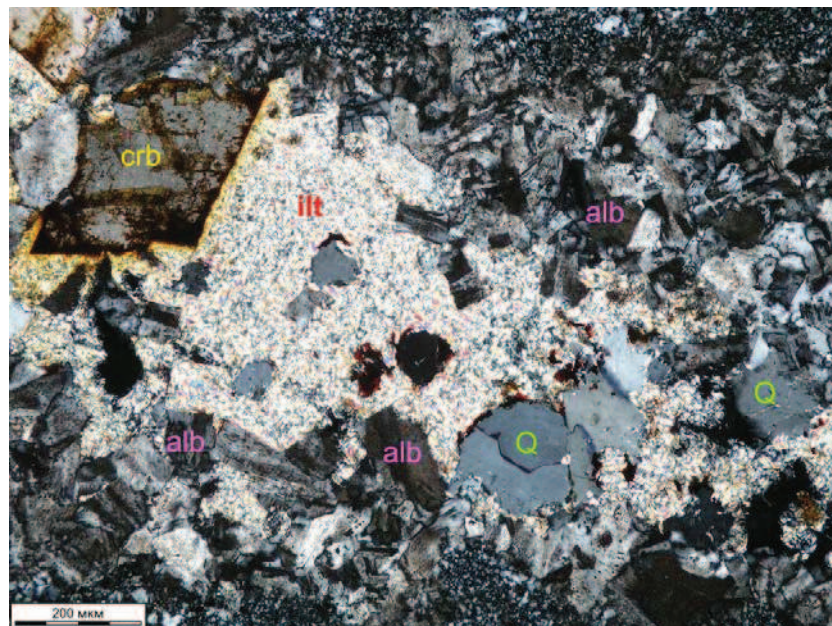


Fig. 2.47. Illite (ilt) fills the central part of a veinlet growing on quartz of the 1<sup>st</sup> postore stage (Q), early ankerite (crb) and albite of the uranium ore stage (alb). Intensive corrosion of quartz and albite by illite is noticeable. Antei deposit. Photomicrograph of thin-polished section St-551d in transmitted light with crossed polarizers.

## 2. Mineralogy of the deposits

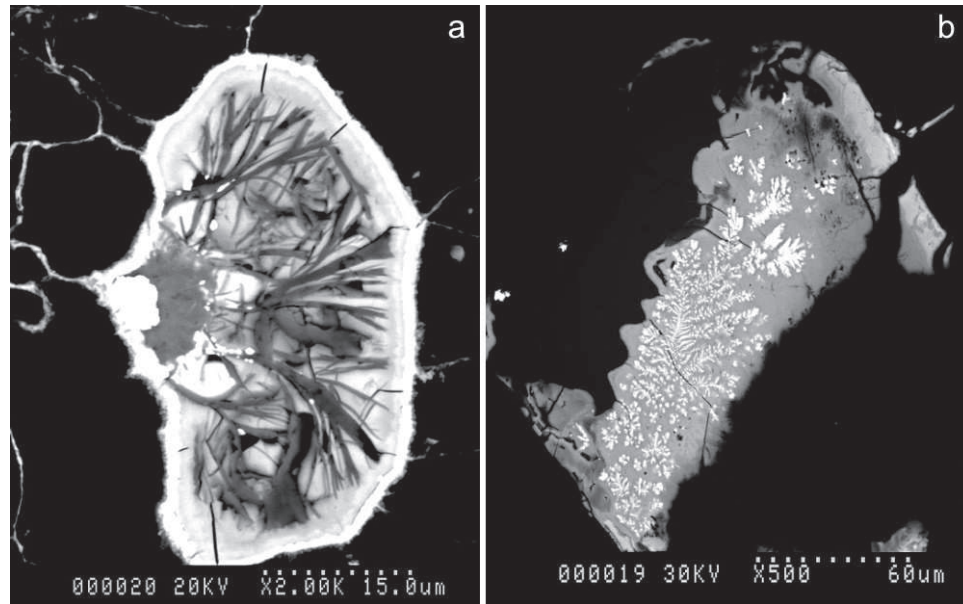


Fig. 2.48. Paragenetic association of polyphase U-Si metagel with chlorite (a) and native antimony (b). Panel (a): more uranium phase of U-Si metagel (white) deposited on the walls of a pore in postore quartz (black) while its central part is filled with more siliceous U-Si metagel (grey) with chlorite flakes (dark-grey). Panel (b): skeleton crystals of native antimony (white) in U-Si metagel (grey); black – quartz of the 1<sup>st</sup> postore stage. Central site of the Streltsovsky deposit. BSE images of thin-polished section St-77a.

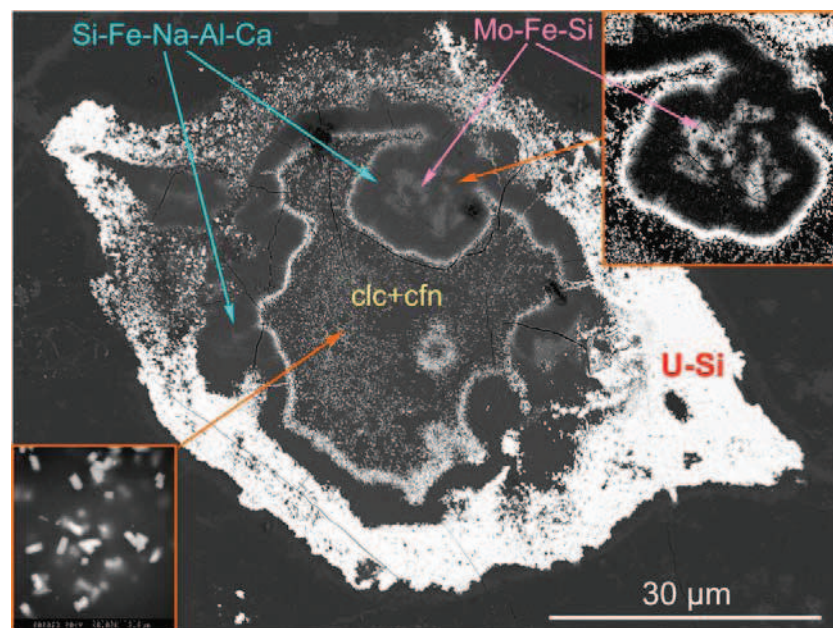


Fig. 2.49. Walls of a pore in dacites are covered by a U-Si metagel (U-Si, white) which is overgrown by a complex gel of variable composition (Si-Fe-Na-Al-Ca, grey) with segregations of a lighter Mo-Fe-Si gel. Central part of the pore is filled by calcite (clc) impregnated with small prismatic coffinite crystals (cfn). Thin light-grey rim in the base of calcite filling is also composed of coffinite crystals. Oktyabrsky deposit. BSE image of thin-polished section St-220-1.



## 2. Mineralogy of the deposits

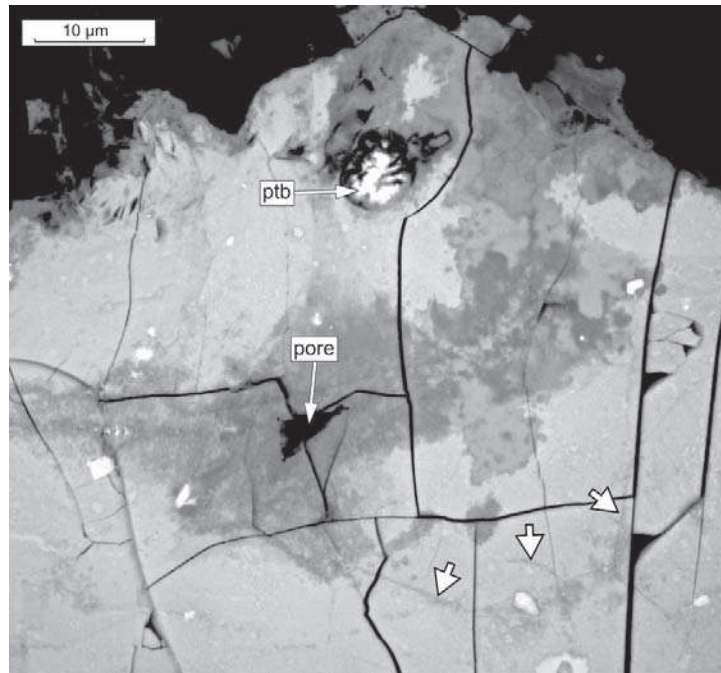


Fig. 2.50. Polyphase U-Si metagel (different shades of grey) in a veinlet in basalts (black at the top) with a relic of pitchblende spherulite (ptb, white). Linear cracks in U-rich phase (light grey) along which diffusion of Si-rich phase (dark grey) occurred are indicated with arrows. Central pore in Si-rich phase and numerous fissures of shrinkage are noticeable. Western site of the Streltsovsky deposit. BSE image of thin-polished section St-396a.

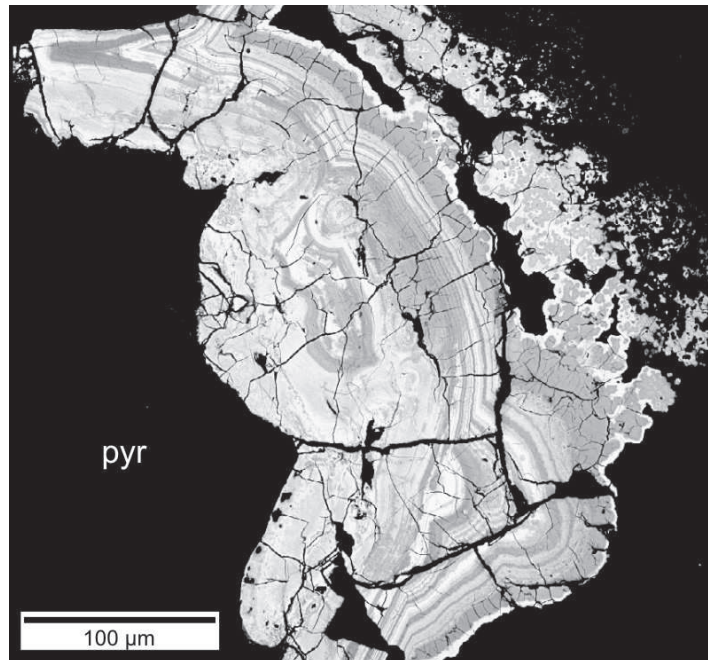


Fig. 2.51. A colloform rhythmically zonal segregation of polyphase U-Si metagel grown on pyrite grain (pyr) in a veinlet of quartz of the 1<sup>st</sup> postore stage. More uranium phases are brighter and more siliceous – darker. Antei deposit. BSE image of thin-polished section St-501.

## 2. Mineralogy of the deposits

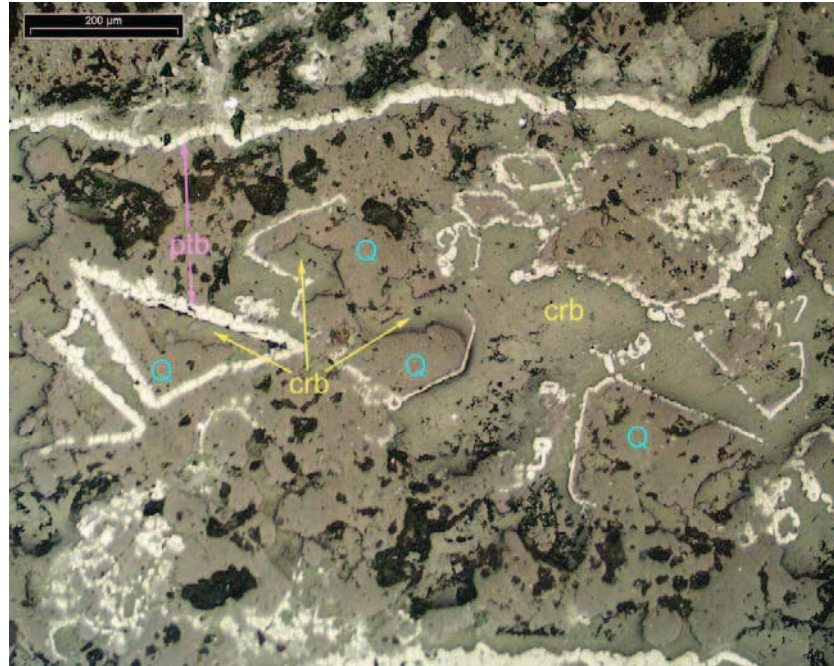


Fig. 2.52. Fluorite crystals overgrown by pitchblende (ptb) were lately completely replaced by quartz (Q) and carbonate (crb) of the 1<sup>st</sup> postore stage. Fluorite presence may be indicated only by the shape of protocrystals decorated by pitchblende. Western site of the Streltsovsky deposit. Photomicrograph of thin-polished section St-125 in plane reflected light.

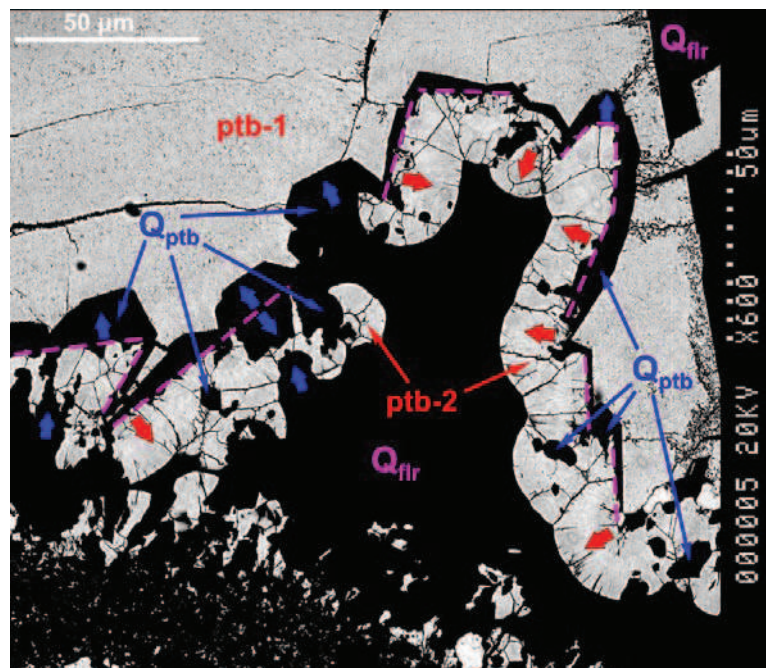


Fig. 2.53. Coarse-spherulitic pitchblende (ptb-1) grew on what were presumably fluorite crystals (former contours are shown by magenta dashed line). After complete dissolution of fluorite and conceivably some part of pitchblende during episyenitization (?), redeposited pitchblende (ptb-2) precipitated on the cavity walls (growth directions are indicated by red arrows). The rest of the vug was filled by quartz ( $Q_{flr}$ ). Some part of coarse-spherulitic pitchblende (ptb-1) and redeposited pitchblende (ptb-2) was metasomatically replaced by quartz ( $Q_{ptb}$ ). Directions of metasomatic quartz development are pointed by blue arrows. Centralny site of the Streltsovsky deposit. BSE image of thin-polished section St-77b.



## 2. Mineralogy of the deposits

---

the color and size of flakes. Often fine chlorite flakes are in close association and even intergrown with illite indicating their synchronous deposition.

Illite began to deposit after early carbonates and the first generation of quartz. This is corroborated by intersection of early calcite crystals by thin illite veinlets and inlayers of intermediate growth zones of quartz crystals with illite flakes (Fig. 2.41). Besides this, quartz-illite paragenesis is confirmed by the presence of illite solid phases (proved by Raman microspectroscopy) in primary fluid inclusions in quartz. However, the bulk of illite was formed after quartz as it usually fills central pores and interstitial space between quartz grains (Fig. 2.47).

U-Si polyphase metagel was previously identified as coffinite. The author's studies have revealed its primary colloidal nature, polyphase composition, and location in the paragenetic scheme. It was formed after pyrite and fluorite in paragenesis with chlorite, pyrrhotite and native antimony (Fig. 2.48a,b), and before late calcite. Numerous instances of pyrite corrosion and intersection by U-Si metagel and overgrowth of fluorite cubes by this uranium phase distinctly define the beginning of its formation.

The composition of U-Si metagel varies widely, U:Si ratio changes from approximately 50:1 (in at.%) to 1:3. Usually its deposition began with more uranium rich varieties, the next generations possess intermediate composition and precipitation finished with the most siliceous phases (Fig. 2.50). Sometimes crusts of U-Si metagel are composed of numerous zones with periodically changing U:Si ratio, up to a dozen rhythms may be observed (Fig. 2.51).

Early U-rich phases are often fractured and late Si-rich phases diffuse along cracks into the early phase (Fig. 2.48). It indicates that uraniferous phases were solidified by the time of injection of siliceous gel and relieved tension as brittle deformation.

A unique segregation has been found in a rich ore body in dacites of the Oktyabrsky deposit. A pore was filled from the periphery to the center by polyphase U-Si metagel, and then by complex silicate non-uraniferous gel of extremely variable composition with Si, Fe, Na, Al, and Ca as major components, with small colloidal segregations of predominantly Mo-Fe-Si composition. The central part of the pore was filled by calcite finely impregnated with small (~1  $\mu\text{m}$ ) prismatic coffinite crystals (Fig. 2.49). It is the only case when real coffinite crystals have been observed in the SOF deposits.

As it follows from the mineral succession, molybdenum silicate gel was formed directly after U-Si phase. It helps to define the location of Mo-S metagel (jordisite) in the

## 2. Mineralogy of the deposits

---

paragenetic scheme as virtually simultaneous with uranium metagel. Common joint location of U-Si metagel and jordisite in ores corroborates this conclusion.

Calcite often cements fragments of pitchblende replaced by U-Si metagel and overgrows its segregations (Fig. 2.49). In some cases, drops of U-Si metagel were found in the early zones of calcite segregations that evidence their partial joint growth. Thus, formation of U-Si metagel was a relatively prolonged processes which occurred on a background of tectonic movements and unidirectional or oscillating change of U and Si concentration in the fluid.

The most usual form of U-Si gel development in ores is the replacement of primary U minerals (pitchblende, brannerite and uraninite). Two mechanisms of replacement have been established – diffusive and corrosive ones. Diffusive development of U-Si phase is typical of relatively low intensity of pitchblende alteration. It occurs along fibres of spherulites evenly replacing the bulk of pitchblende but along some less resistant zones replacement is more intensive (Fig. 2.54a). With increasing intensity of replacement, separated fine phases of U-Si metagel merge together and replacement begins to spread “front-by-front” (Fig. 2.54b). As uranium content in U-Si metagel is less than in pitchblende (78 wt.% and 56 wt.% on average respectively), and its density is also half as much as that of pitchblende, uranium was leached out from pitchblende when the replacement occurred. It was redeposited as the same metagel in the vicinity of replaced pitchblende. The maximum observed distance of redeposition amounted to only several centimeters.

Besides the U-Si metagel, other uranium phases were found in the 1<sup>st</sup> postore mineral complex in negligible amounts. Pitchblende presumably redeposited after episyenitization was formed at the beginning of the 1<sup>st</sup> postore stage before quartz. As could be seen in Fig. 2.53, this generation of pitchblende is replaced by quartz. The U-Si metagel also replaces pitchblende and develops in cracks in quartz granular aggregates. Zonal and spherulitic texture of this uranium oxide undoubtedly shows that it is a crystalline species – pitchblende, different from later metacolloidal U-Si phases.

Another uranium oxide with uraninite cubic lattice was detected in U-rich U-Si metagel by microdiffraction under HRTEM. It was found as numerous submicroscopic nuclei (3-5 nm) impregnating amorphous U-Si metagel. It will be examined in more detail in the chapter on typomorphic features of U-Si metagel.

Different from pitchblende by crystallinity but similar in composition and appearance, a pure uranium variety of U-Si metagel was found in isolated instances. As exemplified by Fig. 2.22 and 2.55, uranium metagel being in close intergrowth with fine

## 2. Mineralogy of the deposits

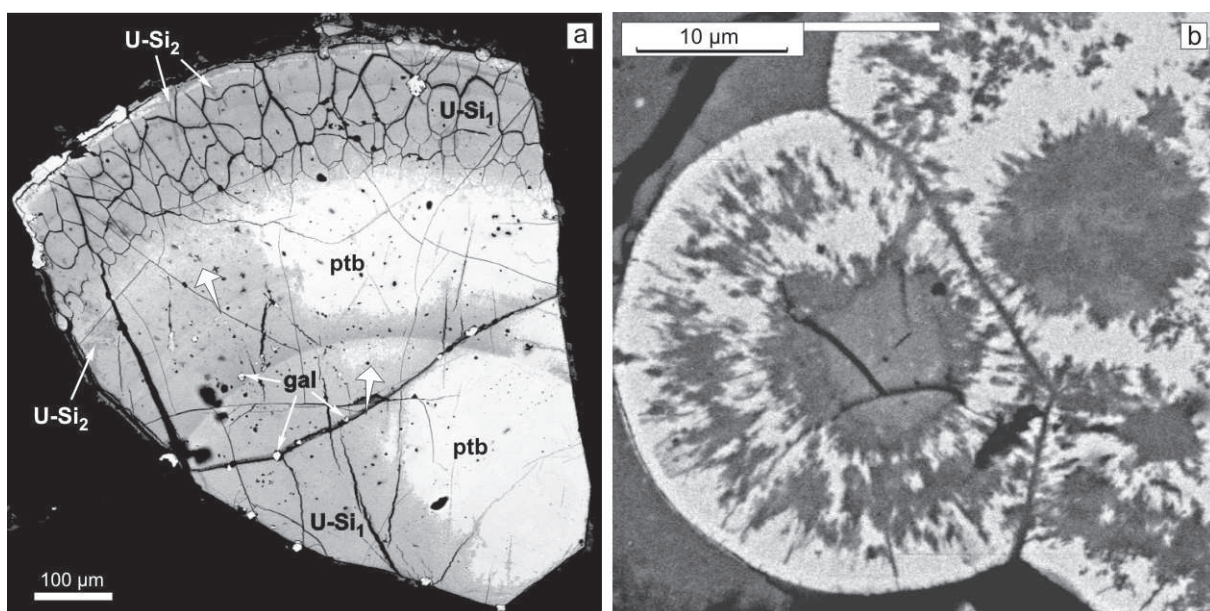


Fig. 2.54. Different forms of pitchblende replacement by U-Si metagel – diffusive (a) and corrosive (b). Panel (a): Two U-Si metagel phases developed after pitchblende (ptb): early more uranium (light-grey, U-Si<sub>1</sub>) and late more siliceous (dark-grey, U-Si<sub>2</sub>). Gal – galena segregations. Fuzzy areas of incomplete diffusive replacement of pitchblende are indicated by arrows. Pane (b): Core parts of pitchblende spherulites (light-grey) are corroded by two phases of U-Si metagel (grey, dark-grey). The latter also corrosively replaces intermediate spherulite zone along pitchblende fibers. Oktyabrsky deposit. BSE image of thin-polished section St-220.

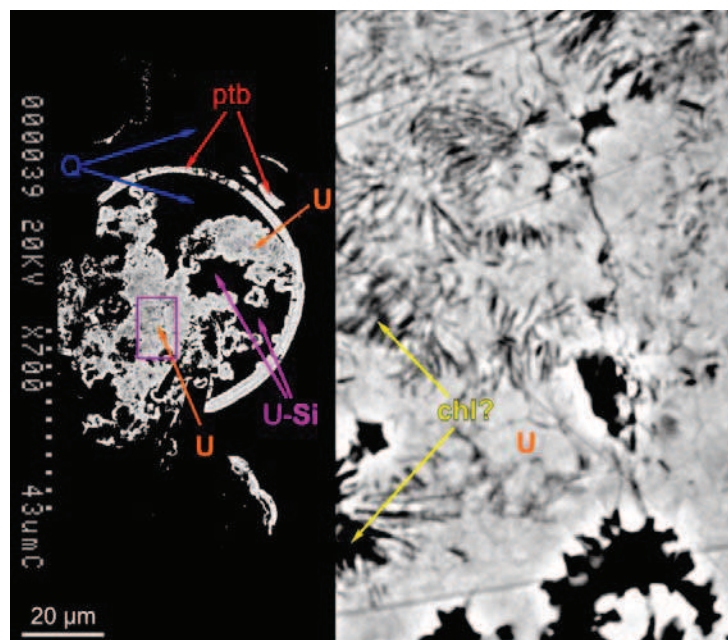


Fig. 2.55. A pitchblende spherulite (ptb) resorbed during episyenitization (?) and cemented by quartz of the 1<sup>st</sup> postore stage (Q). The latter was replaced by U metagel (U) in close intergrowth with fine chlorite (?) flakes (chl) and later – by siliceous U-Si metagel (U-Si). Area outlined by a violet rectangle in the left part of the figure is exhibited in the right part. A fragment from Fig. 2.20. Western site of the Streltsovsky deposit. BSE image of thin-polished section St-143d.

## 2. Mineralogy of the deposits

---

flakes of chlorite (?), replaced quartz of the 1<sup>st</sup> postore stage which in its turn filled from inside relics of pitchblende spherulite. Patchy replacement of quartz by the usual U-Si metagel occurred after the pure uranium variety. The metacolloidal nature of the latter is induced from the absence of spherulitic texture, colloform appearance and fine intergrowth with chlorite flakes atypical of pitchblende and observed for U-Si metagel (Fig. 2.48a). Detected Si concentration in the area of intergrowth with chlorite amounted only 0.3 wt.% while U reaches 78-79 wt.%, Pb – 1.4–1.8 wt.%, Ca – 1.7 wt.%, Zr – 1.3–1.4 wt.% which is typical of pitchblende (2 points of microprobe measurement). Since 0.3 wt.% Si may be explained by chlorite admixture, pure uranium composition should be inferred for the phase. Thus, this obviously metacolloidal uranium oxide was formed after quartz (differently from pitchblende redeposited at the beginning of the 1<sup>st</sup> postore stage), in paragenetic association with chlorite (?) and before U-Si metagel.

Fine films (0.3-0.5  $\mu\text{m}$  thick) of similar composition have been observed in cleavage fissures of late calcite. Seemingly, pure uranium varieties of U-Si metacolloidal matter developed repeatedly during the 2<sup>nd</sup> half of the 1<sup>st</sup> postore stage.

A  $\text{U}^{6+}$  mineral – becquerelite  $[\text{Ca}(\text{UO}_2)_6\text{O}_4(\text{OH})_6 \cdot 8(\text{H}_2\text{O})]$  has been found as a pseudomorph after pitchblende in a rich ore body in the Oktyabrsky deposit (Fig. 2.42). Its composition was determined from 7 microprobe analyses (variation limits in brackets and the average content in denominator, wt.%): U – (70.8-74.6)/72.5, Ca – (1.2-2.9)/1.9, Pb – (1.5-1.8)/1.7, Zr – (0.6-0.7)/0.7. The ore body is located in a large fault zone at a depth of about 350 m so theoretically it may be hypogene oxidation of pitchblende under the influence of meteoric waters circulated through the fault. However, cementation and replacement of becquerelite by hypogenous yellow U-Si metagel has been observed (Fig. 2.43). The position of becquerelite in the paragenetic scheme is conditionally determined by its earlier formation regarding U-Si metagel. Apparently, it was formed before such an indicator of reducing conditions as pyrite.

As will be discussed below, development of becquerelite and yellow color of U-Si metagel indicating  $\text{U}^{6+}$  prevalence in the phase, reflects local essentially oxidizing conditions in rich uranium ore bodies which may be caused by water radiolysis. Another indicator of relatively oxidizing conditions is a hematite-chlorite paragenesis. Relatively coarse-flaked hematite was found in close intergrowth with chlorite flakes in quartz-hematite-chlorite veinlets of the 1<sup>st</sup> postore stage. It obviously accounts for boundary Eh conditions between  $\text{Fe}^{2+}$  and  $\text{Fe}^{3+}$ .



## 2. Mineralogy of the deposits

Molybdenum sulfide is known in the SOF deposits in two states: crystalline (molybdenite) and amorphous (jordisite). The latter sharply predominates. Anisotropic flakes of molybdenite which may reach up to 1 mm in size are often merged into amorphous jordisite. Seemingly, they reflect different stages of crystallization of one and the same matter. If so, they should be regarded as simultaneous minerals.

Jordisite is heterogeneous in many cases. It contains flaky cotton-like segregations of essentially lead composition with smaller amounts of sulfur. Sometimes the latter forms globular ring-shaped fuzzy segregations typical of colloidal matter (Fig. 2.54). Lead, molybdenum and sulfur content varies in wide proportions in such sub-phases from microprobe analyses data. This probably corresponds to galena with deviations from normative galena composition.

Once a polyphase Mo-S segregation has been found in an ore body of the Antei deposit. Filling of a pore from the periphery to the center indicates the succession of the phases deposition: light-grey phase → grey phase → light-grey phase somewhat darker than the first one (Fig. 2.57). Fissures of shrinkage typical of metacolloid matter develop in all three phases but they are the most abundant in the 2<sup>nd</sup> grey phase.

The composition of the phases is surprising. The 1<sup>st</sup> and the 3<sup>rd</sup> are similar in concentration of major elements (Table 2.3):

Table 2.3. Average composition of polyphase Mo-S metagel (average from 2 analyses for each phase, from SX-100 microprobe data, in wt.%).

Phases	1	2	3
Mo	33.3	45.5	37.3
S	25.7	6.2	25.5
Fe	5.3	0.8	5.4
Sb	3.7	0.1	2.0
TOTAL	69.4	52.7	70.9
S:Mo (at.%)	2.3	0.4	2.0

As seen from the table, the 1<sup>st</sup> and the 3<sup>rd</sup> phases are virtually identical each other by composition. Theoretically, the 3<sup>rd</sup> phase might be the apical parts of the 1<sup>st</sup> phase covering domes of the pore wall and cut by the section plane but it is noticeably darker than the 1<sup>st</sup> phase in reflected light and BSE. The 2<sup>nd</sup> phase is the darkest one despite it possesses the highest Mo content (the heaviest metal in the composition). Obviously, it is reasoned by the lowest total (52.7 wt.% against 70 wt.% for other phases) presumes the lowest density of

## 2. Mineralogy of the deposits

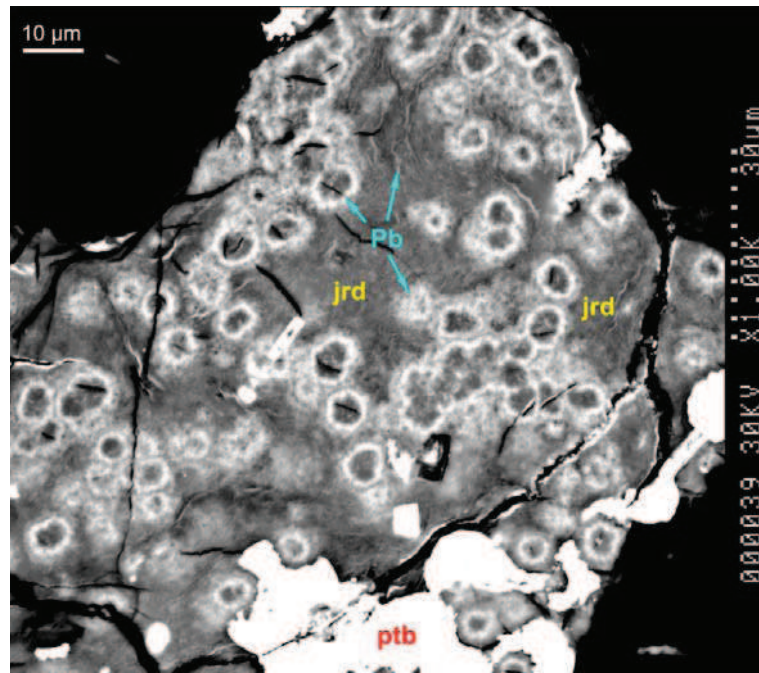


Fig. 2.56. Pitchblende (ptb) is intensively corroded by jordisite (jrd) containing globular (ring-shaped) and flaky segregations of lead sulfide (Pb). Streltsovsky deposit. BSE image of thin-polished section St-85/67a (the sample was kindly presented by Dr. Igor V. Mel'nikov).

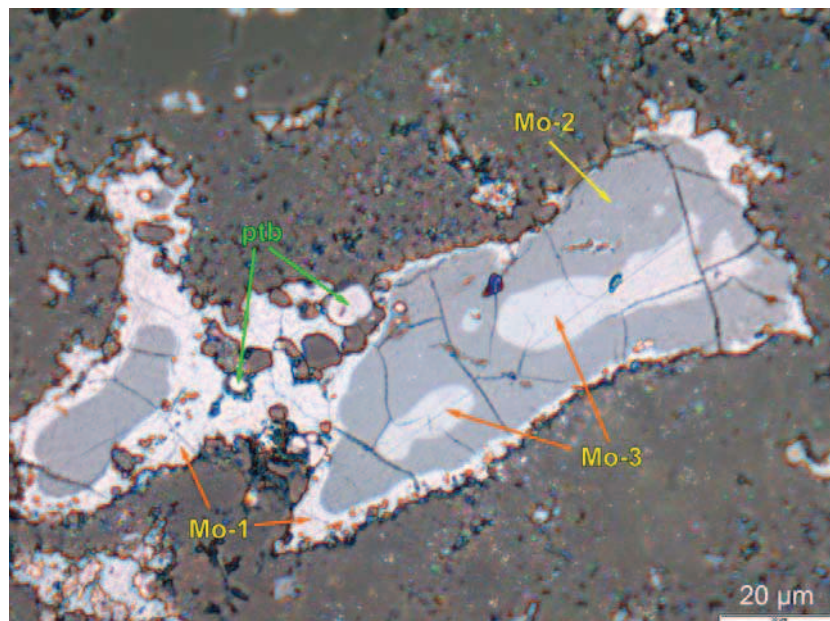


Fig. 2.57. Polyphase Mo-S metagel. Early light-grey phase (Mo-1) covers the walls of the pore. It is overgrown by intermediate grey phase (Mo-2), and the central part of the pore is filled by late light-grey phase (Mo-3). Shrinkage fissures are the most marked and abundant in the 2<sup>nd</sup> grey phase. PtB – fine pitchblende spherulites. Antei deposit. Photomicrograph of thin-polished section St-366b in plane reflected light.

## 2. Mineralogy of the deposits

---

the phase on one hand and the lowest Fe content (0.8 wt.% against 5.3-5.4 wt.%) on the other. Sulfur/molybdenum ratio (in at.%) indicates that the 1<sup>st</sup> and the 3<sup>rd</sup> phases correspond to the normative molybdenite composition (MoS<sub>2</sub>) while the 2<sup>nd</sup> phase exhibits a tremendous sulfur deficit.

Thus, Mo-S gel deposition features periodical fluctuation. If we take into account cases of sulfur-free Mo-Fe-Si gel formation approximately at the same position in the mineral succession (Fig. 2.49), one may infer that sulfur in Mo-S gel may be substituted by silica under favorable conditions.

According to the author's observations, jordisite was formed partly in paragenesis with lead sulfide (as an admixture in jordisite) and partly after galena which is evidenced by cementation of galena by jordisite. Occurrences of evenly distributed lamellar pyrrhotite crystals in jordisite also testify to their paragenesis. In cases of superposition of molybdenum and uranium mineralization, jordisite occurs in tight spatial relation with U-Si metagel. No clear ontogenic evidences of their paragenesis or disequilibrium have been obtained probably because of their metacolloid nature but the fact of spatial contingency indirectly testifies their contemporaneous formation. Deposition of Mo-Fe-Si metagel right after U-Si metagel (Fig. 2.49) is also circumstantial evidence of nearly simultaneous formation of jordisite and U-Si metagel.

Polymetallic mineralization is close to jordisite in time. Low-Fe sphalerite (cleophane) is the most abundant among the group. It was formed after galena since it forms overgrowths with galena crystals and fills the central parts of the vugs while galena occurs on the walls. Fahlore with chalcopyrite impregnation forms close intergrowths with cleophane and seemingly was deposited simultaneously with sphalerite. Pyrrhotite was observed in rare cases as lamellar, fibrous aggregate merged into siliceous variety of U-Si metagel and impregnated into jordisite mass.

### *2.2.4. Mineral assemblages of the 2<sup>nd</sup> postore stage*

Fluorite is the most abundant and protractedly formed mineral in the 2<sup>nd</sup> postore mineral complex. It differs from fluorite of preceded uranium ore stage and the 1<sup>st</sup> postore stage by its polychrome color and porcelain-like appearance (Fig. 2.58). However, fluorite of the last stage is also characterized by dark-violet color typical of fluorite of the earlier stages.

Pulsation is an appropriate feature of mineral deposition during the 2<sup>nd</sup> postore stage and fluorite reflects it better than any other minerals. Rhythms of fluorite precipitation are

## 2. Mineralogy of the deposits

---

exhibited as recurrent color change, reiterated pyrite and quartz rims on fluorite combs, and repeated layers with admixture of kaolinite and so on (Fig. 2.59). When filling open fissures and cavities in veins, fluorite with an admixture of rock debris and kaolinite forms mineralogical levels due to gravitation influence on admixture precipitation (Fig. 2.59). It is also a feature typical of the 2<sup>nd</sup> postore stage.

Porcelain-like appearance of fluorite is caused by fine admixture of kaolinite flakes (from several microns to 20-30  $\mu\text{m}$ ) impregnating fluorite crystals (Fig. 2.60). Sometimes chlorite makes globular segregations evenly distributed in fluorite. At least two varieties of chlorite have been observed in fluorite – a more ferrous variety corresponding to chamosite (thuringite) and a less ferrous, more magnesian one corresponding to Fe-prochlorite.

Kaolinite forming intergrowths with quartz in the Streltsovsky deposit precipitated later than chlorite-fluorite aggregate (Fig. 2.61). However, in the Antei deposit the most ferrous chamosite has been found as fine flakes (from 1 to 10  $\mu\text{m}$ ) in close intergrowth with contemporaneous kaolinite flakes (Fig. 2.62). Even distribution of kaolinite and chlorite in this aggregate and comparable size of their individuals testify the synchronous formation of these minerals. Therefore, kaolinite was formed partly in paragenesis with chlorite and partly – after chlorite.

When relatively narrow zones of kaolinization are superimposed on ore bodies with synore hematization, hematite dissolves providing bleaching of brownish-red rocks. In the zones of incomplete hematite removal, Fe oxides are partly redeposited with kaolinite and chlorite (Fig. 2.63) causing orange and light yellow color of rocks. This case is similar to incomplete Fe decomposition in the zones of quartz-chlorite-carbonate-illite alteration of the 1<sup>st</sup> postore stage.

Pyrite is the most abundant sulfide in the 2<sup>nd</sup> postore mineral complex. It was formed repeatedly with fluorite where it covers different combs of fluorite (Fig. 2.59) and makes up dissemination of fine crystals in various fluorite generations with kaolinite and chlorite.

Molybdenum and zinc sulfides have been found by the author in the 2<sup>nd</sup> postore mineral complex for the first time. Molybdenite occurs as relatively large flakes (up to 40  $\mu\text{m}$ ) with strong anisotropy in large fluorite crystals and smaller flakes in intergranular space of fine-grained fluorite aggregate (Fig. 2.63). Along with it, small allotriomorphic fuzzy segregations of molybdenum sulfide looking like typical jordisite have been observed intergrown with chlorite (Fig. 2.61) and kaolinite.



## 2. Mineralogy of the deposits

---



Fig. 2.58. Polychrome (blue, violet and yellow) fluorite of the 2<sup>nd</sup> postore stage. Porcelain-like variety of fluorite (light-pinky) is the latest generation filling the cavity between crusts of yellow fluorite and “garbage” aggregate of rock debris and blue fluorite. Central site of the Streltsovsky deposit. Sample St-176.

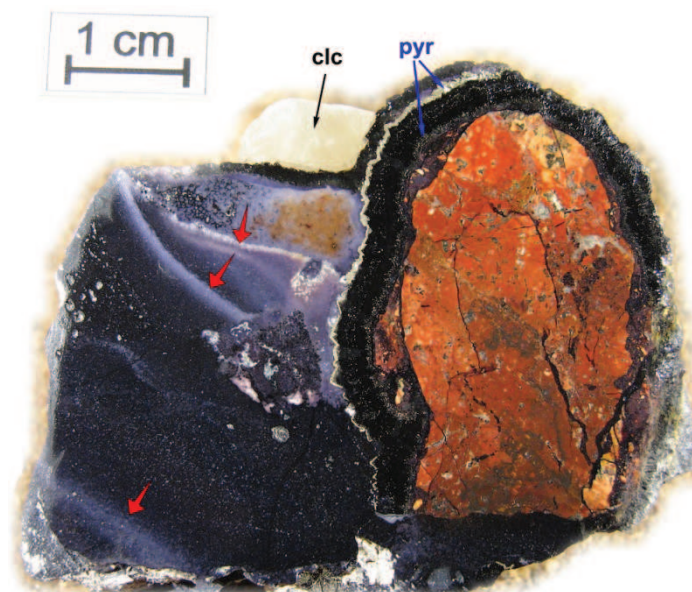


Fig. 2.59. A fragment of hematized dacite is overgrown by rhythmical crusts of dark-violet fluorite and pyrite (pyr). This aggregate was later cemented by “garbage” dark-blue fluorite interlaid with porcelain-like light-blue fluorite. Then that all was overgrown by thin dark-violet fluorite crust and calcite (clc). Mineralogical levels composed of porcelain-like fluorite are shown by red arrows. Central site of the Streltsovsky deposit. Sample St-176.

## 2. Mineralogy of the deposits

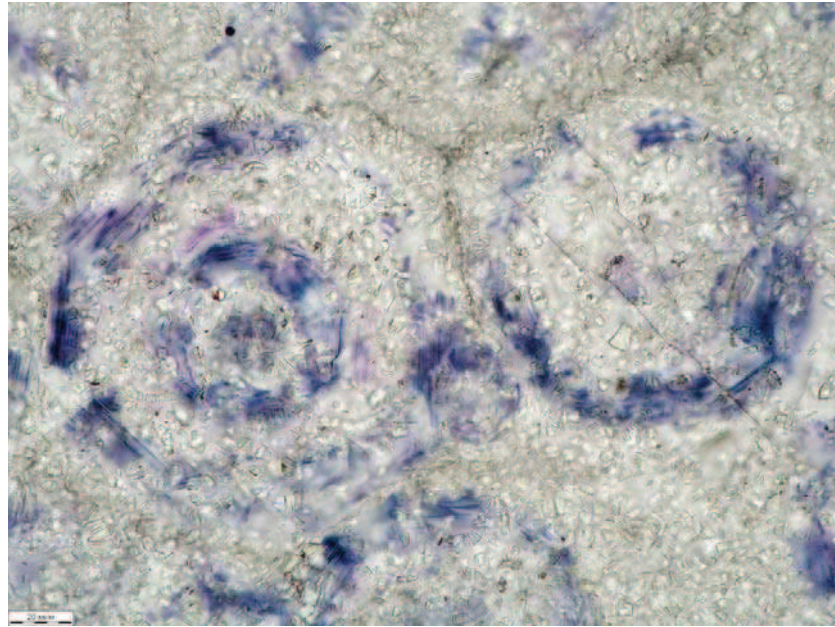


Fig. 2.60. Porcelain-like fluorite composed of grains of colorless, blue and pinky fluorite intensively impregnated by fine kaolinite flakes. Density of the latter is higher in outer parts of crystals and in intergranular space. Central site of the Streltsovsky deposit. Photomicrograph of thin-polished section St-176 in plane transmitted light. Scale bar – 20  $\mu\text{m}$ .

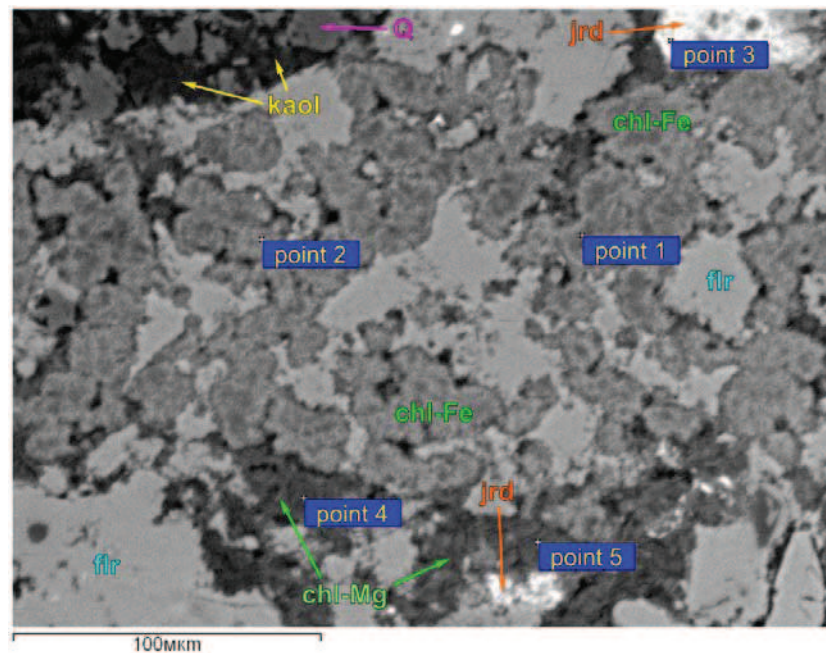


Fig. 2.61. Chlorite-fluorite aggregate with jordisite (jrd) segregations. Two chlorite generations are noticeable in fluorite (flr): more Fe-rich (chamosite, chl-Fe in the figure) and less Fe, more Mg (Fe-prochlorite, chl-Mg). Kaolinite (kaol) forms close intergrowth with quartz (Q). Central site of the Streltsovsky deposit. BSE image of thin-polished section St-176. Points of EDS analysis are shown.



## 2. Mineralogy of the deposits

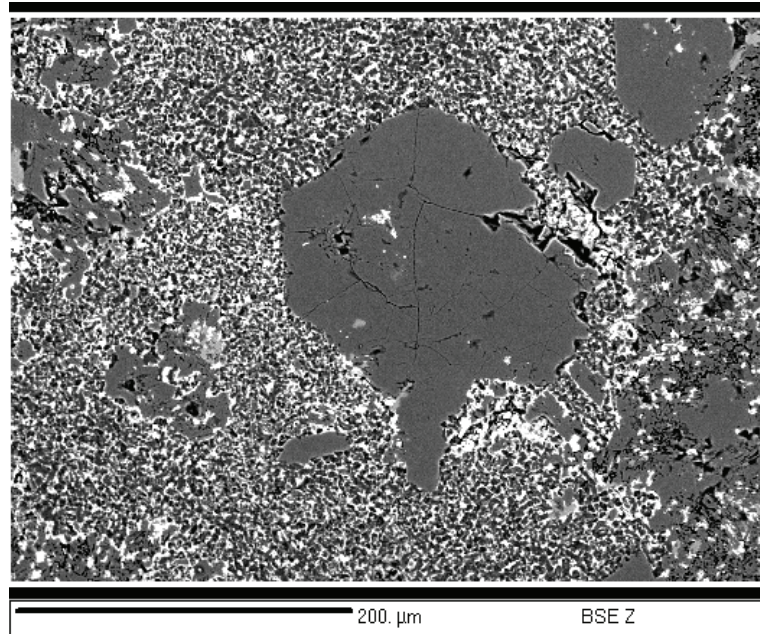


Fig. 2.62. Idiomorphic quartz crystals of the 2<sup>nd</sup> postore stage (grey) are partly resorbed and overgrown by fine chlorite-kaolinite aggregate. Chlorite (small white dots and flakes) is in tight even intergrowth with synchronous kaolinite individuals (fine grey phases) that testifies to their paragenesis. Antei deposit. BSE image of thin-polished section St-517a.

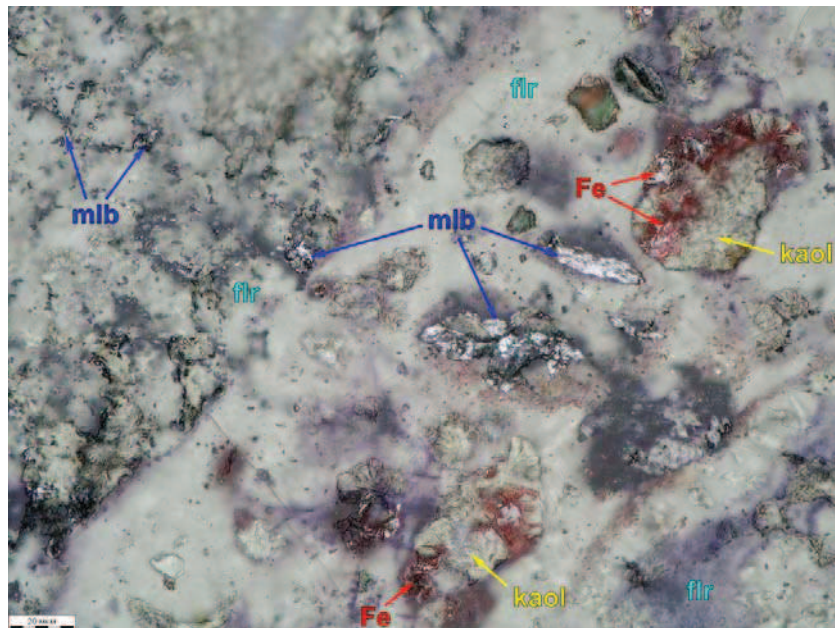


Fig. 2.63. Large flakes of molybdenite (mlb) are located in colorless, light-violet and pinky fluorite (flr). Similar fine molybdenite flakes occur in intergranular space of fine-grained fluorite in the upper left corner of the figure. Kaolinite segregations (kaol) are saturated with Fe oxides (Fe). Central site of the Streltsovsky deposit. Photomicrograph of thin-polished section St-176 in both transmitted and reflected plane light. Scale bar – 20  $\mu\text{m}$ .

## 2. Mineralogy of the deposits

---

Low-Fe sphalerite (cleophane with 0.8 wt.% Fe from microprobe data, Jeol JSM-5300, O.A.Doinikova) was detected between large kaolinite segregations. Cleophane was also observed in fluorite in similar positions to pyrite and molybdenite.

Baryte proved by microprobe was found as a veinlet of 10 µm thick crosscutting fluorite and kaolinite. Its position in the paragenetic chart was conditionally determined based on a presumption that it was formed after sulfides with an increase of oxygen fugacity.

Formation timing of zeolite and smectite is still obscure. Affiliation of these minerals with the 2<sup>nd</sup> postore mineral complex started from the assumption of O.V.Andreeva and V.A.Golovin (1998), which is based on difference of smectite-zeolite alteration developed in the vicinity of the Dal'ny deposit from illitization typical of the other SOF deposits. Smectite and zeolite were arbitrarily positioned as simultaneous minerals with kaolinite as an acidic analogue of the same type of alteration. The only proved relationship is postore Ca-zeolite formation (Fig. 2.23).

Calcite accomplishes mineralization of the 2<sup>nd</sup> postore stage. It is not as widespread as carbonate of the 1<sup>st</sup> postore stage and occurs in central part of veins and in cavities overgrowing fluorite and other minerals (Fig. 2.59).

### 2.3. Typomorphism of minerals

General features of minerals and their associations were described in the previous parts. Additional specific features of the most important or the most widespread minerals are the subject of this section.

#### 2.3.1. Pitchblende

Pitchblende is the main uranium mineral in the SOF deposits so it expectedly attracts the author's interest (Aleshin et al., 2002). It was studied using optical and scanning electron microscope with EDS analysis, electron microprobe analysis (electronic annex II), and ionic microprobe analysis.

The average contents of major and trace elements are represented in Table 2.4. Elements missed in the table are contained in amounts below the limit of detection (LOD). The total sampling on pitchblende composition includes all analyses of unaltered pitchblende located in different deposits and in different rocks. As pitchblende is usually replaced by the U-Si metagel with different intensity, increased Si contents have been detected in some of the



## 2. Mineralogy of the deposits

analyses of outwardly unaltered pitchblende. To avoid the influence of such data on the total sampling, analyses with Si content of above 0.5 wt.% were filtered out.

As shown in the table, the most significant trace elements in the pitchblende are Pb (as radiogenic lead), Ca, and Zr which concentrations exceed 1 wt.%. Other elements (As, Ti, Fe) are contained in less but reliably detected amounts (above 0.1 wt.%). Samarium concentrations are at the LOD while Si is actually absent (0.01 wt.% on average). Detectable quantities of the latter apparently are related to the superimposed U-Si metagel.

Analyses of particular samplings of the pitchblende grouped by the host rocks (basalts, dacites, granites) revealed clear dependence of trace element contents in the pitchblende from those in the related host rocks. As it appears from the results of statistical treatment of the samplings (Table 2.5), the concentrations of Ca, Zr, and Fe differ in different samplings. Comparison of contents of these elements in the pitchblende and in enclosing rocks revealed their strong correlation (Fig. 2.64, 2.65).

Table 2.4. The average contents of elements and the main statistical parameters of their distribution in the pitchblende (from the data of electron microprobe SX-50 and SX-100, in wt.%).

<b>Var</b>	<b>Vol</b>	<b>Dstrb</b>	<b>Min</b>	<b>Max</b>	<b>Avr</b>	<b>Stand</b>
<b>U</b>	995	norm.	59.0	83.3	78.33	2.02
<b>O</b>	995	norm.	8.9	13.0	12.10	0.42
<b>Pb</b>	995	norm.	0.0	18.9	1.77	0.30
<b>Ca</b>	995	norm.	0.1	2.1	1.44	0.33
<b>Zr</b>	995	norm.	0.0	2.5	1.19	0.56
<b>As</b>	963	norm.	0.0	1.0	0.48	0.16
<b>Ti</b>	995	norm.	0.0	1.0	0.20	0.14
<b>Fe</b>	995	norm.	0.0	1.0	0.17	0.11
<b>Sm</b>	30	norm.	0.0	0.3	0.12	0.10
<b>Si</b>	995	logn.	0.0	0.5	0.01	0.06
<b>Total</b>	995	norm.	81.0	100.4	96.03	1.70

Note: here and below: **Var** – variable (elements and Loss On Ignition), **Vol** – number of analyses, **Dstrb** – the most appropriate distribution law (norm. – normal, logn. – logarithmically normal), **Avr** – mean according to the distribution law (average for normal law and geometric mean for logarithmically normal law), **Stand** – standard deviation.

Local variations in the pitchblende composition have been studied by analyzing the aggregates of this uranium oxide by the electron microprobe. Heterogeneity in the composition was disclosed in numerous pitchblende aggregates. For example, the coarse-spherulitic pitchblende sampled in the Central site of the Streltsovsky deposit in the main ore-controlling fault no.41, has an extreme heterogeneity reflected in clear zonation. The latter is exhibited in the difference of pitchblende reflectance under the optical microscope and, more

## 2. Mineralogy of the deposits

clearly, by the different shades of grey in the BSE images (Fig. 2.66). The latter is caused by the variation of the average atomic number of the analyzed matter.

A detailed microprobe profile performed across the zoned pitchblende spherulites (the step is 17  $\mu\text{m}$ , 50 points in total) revealed a clear dependence between the brightness of the pitchblende in the BSE image from one side, and contents of trace elements (Ca, Zr, Fe, Ti, As) – from the other. As it is shown in Fig. 2.67 and 2.68, darker zones contain evidently higher concentrations of the trace elements mentioned above relative to the lighter ones. Lead concentrations do not depend on pitchblende brightness in the BSE image which additionally testifies to the radiogenic nature of this element in the pitchblende.

Table 2.5. The average contents of elements and the main statistical parameters of their distribution in the pitchblende grouped by the host rocks (from the data of electron microprobe SX-50 and SX-100, in wt.%).

Var	Rocks	Vol	Dstrb	Min	Max	Avr	Stand
<b>U</b>	basalts	33	logn.	76.5	83.3	79.5	2.3
	dacites	657	norm.	66.1	82.8	77.6	1.8
	granites	91	norm.	59.0	81.7	79.0	2.6
<b>O</b>	basalts	33	logn.	11.7	13.0	12.2	0.3
	dacites	657	norm.	8.9	12.8	12.1	0.4
	granites	91	norm.	9.3	12.8	11.9	0.9
<b>Pb</b>	basalts	33	logn.	1.4	2.6	1.9	0.3
	dacites	657	logn.	1.1	2.9	1.7	0.3
	granites	91	logn.	1.0	18.9	1.8	0.7
<b>Ca</b>	basalts	33	norm.	0.7	2.1	1.5	0.5
	dacites	657	norm.	0.1	2.1	1.4	0.2
	granites	91	norm.	0.5	1.6	1.0	0.2
<b>Zr</b>	basalts	33	logn.	0.0	1.4	0.1	0.4
	dacites	657	norm.	0.2	2.5	1.4	0.5
	granites	91	logn.	0.5	2.2	1.2	0.4
<b>As</b>	basalts	27	norm.	0.0	0.5	0.2	0.1
	dacites	654	norm.	0.0	0.9	0.5	0.2
	granites	80	logn.	0.1	0.8	0.4	0.1
<b>Ti</b>	basalts	33	logn.	0.1	0.7	0.29	0.16
	dacites	657	norm.	0.0	1.0	0.22	0.13
	granites	91	logn.	0.1	0.9	0.29	0.16
<b>Fe</b>	basalts	33	norm.	0.0	1.0	0.3	0.2
	dacites	657	norm.	0.0	0.5	0.2	0.1
	granites	91	norm.	0.0	0.6	0.1	0.1
<b>Sm</b>	basalts	6	norm.	0.0	0.2	0.12	0.09
	dacites	3	norm.	0.2	0.3	0.27	0.07
	granites	11	logn.	0.0	0.2	0.01	0.06
<b>Si</b>	basalts	33	norm.	0.0	0.5	0.2	0.2
	dacites	657	logn.	0.0	0.5	0.0	0.1
	granites	91	norm.	0.0	0.3	0.1	0.1

## 2. Mineralogy of the deposits

Another conclusion consists of the regular change of contents of the trace elements with the growth of the spherulites. As is exhibited in Fig. 2.67, Zr concentrations generally increase with time while Ca contents are stable or slightly decrease. On the background of

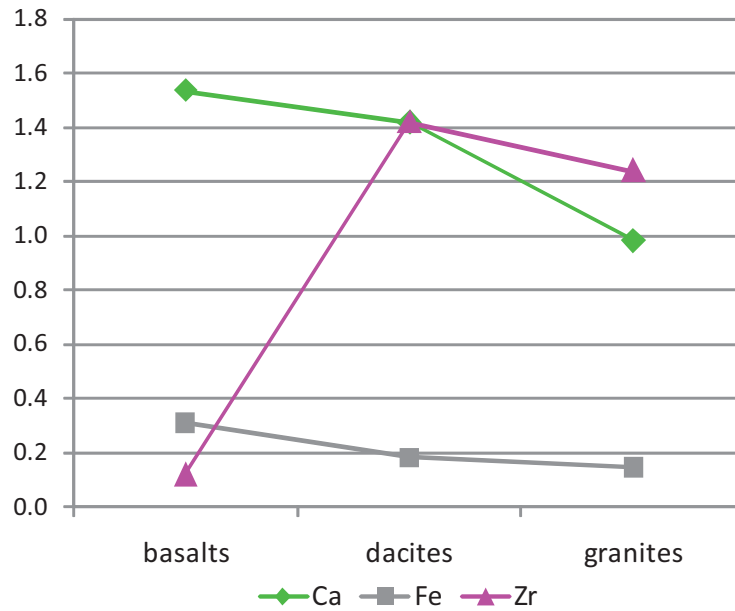


Fig. 2.64. The average contents of Ca, Zr, and Fe in pitchblende located in different rocks (basalts, dacites, granites). Data from electron microprobe analysis (in wt.%).

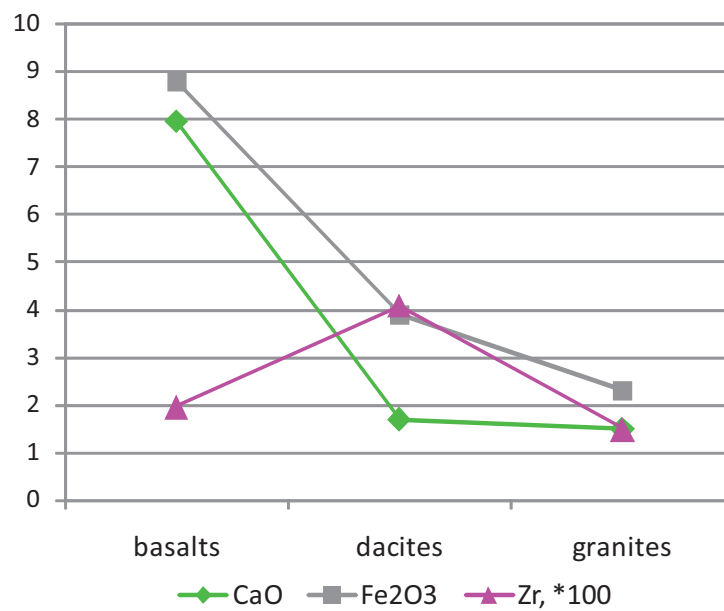


Fig. 2.65. The average contents of Ca, Zr, and Fe in the least altered host rocks of the SOF deposits (basalts, dacites, granites). Data from ICP-AES and XRF analyses (in ox.%).

## 2. Mineralogy of the deposits

these gradual changes, Ca and Zr concentrations demonstrate particular fluctuations due to fine zonation of the spherulites. Iron and titanium concentrations clearly decrease with time whereas As firstly decreases in content but then begins to increase (Fig. 2.68).

Besides giving an indication on the evolution of the ore-forming fluid, regular variations in trace element content evidence their primary accumulation in the pitchblende. Strict coincidence of local variations of these elements only with primary heterogeneities of the pitchblende (with its zonation), also corroborates this conclusion.

Rare earth elements occurred as another informative typomorphic feature indicating possible uranium source for the SOF deposits. It will be considered below.

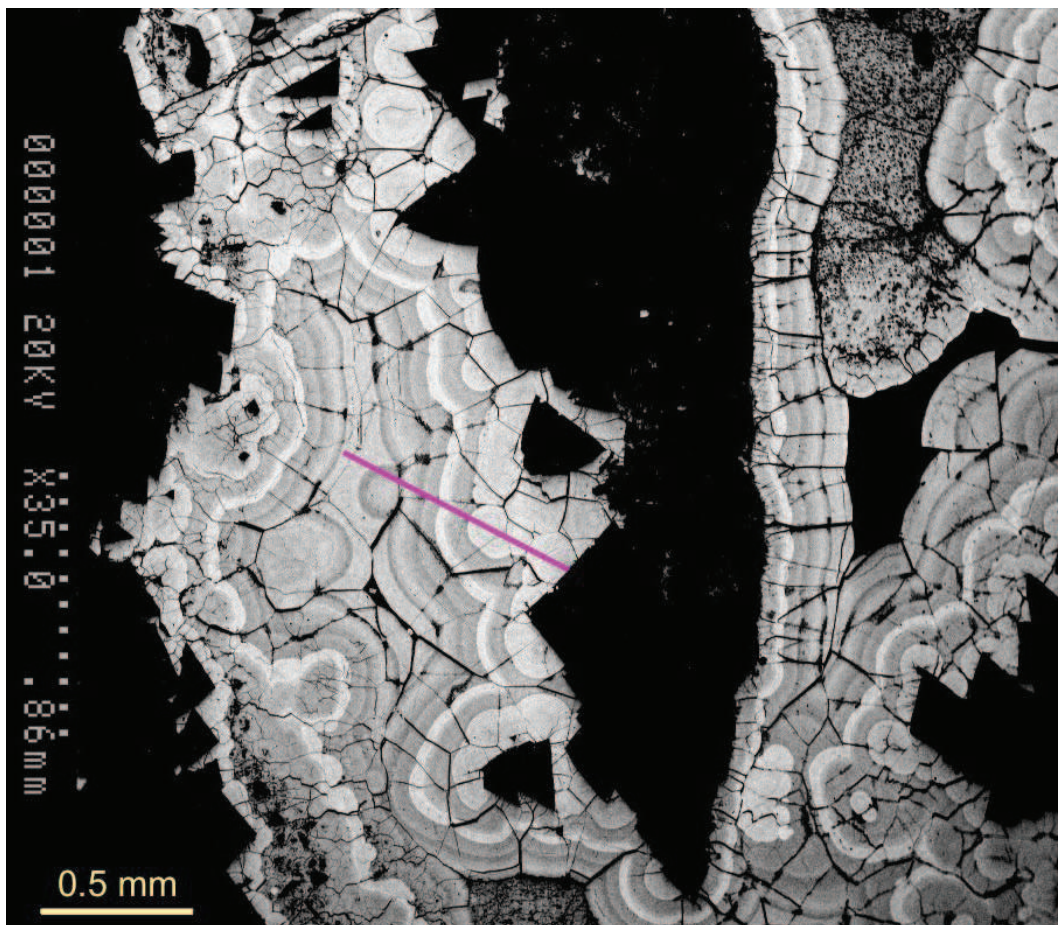


Fig. 2.66. Aggregate of the zonal coarse-spherulitic pitchblende (different shades of grey) overgrown fluorite crystals and fragments of dacites (black). Magenta line – a profile of electron microprobe analysis presented in Fig. 2.67 and 2.68. Central site of the Streltsovsky deposit. BSE image of thin-polished section St-77c. SEM Hitachi S-2500.



## 2. Mineralogy of the deposits

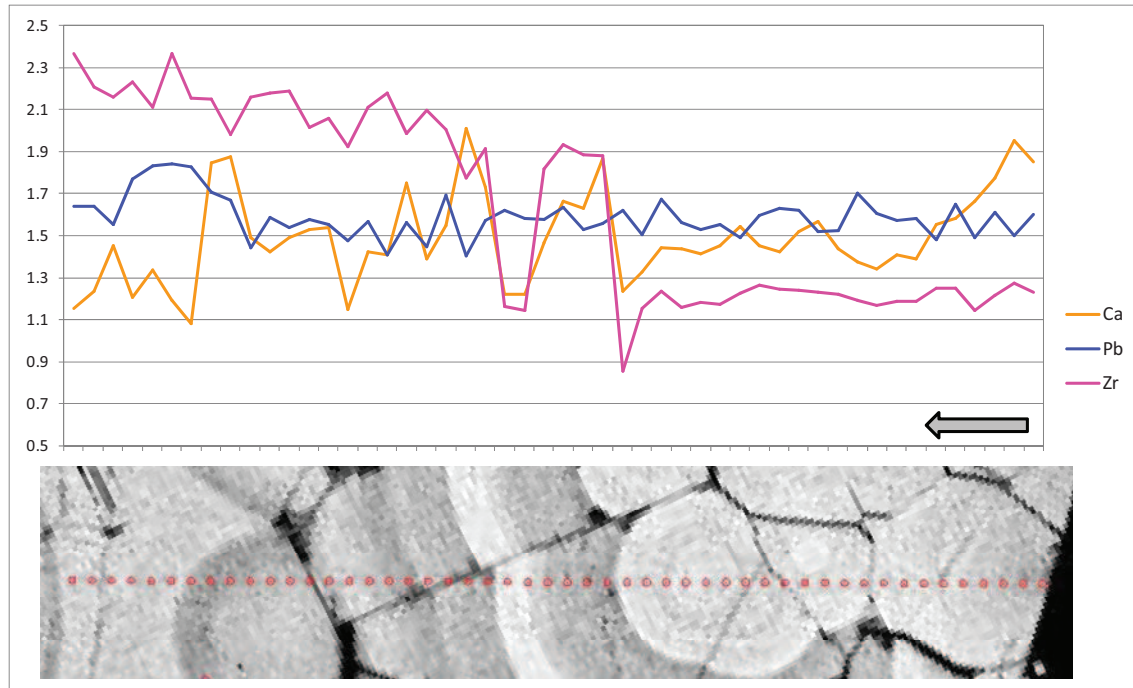


Fig. 2.67. Contents of Ca, Pb, and Zr (in wt.%) along the profile of electron microprobe analysis shown in Fig. 2.66. The detailed BSE image along the profile is shown in the low part of the figure. The direction of the pitchblende growth is indicated by an arrow.

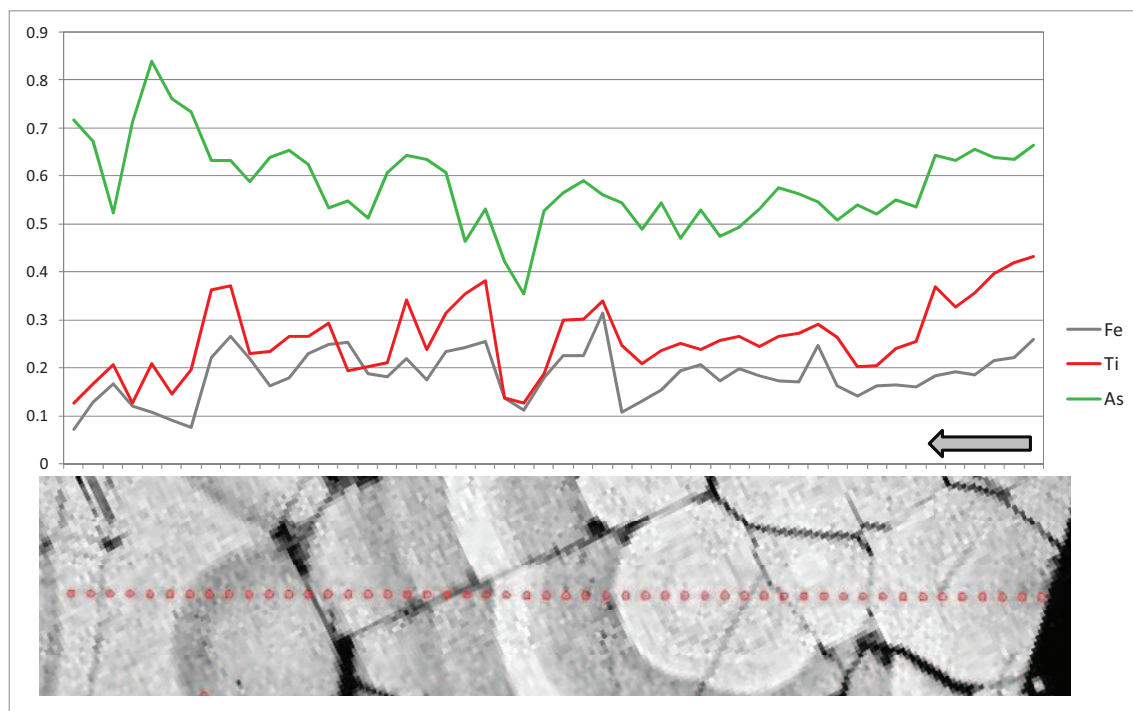


Fig. 2.68. Contents of Fe, Ti, and As (in wt.%) along the profile of electron microprobe analysis shown in Fig. 2.66. The detailed BSE image along the profile is shown in the low part of the figure. The direction of the pitchblende growth is indicated by an arrow.

## 2. Mineralogy of the deposits

### 2.3.2. U-Si metagel

This U-Si phase was firstly described in the SOF deposits by the author as a primary metacolloid which previously was known as a crystalline coffinite. Numerous observations of so-named “coffinite” under the microscope have not revealed any crystalline shape of its segregations. Instead, widespread fissures of shrinkage, polyphase composition (Fig. 2.50) and primary colloform textures (Fig. 2.51) were established (Aleshin et al., 2006<sub>2</sub>). It forced the author to provide additional detailed investigation of this phase to clarify its nature.

Composition. Plentiful electron microprobe analyses revealed that Ca is the only dopant in the U-Si metagel. Its contents permanently exceed 1 wt.%. Aluminium was detected in the phase sporadically, other elements (P, Pb, Fe, Zr) are present in even less amounts. The average composition of the U-Si metagel is represented in Table 2.6.

Table 2.6. Average composition of the U-Si metagel from the data of electron microprobe analysis (in wt.%).

Var	Vol	Dstrb	Min	Max	Avr	Stand
U	293	norm.	18.0	76.5	58.60	8.88
O	293	norm.	7.3	28.2	17.71	3.25
Si	293	norm.	0.2	14.0	6.71	2.92
Ca	293	logn.	0.6	31.0	2.01	1.75
Al	293	norm.	0.0	3.8	0.67	0.44
P	44	norm.	0.0	0.7	0.23	0.19
Pb	293	logn.	0.0	5.1	0.11	0.50
Fe	293	logn.	0.0	14.0	0.11	0.76
<b>Total</b>	293	norm.	41.7	96.8	88.99	6.52

Proportions between U, Si, and Ca concentration are shown in the ternary diagram in Fig. 2.69. As it results from the diagram, the U-Si metagel has extremely wide variation in U and Si contents. Their ratios (in at.%) change from approximately 50:1 to 1:3. No breaks in this range are observed. Such tremendous variations in composition indirectly testify to the colloidal nature of this substance.

Calcium is generally contained in the U-Si phase in the amounts of up to 25 at.%. Several analyzed phases have extremely high Ca concentrations. They cannot be attributed to carbonate impurities because the total of the analyses does not show any decrease compared

## 2. Mineralogy of the deposits

---

to neighbour points with lower Ca contents. This indicates rare but considerable prevalence of Ca over U and Si in the U-Si metagel.

Color. Usually the U-Si metagel has dark-brown to brown color which is also typical of coffinite. Rarely a dark-green color, or alternating brown and green fine zones were observed (Fig. 2.70). Sometimes green varieties of the metagel are richer in uranium compared to brown ones but it is not a general rule.

In local sites of the high-grade uranium ore bodies, orange and yellow varieties of the U-Si metagel have been found. Becquerelite was identified once in a rich ore body associated with the yellow U-Si metagel (Fig. 2.42, 2.43). In some cases the color of the U-Si metagel may change from yellow to brown in an individual segregation (Fig. 2.71). No dependence between the color and contents of U, Si, and Ca in the U-Si metagel was established. It allows the conclusion that the only reason for the color change from brown or green to yellow is the change of U valency from  $U^{4+}$  to  $U^{6+}$ .

As it was discussed above, local oxidation due to water radiolysis is the only possible reason for orange and yellow color of the U-Si metagel. These observations indicate that the locality of oxygen influence on mineral aggregates may be less than a millimeter.

Fine structure. The conclusion about primary colloidal state of the U-Si metagel is based on sufficient but indirect evidence mentioned above. To resolve this question definitely, a study of the phase structure was provided.

X-ray diffraction of the U-Si metagel fragments has been fulfilled in IGEM. It revealed the absence of crystalline lattice in the analyzed samples. However as is known, XRD may not detect partly disordered lattice while electron microdiffraction can reveal it.

High-resolution transmitting electron microscopy (HRTEM) with EDS analysis has been performed in UHP using Philips CM-20 microscope (analyst Jaafar Ghanbaja). Chemical composition was determined by energy dispersive X-Ray spectroscopy (EDXS). EDX spectra were recorded by means of an PGT spectrometer mounted on the microscope operated at 200 kV and equipped with an ultrathin window X-Ray detector. The analyses were carried out in nanoprobe mode with a diameter of the probe of 10 nm. Lattice parameters were calculated from microdiffraction images in the Laboratory of electron microscopy (IGEM) by Anatoly Sivtsov.

A segregation of the U-Si metagel from the Antei deposit located at the horizon +62 m (600 m from the surface) has been studied. This segregation, adjacent and similar to that shown in Fig. 2.51, was picked out from thin-polished section St-501 with a diamond needle.

## 2. Mineralogy of the deposits

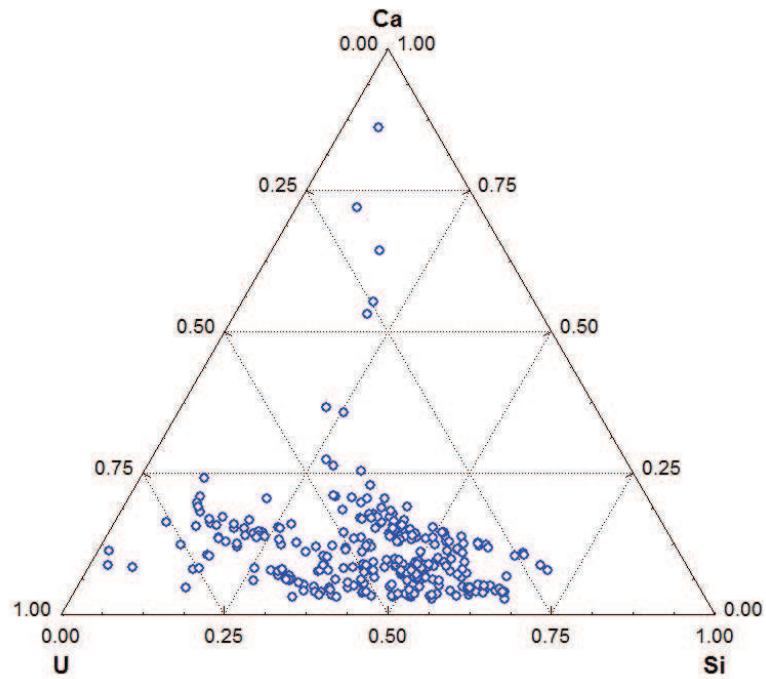


Fig. 2.69. Ternary diagram of U, Si, and Ca contents in the U-Si metagel (from the data of the electron microprobe analysis, in at.%).

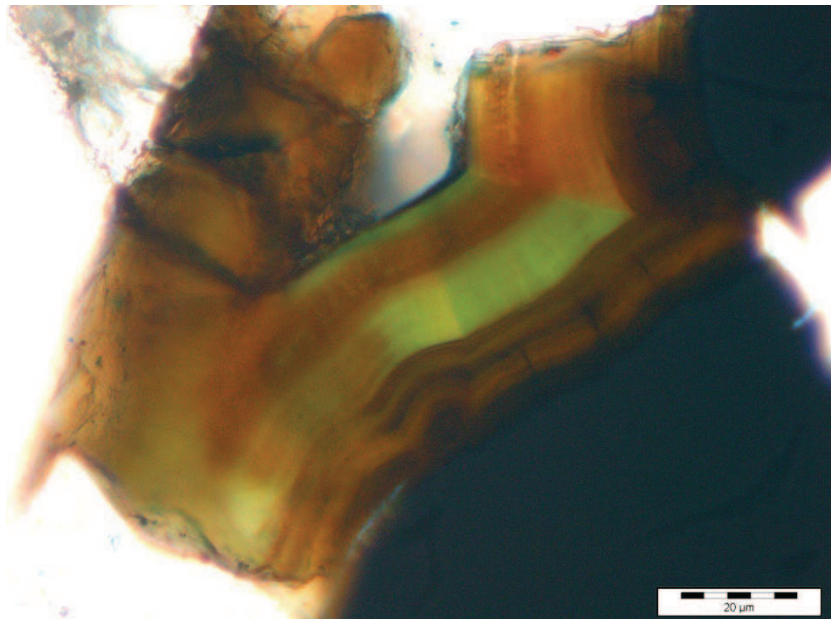


Fig. 2.70. Thin crust of the U-Si metagel grown on the pyrite grain (black). Alternating of brown and green zones in the metagel is visible. Antei deposit. Photomicrograph of thin-polished section St-501 in plane transmitted light.



## 2. Mineralogy of the deposits

---

The fragments were crushed between glass plates to powder state and were applied onto the copper grid of the microscope object holder.

The study revealed that the majority of the investigated particles were amorphous, with the “orange-skin” globular structure of the surface typical of metacolloid substances. Microdiffraction produced wide diffuse halos (Fig. 2.72). However, some of the particles contain numerous ultrafine crystallites of 3-5 nm in size. Individual crystallites reach 20 nm. Microdiffraction established the sharp predominance of ring reflexes of cubic  $\text{UO}_2$  phases and rare point reflexes belonging to coffinite (Fig. 2.73). It allows the presumption that numerous ultrafine crystallites are uraninite while larger individual crystallites (15-20 nm) may be identified as coffinite.

Thus, this study concludes that the U-Si phase, being the second most abundant uranium mineral in the SOF deposits, is not a real coffinite. It is a primary metagel of U-Si composition with permanent admixture of Ca. Large variation in the U:Si ratios evidently reflects primary concentrations of these elements in the colloidal solution. Upon dehydration of the U-Si gel, fissures of shrinkage have been formed. The excess of uranium in some of U-rich varieties of the U-Si metagel began to crystallize as fine nuclei of uraninite and rarely coffinite.

### 2.3.3. *Micas*

Illitization in the SOF deposits has been thoroughly studied by O.V.Andreeva, V.A.Golovin, G.T.Volostnukh and other researches. However, the composition and structure of micas were studied mainly by wet chemistry and XRD after mica extraction from whole-rock samples. These approaches let the precise determination of complete composition of micas and their structure but evidence nothing about temporal relationships of investigated micas with other minerals. In other words, very little reliable information for paragenic analysis could be taken from these studies.

For determination of the composition of micas *in situ*, electron microprobe analysis was used. The author is aware that this method does not allow reliable definitions of micas as it does not provide data on their structure. However, it is possible to differ main light micas in the SOF by composition: illite is the richest in K (up to 7-8 wt.%), mixed-layered illite-smectite contains K between these maximum values and 0 wt.%. There are two K-free micas – kaolinite (dikkite) and smectite. They differ from each other by the Al:Si ratios which should be around 1:1 (in at.%) for kaolinite-dikkite and 1:2 for smectite. Usually they

## 2. Mineralogy of the deposits

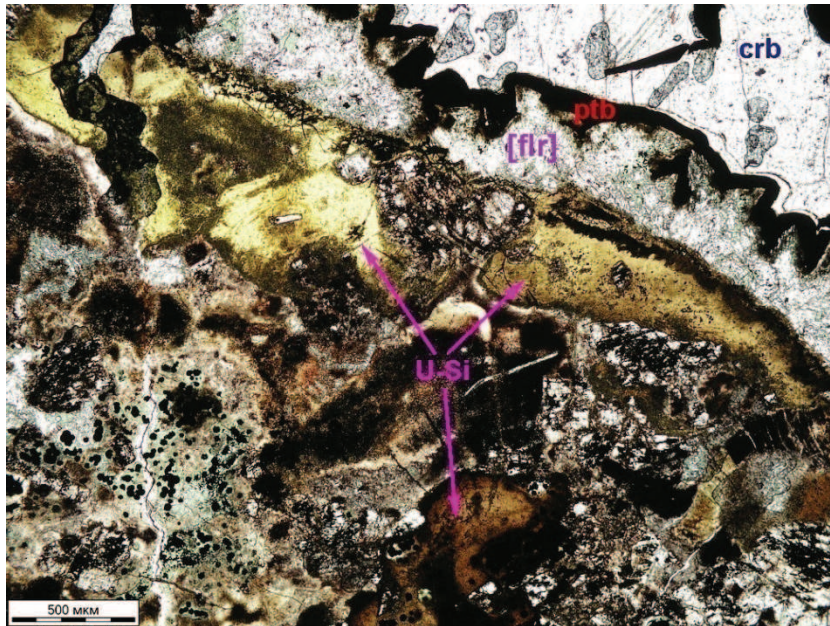


Fig. 2.71. Different colors of the U-Si metagel (U-Si) – light-yellow, light-brown and dark-brown – in neighbouring segregations. Exocontact zone of the pitchblende veinlet (ptb) with calcite (crb) and former fluorite ([flr]). The latter was completely replaced by chlorite-carbonate aggregate during the 1<sup>st</sup> postore stage. High-grade ore body in the Oktyabrsky deposit. Photomicrograph of thin-polished section St-220-3 in plane transmitted light.

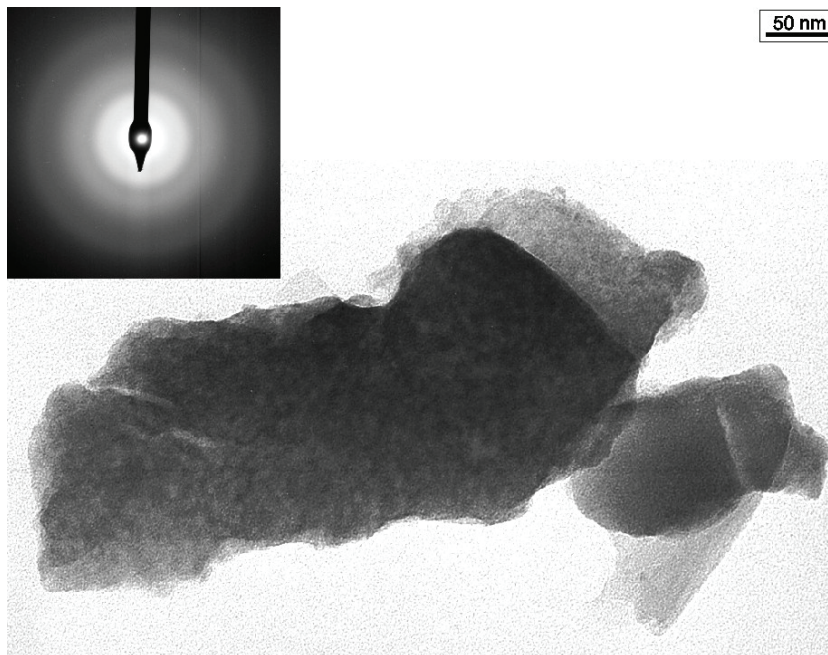


Fig. 2.72. Amorphous particles of the U-Si metagel with diffused microdiffraction halos. HRTEM image in bright field.

## 2. Mineralogy of the deposits

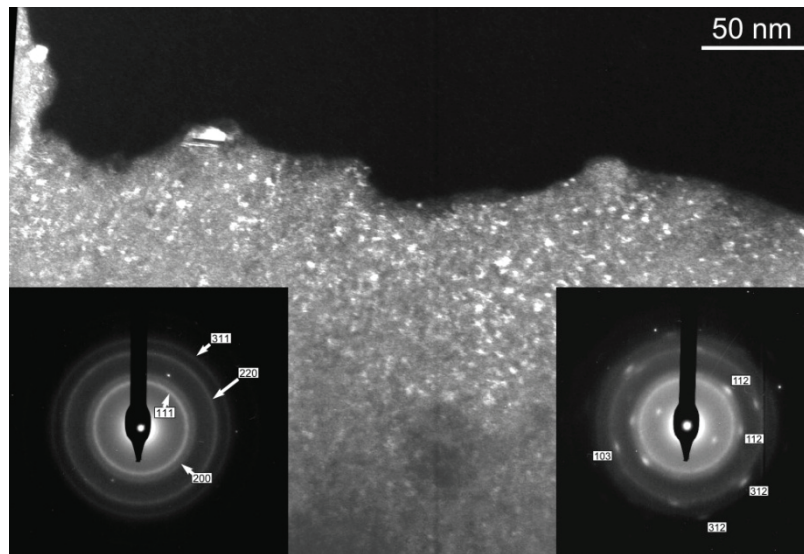


Fig. 2.73. A particle of the U-Si metagel saturated with fine (3-5 nm) crystallites of uraninite (ring reflexes in the left insertion) and a larger crystallite of possibly coffinite (point reflexes in the right insertion). HRTEM image in dark field (crystalline phases are bright).

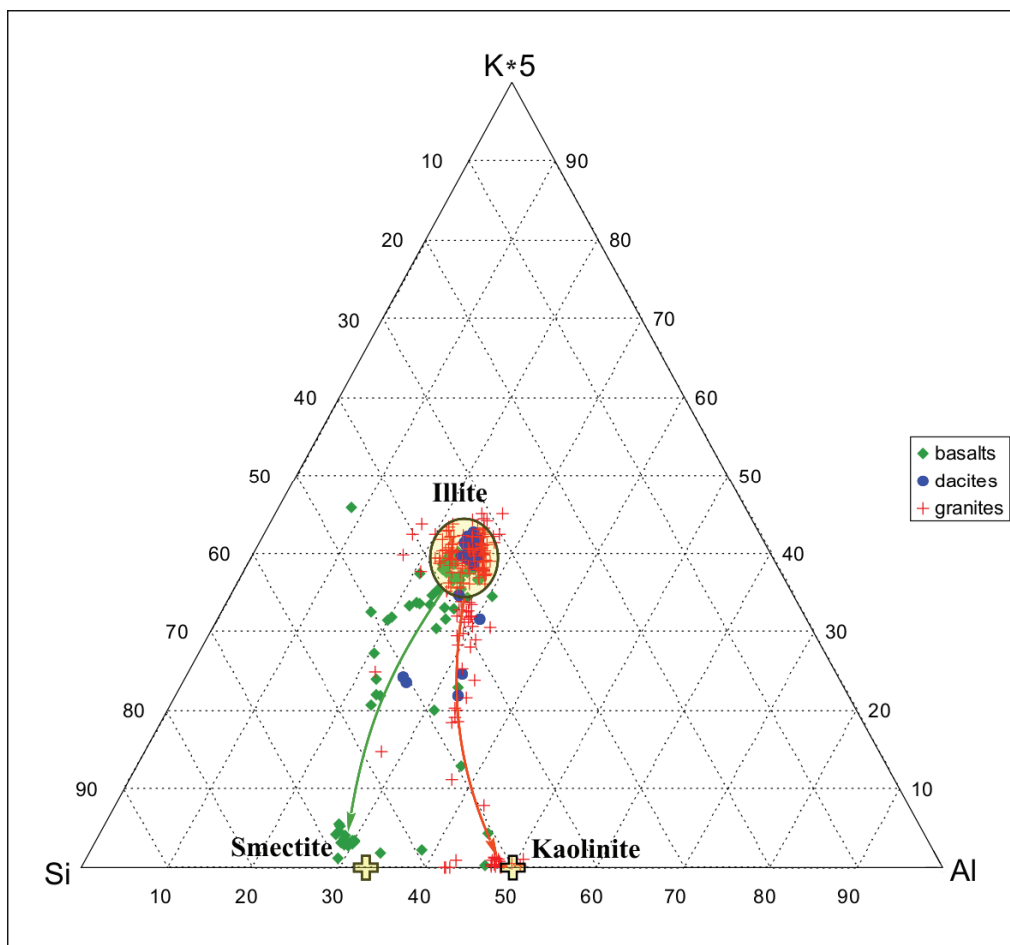


Fig. 2.74. Composition of light micas located in different rocks (from electron microprobe data, in at.%). Figurative points of normative composition of smectite and kaolinite are indicated by yellow crosses, and illite – by an oval. Trends of the composition change are shown by arrows.

## 2. Mineralogy of the deposits

---

may be distinguished by the morphology of their aggregates: well-defined relatively short-prismatic flakes are typical of kaolinite while smectite is characterized by fine poorly organized flakes.

The results of electron microprobe data on mica composition located in different rocks (basalts, dacites, granites) are exhibited in the ternary diagram (Fig. 2.74). Potassium contents are multiplied by 5 for better recognition. As it follows from the diagram, illite is the most widespread mica that is present in all the types of rocks. Pure kaolinite predominates in granites while smectite is the most abundant in basalts. Micas of intermediate compositions are traced between illite and smectite, and illite and kaolinite likely designating mixed-layered varieties. A narrow group of four points located between kaolinite and smectite probably indicates a mixed-layered smectite-kaolinite variety. However, this preliminary conclusion requires additional structural investigations.

Metasomatic zonation in terms of mica composition was studied in the basalts of the Streltsovsky deposit. Bleached zones of approximately 1 cm thick, superimposed on hematized basalts in the peripheral parts of the ore body, contain illite-cryptocrystalline veinlets in their central parts (Fig. 2.17). Background slightly altered basalts, as well as hematized basalts, are characterized by illitized and carbonatized groundmass, by phenocrysts completely replaced by quartz, carbonate and chlorite, and by leucoxenized Ti-magnetite while ilmenite remains partly stable. The bleached basalts demonstrate a higher intensity of silicification, carbonatization and illitization; ilmenite is completely replaced by leucoxene as well as Ti-magnetite.

Electron microprobe analysis revealed pure illite composition of light mica in the central cryptocrystalline quartz veinlets. Relatively large-flaked mica with a high birefringence (up to the 3<sup>rd</sup> order) has the highest K and Fe contents (up to 8 and 5.5 wt.% respectively) (Fig. 2.75). Mica in the bleached zones is represented by the mixed-layered illite-smectite with K content being in the range of 1-3 wt.%. Iron concentrations in the illite-smectite are also lower than in the illite of the quartz veinlets (0.5-2 wt.%). Background basalts located at the distance of 1-2 cm apart from the quartz veinlet, are characterized by pure smectite or by low-K illite-smectite with K contents falling in the range 0.5-1 wt.%. Iron concentrations are about the same as in the illite-smectite of the bleached basalts.

Thus, an evident metasomatic zonality expressed in the regular change of mica composition at the distance of 1-2 cm has been established in the basalts. In contrast to the basalts, no regular tendencies in the mica composition regarding the distance from fractures



## 2. Mineralogy of the deposits

---

and veinlets, were observed in dacites and granites. This may arise from known buffering properties of basalts concerning acidic fluids.

### *2.3.4. Chlorites*

Similar to micas, chlorite composition was studied in different deposits located in different rocks. The results of the electron microprobe analysis were plotted on the Winchell-Tröger diagram. This diagram reflects proportions between the marginal members Si and Al, and Fe and Mg (antigorite–Fe–antigorite–daphnite–amesite) and requires the calculation of figurative points of chlorite composition from element concentrations in at.%. Following the diagram (Fig. 2.76), chlorites developed in the SOF deposits occupy a wide range along the Mg-Fe axis (from Mg-prochlorite-delessite to Fe-chamosite) and rather narrow area in the Si-Al direction.

Analysis of the chlorite composition regarding host rocks reveals the following dependence. Despite overlapping of the areas occupied by chlorites from different rocks, it is noticeable that chlorites from basalts are the most Mg-rich ones – from Mg-prochlorite to Fe-prochlorite with the average in the Fe-prochlorite field. Chlorites hosted by dacites are richer in Fe, they span from prochlorite to the most Fe-rich chamosite. However, their average is also located in the Fe-prochlorite field but further towards Fe-rich varieties relative to those from basalts. Chlorites developed in granites are the richest in Fe, they vary from the most Fe-rich varieties of Fe-prochlorite to chamosite. Their average is located essentially higher than even that of chlorites from dacites, and slightly towards the Al side of the diagram. A separate group of Mg-rich compositions is formed by chlorites pseudomorphously replaced biotite in granites. In this case, Mg apparently was inherited from biotite which is richer in Mg than chlorite. The average Mg:Fe ratio for biotite from granites is 3 times as much as for chlorite from these rocks (0.31 and 0.1 respectively).

Thus, the study of chlorite compositions in the SOF revealed its dependence on host rocks. Granites contain the most Fe-rich chlorites while basalts are characterized by the Mg-rich varieties. Chlorites located in dacites are intermediate in composition. This is evidence fluid-rock interaction during the hydrothermal alteration.

### *2.3.5. Fluorite*

Fluorite is a mineral widespread in many deposits of different types. It is well-known, along with many other features, because of its ability to concentrate REE and other doped

## 2. Mineralogy of the deposits

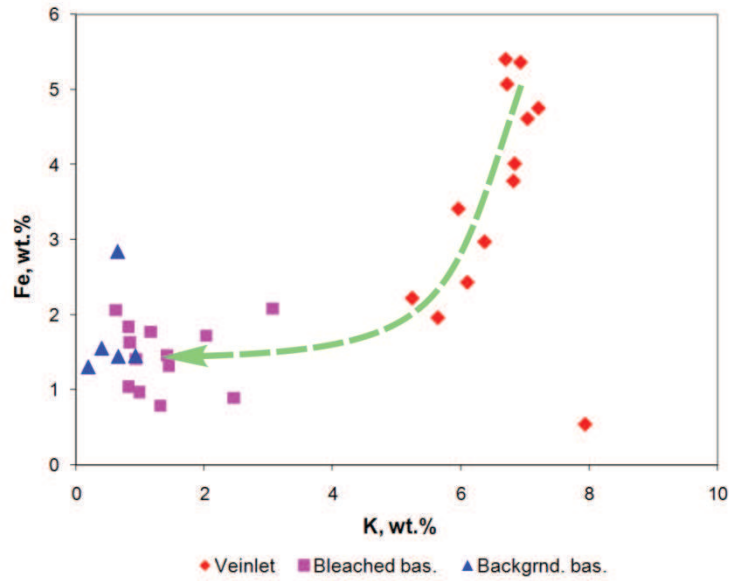


Fig. 2.75. Composition of light micas in the quartz veinlet, bleached basalts and background basalts (from the data of electron microprobe analysis, in wt.%). Western site of the Streltsovsky deposit, sample St-139.

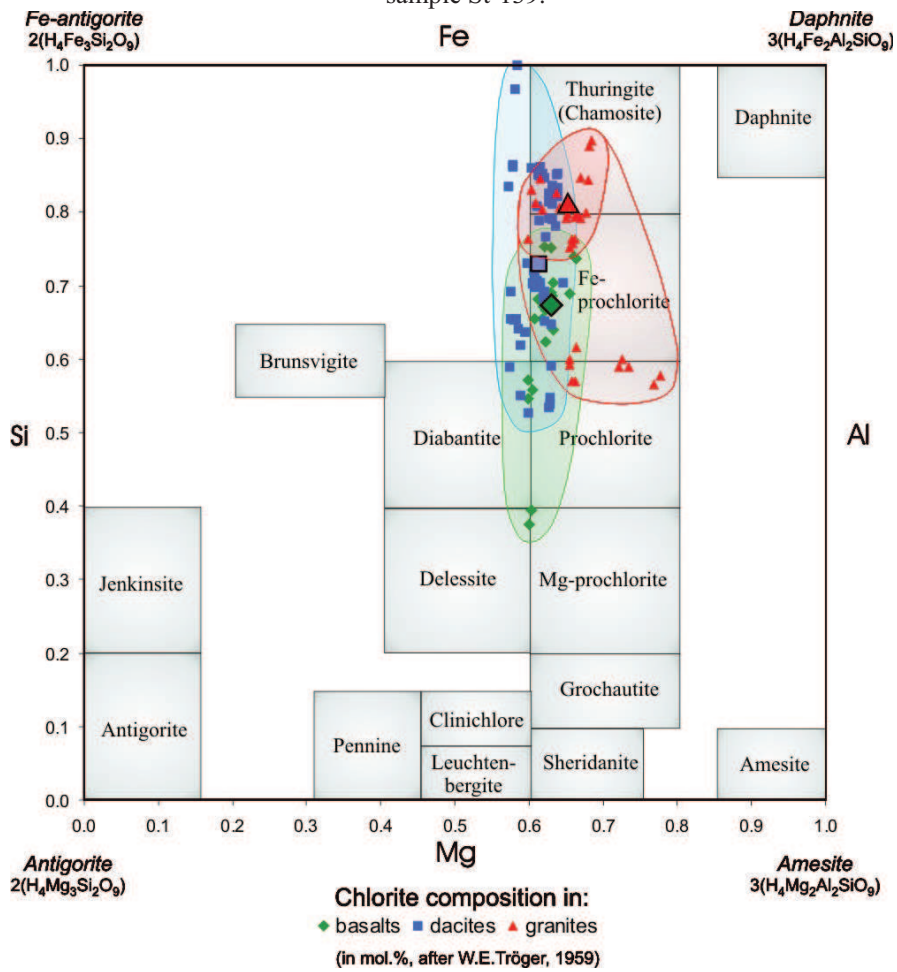


Fig. 2.76. Composition of chlorites developed in the SOF deposits in different rocks (from electron microprobe analyses, calculated from at.%) plotted on the Winchell-Tröger diagram (Tröger, 1959). Large symbols denote the average compositions of chlorites located in the appropriate rocks.

## 2. Mineralogy of the deposits

---

elements in its crystal lattice and to luminesce under X-ray and photo (UV) excitation. REE partitioning in fluorite can provide important geochemical information concerning physico-chemical conditions of mineral assemblage formation and matter source. An attempt to reveal dependencies between luminescence spectra of fluorite at the Streltsovsky deposit and uranium concentration in sites of sample location, as well as difference of spectra of fluorite sampled in two fluorite deposits, has been provided using the X-ray (XRL), cryophoto (CPL) and laser-excited (LEL) luminescence technique by Victor Rassulov (VIMS, Moscow).

Experimental methods and samples. Luminescence spectra of fluorite are rather complex due to great number of lines of different optical centers caused mainly by dopant of REE with different valence, charge compensators, local symmetry, superposition and sensibilization (redistribution of energy between different optical centers) and so on. Intensities of spectral lines reflect concentrations of optical centers which, in turn, depend on REE content in fluorite lattice. Apart from bulk sample analysis (ICP-MS, XRFS and others), only REE incorporated in crystal lattice, i.e. syngenetic with fluorite, are detectable by luminescence. Another important difference is that many REE can be characterized by their valence, site coordination in lattice, compensators and so on which provides additional information about formation conditions (pH, Eh, temperature).

XRL spectra were obtained in VIMS using a device consisted of X-ray source IRIS-3m, the tube 5BXV-7 (Re cathode, voltage 40 kV, current 30 mA), MDR-23 monochromator in combination with FEU-100 photomultiplier. Registration system is based on a photon counting method with data recording on a PC. More than 80 spectral lines are detectable. Most informative among them are the following: wide peak of proper fluorite luminescence induced by hole-type  $V_k$  center, line of doped  $Gd^{3+}$  center at 313 nm ( $Gd_{313}^{3+}$ ),  $Ce_{340}^{3+}$ ,  $Tb_{380}^{3+}$ ,  $Eu_{420}^{2+}$ ,  $Dy_{475}^{3+}$ ,  $Er_{540}^{3+}$ ,  $Sm_{565}^{3+}$ ,  $Sm_{604}^{3+}$  and  $Dy_{670}^{3+}$ . Spectra were measured without correction on hardware function which produced a shift of wide  $V_k$  peak from its usual position at 290 nm to around 350 nm.

Cryophotoluminescence was induced by UV light from a quartz lamp at the liquid nitrogen temperature (77K). It allows the detection of not only  $Eu^{2+}$  and  $Sm^{2+}$  luminescence but also  $Yb^{2+}$ . Intensity of the  $Sm^{2+}$  line ( $I(Sm^{2+})$ ) increases 10 times relative to room temperature. Use of a microscope-based registration system enabled CPL spectra from samples of 50-100  $\mu m$  in size to be obtained.

## 2. Mineralogy of the deposits

---

Laser-excited luminescence is induced by UV nitrogen laser LGI-505 ( $\lambda_{\text{exc}} = 337.1$  nm). The device is built up on the base of microspectrofluorimeter MSFU L-312 and include CAMAC registration block with data recording on a PC. Probe size is the same as for CPL. Spectral lines of  $\text{Eu}^{2+}$ ,  $\text{Dy}^{3+}$ ,  $\text{Sm}^{3+}$ ,  $\text{Eu}^{3+}$ ,  $\text{Tb}^{3+}$  and  $\text{Er}^{3+}$  could be detectable.

Fluorite samples from the Streltsovsky deposit, the Gozogor fluorite deposits located 5 km west of the Streltsovsky deposit, and the Abagaityi fluorite deposit located 20 km south of the SOF were investigated.

At the Streltsovsky deposit, fluorite of the 1<sup>st</sup> postore stage was sampled from veinlets at different distances from the large fault controlling the rich ore body in trachydacites: sample St-77 – 0 m, St-80 – 0.5 m, St-89 – 5 m, St-85 – 12 m. Correspondingly, U content in sample locations differs: St-77 – 8%, St-80 – 2.7%, St-89 – 1.36%, St-85 – 0.6%. Besides these, 3 samples located in basalts in the vicinity of the ore body controlled by a large fault passing down to granites of the caldera basement were investigated. Fluorite of the 1<sup>st</sup> postore stage is characterized by dark-violet (to black) color with rare thin zones of light-violet and blue color. One fluorite sample of the 2<sup>nd</sup> postore stage of light-yellow color was also studied (St-174).

Fluorite from the Gozogor deposit is uncolored while fluorite from the Abagaityi deposit composes zonal vein with zones of different tints of green and light-violet color.

Results and discussions. Chondrite normalized REE partitioning in fluorite was determined by ICP-MS (CRPG, Nancy, France) (electronic annex III). It differs for different deposits and generations. Fluorite of the 1<sup>st</sup> postore stage from the Streltsovsky deposit is characterized by distinct predominance of medium REE (MREE – Sm, Eu, Gd) relatively to heavy REE (HREE) and, more over, light REE (LREE) (Fig. 2.77a). REE patterns in post-ore fluorite have similar tendencies but are not so distinct (Fig. 2.77b). Fluorite from the Gozogor deposit is distinguished by low overall REE content with some abundance in LREE (Fig. 2.77c). A distinguishing feature of the fluorite from the Abagaityi deposit is the evident negative Eu anomaly (Fig. 2.77d).

In contrast to uncolored and light fluorite, dark-violet fluorite of the 1<sup>st</sup> postore stage exhibits quenched XRL spectra sometimes at the noise level (Fig. 2.78a). This made it necessary to decolorize samples in order to increase intensities ( $I$ ) of REE lines and to make spectra of different fluorite samples comparable. Ignition at 550 °C during 1 hour in the air was used. All samples were decolorized without marked destruction. After ignition,  $I(\text{REE})$  increased more than an order of magnitude keeping ratios between them constant (Fig. 2.78a,b).



## 2. Mineralogy of the deposits

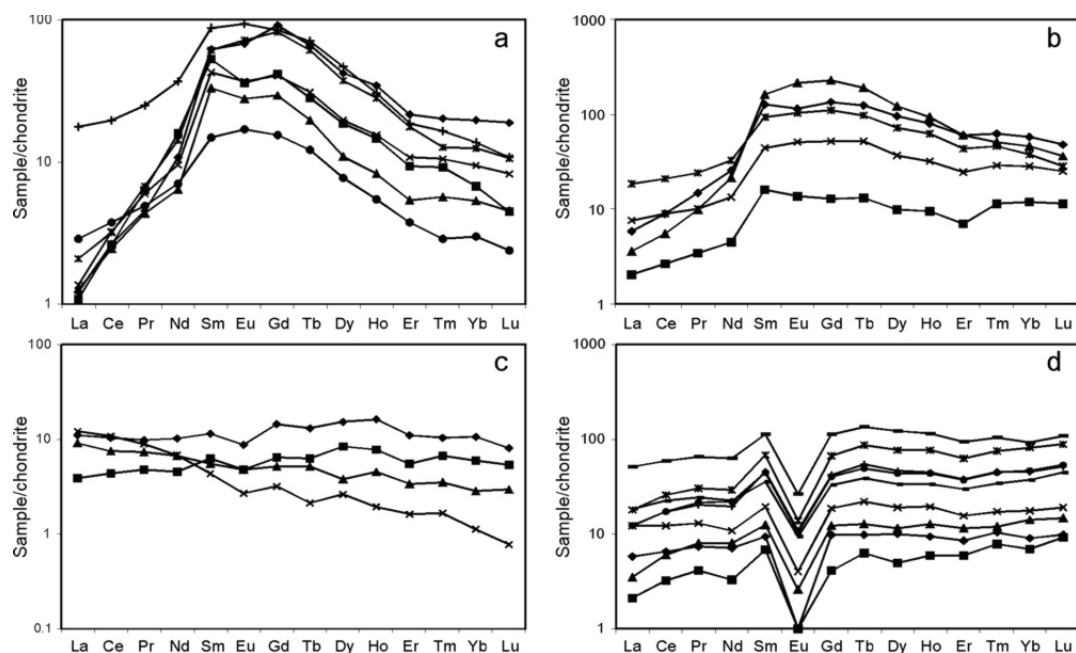


Fig.2.77. Chondrite normalized REE patterns in fluorite of the 1<sup>st</sup> postore stage (a) and the 2<sup>nd</sup> postore stage (b) of the Streltsovsky deposit, Gozogor (c) and Abagaityi (d) deposits (data from ICP-MS analysis)

Direct relations between  $I(\text{REE})$  in XRL and CPL spectra and U content in fluorite locations has been revealed (Fig. 2.78b,e, 2.79a). It appeared the most evident for  $\text{Gd}_{313}^{3+}$ ,  $\text{Eu}_{420}^{2+}$  and  $\text{Sm}_{604}^{3+}$  which may be seen from the relationship between ratios of  $I(\text{REE})$  indicated and  $I(\text{HREE}) - \text{Er}^{3+}$  and  $\text{Yb}^{3+}$  – from one side and U content from the other (Fig. 2.79b). It corresponds with ICP-MS data where MREE predominate over HREE in the patterns (Fig. 2.77a).

High  $I(\text{REE})$  in luminescence spectra of fluorite located in basalts does not match the relatively low U content (less than 0.1%). This could be explained by abnormally high temperature of quartz-fluorite assemblage formation revealed from the study of fluid inclusions in quartz in the same samples (260-380°C against the usual 180-260°C). It is well known that REE concentration in fluorite depends directly on temperature.

Matching of REE content in fluorite obtained from ICP-MS data and  $I(\text{REE})$  from luminescence spectra demonstrates general comparability: (1) MREE/HREE from ICP-MS analysis of fluorite of the 1<sup>st</sup> postore stage is higher than that for the 2<sup>nd</sup> postore stage, the same as from  $I(\text{Gd}_{313}^{3+}, \text{Eu}_{420}^{2+}, \text{Sm}_{604}^{3+})/I(\text{Dy}^{3+}, \text{Er}^{3+})$  (Fig. 2.77a,b and 2.78b,c,f); (2) low total REE

## 2. Mineralogy of the deposits

content in fluorite of the Gozogor deposit (Fig. 2.77c) corresponds to low  $I(\text{REE})$  on spectra;

(3) the highest concentration of LREE in fluorite from the Abagaityi deposit among all

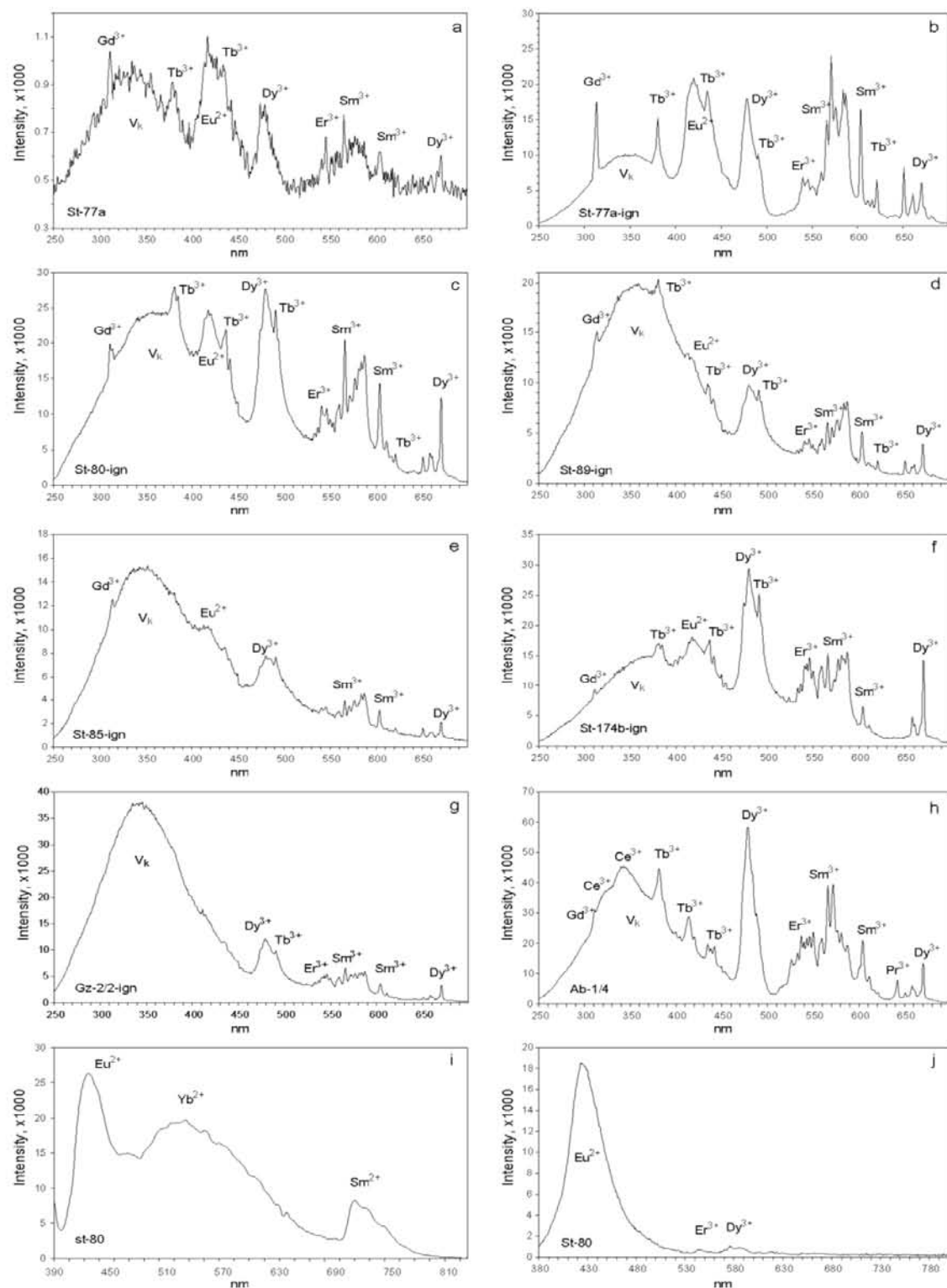


Fig.2.78. Spectra of X-ray (a-h), cryophoto (i) and laser-excited (j) luminescence of fluorite: a – sample St-77 before ignition, b – sample St-77 after ignition, c-e – fluorite of the 1<sup>st</sup> postore stage from sites with different U content from the Streltsovsky deposit after ignition, f – fluorite of the 2<sup>nd</sup> postore stage from the Streltsovsky deposit, g – fluorite from the Gozogor deposit after ignition; h – fluorite from the Abagaityi deposit; i-j – CPL and LEL spectra of fluorite of the 1<sup>st</sup> postore stage from the Streltsovsky deposit.

## 2. Mineralogy of the deposits

samples investigated (Fig. 2.77d) reflects in lines of  $Ce^{3+}$  and  $Pr^{3+}$  appearance in spectrum (Fig. 2.78h).

Laser-excited luminescence is less informative than XRL and CPL. Only the  $Eu^{2+}$  intensive peak can be observed in the spectra (Fig. 2.78j). Authors are going to improve the technique using time-resolve LEL which leads to quenching of short-lived  $Eu^{2+}$  line and allows the detection of long-lived lines of other REE ( $Eu^{3+}$  in particular).

Conclusions. Investigations conducted allow the following conclusions to be made: (1) luminescent spectroscopy of fluorite has some advantages over bulk sample analysis – it is an express non-destructive sensitive method with high locality which permits the testing of small grains, raw samples, polished and thin-polished sections; (2) intensities of doped REE optical centers generally reflect rare earths content in fluorite; (3) additional information concerning physico-chemical conditions of mineral formation can be retrieved from spectra; (4) REE partitioning in fluorite from deposits of different types as well as luminescent spectra are their typomorphic features; (5) direct relationship between intensities of REE lines (mostly  $Gd^{3+}$ ,  $Eu^{2+}$  and  $Sm^{3+}$ ) in fluorite spectra and U content in host rocks has been revealed at the Streltsovsky deposit

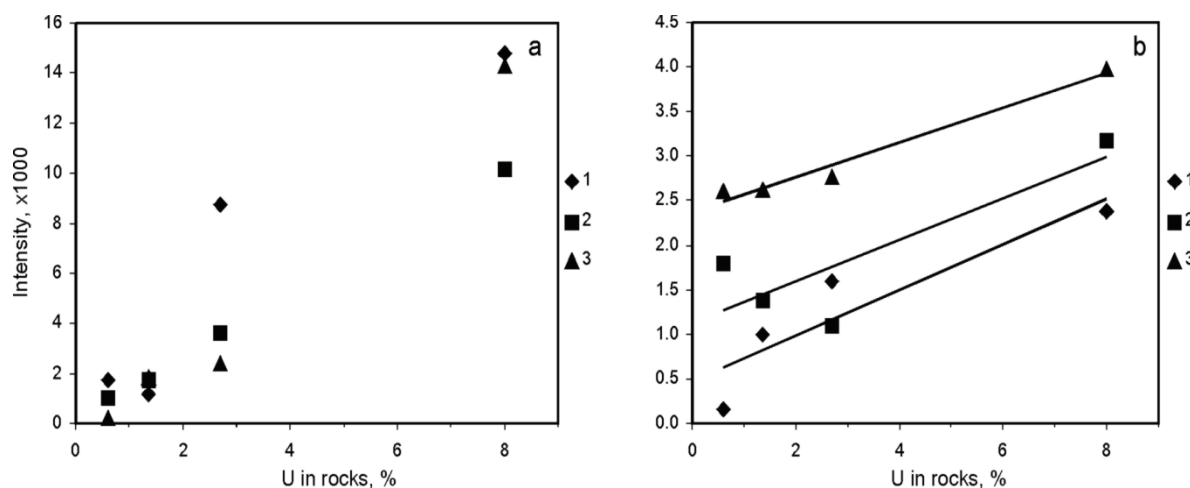


Fig.2.79. Dependence between intensities of REE in luminescence spectra of fluorite and U content in host rocks: a – relation between  $I(Eu^{2+}, XRL)$  (1),  $I(Gd^{3+}, XRL)$  (2),  $I(Eu^{2+}, CPL)$ , (3) and U in dacites; b – relation between ratios of  $Eu^{2+}/Yb^{2+}$  (CPL) (1),  $Gd^{3+}/Er^{3+}$  (XRL) (2), ( $Sm_{604}^{3+}/Er^{3+}$  (XRL) (3) and U in dacites.





### **3. Behavior of elements during the Late Mesozoic hydrothermal process**

At the beginning of the study the main goal of these investigations was to reveal geochemical specialization of different mineral complexes. However, as it was established during the study, superposition of mineral assemblages belonging to various stages on each other is a typical case in the SOF deposits. It caused difficulty in sampling separate host rocks (basalts, dacites, rhyolites, granites, tuffs, etc.) with developed individual mineral complexes, without any significant superposition. So the results obtained from the geochemical investigations do not characterize geochemistry of the whole Late Mesozoic hydrothermal process but mainly clarify some of its specific aspects.

#### **3.1. Uranium and other elements behavior during the preore and postore metasomatic alteration of the host rocks**

Rocks enclosing uranium ore bodies and underlying them in the caldera basement might be one of possible sources for uranium. In accordance with one of generally accepted points of view (Modnikov et al., 1984; Naumov et al., 1985; Ishchukova et al., 1991; Chabiron et al., 2003), uranium was leached out from host rocks during the preore metasomatic alteration. It attracted this author's interest to uranium and other elements behavior in this process.

As has been shown in the mineralogical chapter, the intensive quartz-chlorite-carbonate-illite alteration followed by the rock bleaching was related to the 1<sup>st</sup> postore stage. The weak rock alteration of similar type was conditionally related to the preore stage based on isotope chronology and general deduction, as no clear mineralogical evidence has been obtained. In fact, slightly altered rocks may be considered as background rocks which later were subjected to more intense alteration of the same type. Consequently, element behavior during the postore alteration should reflect general tendencies both for the preore and postore processes. Uranium has to be excluded from examination because it enriched host rocks between these two processes and may affect the postore samplings. Additional studies have been provided for clarifying the uranium behavior.

## 3. Behavior of elements in hydrothermal process

### 3.1.1. Whole-rock geochemistry

The results of whole-rock analyses obtained by ICP-AES and –MS spectroscopy, and to a lesser extent, by XRF and INAA methods, were grouped by rock types (basalts, dacites and granites). Samples in each group was grouped in turn by the intensity of illitization with associated quartz-chlorite-carbonate alteration. In the geochemical database of rocks (electronic annex IV), intensity of rock alteration in samples was evaluated qualitatively as low (background rocks), moderate, and intensive. These estimations were encoded by numbers (from 1 to 3 accordingly), so weak illitization was indicated as “ilt-1” in the “Alteration” column of the database.

Six samplings have been compiled: basalts, dacites and granites subjected to weak illitization (ilt-1), corresponded to rocks altered during the preore stage, and the same rocks with moderate (ilt-2) and intensive (ilt-3) illitization, related to the alteration of the 1<sup>st</sup> postore stage. The composition of the samplings is represented in Table 2.7.

The results have been statistically treated in accordance with the approaches described in the chapter “Methods of investigation and factual material”. These results are shown in tables of Annex I.

Table 2.7. Composition of samplings on geochemical analyses of host rocks affected by the preore and the postore alteration.

Rocks	Samples	
	Weak illitization	Moderate and intensive illitization
Basalts	<u>16 samples:</u> St-131a, St-138, St-357, St-539, St-540, T05-50a-1, T05-51a-1, T05-53b, St-110, St-124a, St-136a, St-456a, St-457, St-458a, St-139c, St-357	<u>5 samples:</u> St-131b, St-124b, St-136b, St-456b, St-458b
Dacites	<u>5 samples:</u> St-171, St-247a, St-255c, St-256, St-271a	<u>8 samples:</u> St-170, St-182a, St-82, St-87c, St-222a, St-247b, St-271b, St-323a
Granites	<u>17 samples:</u> St-64, St-65, St-32, St-37, St-65a, St-596b, 9c-93, 9c-90a, 9c-89, St-64, St-65a, St-596b, T03-65, 7c-X1, 9c-145, 9c-245, 9c-267a	<u>8 samples:</u> St-63a, St-75, St-591, St-63a, St-359, 9c-81, 9c-146, 9c-209

### 3. Behavior of elements in hydrothermal process

---

Total number of analyzed elements in different samplings varies from 50 to 60, so it is difficult to describe all of them. To reveal the most important tendencies, a ratio  $R_{element}$  between the average element contents in samplings on intensively ( $\bar{C}_{element}^{ilt-2+3}$ ) and weakly altered rocks ( $\bar{C}_{element}^{ilt-1}$ ) have been calculated for each type of rocks:

$$R_{element} = \frac{\bar{C}_{element}^{ilt-2+3}}{\bar{C}_{element}^{ilt-1}}$$

As it follows from the equation, the ratio reflects gain (if more than 1) and loss (if less than 1) of elements in the process of intensive postore alteration.

Then, the average ratios for different rocks for each element was calculated and all the ratios were sorted in the descending order to separate elements which predominantly enriched host rocks during intensive illitization from those which mainly were lost. The results are exhibited in Fig. 2.80. Sulfur and arsenic were excluded from the diagram because of too high values ( $R_S^{basalts}=247$ ,  $R_S^{granites}=22$ ,  $R_{As}^{granites}=19$ ;  $R_S$  and  $R_{As}$  for other rocks were not calculated because of lack of data on these rocks).

The most significant gain in various rocks is noticed for U, some chalcophile (S, As, Cd, Cu, Pb), siderophile (Mo, Ni, Co), and lithophile (Ba, Be, W, Cr, Cs) elements. Behavior of W, Cr and Cs is different in different rocks – they were accumulated in dacites and granites but were leached out from basalts. Similarly, Ni and Cu were gained in basalts and dacites while they were lost in granites.

These regularities may be explained from mineralogy as deposition of sulfides (pyrite, marcasite, arsenopyrite, molybdenite with jordisite) during the 1<sup>st</sup> postore stage. Sulfide dissemination is often observed in the quartz-chlorite-illite-carbonate veinlets and in the central parts of alteration zones developed along fractures. Behavior of uranium will be examined below.

From the other side of the range, elements of preferential loss are grouped. They are Fe and Mn which is accounted for by Fe-oxides dissolution in bleached zones. Ca, Na, and Sr were also leached out, most likely due to plagioclase replacement by illite. Scandium may be disseminated in replaced silicates.

The revealed tendency for U to enrich different rocks during the postore intensive alteration nearby and at a distance from the uranium ore bodies is corroborated by the investigation of particular metasomatic zones. Following whole-rock analyses of hematized dacites and basalts compared to bleached zones superimposed on halos of synore

### 3. Behavior of elements in hydrothermal process

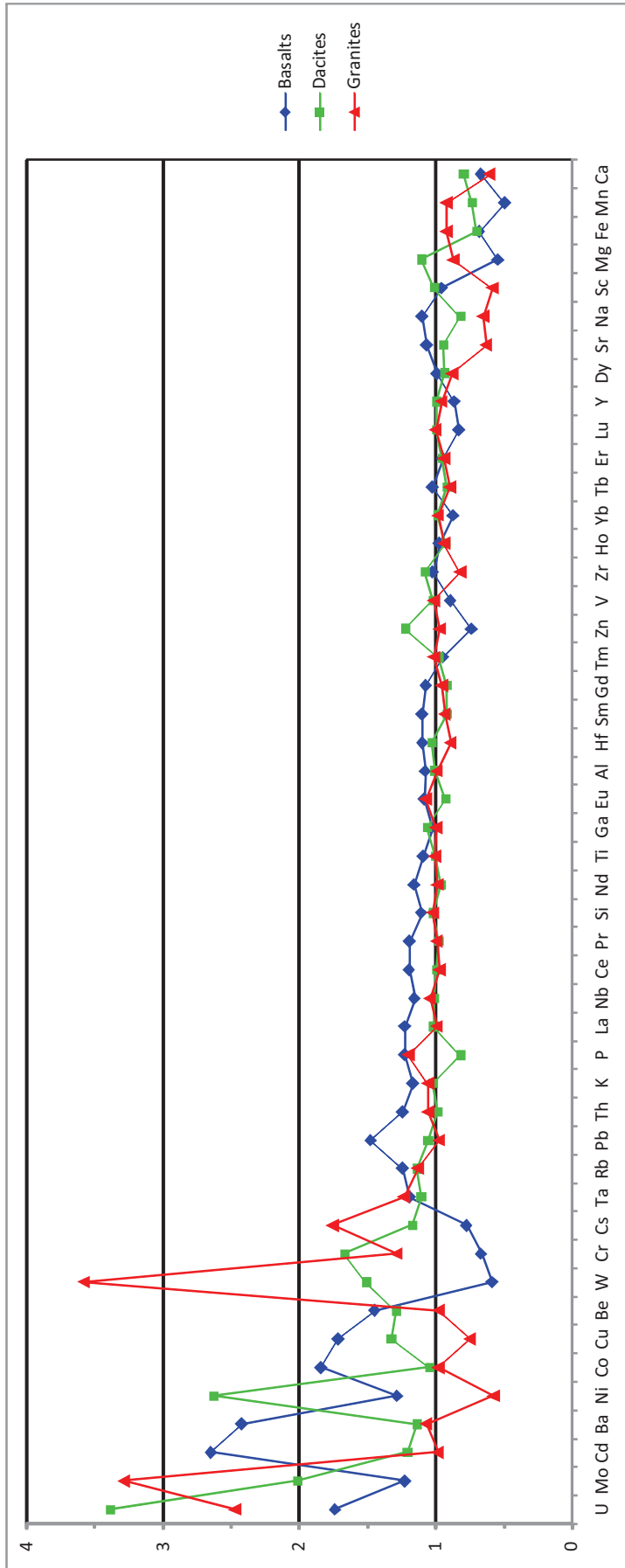


Fig. 2.80. Diagram of the ranged  $R_{element}$  ratios in basalts, dacites, and granites reflected the gain ( $if > 1$ ) and the loss ( $if < 1$ ) of elements during intensive illitization of host rocks.



### 3. Behavior of elements in hydrothermal process

---

hematization, U contents in the zones of the postore alteration are generally higher than in hematized rocks nearby.

For example, bleached basalts with the intensive quartz-carbonate-illite alteration along fractures at the peripheral parts of the uranium ore body contain 410 ppm U (sample St-139b) while moderately hematized basalts around these bleached zones (St-139a) contain only 47.5 ppm of U (Fig. 2.17). Similarly, dacites in narrow bleached zones along fractures (St-179b) are characterized by essentially higher U concentration (236 ppm) relative to the enclosing hematized dacites (St-179a, 84.2 ppm U).

Uranium contents may be approximately equal in bleached and hematized dacites (consequently samples St-323a, 326 ppm U, and St-323b, 401 ppm U) (Fig. 2.9). Moreover, uranium may be slightly leached out from intensively illitized rocks. As shown in the diagram of U and Th contents in intensively altered rocks (Fig. 2.81), along with high U concentrations regarding Th, some part of dacite and granite samples exhibit U deficit compared to Th. These samples have Th/U ratios between 4 to 10 which may indicate uranium leaching from altered rocks.

To study the uranium behavior during the weak preore alteration, a diagram of U and Th concentrations in slightly altered background basalts, dacites and granites have been built (Fig. 2.82). As a whole, Th/U ratios in slightly and intensively altered rocks are similar except extreme uranium concentrations in the latter. Resembling Th/U ratios for differently altered granites, being mostly above 4, may evidence in favor of primary character of the ratio rather than in favor of U leaching during the superimposed alteration. If the latter is the case, Th/U ratio should increase with the increase of illitization intensity.

Thus, the enrichment of bleached zones with uranium may be explained by its remobilization by the postore hydrothermal fluids which circulated through the high-grade uranium mineralization in the central parts of ore bodies, replaced primary uranium minerals with the U-Si metagel and redeposited leached U on leucoxene, relict Fe-hydroxides and other possible sorbents in the bleached zones in the outer parts of ore bodies. If the postore fluids did not affected uranium mineralization, bleached rocks may contain similar or somewhat lower uranium concentrations than hematized rocks nearby.

### 3. Behavior of elements in hydrothermal process

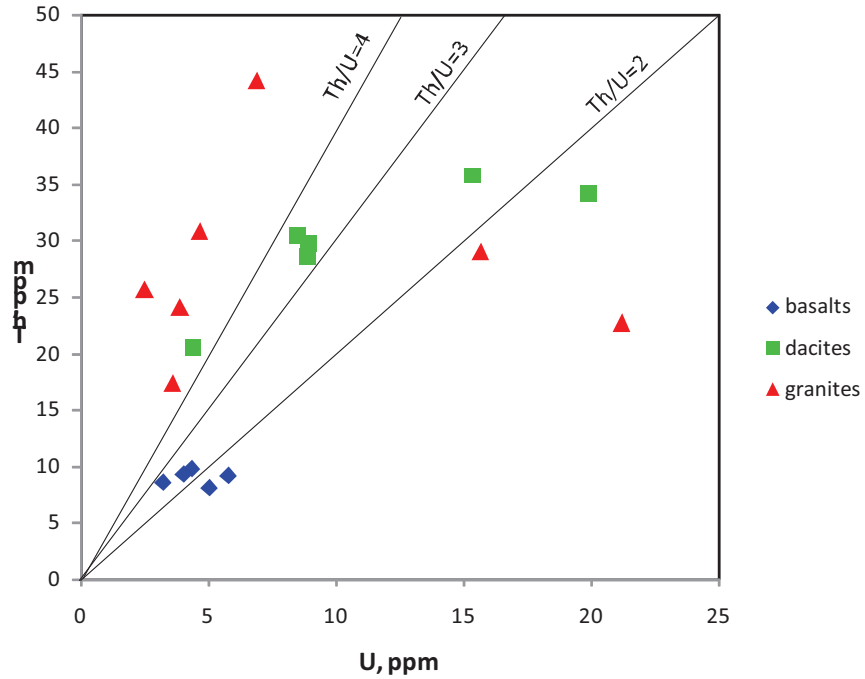


Fig. 2.81. U and Th contents in basalts, granites and dacites subjected to moderate and intensive postore alteration (from ICP-MS and INAA data). Data with high U contents in the dacites (up to 396 ppm U) and in the granites (up to 274 ppm U) are trimmed.

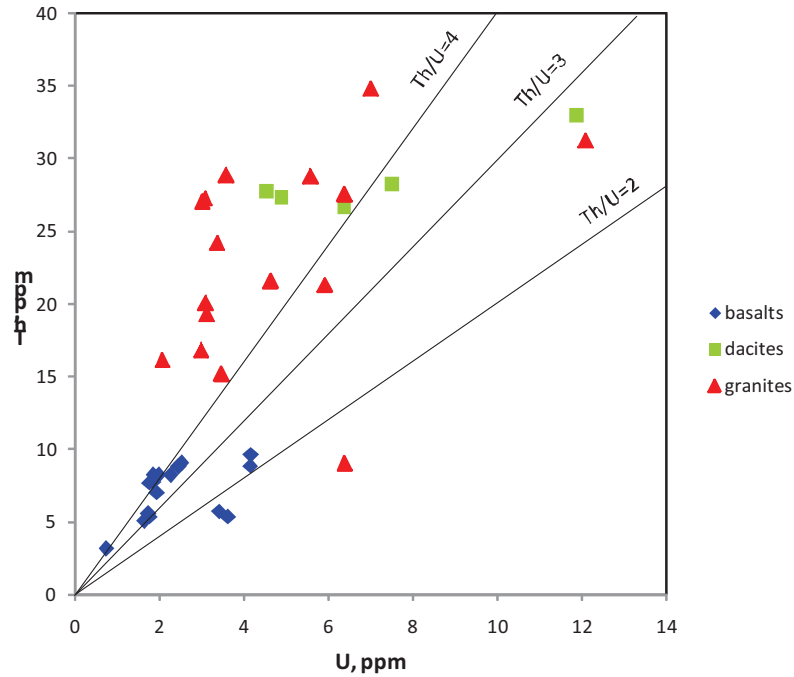


Fig. 2.82. U and Th contents in background basalts, granites and dacites subjected to weak preore alteration (from ICP-MS and INAA data).

## 3. Behavior of elements in hydrothermal process

---

### *3.1.2. Dispersion halos of uranium around ore bodies*

Whole-rock geochemistry can reveal general parameters of element distribution in different rocks and, in that way, general tendencies of geochemical evolution in different processes. Nevertheless, it suggests nothing about the occurrence of forms of uranium and its local distribution in minerals and mineral aggregates in rocks. To clarify this question, additional studies by fission track radiography have been undertaken.

An individual small ore body in basalts of the Western site of the Streltsovsky deposit, located at the depth of 350 m below the surface, has been chosen as an object of investigation. The vein-type ore body with a thickness of less than 50 cm is controlled by a steeply dipping fracture of NW strike. This fracture is located 30 m east of the main ore-controlling fault of the Western site striking also NW. Rocks in the exocontact zone of the fracture are intensively albitized, hematized and contain finely disseminated pitchblende (sample St-112) at a distance of 15-20 cm (Fig. 2.83). The outer zone is represented by bleached basalts with dispersed Fe-hydroxides producing the light-yellow to orange color of basalts (St-111). This zone is spread over less than 50 cm from the fracture. Enclosing rocks are greenish-grey basalts exposed to illitization with associated carbonatization and chloritization of low intensity (St-110). A postore calcite vein 10 cm thick developed along the fracture in the central part of the ore body.

The least altered basalts were sampled at the distance of 20 m west of the ore body (St-138). It is interesting that they are located only 6 m to the east of the high-grade ore body controlled by the fault 60b. These rocks have dark-grey to black color. They were subjected only to weak carbonatization and illitization, and contain relatively fresh olivine partly replaced by calcite.

Studies of thin-polished sections of the described above samples made on quartz glass, and lavalan detectors etched by KOH for track development, have been performed. Heterogeneities of uranium distribution on lavalan detectors were confronted with sections to reveal minerals and their aggregates accumulated uranium. Special computer techniques were used to automatically calculate uranium contents in interesting places. Uranium concentrations were determined for three groups of rock components – groundmass (matrix), phenocrysts, and leucoxene replacing Ti-accessories. Results of U determination in different groups are presented in Table 2.8.

### 3. Behavior of elements in hydrothermal process

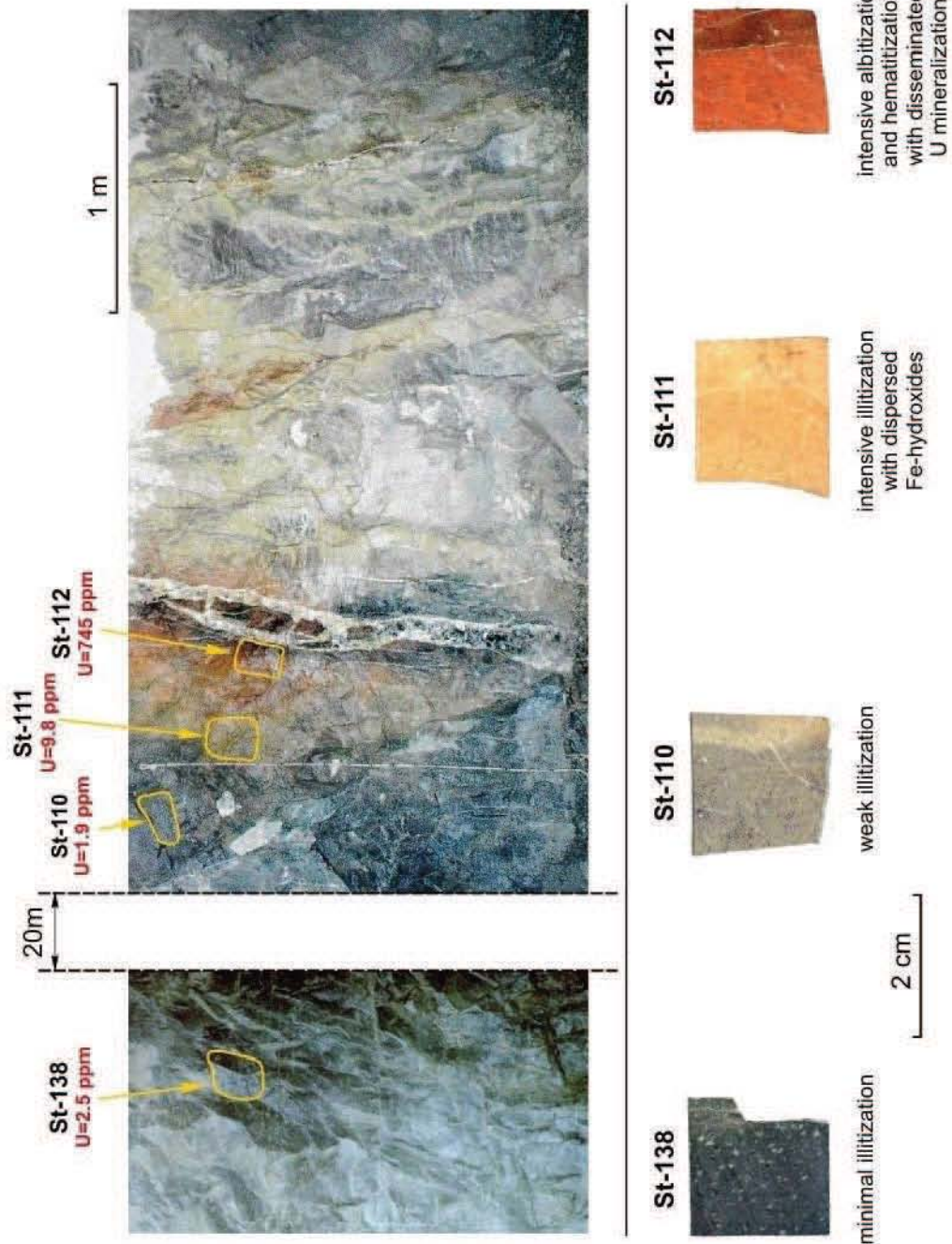
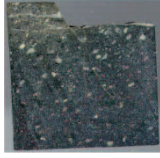
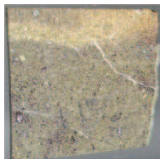
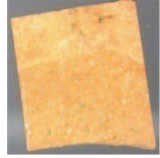
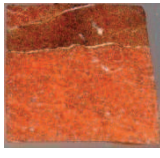


Fig. 2.83. An ore body in basalts with associated albitization and hematization, and superimposed bleached zones along fissures. The ore body is crosscut by a vein of the postore calcite. Samples of differently altered rocks are shown in the lower part of the figure. The northern wall of the gallery in the Western site of the Streltsovsky deposit, horizon +383 m.



### 3. Behavior of elements in hydrothermal process

Table 2.8. Statistical results of U quantification in different components of basalts by fission track radiography (in ppm).

Sample	Image	Object	Num	U content, ppm		Variance
				Average*	Min-Max	
St-138		matrix	12	0.91	0.55-1.19	0.037
		phenocryst	12	0.007	0-0.023	5.78E-05
St-110		matrix	9	0.57	0.38-0.71	0.01
		phenocryst	6	0.157	0.011-0.38	0.018
		leucoxene	5	9.41	6.06-10.1	2.90
St-111		matrix	6	1.33	0.92-1.94	0.187
		leucoxene	9	604	44.9-947.0	1.33E+06
St-112		matrix	5	12.73	8.28-15.7	10.92
		phenocryst	7	1.04	0.01-1.96	1.21
		leucoxene	8	7522	1873-20021	5.24E+07

Note: **Num** – number of observations, **Average** – median values

Uranium is distributed evenly in the groundmass of sample St-138 as fine stellar segregations and is practically absent in the phenocrysts (Fig. 2.1 a,b). Partial replacement of olivine by calcite did not cause any changes in U concentration. As Ti-accessories are stable in this sample, no leucoxene was formed and the appropriate data are absent in the Table 2.8.

Groundmass in sample St-110 is replaced by illite and carbonate. Phenocrysts of mafic minerals are completely replaced by carbonate with subordinate amounts of quartz. Titanite is completely leucoxenized while ilmenite and Ti-magnetite remain stable. Uranium is distributed evenly in the groundmass like in sample St-138. Rare tracks of U are located in the carbonatized mafic minerals along the microfissures and in the intergranular space. The maximum U concentrations (9.4 ppm on average) are confined to leucoxenized Ti-accessories.

### 3. Behavior of elements in hydrothermal process

---

Intensively altered basalts in sample St-111 differ from those in sample St-110 by more intensive development of illite which replaces microlitic plagioclase and mafic minerals in the groundmass but also occurs as thin stringers in the rock. All the Ti-accessories are completely replaced by leucoxene. Uranium content is markedly higher than in sample St-110. It occurs in high concentrations in leucoxene which forms complete pseudomorphs after accessory minerals and also develops as thin seams in the rock (Fig. 2.1 c,d)

Basalts in sample St-112 are intensively fractured and replaced by fine-crystallized albite and hematite. Quartz and carbonate occur in more significant quantities than in previous samples. Uranium distribution is similar to that in sample St-111 but differs by essentially higher contents (Table 2.8) and by the presence of the pitchblende and brannerite.

Variations in U contents with the decrease of distance from the ore body and with the increase of the intensity of different alterations are presented in Fig. 2.84. It is noticeable that the main U concentrator is the leucoxene. It is the most variable phase on U contents – they change from 9.4 ppm in slightly altered basalts to 7522 ppm in intensively albitized, hematized, illitized and carbonatized rocks, i.e. approximately on 3 orders of magnitude. Basalt matrix is significantly less variable – even in intensively illitized basalts with dispersed Fe-hydroxides (St-111) U concentrations in the groundmass is similar to that of the freshest rocks (St-138). Only in mineralized basalts, U content increases by an order of magnitude relative to illitized rocks (from 1.3 to 12.7 ppm U). A similar tendency is observed for phenocrysts. The difference from the groundmass is that phenocrysts consist of half an order lower total U concentrations and the actual absence of U in an unaltered phenocryst in sample St-138 (0.007 ppm).

As in basalts, similar studies were provided in the dacites of the Oktyabrsky deposit in the exocontact of the high-grade uranium ore body. Insignificant uranium migration at the distance of several meters has been established along horizontal fractures accompanied by a bleached zone 10 cm thick. Conversely to the longitudinal migration, U contents abruptly decreased perpendicular to this fracture from 11.8 ppm in the central part of bleached dacites to 6.8 ppm in the nearest proximity (5 cm apart) and further to 3.2 ppm in the background dacites. Leucoxene occurred as the main uranium sorbent in dacites, like in basalts.

Numerous data obtained by radiometric sampling of the ore bodies and their exocontacts, provided in underground galleries in different deposits, demonstrated permanent sharp decrease of U concentrations outside zones of hematization around the ore bodies. It

### 3. Behavior of elements in hydrothermal process

corroborates the conclusion obtained by whole-rock geochemistry and fission track radiography concerning insignificant size of dispersion halos of U nearby the ore bodies.

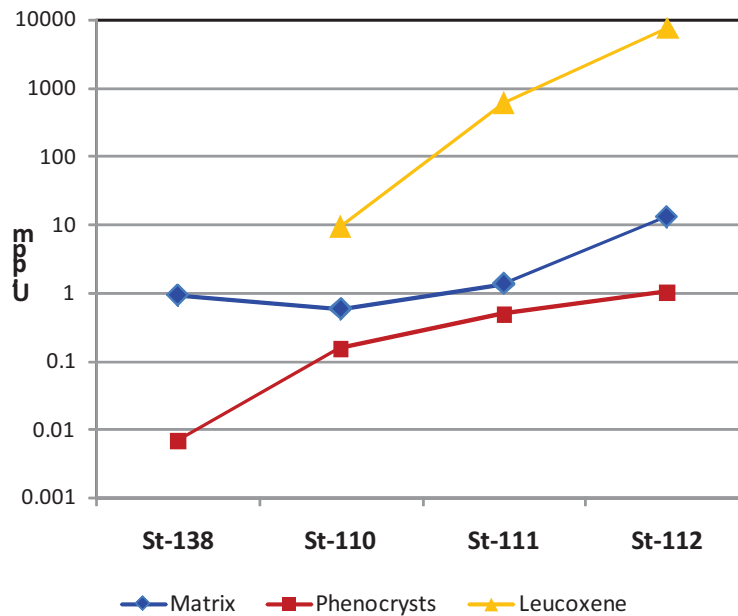


Fig. 2.84. Diagram of U contents in groundmass (in ppm), phenocrysts and leucoxene aggregates in basalts subjected to alteration of different type and intensity.

#### 3.1.3. Conclusions

The studies fulfilled have reveal the main geochemical features of the preore and the postore illitization as well as the uranium ore deposition.

1. During the preore illitization accompanied by silicification, chloritization and carbonatization, no significant gain or loss of uranium in different rocks (basalts, dacites and granites) occurred.
2. Intensive postore alteration of the same type led to general enrichment of rocks by chalcophile (S, As, Cd, Cu, Pb), siderophile (Mo, Ni, Co), and lithophile (Ba, Be, W, Cr, Cs) elements. Certain elements were leached out. The loss of Fe and Mn is accounted for Fe-oxides dissolution in bleached zones. Contents of Ca, Na, and Sr decreased the most likely due to plagioclase replacement by illite.
3. Uranium was locally redistributed in the zones of weak preore alteration without any significant change of its average content. More intensive postore alteration was reflected in uranium gain in the bleached zones in the vicinity of high-grade uranium ore bodies.

### 3. Behavior of elements in hydrothermal process

---

Insignificant gain/loss or the absence of U migration are observed in the intensively illitized rocks outside the ore bodies.

4. Uranium deposition was followed by the development of very narrow dispersion halos which do not exceed the size of aureoles of hematization. In basalts uranium was dispersed at a distance of less than 50 cm from the ore body and even intensive postore alteration could not enlarge this halo. Leucoxene is the main sorbent of U in the dispersion zones.

#### 3.2. Geochemistry of episyenitization

Episyenites in the SOF deposits have been established by the author for the first time as the beginning of the 1<sup>st</sup> postore stage. Confirmation of belonging of these dequartzification zones to episyenites required geochemical evidences in addition to mineralogical observations. The results of whole-rock XRF and ICP-AES analyses provided for this purpose, have revealed the change in major element content as a consequence of the alteration.

Episyenitization occurred the most evidently in the Antei deposit at various depths. Zones of increased porosity due to quartz leaching are generally controlled by the main fault of the Antei deposit (fault 160) which hosts the uranium mineralization. However, zones of episyenitization may deviate from the fault at a distance up to 20 m. The best observed zone of episyenitization is located at the horizon +84 m (about 600 m below the surface). It was sampled thoroughly across the zones of episyenitization, illitization, synore hematization with dispersed uranium mineralization, and across the ore body in the fault (Fig. 2.19).

Samples representing the episyenitized granites are St-615–St-621, the illitized granites are characterized by samples St-622–St-624, and the hematized granites with disseminated and vein uranium mineralization are represented by samples St-625–St-636. Granites in samples St-615 and St-620 were intensively carbonatized what exhibited in filling of vugs by the calcite of the 1<sup>st</sup> postore stage.

Whole-rock composition with respect to silica and alkalis ( $\text{SiO}_2$  vs.  $\text{K}_2\text{O}+\text{Na}_2\text{O}$ ) is shown in Fig. 2.85. As it follows from the Le Bas diagram, an evident trend of the silica decrease along with the alkalis increase is noticeable from the background granites (red crosses in the diagram) towards the episyenitized varieties (magenta circles). Background granites are represented by weakly illitized rocks sampled outside this section (samples St-596b, 9c-93, 9c-90a, St-64, St-65a, T03-65, 9c-145, 9c-210, 9c-245, see Table 2.7). The



### 3. Behavior of elements in hydrothermal process

decrease of  $\text{SiO}_2$  against the increase of  $\text{K}_2\text{O}+\text{Na}_2\text{O}$  is explained by quartz dissolution which caused relative increase of the feldspars remaining in the rock.

Illitization of the granites and development of the vein and metasomatic quartz produce expected shift of points on the diagram towards higher silica contents (samples St-622–St-624). Separate locations of figurative points of samples St-615 and St-620 in the area of low silica contents is explained by the replacement of quartz, possibly remaining after episyenitization, and mainly feldspar by carbonate which is observed under the microscope.

Thus, the provided study of geochemical whole-rock analyses of altered granites testifies to their belonging to episyenites and explains observed mineral replacements from a geochemical point of view.

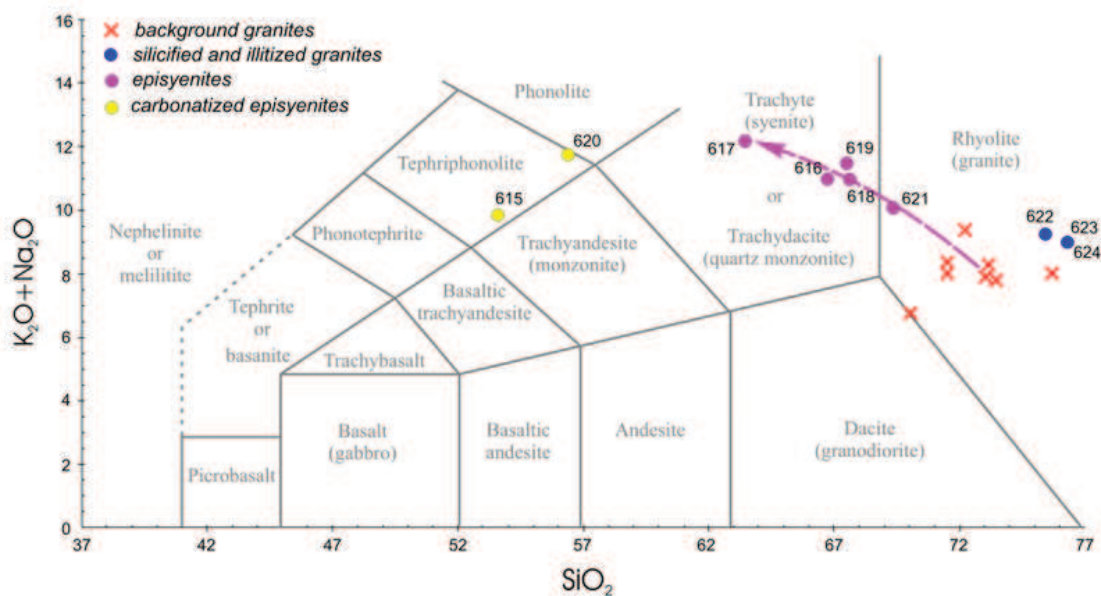


Fig. 2.85. Chemical composition of episyenitized granites on the Le Bas diagram indicating relative alkali gain against the silica loss. Numbers near points on the diagram correspond to sample numbers. Background granites have been sampled outside the considered cross-section.



#### 4. REE in pitchblende and host rocks

The behavior of REE in geochemical processes has attracted the attention of researchers for many years. Both products of magmatic activity, including that in the eastern Transbaikal region (Badanina et al., 2004, 2006), and hydrothermal mineralization, including uranium mineralization (Fryer and Taylor, 1987; Hidaka and Gauthier-Lafaye, 2001; Aleshin et al., 2006<sub>1</sub>) have been studied in this respect. New data on the REE distribution in rocks and minerals have been obtained recently from experiments on magmatic and hydrothermal systems (Shmulovich et al., 2002; Veksler, 2004; Veksler et al., 2005). Some specific features of REE behavior were interpreted in terms of quantum mechanics (Mioduski, 1997; Dzhurinsky, 1980; Fidelis and Siekierski, 1971). Taking into account the new data, the author has studied the REE distribution in pitchblende and igneous rocks of the SOF to obtain additional genetic information.

The REE contents in pitchblende hosted in granite at the Antei deposit, in trachybasalt at the Streltsovsky deposit, and in trachydacite from the Streltsovsky and Oktyabrsky deposits were determined with a Cameca IMS-3f ion microprobe (analyst J. Bonhoure, CRPG, France). The REE contents in host rocks were measured with ICP-MS (CRPG, IEM RAS). It has been established that sharp depletions in LREE (La, Ce, Pr, and Nd) and enrichment in Sm, Eu, and Gd relative to other REEs is a characteristic feature of pitchblende hosted in any rock (Aleshin et al., 2006<sub>1</sub>). As a result, a pronounced Sm–Nd discontinuity is observed in the chondrite-normalized REE patterns (Fig. 2.86).

The REE patterns in the most abundant host rocks of the SOF (granite, rhyolite, dacite, and basalt) are generally typical of these kinds of rocks. The slight fractionation of REE in basalt is expressed in a low-angle pattern (Fig. 2.87a). Dacite is characterized by a poorly expressed negative Eu anomaly and somewhat elevated HREE (Er, Tm, Yb, and Lu) contents in comparison with basalt (Fig. 2.87b). The Hercynian granite in the basement of the Streltsovsky caldera reveals a more distinct Eu minimum and enrichment in HREE and depletion in LREE relative to dacite (Fig. 2.87c). Rhyolite is distinguished by the deepest Eu minimum and the highest HREE contents (Fig. 2.87d). The REE distribution was analyzed in rocks affected by metasomatic alteration of various intensity, from slightly altered “background” rocks to rocks intensely replaced by hydromica, carbonate, and chlorite. As can be seen from Fig. 2.87, the alteration does not affect the REE patterns.

## 4. REE in pitchblende and host rocks

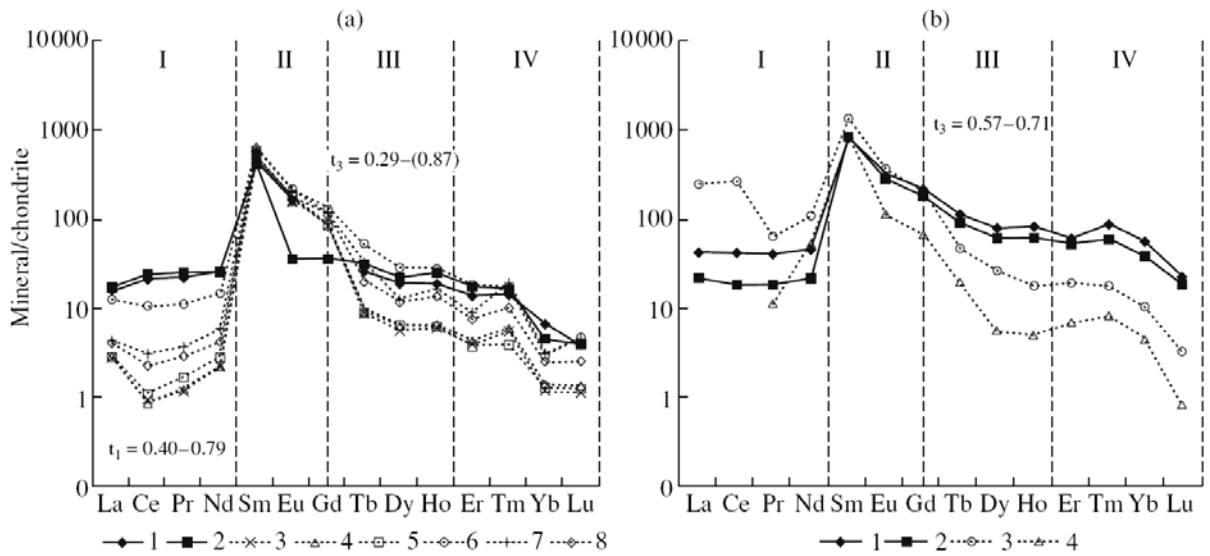


Fig. 2.86. Chondrite-normalized REE patterns of pitchblende. (a) Hosted in dacite, (1, 2) sample St-220h, (3-8) sample 85-67a from the collection of I.V. Mel'nikov; (b) hosted in granite, (1, 2) sample St-602, and basalt, (3, 4) sample St-391. (I-IV) Tetrads;  $t_1$  and  $t_3$  are the values of the tetrad effect in tetrads I and III, respectively.

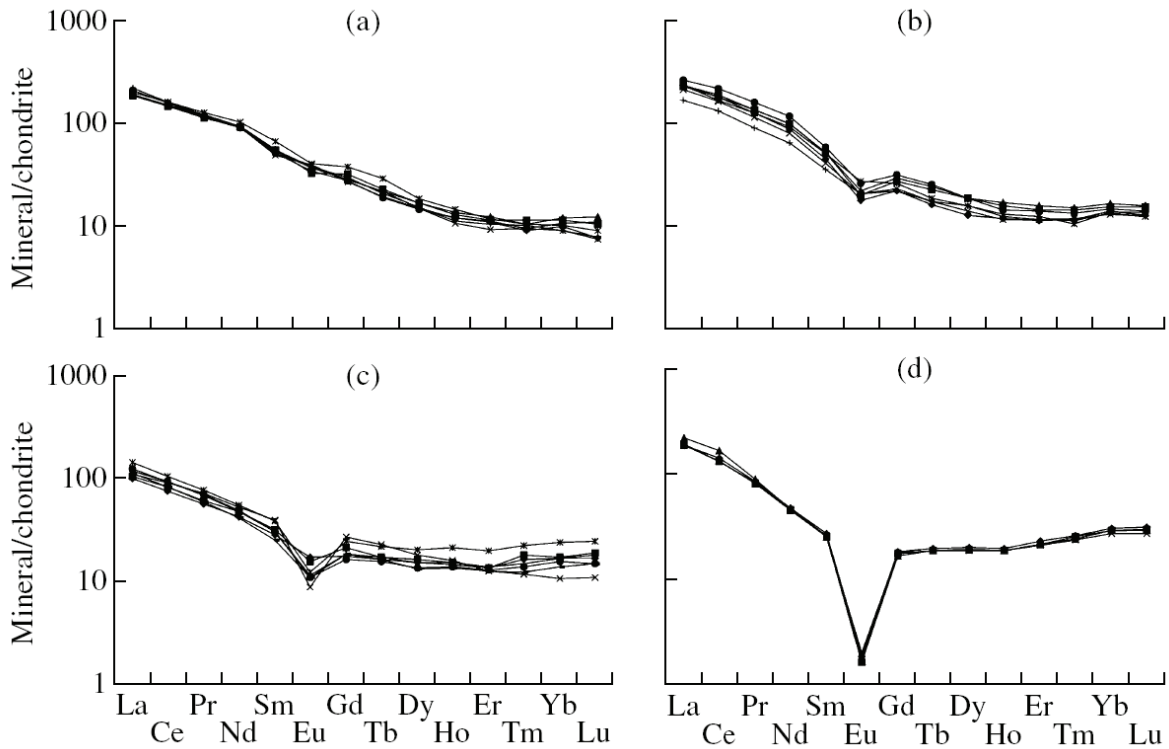


Fig. 2.87. Chondrite-normalized REE patterns of (a) basalt, (b) dacite, (c) Variscan granite, and (d) rhyolite in the SOF from ICP-MS data.



## 4. REE in pitchblende and host rocks

The comparison of the REE patterns of pitchblende hosted in basalt, dacite, and granite with the REE patterns of host rocks reveals a positive correlation of the LREE/HREE ratio. This ratio progressively increases in the series granite–dacite–basalt, and this increase is expressed in a steeper slope of chondrite-normalized REE patterns (Fig. 2.87). A similar trend is traced for REE patterns of pitchblende hosted in the respective rocks (Fig. 2.88). Thus, the host medium exerts some effect on LREE and HREE contents in pitchblende, but high Sm, Eu, and Gd contents are retained in uranium oxide from all host rocks.

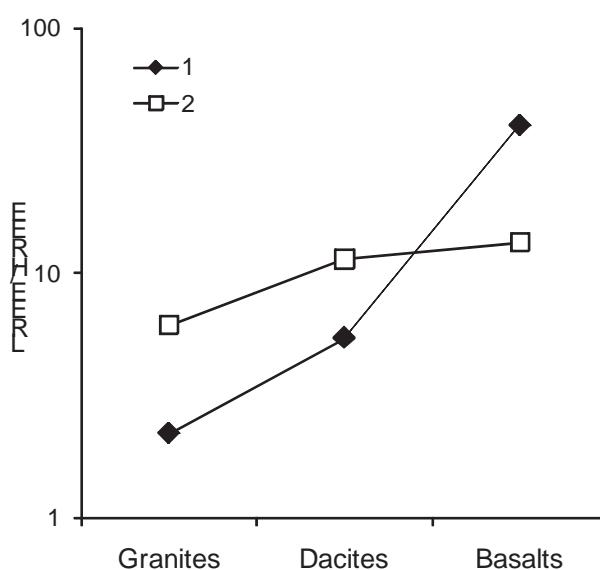


Fig. 2.88. LREE/HREE ratio of pitchblende hosted in granite, dacite, and basalt and of host rocks. (1) Pitchblende, (2) rocks.

The tetrad effect is another characteristic feature of the REE pattern of pitchblende. This effect is of great importance with regard to suggestions on the source of REE and U. This phenomenon of anomalous REE fractionation was established for the first time experimentally in immiscible liquids (Fidelis and Siekierski, 1966), and subsequently it was revealed in various natural systems, including seawater and marine sediments, meteoric hydrocarbonate water (Takahashi et al., 2002), F-bearing carbonatite (Bunh et al., 2003; Veksler et al., 2005), and silicic Li–F melts, whose evolution is controlled by separation into immiscible melts and fluids to a greater extent than by crystal fractionation (Badanina et al., 2006; Monecke et al., 2002; Irber, 1999; Bau, 1996).

An anomalous character of REE fractionation is expressed in the division of gentle chondrite-normalized patterns into four segments consisting of convex (M-type) or concave

## 4. REE in pitchblende and host rocks

---

(W-type) arcs named tetrads: the first tetrad (La, Ce, Pr, Nd), the second tetrad ((Pm), Sm, Eu, Gd), the third tetrad (Gd, Tb, Dy, Ho), and the fourth tetrad (Er, Tm, Yb, Lu), as can be seen from Fig. 2.86. Promethium, which does not occur in nature, is not shown in this figure. The different behavior of geochemically cognate elements with the same charge 3+ (except Ce<sup>3+,4+</sup>, Eu<sup>3+,2+</sup>, and some others) and systematically decreasing ionic radius is caused by different stability of their organic, carbonate, and halogen compounds owing to a different degree of occupancy of the 4f orbital by electrons. REE with the 4f shell occupied multiply to 1/4 (La, 0; Nd, (Pm), 1/4; Gd, 1/2; Ho, Er, 3/4; Lu, 1) differ in the force of bonding with ligands in complex compounds from REE with the 4f orbital occupied nonmultiply (Fidelis and Siekierski, 1971). The enrichment of one part of the melt–fluid or fluid–fluid system in REE with a multiply occupied 4f orbital gives rise to the depletion of another part of the system in these REE and, thus, to the existence of complementary mirror M- and W-types of the tetrad effect in the normalized REE patterns.

The value of the tetrad effect was calculated according to Monecke et al. (2002). Tetrad effects with a value of >1.2 for the M type and <0.8 for the W type are thought to be statistically significant. Irber (1999) proposed less strict criteria of significance: >1.1 and <0.9, respectively. The second tetrad is not considered because of the absence of Pm in nature and the anomalous behavior of Eu. The first tetrad is also less significant due to the anomalous behavior of Ce, while the fourth tetrad is commonly less expressed owing to the higher degree of occupancy of the 4f orbital and its closeness to the core (Irber, 1999). Thus, the third tetrad is the most stable and clearly expressed.

A significant effect of W type in the third tetrad ( $t_3 = 0.29\text{--}0.87$ ) is displayed everywhere in pitchblende from the SOF (Fig. 2.86). In some segregations of pitchblende hosted in dacite (sample 85-67a), this effect is also displayed in the first tetrad ( $t_1 = 0.40\text{--}0.79$ ). The composition of the host rock does not exert any effect on the intensity and type of the tetrad effect. For example, pitchblende hosted in dacite demonstrates an intense effect in the third tetrad and a clearly expressed effect in the first tetrad along with a poorly expressed effect in the third tetrad and the absence of an effect in the first tetrad (Fig. 2.86a). At the same time, pitchblende hosted in such contrasting rocks as basalt and granite shows a similar effect in the third tetrad (Fig. 2.86b).

The REE patterns in uranium oxide from deposits of different genesis and age (69–2000 Ma) vary widely (Fryer and Taylor, 1987; Hidaka and Gauthier-Lafaye, 2001) in total REE content, fractionation of LREE and HREE, sense and intensity of the Eu anomaly, and other attributes. It is supposed that the REE pattern is controlled to a greater extent by

## 4. REE in pitchblende and host rocks

---

properties of the hydrothermal fluid (its Eh and type of complex anion) and by the source of U and REE rather than by the crystal chemistry of this mineral.

The REE pattern of pitchblende bears additional information on the possible source of uranium at the SOF deposits. The sharp Sm–Nd discontinuity caused by depletion in LREE might be explained by their fixation in an LREE-containing mineral, but such a mineral is unknown in ore. However, the same effect may be achieved by fractionation of monazite in the silicic magma as a potential source of uranium. Numerous analytical data on granites and modeling calculations corroborate such a possibility (Yurimoto et al., 1990; Sevigny, 1993).

The W-type tetrad effect is another specific feature of the REE pattern of pitchblende. Of all the aforementioned natural settings where this effect was established, only the evolved Li–F silicic melt is suitable for the SOF. This suggestion is confirmed by the abundance of rare-metal Li–F granites, ongonites, and rhyolites in the eastern Transbaikal region. The ages of these rocks are close to the age of uranium ore mineralization in the SOF (144–138 and  $135 \pm 2$  Ma, respectively).

The upper crustal magma chamber at a depth of  $\sim 5$  km, the emptying of which during eruption of rhyolitic melt led to the subsidence of the Streltsovsky caldera, is the most obvious candidate for such a source. However, rhyolites derived from this magma chamber do not reveal either a Sm–Nd discontinuity in the REE pattern or a tetrad effect typical of the REE pattern of pitchblende (Figs. 2.86, 2.87d). Moreover, the Y/Ho and Zr/Hf ratios of rhyolites (36.4–36.9 and 25.0–26.4, respectively) indicate that these rocks are not highly evolved because their geochemical signature is close to the CHARAC field, which corresponds to the normal behavior of CHARGE-and-RADIUS-Controlled elements. This field is characterized by  $Y/Ho = 24–34$  and  $Zr/Hf = 26–46$ , whereas anomalous ratios typical of evolved melts may differ from the normal ratios by many times toward either greater or lesser values (Bau, 1996).

Thus, the REE pattern and other geochemical attributes of rhyolites do not testify to the advanced fractionation of the silicic melt, development of the tetrad effect, and fractionation of monazite. This reasoning does not allow us to regard the U- and F-rich silicic melt derived from the upper crustal magma chamber as a source of uranium for deposits of the SOF.

Rhyolites of the Streltsovsky caldera are close in geochemistry and age to the rare-metal Li–F granites and ongonites of the eastern Transbaikal region enriched in uranium. The REE patterns in different phases of the Khangilai granitic complex (Badanina et al., 2004, 2006) turned out to be helpful for interpretation of the REE pattern of pitchblende from the

## 4. REE in pitchblende and host rocks

---

SOF. The Khangilai pluton is situated in the Aginsky Block 250 km northwest of the SOF and is composed of granitic rocks varying from the least evolved biotite granite to highly evolved amazonite–microcline–albite–lepidolite leucogranite with accessory topaz and fluorite. The late phases are accompanied by Ta mineralization (the Orlovka deposit) and W ore (the Spokoiny deposit).

The early biotite and two-mica granites are characterized by chondrite-normalized REE patterns without a Sm–Nd discontinuity or tetrad effect and are similar in this respect to rhyolites from the Streltsovsky caldera. In the younger four phases, these attributes appear with progressively increasing intensity up to a distinct M-type effect in several tetrads ( $t_1=1.9$ ,  $t_3=1.5$ ,  $t_4=1.3$ ) and a pronounced Sm–Nd discontinuity.

The comparison of the chondrite-normalized REE patterns of the most evolved granites of the Khangilai pluton and of pitchblende from the SOF demonstrates their similarity in the occurrence of the Sm–Nd discontinuity and a mirror tetrad effect of M type in granite and W type in pitchblende. The first attribute is interpreted as a result of fractionation of monazite that retains LREE and depletes residual melt enriched in H<sub>2</sub>O, F, and U in these elements.

The mirror tetrad effect is caused by release of fluid from the U- and F-bearing melt at the late stage of its evolution with enrichment of fluid in U, F, and complex REE compounds with a multiply occupied 4f orbital; the melt becomes enriched in REE with the 4f shell occupied nonmultiply, which causes development of an M-type tetrad effect.

The real possibility of derivation of Na–Al–F fluid from the melt with formation of complementary pairs of M- and W-type tetrad effects has been demonstrated by experiments carried out by Veksler et al. (2005). The tetrad effect of W type was observed in cryolite (Na<sub>3</sub>AlF<sub>6</sub>), whereas in magmatic fluorite (CaF<sub>2</sub>) this tetrad effect was not detected. It was concluded that the tetrad effect is caused by fractionation of aluminium fluoride rather than fluoride REE complexes. A similar conclusion on two types of fluids derived from melt—diluted aqueous fluid that causes greisenization of host rocks and Na- and F-bearing brine that gives rise to albitization of rocks—has been drawn as a result of comprehensive study of the granitic Khangilai pluton (Badanina et al., 2004, 2006).

Thus the REE patterns of pitchblende may be explained by the formation of uranium mineralization from postmagmatic fluids derived from the evolved U and F-bearing silicic magma. If the magmatic source of uranium and REE is accepted as the most probable, then the discovery of the W-type tetrad effect in pitchblende as a natural postmagmatic mineral is



## 4. REE in pitchblende and host rocks

---

the first case in world practice and a missing link in the system of evidence for magmatic fractionation of REE with formation of the tetrad effect.

## Part III. Physicochemical conditions of mineralization



## **1. Fluid inclusions study**

Thermobarogeochemical studies in the SOF deposits have been performed by numerous researchers since initial exploration. The most advanced contribution has been made by specialists from GEOKhI (Vernadsky institute of geochemistry and analytical chemistry, Russian academy of sciences, Moscow) – G.B.Naumov, M.V.Mironenko, A.N.Salazkin, A.A.Nikitin and others (Naumov et al., 1985, Mironenko, 1985). The author regards the results of fluid inclusions (FIs) studies obtained by different researchers as the most consistent ones compared to mineralogy, isotopy, and geochemistry. According to a generally recognized point of view, uranium ore formation occurred from sodium-hydrocarbonate-chloride fluids circulated at temperatures below 200°C (most probably 120-170°C). Primary uranium mineralization precipitated at pressure drop, fluid boiling, uranyl-carbonate complexes decomposition, and U<sup>6+</sup> reduction on carbonaceous matter and other reductants such as sulfides, hydrocarbons, methane and so on (Naumov et al., 1985, Naumov, 1998).

This study obtains new data which contradicts with the commonly accepted view. It mainly concerns the temperature of ore forming fluid which occurred twice as high as previous estimations (530-300°C). This might be explained by the fact that in the past, fluid inclusions were measured in widely developed comb-like quartz of the 1<sup>st</sup> postore stage according to our notion. Cases of crosscutting and overgrowth of comb-like quartz by the uranium variety of U-Si metagel could confuse researchers and constrain them to considering it as synore quartz generation. This presumption is confirmed by high CO<sub>2</sub> concentrations reported for “synore” quartz whereas it is typical of postore quartz developed outside ore bodies in compliance with our data.

Actual synore quartz is markedly less common than postore quartz and its grain size usually does not exceed 50-100 μm. These two circumstances explain the absence of data on synore FIs. To succeed in getting new results, the author was forced to provide reliable ontogenic evidence of quartz-pitchblende paragenesis and to make himself a great number of double-polished sections with optimal thickness of about 100-200 μm for these specific studies.

### **1.1. Preore stage**

Predominant development of extensive metasomatic processes is the typical feature of the preore stage while the vein mineralization, quartz in particular, is essentially subordinate.



## 1. Fluid inclusions study

---

Moreover, cryptocrystalline and calcedony-like varieties of quartz are widespread in the preore mineral complex compared to well-crystallized quartz. This was the reason for the scarcity of data obtained on pre-uranium hydrothermal processes.

Few quartz crystals suitable for FI measurement have been found in samples from the Antei deposit. These crystals grew on the walls of fissures and were later overgrown by albite of the ore stage. The study of individual inclusions in quartz of the preore stage showed that the mineral formation proceeded from relatively concentrated solutions (8.3–9.5 wt. % NaCl equiv) of sodium chloride composition at 210–190°C.

### 1.2. Fluid inclusions in quartz of the ore stage

Three quartz generations have been established in the uranium ore mineral complex (Fig. 2.30, 2.31). Quartz of the first generation ( $Q_1$ ) is presented by micrograin aggregate of isometric grains saturated by finely dispersed iron oxides. Fluid inclusions (<15-20  $\mu\text{m}$ ) are composed of two phases (liquid+gas) with the gas phase occupying 50-60 vol.%. Homogenization temperature varies in the range of 530-500°C (Fig. 3.1, 3.2). The fluids feature Na-Cl composition with possible negligible admixture of hydrocarbonate ion. It was impossible to determine the composition of the last melted phase, probably it was salt hydrates. If it is the case, the concentration matches 23.2-26 wt.% NaCl equiv.

Quartz of the 2<sup>nd</sup> generation ( $Q_2$ ) is overgrown by brannerite and pitchblende with their particular joint growth (Fig. 2.30b, 2.32) testifying to their paragenesis. More precisely, quartz was formed slightly earlier than the bulk of brannerite and pitchblende so FIs in quartz exhibit physicochemical conditions of the beginning of pitchblende deposition.

All investigated inclusions in quartz  $Q_2$  at the Streltsovsky deposit possess two-phase compositions with constant ratios between phases. Boiling features were not observed.  $T_{\text{hom}}$  varies in the range of 415-280°C. In some inclusions, homogenization occurred with the meniscus disappearance that indicates transcritical fluid state along with calculations in the FLINCOR software (Brown, 1989). In the Antei deposit, some inclusions contained a solid phase. Boiling features were not detected, similar to the Streltsovsky deposit. Upper limit of  $T_{\text{hom}}$  at the Antei deposit is somewhat higher than at the Streltsovsky, total range matches 460-280°C. Summarizing, deposition of brannerite and pitchblende took place after quartz  $Q_2$  formation at the temperature decrease to 350-300°C.

Ore forming fluids at the Streltsovsky deposit possess Na-Cl compositions. At the Antei deposit, mineralization occurred from Na-Cl fluids, with sometimes  $\text{HCO}_3^-$  ions

# 1. Fluid inclusions study

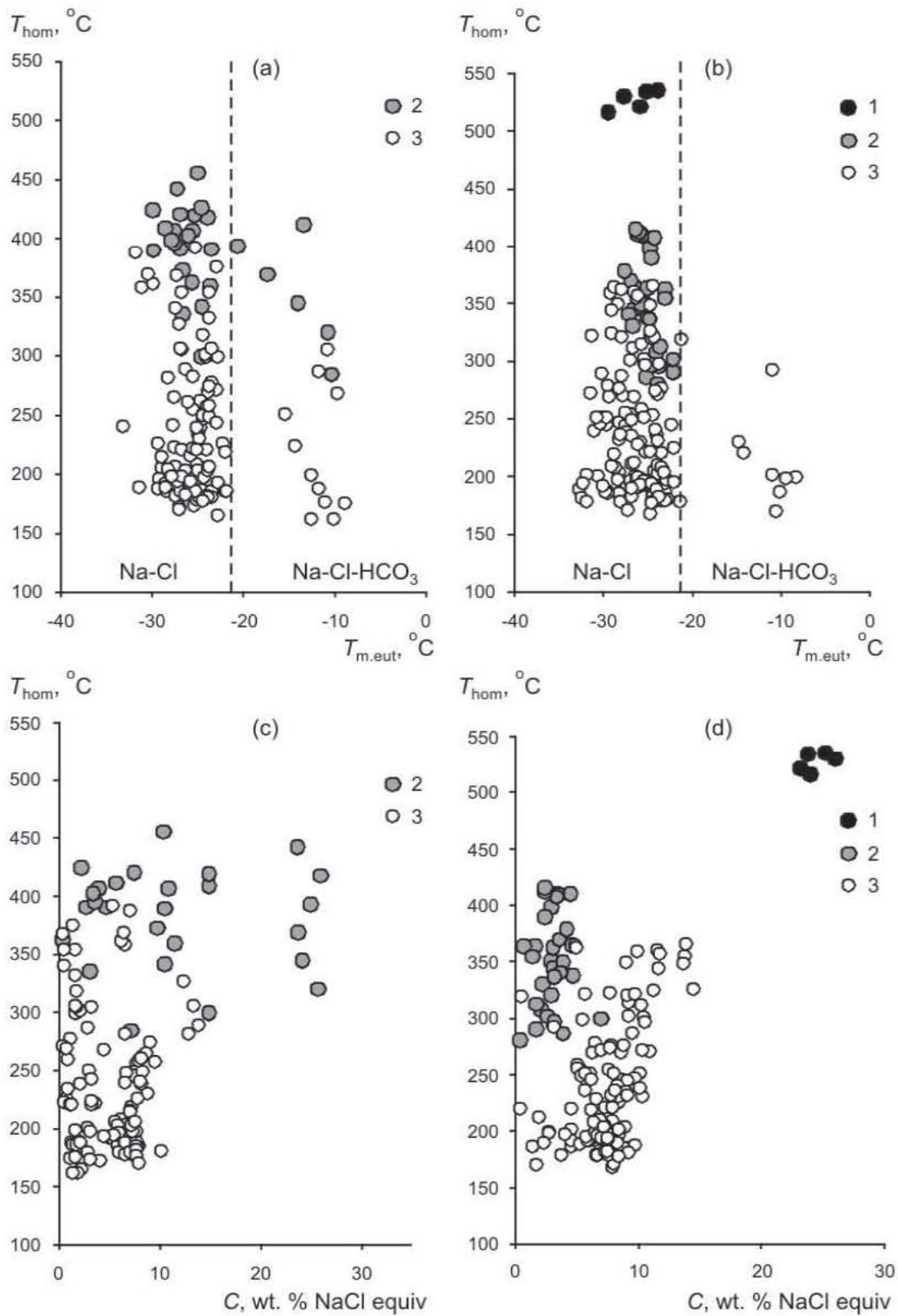


Fig. 3.1. (a, b)  $T_{\text{hom}}$  vs.  $T_{\text{m.eut}}$  and (c, d)  $T_{\text{hom}}$  vs.  $C$  for FIs for the (a, c) Antei and (b, d) Streltsovsky deposits. (1) Quartz  $Q_1$  and (2) quartz  $Q_2$  of the uranium ore stage; (3) quartz of the 1<sup>st</sup> postore stage. The dashed line separates the fields of sodium chloride and sodium bicarbonate–chloride solutions.

# 1. Fluid inclusions study

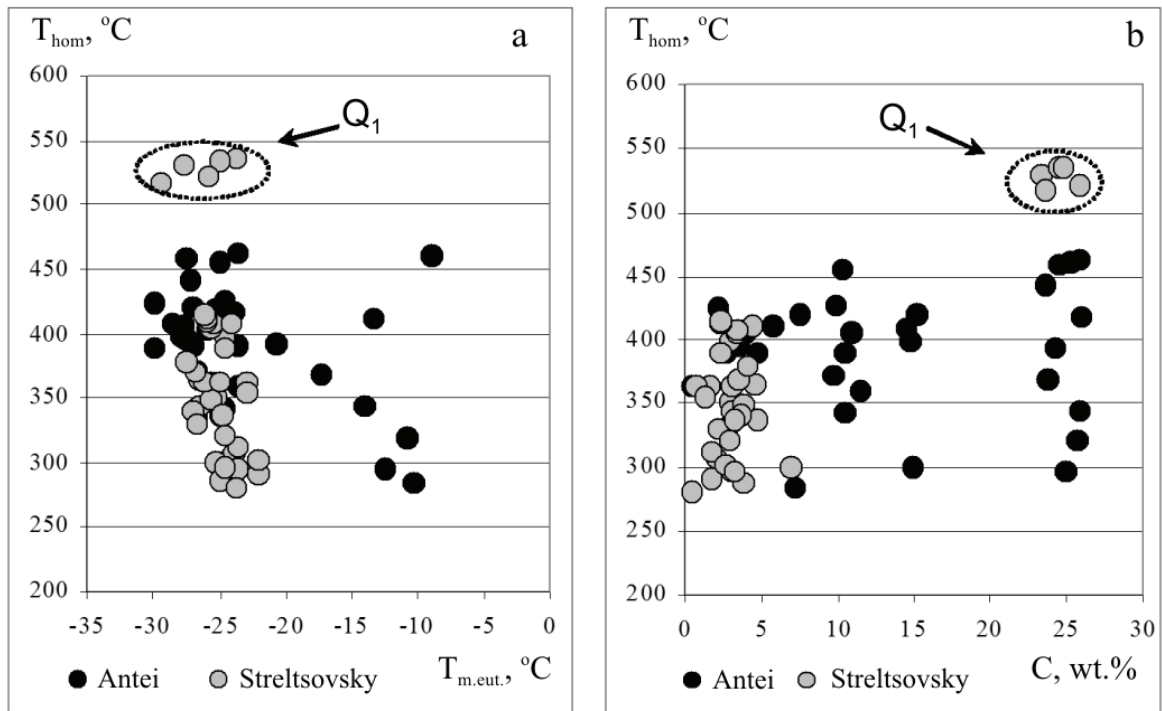


Fig. 3.2.  $T_{\text{hom}}$  vs.  $T_{\text{m.eut}}$  (a) and  $T_{\text{hom}}$  vs.  $C$  (b) for FIs in quartz of the ore stage in the Streltsovsky and the Antei deposits. High-temperature quartz of the 1<sup>st</sup> generation ( $Q_1$ ) is marked with the dashed area.

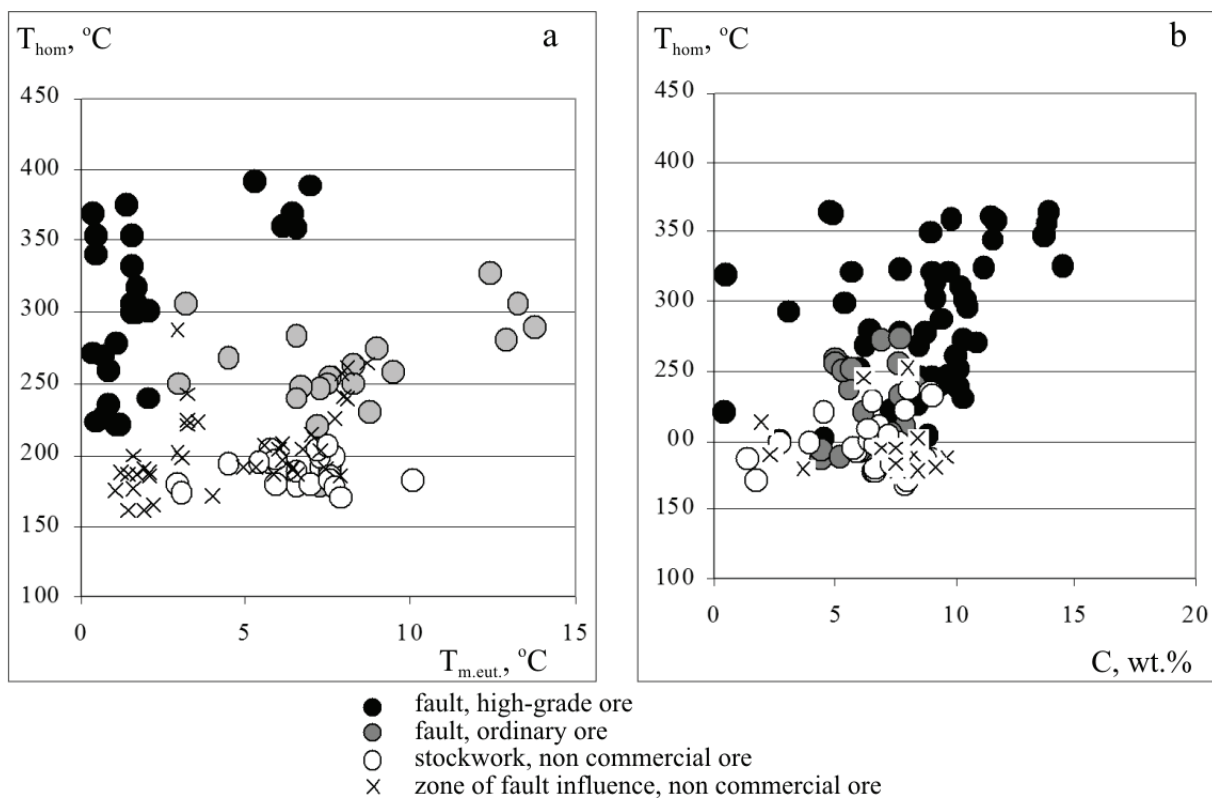


Fig. 3.3.  $T_{\text{hom}}$  vs.  $T_{\text{m.eut}}$  (a) and  $T_{\text{hom}}$  vs.  $C$  (b) for FIs in quartz of the 1<sup>st</sup> postore stage in the Streltsovsky and the Antei deposits located in ore bodies of different grade.

# 1. Fluid inclusions study

(Fig. 3.1, 3.2) that indicates a slightly alkaline environment. A solid phase with  $T_{\text{hom}}=370^{\circ}\text{C}$  was determined as nahcolite ( $\text{NaHCO}_3$ ). Ore forming fluids at the Antei deposit differ from those at the Streltsovsky deposit not only in higher temperatures and alkalinity but higher salinity as well. Its concentration at the Streltsovsky deposit varies from 7 to 1 wt.% NaCl equiv while at the Antei deposit it was essentially higher (especially the upper limit) and ranged from 26 to 0.5 wt.% NaCl equiv.

Gas phases in fluids of the uranium ore stage possessed aqueous composition. Only molecular  $\text{O}_2$  (from 100 to 88 mol.%) and  $\text{H}_2$  which are water radiolysis products have been detected in the gas phase by Raman microspectroscopy. Carbon dioxide was detected in two FIs at the Antei deposit. Methane and other gases were not detected.

Pressure calculated with the use of the FLINCOR software was the highest in the first quartz generation  $Q_1$  amounting to 825 bar (Table 3.1). Pressure in FIs located in quartz  $Q_2$  is smaller – it varies in the range 299-60 bar in the Streltsovsky deposit and 492-203 bar in the Antei deposit. Presumably, higher pressure in the Antei deposit reflects a higher depth of ore formation. Fluid density is approximately equal for synore quartz in all investigated deposits.

Table 3.1. Main physicochemical parameters of hydrothermal fluids in the Streltsovsky and Antei deposits, from fluid inclusion studies in quartz.

Quartz	Streltsovsky deposit				Antei deposit			
	$T_{\text{hom}}^*$ $^{\circ}\text{C}$	$C^*$ wt.%	$D$ , g/cm <sup>3</sup>	$P$ , bar	$T_{\text{hom}}^*$ $^{\circ}\text{C}$	$C^*$ wt.%	$D$ , g/cm <sup>3</sup>	$P$ , bar
<b>Uranium ore stage</b>								
quartz $Q_1$	530	23-26	0.72-0.67	825-748				
quartz $Q_2$	340	2.9	0.79-0.48	299-60	390	10	0.81-0.48	492-203
<b>1-st postore stage</b>								
high-grade ore	292	9.1	0.93-0.62	185-13	305	1.7	0.78-0.51	240-21
ordinary ore	191	6.7	0.94-0.84	39-11	255	8.3	0.94-0.73	118-8
low-grade ore	195	9.0	0.96-0.86	32-8	189	6.2	0.94-0.76	67-6
non-commercial ore	194	7.5	0.95-0.86	32-8	180	7.6	0.96-0.85	28-7

\* modal values



# 1. Fluid inclusions study

---

## 1.3. Fluid inclusions in quartz of the 1<sup>st</sup> postore stage

Quartz of the 1<sup>st</sup> postore stage is developed much more extensive than quartz of the ore stage. It allowed us to constrain physicochemical conditions of its formation in different environments – in various rocks at different depth and distance from faults, and in ore bodies of different grade. The latter were conditionally subdivided into four groups – high grade ore (above 0.5% of U), ordinary ore (0.1-0.5%), low grade ore (0.03-0.1%) and non commercial (off-balance) ore (0.01-0.03%).

Homogenization temperature and composition of fluids in the Streltsovsky and the Antei deposits are similar. Temperature regularly decreases at the increase of distance from large fluid conductors – fault zones. In the Streltsovsky deposit,  $T_{\text{hom}}$  in large faults varies in the range of 365-200°C while it does not exceed 250°C in the exocontact zone of faults and in stockwork zones outside faults. The Antei deposit is strictly controlled by a large fault zone, no. 160. Postore quartz was formed in the fault zone at the temperature 390-180°C while in the exocontact zone it decreases down to 210-170°C. High temperature of postore mineralization in the ore controlling fault is close to the temperature of ore formation. This probably indicates the absence of a significant temporal break between deposition of uranium and posturanium mineralization.

The fluids possessed Na-Cl or Na-HCO<sub>3</sub>-Cl composition, their concentration varies from 14 to 1 wt.% NaCl equiv. Maximum  $T_{\text{hom}}$  are typical of fluids circulated through large faults. The gas phase contains CO<sub>2</sub> and molecular O<sub>2</sub> and H<sub>2</sub> in various proportions. Carbon dioxide and HCO<sub>3</sub><sup>-</sup> ion concentration increases with the distance from faults. Methane has been determined in singular FIs outside large faults in amounts of more than 2.5 mol.%. Evidently, such regular compositional change is caused by fluid interaction with host rocks. Concluding, postore mineralization in large faults precipitated at maximum temperatures from essentially aqueous Na-Cl solutions, while in host rocks the temperature decreases and CO<sub>2</sub> starts to play more significant role.

Similar tendencies have been observed for postore hydrothermal fluids regarding the grade of uranium mineralization through which there were circulated. In both the Streltsovsky and the Antei deposits  $T_{\text{hom}}$  regularly decreases in FIs in quartz from high-grade ore to barren rocks. The most evidence is exhibited in the Antei deposit (Table 3.1). Molecular oxygen prevails in FIs from high-grade ore while it changes to CO<sub>2</sub> in low-grade and non-commercial ore. Hydrogen is most abundant in ordinary and low-grade ore in both the Streltsovsky and

## 1. Fluid inclusions study

the Antei deposits. Its amount decreases in high-grade and non-commercial ore at the expense of O<sub>2</sub> in the first case and CO<sub>2</sub> in the second one (Table 3.2, 3.3).

Besides fluid composition, T<sub>hom</sub> also exhibits regular change regarding ore grade. Similar to the dependency revealed concerning fault zones, T<sub>hom</sub> is the highest in high-grade ore and decreases with the decrease of the ore grade. In the Antei deposit, this regularity is manifested more clearly compared to the Streltsovsky deposit (respectively Tables 3.3 and 3.2). The similarity of T<sub>hom</sub> behavior regarding fault zones and the grade of ore bodies may be explained most easily by the fact that high-grade uranium mineralization is located in large fault zones in comparison with low-grade and non-commercial ore. In this way, common temperature dissipation from faults during the formation of postore quartz can be superimposed on the general tendency of high-grade ore location in fault zones.

Table 3.2. Temperature, salinity and gas composition in comb-like quartz of the 1<sup>st</sup> postore stage regarding the grade of uranium mineralization in the Streltsovsky deposit.

Ore grade	T <sub>hom</sub> , °C	C, wt. %	CO <sub>2</sub>	CH <sub>4</sub>	H <sub>2</sub>	O <sub>2</sub>
			mol. %			
High grade	365-200 (292)	14,5-0,4 (9.1)	0-3.1	n.d.	16.7-4.0	97.6 - 83.3
Ordinary	274-178 (191)	8.3-4.5 (6.7)	0.5-6.5	n.d.	29.7 - <0.5	83.0 - 38.8
Low grade	236-171 (195)	9.1-1.4 (9.0)	98.5-51	0 - <2	48.0 - 1.5	33.0 - 0
Non commercial	251-177 (194)	9.7-1.9 (7.5)	93-83.5	0 - <2.5	11.0-1.5	0.25 - 0

n.d. – not detected. Modal values in brackets.

Table 3.3. Temperature, salinity and gas composition in comb-like quartz of the 1<sup>st</sup> postore stage regarding the grade of uranium mineralization in the Antei deposit.

Ore grade	T <sub>hom</sub> , °C	C, wt. %	CO <sub>2</sub>	CH <sub>4</sub>	H <sub>2</sub>	O <sub>2</sub>
			mol. %			
High grade	392-221 (305)	7.0-0.4 (1.7)	n.d.	n.d.	7.8 - <0.2	99.8 - 90.5
Ordinary	305-178 (255)	13.8-3.0 (8.3)	75.0- 0	2.3 - 0	63.0-13.7	82.0-0
Low grade	287-162 (189)	8.7-1.2 (6.2)	100 - 0	6.0 - 0	100 - <1.0	≤0.3 - 0
Non commercial	206-170 (180)	10.1-2.9 (7.6)	99.5- 84.0	1.0 - 0	13.0 - ≤0.5	≤2 - 0

n.d. – not detected. Modal values in brackets.



## **2. Physicochemical conditions of Late Mesozoic mineralization: thermobarogeochemical and mineralogical evidences**

Physicochemical conditions of formation of preore, uranium-ore and postore mineralization in the SOF deposits has been constrained on the basis of fluid inclusion studies together with considerable use of mineralogical evidence and the geological setting of ore and barren mineral bodies.

Fluorine should occur in the ore-forming hydrothermal system in significant amounts, supported by the abundance of fluorite in the ore mineral assemblages. During the 1<sup>st</sup> postore stage, fluorite was replaced by quartz, carbonate, hydromica, and chlorite.

As appears from the occurrence of albite and nearly coeval brannerite, the mineral-forming fluid at the beginning of the uranium ore stage was characterized by elevated alkalinity. Further, the solution was likely neutralized, with formation of pitchblende. The high temperature of the ore-forming hydrothermal system appreciably exceeded the previous estimates, and comes into conflict with the “uranyl–carbonate” model of transport and deposition of uranium (Naumov, 1978, 1998) because uranyl–carbonate complexes are not stable at temperatures above 300–200°C (Romberger, 1988). In addition, carbon dioxide and hydrocarbonate ions are detected in FIs only in rare cases; indications of boiling and degassing of carbon dioxide were not established.

The absence of appreciable amounts of carbon dioxide in ore-bearing solutions is supported by the absence of carbonates in the uranium ore mineral complex even in basalts rich in  $\text{Ca}^{2+}$ ,  $\text{Fe}^{2+}$ , and  $\text{Mg}^{2+}$ . In the presence of  $\text{CO}_2$  or  $\text{HCO}_3^-$  in the ore-bearing fluid, these cations should be fixed in the form of carbonates.

Inadmissibility of the “uranyl–carbonate” model of  $\text{U}^{6+}$  transfer in the fluid phase at the SOF deposits is also supported by the absence of evidence for existence of  $\text{U}^{6+}$  in solution. Pitchblende and brannerite do not exhibit spatial relation to minerals-reductants (pyrite and other sulfides) or organic matter that is contained in tuffaceous and sedimentary interlayers of the caldera pile. The results of sampling of host rocks for organic carbon provided in the Tulukui open pit (data of I.V. Mel'nikov et al., IGEM RAS) demonstrate that the ore bodies are spatially separated from halos of elevated  $\text{C}_{\text{org}}$  contents (0.01–0.04%) or show crosscutting relations in areas of their co-location. The basement rocks and volcanics within the caldera contain carbonaceous matter in concentrations less than tenths of a percent, which cannot provide reduction of the great mass of uranium in local high-grade ore bodies. The absence of a noticeable influence of carbonaceous matter on the formation of hypogene



## 2. Physicochemical conditions of mineralization

---

uranium minerals in the SOF was confirmed by special investigations carried out by Uspensky et al. (1986). No indications on the presence of potential reductants ( $\text{H}_2\text{S}$ ,  $\text{CH}_4$ , etc.) in the ore-bearing solution, which could reduce  $\text{U}^{6+}$  after supposed decomposition of the uranyl-carbonate complexes, were revealed either.

Thus, taking into account new data on the high temperatures of hydrothermal ore-forming fluid, high fluorine activity in the process of uranium ore formation inferred from the mineralogical data, and the absence of signs which would support the existence of  $\text{U}^{6+}$  in solution, complex fluoride compounds of  $\text{U}^{4+}$  should be regarded as the most probable species of the uranium transport. Since uranium ore is localized in virtually all varieties of intrusive, volcanic, sedimentary, and metamorphic rocks (Ishchukova et al., 1998), their chemical composition hardly exerted a substantial effect on the stability of complex uranium compounds. Under these conditions, a drop of temperature down to 350–300°C was the crucial factor of ore deposition. This conclusion is consistent with thermodynamic computations carried out by B.N.Ryzhenko (unpublished data, 2006).

The physicochemical parameters of hydrothermal solutions at the 1<sup>st</sup> postore stage were determined on the basis of FIs study in comb-like quartz. Homogenization temperatures range from 396 to 168°C, largely being within 250–200°C; the highest temperature is typical of postore quartz from high-grade orebodies localized in large fault zones. The pressure of postore solutions approximately estimated with the Flincor program is 25–49 bar.

Fluid inclusions in quartz of the 1<sup>st</sup> postore stage are filled with sodium chloride and, less frequently, sodium hydrocarbonate–chloride solutions (Fig. 3.1). The mineralization of the solutions varies from 0.4 to 15 wt. % NaCl equiv. In the gas phase of FIs captured by quartz localized in high-grade orebodies, oxygen is sharply predominant (89.0–99.8 mol %). The hydrogen content is 0.2– 9.5 mol %. In FIs entrapped in quartz that occurs in ordinary and low-grade ore, the oxygen concentration falls and the leading role belongs to  $\text{H}_2$  and  $\text{CO}_2$ . In barren rocks, carbon dioxide is the main component; oxygen is absent, and hydrogen is noted rarely.

The radiolysis of water is the most probable cause of production of free oxygen and hydrogen in uranium-bearing fluids (Dubessy et al., 1988). The preferential accumulation of  $\text{O}_2$  in comparison with  $\text{H}_2$  in solutions circulating within ore bodies at both the uranium ore and postore stages is most likely explained by a higher diffusion coefficient of hydrogen (Vovk, 1979). The depletion of oxygen beyond ore bodies may be caused by its consumption for oxidation of  $\text{Fe}^{2+}$ -bearing silicates in the course of percolation of oxygen-bearing solutions through rocks (Perez et al., 2005). The accumulation of oxygen in ore bodies explains the

## 2. Physicochemical conditions of mineralization

---

hypogene replacement of pitchblende contained in high-grade ore by becquerelite  $[\text{Ca}(\text{UO}_2)_6\text{O}_4(\text{OH})_6 \cdot 8(\text{H}_2\text{O})]$  (Fig. 2.42, 2.43) and the prevalence of  $\text{U}^{6+}$  over  $\text{U}^{4+}$  in the U–Si metagel under unlikely conditions for development of supergene alteration.

The initial stages of postore solutions most likely were characterized by elevated acidity, as is evidenced by the occurrence of hydromica and the increase in porosity at the expense of leached plagioclase. By the end of the postore stage, the solutions were neutralized and inverted toward an increase in alkalinity, which provided for crystallization of carbonate and formation of coffinite instead of the U–Si metagel.



## Part IV. Genetic model of the uranium ore formation





## 1. Critical review of existing genetic models

The comprehensive studies of the SOF deposits allow the author to consider critically the existing genetic models of uranium ore formation and argue for a refined model of postmagmatic ore generation, which, from the author's opinion, explains the available data more consistently. As it was mentioned above, three genetic models discriminating on the source of uranium are the most popular at present for the SOF deposits: (1) uranium leached from host rocks during preore alteration, (2) uranium derived from mantle basic melt, and (3) uranium derived from uppercrustal acidic magma chamber.

The rocks that host the uranium mineralization in the caldera and the underlying basement cannot be regarded as the main source of economic uranium reserves. The following facts come into conflict with such an interpretation.

As has been shown by Andreeva et al. (1990, 1996<sub>1</sub>) and supported by the author's observations, the background low-intensity metasomatic alteration, although it converts a part of syngenetic uranium into a mobile state, does not lead eventually to its removal. In this regard, the argument for leaching of a considerable amount of uranium from rocks at the preore stage and its redeposition in ore bodies seems to be unconvincing.

As has been established from mineralogical study of the ore field, postore metasomatism led to the replacement of an appreciable portion of the primary uranium mineralization (pitchblende and brannerite) with a U–Si metagel and intense alteration of host rocks expressed in their replacement by hydromica, chlorite, quartz, and carbonate. The intensity of this alteration was higher than that of similar alteration at the preore stage. The removal of uranium from host rocks observed at the middle and upper levels of the deposits was most likely caused by postore alteration (Ishchukova et al., 1998, p. 500).

The high temperature (530–300°C) of uranium-bearing solutions, markedly exceeding the temperature of preore solutions (250–200°C), also contradicts hypothesis of uranium leaching from host rocks. According to this model, the temperature of postmagmatic solutions must progressively fall from early to late portions. On the other hand, if such a high-temperature fluid penetrated through large domain of rock for uranium leaching, its temperature should rapidly decrease and extensive halos of high-temperature alteration should develop. This is not in fact observed in the SOF. The only possibility for the fluid to preserve its high temperature would be a fast ascent along fault zones without any significant heat (and consequently mass) exchange with host rocks.

# 1. Critical review of genetic models

---

According to another model of uranium leaching from the upper flows of U-bearing rhyolites, the uranium ore was formed as a result of convective circulation driven by a thermal anomaly related to the upper crustal magma chamber. It is suggested that this process gave rise to the leaching of uranium from rhyolites, its transfer to a depth of a few kilometers, heating of solutions, and their subsequent ascent with formation of deposits (Chabiron et al., 2003). However, as follows from calculations performed by Malkovsky et al. (1994) and Malkovsky and Pek (1993), fluid flows in convective cells, having approached to within a few hundred meters of the surface, should reach it as an ideal fluid conduit and escape into the hydrosphere.

The 3D model of the upper crust constructed with the GeoSpline GIS module shows that the spatial disposition of the main fluid conduits makes the formation of large convective cells unlikely, breaking them into a number of local cells. The master fluid conduits comprise the steeply dipping Meridional and Central fault zones and the boundary caldera faults that reached the upper crustal magma chamber, as well as the NE-trending Argun and East Urulunghui fault zones, inclined to the northwest (Fig. 1.6-1.8). The latter fault zones do not open the magma chamber and partly screen the supposed ascending flows.

In terms of the model under consideration, it is difficult to explain the transfer of uranium from the upper level of oxygen-rich subsurface water, where uranium should largely occur in the form of  $U^{6+}$ , to deeper levels that are characterized by reducing conditions. In this case,  $U^{6+}$  must be reduced to  $U^{4+}$  with formation of a secondary enrichment zone, which is not actually observed.

The mantle-derived basaltic melts can hardly be the most probable source of uranium as suggested by Ishchukova et al., (1998) for the following reasons.

1. The Sm–Nd discontinuity in chondrite-normalized REE patterns of pitchblende may be explained only by fractionation of monazite in silicic melt.
2. Although the level of U content in basalts is elevated by three to four times relative to the global average, it remains not very high and insufficient for the formation of concentrated ore-bearing solutions.
3. The highest U and F contents have been detected in the lower basaltic flows, dated at 170–160 Ma, whereas the younger basalts are distinguished by lower concentrations of these elements, testifying to the depletion of basaltic magma in uranium long before the ore formation.

The results of our comprehensive investigations agree best with the magmatic model of uranium ore formation developed by F.I. Wolfson and his team (IGEM). According to this

## 1. Critical review of genetic models

---

model, the upper crustal chamber of silicic magma was a source of uranium, which was separated into the fluid phase, transported by hydrothermal solutions in the form of uranyl–carbonate complexes, and deposited as ore at a reducing barrier. The data obtained have allowed us to refine some aspects of this model.

It is suggested that another silicic magma rather than rhyolite derived from the upper crustal magma chamber served as a source of uranium. According to experimental results (Peiffert et al., 1996; Zharikov et al., 1987), the coefficient of uranium partitioning between haplogranitic melt and fluid indicates that the melt should be enriched in uranium and the fluid, depleted in this element.

The Sm–Nd discontinuity in the REE patterns of pitchblende is explained by monazite fractionation in the inferred parental silicic melt, and the tetrad effect of W type, as a result of separation of the evolved melt into immiscible phases. None of these features are detected in rhyolites that fill the Streltsovsky caldera.

The chronological gap of ~5 Ma that separates the last injections of granosyenite porphyry dikes along the faults bounding the caldera (140 Ma) and uranium ore deposition (135 Ma) is too long for the existence of a melt completed by derivation of ore-bearing solutions. According to numerical modeling of conductive heat transfer taking into account the latent heat of crystallization carried out by Malkovsky and colleagues at IGEM RAS with the finite difference method, an upper crustal magma chamber should crystallize within 26–60 ka after cessation of volcanic activity. All these data argue against the hypothesis that regards the upper crustal magma chamber as a potential source of uranium.





## **2. Assessment of crystallization timing of the upper crustal magma chamber by finite difference method**

This study was fulfilled by Victor Mal'kovsky and Alexander Pek (Laboratory of radiogeology and radiogeoeology, Modeling department) with the author's participation. The latter consisted in general target setting and providing of geological and physicochemical boundary conditions for the modeling. The main goal of the study was to evaluate quantitatively the probability of the acidic magma in the uppercrustal chamber to remain melted by the time of the uranium ore formation on the hypothesis that it was a source of postmagmatic uranium-bearing fluids. The results were published in the journal "Geology of Ore Deposits" (Mal'kovsky et al., 2007). The most important parts of the paper are quoted below omitting mathematical procedures.

### **2.1. Introduction**

According to the hypothesis developed by F.I. Wolfson and his associates, the silicic melt of the upper crustal magma chamber located at a depth of ~5 km beneath the caldera was the source of both the rhyolite that filled the caldera and the uranium ore hosted therein (Ishchukova et al., 1998). The K–Ar age of granosyenite porphyry dikes emplaced along the boundary faults and the late rhyolitic extrusions and vents is 145–140 Ma. The U–Pb age of pitchblende from uranium ore bodies is  $135 \pm 2$  Ma (Chernyshev and Golubev, 1996). Thus, a temporal gap of at least 5 Ma exists between the cessation of magmatic activity and the beginning of ore formation. This time interval could correspond to the time of cooling of a magma chamber a few thousand square kilometers in area. However, such a long existence of residual melt in a local shallow-seated magma chamber is improbable. One of the objectives of this study was settling this question.

In the context of this problem, the mechanism of uranium transfer with ore-bearing fluids and its precipitation in ore bodies is of great importance. The genetic models of hydrothermal uranium deposits, including those in the Streltsovsky ore field, are based on the conjecture that uranium is transported by ore-bearing fluids in the form of uranyl–carbonate complexes (Naumov, 1998), which are stable up to 300–200°C (Romberger, 1988). It is suggested that uranium is precipitated due to the degassing of carbon dioxide, breakdown of the uranyl–carbonate complexes, and reduction of  $U^{6+}$  to  $U^{4+}$ . As has been established by the recent study of fluid inclusions in quartz from deposits of the Streltsovsky ore field, the captured ore-bearing solutions are devoid of  $CO_2$  and do not bear indications of boiling and

## 2. Modeling of crystallization of uppercrustal chamber

---

degassing (Krylova et al., 2006). The examination of fluid inclusions in quartz grains syngenetic with uranium minerals has shown that uranium precipitated from ore-bearing fluid at a relatively high temperature.

The microgranular quartz of the first generation contains fluid inclusions homogenized at  $T_h = 530\text{--}500^\circ\text{C}$ . Quartz of the second generation, which preceded deposition of primary uranium minerals, crystallized at  $460\text{--}300^\circ\text{C}$  (Krylova et al., 2006). It is evident that the temperature of U-bearing solution in zones of its source and transit was obviously higher than the measured temperature. Thus, the carbonate model of hydrothermal ore formation is inconsistent with the formation conditions of the Streltsovsky ore field (Krylova et al., 2003).

Therefore, it may be suggested that uranium is transferred and deposited in the quadrivalent form without a change of valence state. A temperature drop is regarded as the main cause of ore deposition. This suggestion is consistent with experimental results on solubility of U(IV) complexes in haloid solutions (Zharikov et al., 1987; Red'kin et al., 1988; Peiffert et al., 1996).

Thus, the estimation of the temperature distribution in the caldera and its basement has important implications for discussion of the formation conditions of this unique uranium ore field. It is evident that the effect of the magma chamber beneath the caldera on the temperature of ore formation is crucial in this respect.

### 2.2. Statement of the problem

To calculate the temperature field created by a magma chamber beneath a caldera, it is necessary to know its lateral extent, the depth of its roof, and its vertical extent.

According to the results of modeling of volcanic calderas taking into account elastoplastic behavior of rocks, the horizontal dimensions of magma chambers beneath calderas are delineated by boundary faults, which start to form before the caldera collapse at the stage of uplift under the effect of rising magma. The critical magma chamber dimensions that provide boundary faulting are estimated at  $D/d > 5$ , where  $D$  is the diameter of the chamber and  $d$  is the depth of its roof. Having accepted  $D \sim 12$  km for the Streltsovsky caldera,  $d$  is equal to  $\sim 2.5$  km. The vertical separation along the boundary faults reaches 700 m, the thickness of volcanic and sedimentary fill is 1000 m, and the postore denudation of the Streltsovsky district is estimated at a few hundred meters (Ishchukova et al., 1998). Taking into account the above estimates and the calculation results reported by Guillou-

## 2. Modeling of crystallization of uppercrustal chamber

---

199

Frottier et al. (2000), the depth of the magma chamber below the present-day ground surface may be accepted as ~4 km. This estimate is consistent with the results of structural research and geophysical surveying, according to which the roof of the magma chamber was initially located as deep as ~5 km (Ishchukova et al., 1998).

The estimation of the vertical extent of the magma chamber is more speculative and is based on an analogy with the Sherlova Gora pluton of rare-metal Li–F granite, pertaining to the Kukul’bei Complex and located 150 km west of the Streltsovsky ore field. According to geophysical evidence substantiated by Dukhovskiy et al. (1979), the ratio of the horizontal and vertical dimensions of this pluton is 3:1. The same ratio was obtained for rare-metal granitic plutons of Central Kazakhstan (Dukhovskiy, 1980).

Taking into account the average diameter of the Streltsovsky caldera (12 km) and the slope of boundary faults (80°–85°), the average diameter of the magma chamber beneath this caldera is estimated at 10 km. If the ratio of the horizontal and vertical dimensions of the chamber is 3:1 (see above), its vertical extent is 3.5 km.

The Streltsovsky and Antei deposits are located in the central part of the caldera, where the horizontal component of the temperature gradient is much less than the vertical component. This implies that the variations of temperature in any horizontal direction are small and at any moment of time the temperature depends largely on the vertical coordinate. Thus, a one-dimensional nonstationary approximation may be applied to the computation of conductive heat transfer in the central portion of the caldera.

According to seismic data, the thickness of the Earth’s crust in the southern Argun region is about 38 km (Menaker, 1990). Sedimentary, metasedimentary, granite-gneissic, metadioritic, gray-gneissic, metabasic, and basaltic layers are recognized in the upper crust of the Transbaikalian region from top to bottom. Because the thermophysical properties of the most contrasting crustal rocks beneath the Streltsovsky caldera (granite gneiss and basalt) differ insignificantly, granodiorite is accepted as a modeling rock.

As follows from the above estimates, the initial position of the intrusion boundary may be set as 5 and 8.5 km (upper and lower boundaries respectively). On the basis of study of melt inclusions in quartz phenocrysts from rhyolite (Chabiron et al., 2001), it may be suggested that the initial temperature of rhyolitic melt in the magma chamber beneath the caldera was 1015°C. Because this melt contained less than 2.4 wt. % H<sub>2</sub>O, this temperature apparently was close to the temperature of melt crystallization.

## 2. Modeling of crystallization of uppercrustal chamber

---

### 2.3. Modeling results and discussion

The initial temperature distribution and the evolution of the temperature field from the initial moment to the complete solidification of melt are shown in Figs. 4.1 and 4.2, respectively. It can be seen that the intrusion solidifies rather rapidly and in the given case this process lasts for ~56 ka. Up to the final moment, the melt temperature remains constant and equal to the temperature of melt crystallization. From the moment of complete solidification, the temperature decreases in the entire intrusion. At  $t = 75$  ka, the temperature throughout the intrusion is less than  $907^{\circ}\text{C}$  (Fig. 4.2).

Further evolution of the temperature field is shown in Fig. 4.3. After 100 ka, the temperature anomaly (relative to the linear relationship versus depth) remains rather substantial. The anomaly decreases with time and becomes insignificant after 3 Ma.

The statement of the problem concerning the temperature field of the magma chamber beneath the Streltsovsky caldera was stimulated by the necessity of learning whether this temperature anomaly was able to exert an appreciable effect on the temperature conditions of ore formation.

The Late Mesozoic volcanic and hydrothermal activity in the caldera lasted for millions of years. The gap between rhyolite eruption and formation of uranium deposits covered about 5 Ma. As follows from thermophysical computations presented above, the temperature anomaly of the magma chamber beneath the caldera did not exert a significant effect on the temperature of uranium-bearing solutions, which, however, was much higher than the stationary geotherm. Therefore, another source should be found to explain the origin of the temperature anomaly during ore deposition. It is planned to discuss in a subsequent paper an alternative model that assumes supply of ore-forming fluid from a deep-seated source.

It should be kept in mind that some parameters of the above numerical model cannot be obtained by direct measurements. For example, the average geothermal gradient of the unperturbed temperature field was deduced from the present-day temperature and depth at the Moho discontinuity, although during the formation of the Streltsovsky caldera the gradient could have been different. The sequence of volcanic eruptions indicates that a lower crustal–mantle basaltic magma source was active before and after caldera formation in the SOF. Its temperature likely was about  $1200^{\circ}\text{C}$  (as of basaltic melt), and the upper edge was shallower

## 2. Modeling of crystallization of uppercrustal chamber

---

than 38 km. In this case, the average geothermal gradient would be higher than the value accepted in the above computation. An additional calculation has been carried out at a



## 2. Modeling of crystallization of uppercrustal chamber

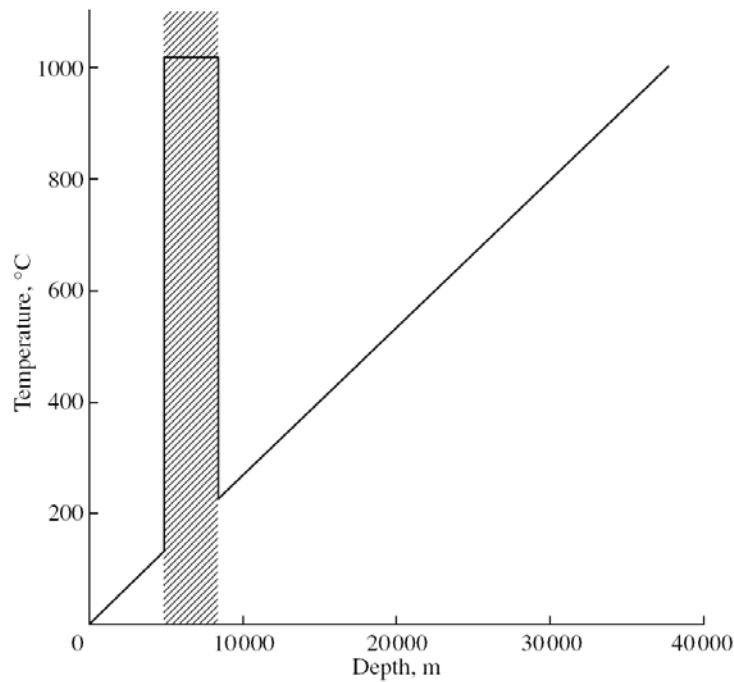


Fig. 4.1. Initial temperature distribution after emplacement of the intrusion (hatched rectangle).

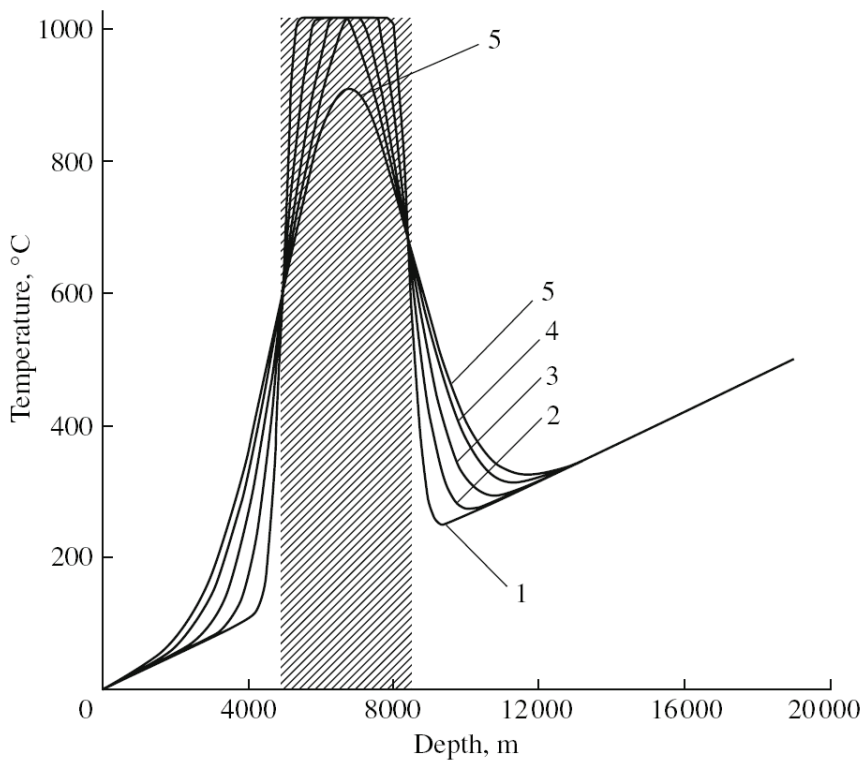


Fig. 4.2. Variation of temperature distribution during crystallization of the intrusion. (1)  $t = 3.25$  ka (region of melt has been reduced by 25%); (2)  $t = 13.7$  ka (region of melt has been reduced by 50%); (3)  $t = 31.4$  ka (region of melt has been reduced by 75%); (4)  $t = 56.3$  ka (intrusion has completely solidified); (5)  $t = 75$  ka (the temperature of the entire intrusion is lower than the temperature of melt crystallization and continues to fall due to thermal conduction to the country rocks). The intrusion is hatched.

## 2. Modeling of crystallization of uppercrustal chamber

wittingly overestimated geothermal gradient of 0.05 K/m, which corresponds to the upper edge of basaltic melt at a depth of 24 km. Furthermore, the thermal conductivity was decreased and the latent heat of crystallization was increased in accordance with the parameters inherent to mafic rocks. The computation results show that in this case the temporal variation of the temperature field and the vertical temperature distribution are quantitatively the same as shown in Figs. 4.2 and 4.3; the time of complete solidification is 132.7 ka. Thus, the conclusions drawn above remain valid.

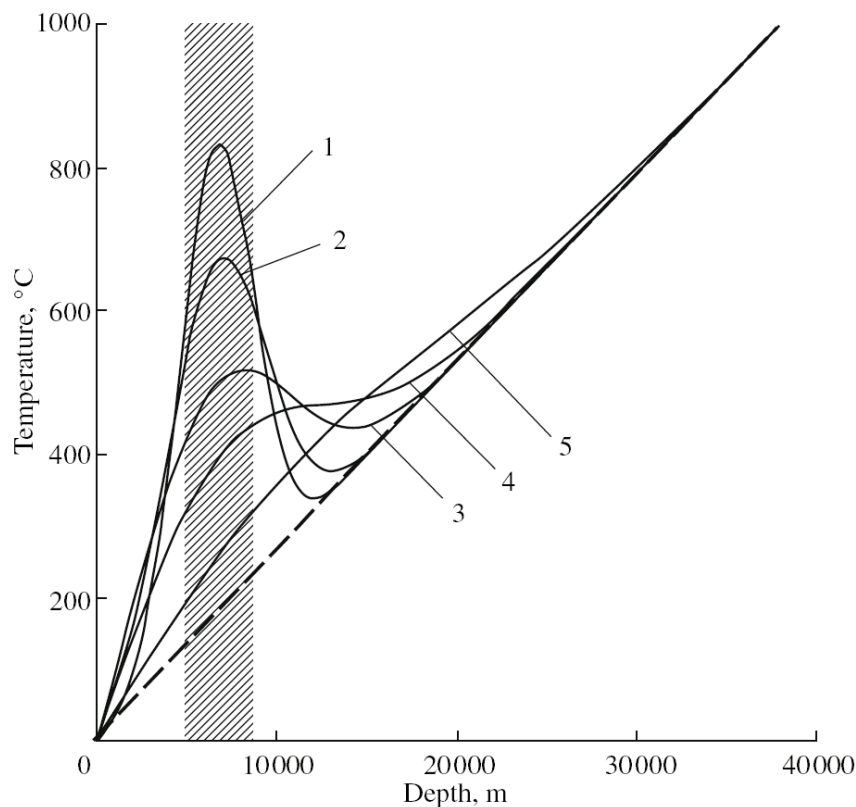


Fig. 4.3. Variation of temperature distribution after complete crystallization of melt.  $t =$  (1) 100 ka, (2) 200 ka, (3) 500 ka, (4) 1 Ma, and (5) 3 Ma. The intrusion is hatched. The dashed line indicates an unperturbed temperature distribution that corresponds to the accepted geothermal gradient.

The performed computation takes into account only thermal conduction and does not take into account convective heat transfer related to fluid flow driven by a temperature anomaly near the intrusion. In any case, convection intensifies heat transfer and increases the rate of magma solidification. Thus, if the contribution of the convective component was significant, the obtained duration of magma crystallization is overestimated.

Even the maximum possible time of magma crystallization in the upper crustal chamber is around 40 times less than the temporal gap between the cessation of magmatic

## 2. Modeling of crystallization of uppercrustal chamber

---

activity and ore deposition. This discrepancy makes the existence of residual melt in the shallow-seated magma chamber practically improbable as a source of ore-bearing hydrothermal solutions.

### **3. Magmatogeneous (post-magmatic) model of the uranium ore formation in the Streltsovsky ore field**

#### **3.1. The ore forming process – from the source to the deposits**

##### ***3.1.1. The area of ore-bearing fluid generation.***

In light of the available evidence, a crustal source of silicic magma enriched in F and U is the most probable source of uranium for the SOF deposits. The source melt is close in composition to the parental magma of the highly evolved Li–F granites of the Khangilai pluton and other rare-metal granites and ongonites of the eastern Transbaikal region. This suggestion is supported by the Sm–Nd discontinuity and the tetrad effect of W type in pitchblende, which have a convincing explanation in separation of U-, F-, and REE-bearing fluid from the evolved Li–F silicic magma.

The magmatic source of uranium is indirectly supported by the U–F geochemical association in volcanic rocks of the ore field. These elements progressively gained in Late Mesozoic rocks from the oldest basic volcanics through the intermediate and moderately silicic rocks to the youngest highly silicic rocks. This accumulation is traced not only in time but also in space if considering magma sources. In this respect, accumulation occurred upwards – from the mantle produced basalts through intermediate space and composition magma (dacites) to uppercrustal acidic magma (rhyolites). If this tendency is applied to the area of the uranium ore deposition, it logically comes to the end in time (170 Ma → 135 Ma) and space (40 km → 0–1.5 km) with the maximum concentration of these elements in the ores. The mantle produced basic magma has already been depleted regarding U and F by the time of the uranium ore formation.

This parallelism in U and F behavior allows the author to suggest the progressive concentration of these elements in magmatic melts from older basic to younger silicic magmas with the subsequent separation of U-bearing fluid and deposition of U and F minerals in ore. The only correction to this logical sequence is that the last magmatic container of U and F was not the acidic melt from the uppercrustal chamber but a deeper chamber of similar composition but more evolved magma.

The occurrence of two types of FIs – brine and low-density solution – in quartz formed at the uranium ore stage in combination with sodic wall-rock metasomatism, is consistent with recent experimental data (Veksler, 2004) and natural observations (Badanina et al., 2004). It was suggested that low-density aqueous fluid and sodic brine with an

### 3. Genetic model of uranium formation

---

anomalously high ability to transport ore components were derived from the F-bearing subalkaline silicic melt.

Experimental studies of fluid-melt systems, provided by Alexander Red'kin in the Institute of experimental mineralogy (IEM, Chernogolovka, Russia) with the author's participation, corroborated relatively low U concentrations in the fluid phase ( $10^{-6}$ – $10^{-5}$  mol/kg H<sub>2</sub>O) derived from F-bearing acid melt with chloride fluid, uraninite and columbite. The melt composition was taken similar to that of rhyolites of the SOF. These runs were made under the conditions of relatively low pressure (1 and 2 kbars) which correspond to the depths of less than 5 km, i.e. modeling the uppercrustal chamber. A fluid of the 1<sup>st</sup> type (one-phase fluid with one critical point) exists under these conditions.

However, last runs provided for similar fluid-melt system under higher pressure (>2 kbars) in the area of the existence of the 2<sup>nd</sup> type fluid (two-phase fluid with two critical points), disclosed essentially higher solubility of U both in the melt and in the co-existing fluid phase. These conditions correspond to higher depths (up to 10 km). Despite the fact that the study is still in progress, the preliminary results show evidence that these conditions are more favorable for uranium extraction to the fluid phase.

The rare-metal Li–F granitic plutons of the Kukulbei complex are widespread in the eastern Transbaikal region. The Kir-Kirinsky pluton of U-bearing morion leucogranite, dated at 145–138 Ma, is situated 40 km north of the Streltsovsky caldera. The large Kibirevsky–Idanginsky leucogranitic pluton, which likely also might belong to the Kukulbei complex, is located 10–15 km to the northeast. Therefore, there are grounds to infer that a similar hidden pluton may exist beneath the SOF as a source of uranium. Unfortunately, geophysical data in the SOF area still does not provide a more or less clear model of the upper part of the earth's crust down to the depth of 10-15 km.

Thus, the absence of evidence for migration of U<sup>6+</sup> and the close relations between U and F allow the author to suggest that uranium migrated as complex fluoride compounds of U<sup>4+</sup>. Rare earth elements also might fractionate into fluid in the form of complex fluoride or aluminofluoride (Veksler et al., 2005) compounds.



## 3. Genetic model of uranium formation

---

### *3.1.2. The area of U transportation.*

The pathways of hydrothermal fluids in the area of uranium deposition (in the caldera and its basement) have been constrained on the basis of morphology and structural controls of ore bodies, zonation of geochemical halos and altered rocks, and orientation of carbonate axes (Ishchukova et al., 1998). It revealed a steep ascending direction of main fluid flows in the basement with the centers in the Krasny Kamen volcanic apparatus and evidently in steeply dipping meridional faults in the east-northern parts of the caldera.

Ascending direction of fluid flows and their high temperature above 500°C unambiguously imply a deep source of the solutions which migrated to the deposition area along deeply rooted fault zones.

The Streltsovsky caldera was formed at the intersection of the meridional deep zone of high magmatic and fluid permeability (Dukhovskiy et al., 1998) with the Urulunghui and the Argunsky steeply dipping shear zones striking NE. As a result of comprehensive geophysical surveying, linear deeply rooted zones of seismic elements (zones of elevated permeability) are traced beneath the Streltsovsky caldera down to depths of 12 km and more (Dukhovskiy et al., 1998). These zones might serve as channels for ascending ore-bearing fluids transported uranium from a deep magmatic chamber to the deposition area.

Preserved high temperatures of the uranium-bearing fluids requires their fast ascent along the faults with minimum interaction with host rocks. Otherwise, heat dissipation is inevitable.

### *3.1.3. The area of ore deposition.*

It is supposed that formation of primary uranium minerals in the SOF deposits occurred due to an abrupt temperature decrease at the interaction of high-temperature fluids with the host rocks, and subsequent decomposition of complex  $U^{4+}$ -F compounds. The first portions of the fluid caused albitization and hematization of enclosing rocks. Then, with the temperature decrease down to 350-300°C, brannerite and pitchblende were formed. The following observations corroborate this conclusion.

1. The composition of host rocks does not affect uranium precipitation as the ore bodies occur in very different rocks – granites, basalts, dacites, rhyolites, tuffs, sandstones, conglomerates, limestones, amphibolites and so on. This is evidence that the chemistry of the fluid-rock interaction is not of great importance for uranium precipitation.

### 3. Genetic model of uranium formation

---

2. Thermodynamic calculations provided by Boris Ryzhenko (GEOKhI, Moscow, unpublished data, 2007) demonstrated that  $U^{4+}$ -F complexes become unstable at the temperatures below 300°C.
3. No evidences of the presence of  $U^{6+}$  in the ore-bearing fluid have been obtained. Organic matter and other possible reductants in the host rocks did not influence the uranium ore formation. Their quantities were unambiguously insufficient for reduction of significant masses of uranium deposited in local high-grade ore bodies. It means that uranium existed in the fluid in reduced state of  $U^{4+}$ .
4. Universally observed paragenesis of brannerite and pitchblende only with fluorite (except quartz) testifies the important role of F in uranium transportation and, hence, deposition.

Narrow halos of uranium dispersion around the ore bodies are in compliance with narrow zones of synore alteration (albitization and hematization). This is evidence that uranium precipitated rapidly during the fluid-rock interaction. It confirms the conclusion about the temperature drop as the driving force of uranium precipitation, when considering the difference between the temperature of the first portions of U-bearing fluids (500-530°C) and the temperature of the environment (150-200°C maximum, inferred from the temperature of the preore illitization).

This conclusion may help to interpret the reasons behind the difference in the grade of the uranium ore bodies. If temperature is the main parameter controlling uranium precipitation, its rapid decrease near individual large faults or localized in space fault zones should lead to concentrated deposition of uranium minerals. If high-temperature fluids circulate along such faults for a long time continuously, the thermal anomaly around the ore body should enlarge and additional masses of uranium minerals should be deposited at a shifted temperature barrier. By that way, a high-grade ore body with large reserves may be formed. This is confirmed by the fact that several pitchblende generations are usually present in rich ore bodies controlled by faults.

In stockworks, a more or less dense network of relatively small fractures produces a dispersed, extended “heat exchanger” between high-temperature fluids and host rocks. Under such conditions, a thermal anomaly near to an individual small fracture in a stockwork zone is not so contrasting as in the case of faults. This provides conditions for preferential development of finely disseminated rather than concentrated uranium mineralization.

Besides the influence of temperature on contrasted or dispersed type of uranium deposition, the role of faults and fractures as ordinary fluid conductors should be considered. As is well-known, mineral precipitation in open faults leads to the formation of veins while

### 3. Genetic model of uranium formation

---

thin veinlets and disseminated metasomatic mineralization are usually formed in stockworks. These two factors – temperature drop and the type of fluid conductors – mutually strengthen each other and intensify the cumulative effect.

Thus, structural factors seem to be the most important for the grade of the uranium ore bodies. It is manifested in the role of faults and fractures as fluid conductors on the one hand, and as “heat exchangers” on the other.

#### **3.2. Relationships between the uranium ore formation and pre- and postore hydrothermal processes**

To provide insights into the origin of mineral complexes pertaining to the preore and the first postore stages and their relationships with uranium ore mineralization, we considered the evolution of the main physicochemical parameters of the hydrothermal system, the geochemical specialization of mineral complexes, and the duration of their formation.

As is shown in the summary chart (Fig. 4.4), the hydrothermal solutions of the preore and the first postore stages are close in their physicochemical parameters. The temperature of the hydrothermal fluids that led to preore alteration and the formation of sulfide–carbonate–cryptocrystalline quartz veins ranges from 250 to 200°C. The temperature of postore solutions generally fits this range, but in high-grade uranium ore bodies localized in large fault zones, it rises to 300–350°C. Most likely, this was caused by thermal anomalies that arose within ore bodies due to the circulation of high-temperature ore-forming solutions. The 1<sup>st</sup> postore stage immediately followed the ore deposition (see below) and thus the thermal anomalies had no time to disappear.

The solutions at the preore stage and at the beginning of the 1<sup>st</sup> postore stage produced illite and were slightly acid (Andreeva and Golovin, 1998). At the end of the first postore stage, when carbonate and coffinite precipitated instead of the U–Si metagel, the solutions were neutralized and became alkaline. The reducing character of solutions of the pre- and postore stages follows from the occurrence of sulfides and chlorite. Only at the onset of the first postore stage did oxidizing conditions exist locally within high-grade ore bodies, providing oxidation of U<sup>4+</sup> to U<sup>6+</sup> and formation of iron hydroxides. This phenomenon was caused by radiolysis of hydrothermal fluid as a result of irradiation by uranium and products of its decay.

### 3. Genetic model of uranium formation

The geochemical specialization of both the preore and the 1<sup>st</sup> postore mineral complexes is characterized by development of sulfides (pyrite, marcasite, jordisite, and

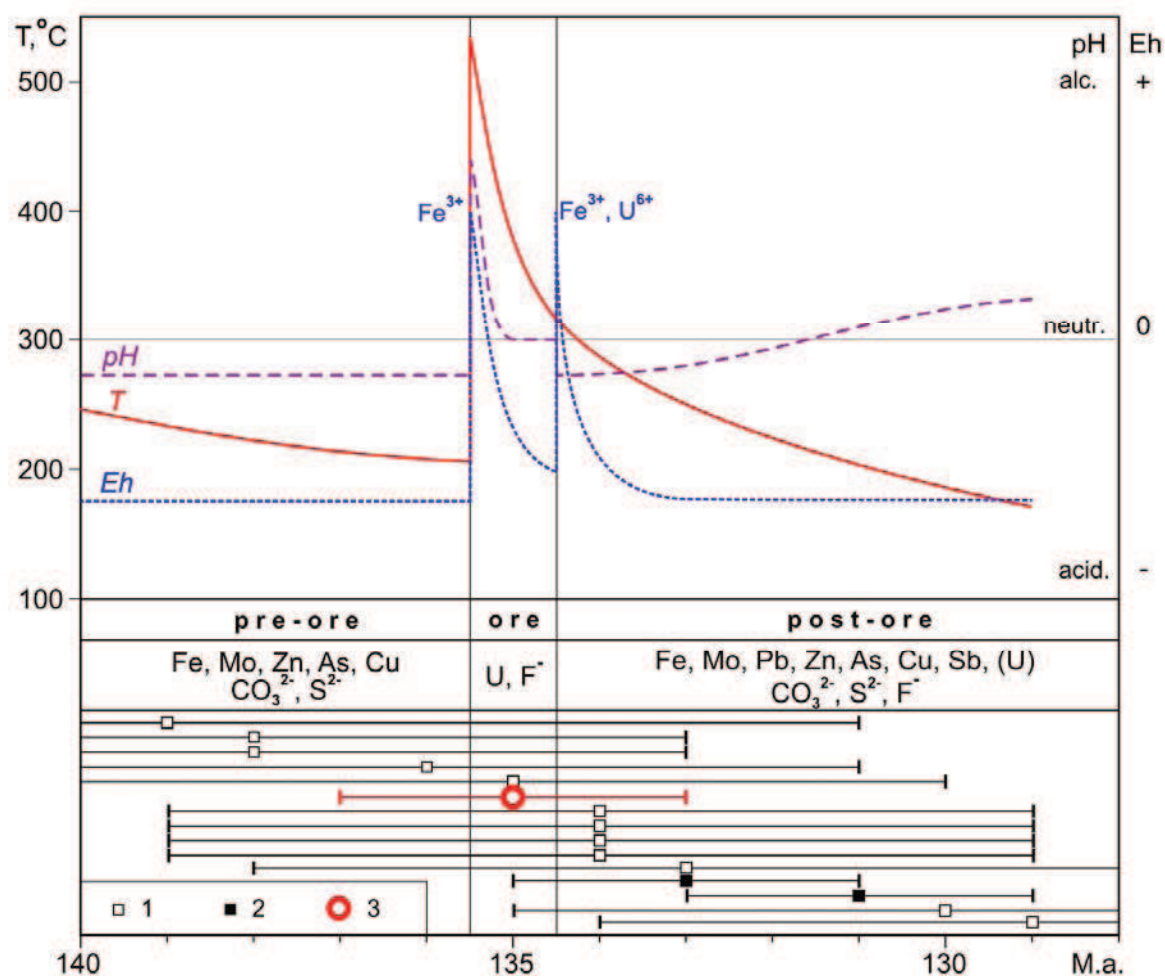


Fig. 4.4. Variation of the main physicochemical parameters of hydrothermal fluids at the preore, uranium ore, and first postore stages and geochemical specialization of the respective mineral complexes. (1–3) Isotopic age of hydromica (Andreeva et al., 1996<sub>2</sub>) and pitchblende (Chernyshev and Golubev, 1996): (1) K–Ar age of hydromica, (2) Rb–Sr age of hydromica and ankerite, (3) U–Pb age of pitchblende.

cleophane) and native Cu, As, and Sb. The crystallization of colloidal solutions resulted in the formation of chalcedony-like quartz, amorphous Mo sulfide, the U–Si metagel, and gels of complex and variable compositions. The duration of the preore and the first postore stages was determined by K–Ar and Rb–Sr dating of illite. According to these data (Andreeva et al., 1996<sub>2</sub>), illite crystallized continuously from 139 to 129 Ma ago.

The ore formation is a sharp anomaly against this background in all respects. This is a high-temperature process (530–300°C against 250–200°C typical of the preore and the first postore stages) that started with alkaline metasomatism and formation of brannerite and

### 3. Genetic model of uranium formation

---

subsequently gave way to neutralization of solutions and deposition of pitchblende. The dispersed iron oxides testify to oxidizing conditions at the beginning of the uranium ore stage; however, by the deposition of brannerite and pitchblende, the environment had changed to reducing one. The purely uranium specialization of the ore mineral complex contrasts with the chalcophilic and siderophile specialization of the preore and the first postore mineral complexes. These complexes also differ in anions: only fluorine is typical of the uranium ore complex, whereas, in both the preore and the 1<sup>st</sup> postore complexes, bicarbonate ions dominate and  $S^{2-}$  occurs as well.

The duration of the uranium ore stage was estimated by Malkovsky and colleagues at approximately 500 ka from the mathematical modeling of heat and mass transfer. The process is described in terms of forced convection and provides formation of uranium reserves at the Streltsovsky and Antei deposits. The modeling was based on geological and physicochemical boundary conditions obtained with the author's participation.

Thus, it may be suggested that the mineral formation at the preore and the first postore stages was a common long-term postmagmatic process likely initiated by emplacement of an upper crustal intrusion and eruption of silicic magmas. The process was interrupted 135 Ma ago by a relatively short-term injection of high-temperature U-bearing solutions derived from another chamber of evolved Li–F silicic magma. After the deposition of ore at a temperature barrier, the ongoing circulation of hydrothermal solutions gave rise to the development of illite and alteration of the primary uranium ore, as well as to more local and intense alteration of host rocks.





# General conclusions

Providing additional combined mineralogical and geochemical investigations in such a well-known and well-studied ore field as the Streltsovsky caldera allowed us to obtain new unexpected results which forced the correction of generally accepted views on physicochemical conditions of the ore formation and the genetic model as a whole.

Geochemical studies revealed close association of U and F which progressively gained in the Late Mesozoic rocks from the oldest basic volcanics (2.0- 2.5 ppm U and 0.3 wt. % F) through the intermediate and moderately silicic rocks (10 ppm U and ? F) to the youngest (140 Ma) highly silicic rocks (15-25 ppm U and ~3 wt. % F). This general trend has led to maximum accumulation of U and F in ore bodies (135 Ma) as a pitchblende-fluorite paragenesis.

Four stages have been distinguished in the Late Mesozoic hydrothermal epoch (140-125 Ma): preore, uranium ore, and the 1<sup>st</sup> and the 2<sup>nd</sup> postore ones. During the preore stage, both basement rocks and the sedimentary-volcanogenic pile of the caldera were subjected to pervasive but not intensive illitization with chloritization, carbonatization and silicification. Metasomatic alteration was accompanied by the formation of cryptocrystalline quartz veins with pyrite and Mo-Zn sulfides. The primary brannerite-pitchblende ore was formed in association with fluorite and quartz during the uranium ore stage. It was followed by narrow zones of albitization and hematization. At the first postore stage, this assemblage was intensively replaced by a U-Si metagel, which was previously identified as coffinite. More local but more intensive alteration similar to that of the preore stage was developed along fissures and quartz-fluorite-carbonate veins with pyrite, sulfides of Mo, Zn, Cu and other chalcophile elements. Veins of polychrome fluorite with quartz and calcite followed by narrow zones of kaolinization were developed during the second postore stage.

The most interesting results in paragenic analysis in terms of their novelty and significance for a genetic model are the following:

- widespread development of intensive fracture-controlled postore quartz-chlorite-carbonate-illite alteration of ores and host rocks similar on composition to the preore one;
- the absence of carbonates and sulfides in the uranium ore parageneses from one hand, and wide occurrence of fluorite instead from the other;
- the presence of Mo and Zn sulfides (jordisite-molybdenite and low-Fe sphalerite) in all stages except the uranium ore stage.

## General conclusions

---

U silicate previously known as coffinite is the second most abundant mineral in the SOF, its average amount comprises 30-40% in ores. Detailed study allowed the revelation of its polyphased composition with wide variation of U:Si ratios (50:1-1:3 in at.%), primary metacolloidal zonal texture of its deposition, numerous fissures of shrinkage, and amorphous state of the majority of the phases. Along with the absence of crystal faces in the segregations, it unambiguously testifies to colloidal nature of the phase. Uraninite and coffinite crystallites of 3-15 nm size were detected in some of U-rich varieties of U-Si phase indicating a beginning of metagel crystallization.

Fluid inclusion study is where the most novel results have been obtained. As it was established, the preore metasomatic alteration and related veined mineralization were formed under the effect of sodium-(bicarbonate)-chloride solution at a temperature of 210°C. The first portions of ore-forming fluids possessed extremely high temperatures of 530-500°C and were characterized by a transcritical state. Brannerite and pitchblende precipitated at 350-300°C from an essentially Na-Cl solution of various salinities. Primary uranium mineralization and host rocks were intensively altered during the 1<sup>st</sup> postore stage under the influence of Na-HCO<sub>3</sub>-Cl fluids at temperatures of 365 to 170°C. T<sub>hom</sub> of FIs regularly decreases from faults to their exocontact and stockwork zones and with the decrease of uranium ore grade. Molecular oxygen and lesser hydrogen are in fact the only constituents of the gas phase of FIs in synore quartz and predominant components in inclusions of postore quartz located in the high-grade ore. The gas phase is enriched in CO<sub>2</sub> outside the faults and the rich ore bodies. Water radiolysis is the reason of O<sub>2</sub> and H<sub>2</sub> production.

Thermobarogeochemical results and mineralogical observations are evidence against the “uranyl-carbonate” model generally accepted for the SOF deposits: high temperatures of the ore-forming fluids far above 200-250°C are destructive for uranyl-carbonate complexes; carbon dioxide presents in the fluid in negligible amounts while fluorine is universally occurred; no signs of fluid boiling have been observed; organic matter and other possible reductants do not affect ore formation indicating the most likely uranium migration in a quadrivalent state; chemical composition of host rocks does not influence precipitation of the uranium mineralization.

The chondrite-normalized REE patterns of pitchblende hosted in trachybasalt, trachydacite, and granite demonstrate a pronounced Sm-Nd discontinuity and a statistically significant tetrad effect of W type. These attributes may be most likely explained by separation of U- and REE-bearing fluid from an evolved silicic Li-F magma similar to that producing rare metal granites and ongonites in the Easter Transbaikalia. These features have

## General conclusions

---

not been established in the REE patterns of the rhyolites derived from the upper crustal magma chamber.

These data and a chronological gap of 5 Ma between silicic volcanism and ore formation do not allow us to suggest that uranium was derived from this magma chamber. According to the proposed model, an evolved silicic Li-F magma was a source of uranium. Quadrivalent uranium, together with REE, was fractionated into the fluid phase as complex fluoride compounds. The uranium mineralization was deposited at a temperature barrier. It is suggested that long-lasting illitization and the formation of molybdenum and zinc mineralization were genetically unrelated to the uranium ore formation which occurred as a relatively short (~500 ka) event against this background.





## Bibliography

- Aleshin A. P., Bonhoure J., Velichkin V. I., and Cuney M., 2006. REE patterns in pitchblende and post-ore mineralization in the Streltsovsky uranium ore field (Russia): scientific and applied aspects. In *Proceedings of IAGOD Symposium on Understanding the Genesis of Ore Deposits to Meet the Demands of the 21st Century*. Moscow, CD-ROM Version. 2.
- Aleshin A. P., Velichkin V. I., Cuney M., and Dymkov Yu. M., 2006. Polyphase coffinite-like uranyl metagel and its role in uranium redistribution in the monomineralic deposits of the Streltsovsky ore field (Transbaikal region, Russia). In *Proceedings of the International Symposium IAEA on Uranium Production and Raw Materials for the Nuclear Fuel Cycle, Vienna, Austria* (IAEA, Vienna, 2006), pp. 265–259.
- Aleshin A. P., Velichkin V. I., Cuney M., et al., 2002. Ontogeny and typomorphic features of uranium mineralization at monomineralic deposits of the Streltsovsky caldera (Transbaikal region, Russia). In *Proceedings of the International Symposium on Uranium Deposits: from Their Genesis to Their Environmental Aspects* (Prague, 2002), pp. 29–32.
- Andreeva O.V., Golovin V.A., 1979. Facial characteristics of argillic and hydromica metasomatites in the uranium deposits and ore potential of different facies. Preliminary report. IGEM, Moscow. 204 p. (in Russian)
- Andreeva O.V., Aleshin A.P., Golovin V.A., 1996. Vertical zonality of wallrock alterations in the Antei-Streltsovsky uranium deposit (eastern Transbaikal region, Russia). *Geologiya rudnykh mestorozhdenii (Geology of ore deposits)*. MAIK “Nauka”, V.38. No.5. P.396-411 (in Russian)
- Andreeva O. V. and Golovin V. A., 1998. Metasomatic processes at uranium deposits of Tulukui caldera, Eastern Transbaikal region Russia. *Geol. Ore Deposits* 40 (3), 184– 196
- Andreeva O. V., Wolfson F. I., Golovin V. A., and Rossman G. I., 1990. The behavior of uranium during low- temperature alteration of host rocks in uranium deposits. *Geokhimiya* 28 (2), 206–215.
- Andreeva O. V., Golovin V. A., Kozlova P. S., et al., 1996. Evolution of Mesozoic Magmatism and Ore-Forming Metasomatic Processes in the Southeastern Transbaikal Region, Russia. *Geol. Ore Deposits* 38 (2), 101–113.
- Anferov V.E., Kotov P.A., Plotnikova T.M., 1995. The Urthui deposit. In: Deposits of the Transbaikal region. Edited by N.P.Laverov. Moscow, Geoinformmark. V.1. Book 2. P.185-189 (in Russian).

## Bibliography

---

- Badanina E. V., Veksler I. V., Thomas R., et al., 2004. Magmatic evolution of Li–F, rare-metal granites: a case study of melt inclusions in the Khangilay complex, Eastern Transbaikalia (Russia). *Chem. Geol.* 210, 113–133 (2004).
- Badanina E. V., Trumbull R. B., Dulski P., et al., 2006. The Behavior of rare-earth and lithophile trace elements in rare-metal granites: a study of fluorite, melt inclusions and host rocks from the Khangilay complex, Transbaikal region, Russia. *Can. Mineral.* 44, 667–692.
- Bau M., 1996. Controls on the fractionation of isovalent trace elements in magmatic and aqueous systems: evidence from Y/Ho, Zr/Hf, and lanthanide tetrad effect. *Contrib. Mineral. Petrol.* 123, 323–333.
- Bocharov A. P., Vishnyakov V. E., Igoshin Yu. A., et al., 1978. Stratigraphic and absolute ages of volcanic rocks in some mesozoic depressions in Transbaikal region. In *Geology of Hydrothermal Ore Deposits* (Nauka, Moscow), pp. 243–256 [in Russian].
- Brown P.E., 1989. FLINCOR. *Amer. Mineralogist.* V. 74. P. 101-127.
- Bunh B., Schneider J., Dulski P., and Rankin A. H., 2003. Fluid-rock interaction during progressive migration of carbonate fluids, derived from small-scale trace element and Sr, Pb isotope distribution in hydrothermal fluorite. *Geochim. Cosmochim. Acta* 67 (23), 4577–4595.
- Chabiron A., Aleshin A. P., Cuney M., et al., 2001. Geochemistry of the rhyolitic magma from the Streltsovsky caldera (Transbaikal region, Russia): a melt inclusion study. *Chem. Geol.* 175, 273–290 (2001).
- Chabiron A., Cuney M., and Poty B., 2003. Possible uranium sources for the largest uranium district associated with volcanism: the Streltsovsky caldera (Transbaikal region, Russia). *Miner. Deposita* 38, 127–140.
- Chernyshev I. V. and Golubev V. N., 1996. The Strel'tsovskoe deposit, Eastern Transbaikal region: isotope dating of mineralization in Russia's largest uranium deposit. *Geochem. Int.* 34 (10), 834–846.
- Dubessy J., Pagel M., Beny J.-M., et al., 1988. Radiolysis evidenced by H<sub>2</sub>–O<sub>2</sub> and H<sub>2</sub>-bearing fluid inclusions in three uranium deposits. *Geochim. Cosmochim. Acta* 52, 1115–1167.
- Dzhurinsky B. F., 1980. Periodicity of Lanthanide Properties. *Zh. Neorg. Khim.* 25, 41–46 (in Russian).

## Bibliography

---

- Dukhovskiy A. A., Artamonova N. A., Molotkova M. N., et al., 1979. Volumetric geological structure of the Sherlova Gora area in Eastern Transbaikalian region. *Dokl. Akad. Nauk SSSR* 247 (6), 1444–1448 (in Russian).
- Dukhovskiy A. A., 1980. Geophysical characteristics of greisen deposits. *Geol. Rudn. Mestorozhd.* 22 (5), 18–27 (in Russian).
- Dukhovskiy A. A., Amantov V. A., Artamonova N. A., et al., 1998. Seismic and gravity images of major ore districts and fields of the southeastern Argun area (Eastern Transbaikalian region, Russia). *Geol. Ore Deposits* 40 (2), 87–99.
- Dymkov Yu.M., 1985. Mineral paragenesis of uranium-bearing veins. Moscow, “Nedra”. 207 p. (in Russian)
- Fidelis I. and Siekierski S., 1966. The regularities in stability constants of some rare earth complexes. *J. Inorg. Nucl. Chem.* 28, 185–188.
- Fidelis I. and Siekierski S., 1971. Regularities of tetrad effect in complex formation by f-electron elements: double-double effect. *J. Inorg. Nucl. Chem.* 33, 3191–3194.
- Fryer B. J. and Taylor R. P., 1987. Rare-earth element distributions in uraninites: implications for ore genesis. *Chem. Geol.* 63 (1–2), 101–108.
- Geology, formation conditions of the Streltsovskiy ore field deposits, and perfection of evaluative-prospecting criteria of hidden uranium mineralization, 1981. Ed. by F.I. Wolfson. Vol. 1: Geology of the Streltsovskiy ore field. Unpublished report, IGEM RAS (in Russian).
- Hidaka H. and Gauthier-Lafaye F., 2001. Neutron Capture Effects on Sm and Gd Isotopes in Uraninites. *Geochim. Cosmochim. Acta* 65 (6), 941–949.
- Guillou-Frottier L., Burov E. B., and Milesi J.-P., 2000. Genetic links between ash-flow calderas and associated ore deposits as revealed by large-scale thermo-mechanical modeling. *J. Volcanol. Geotherm. Res.* 102, 339–361.
- Irber W., 1999. The lanthanide tetrad effect and its correlation with K/Rb, Eu/Eu\*, Sr/Eu, Y/Ho, and Zr/Hf of evolving peraluminous granite suites. *Geochim. Cosmochim. Acta* 63 (3–4), 489–508.
- Ishchukova L.P., Pal'shin I.G., Rogov Yu.G., Philipchenko Yu.A., 1966. Peculiar features of the structure of the Tulukuevskiy block in Priargunie and experience of geophysical methods application for the revealing of its structure. *Proc. of the Academy of Sci. of USSR. Geological series.* No. 12, P. 26–40 (in Russian)

## Bibliography

---

- Ishchukova L. P., Modnikov I. S., and Sychev I. V., 1991. Ore-forming uranium systems of continental volcanic areas. *Geol. Rudn. Mestorozhd.* 33 (3), 16–25 (in Russian).
- Ishchukova L. P., Igoshin Yu. A., Avdeev B. V., et al., 1998. Geology of the Urulyungui Ore District and Molybdenum–Uranium Deposits of the Streltsovsky Ore Field. Geoinformmark, Moscow. 526 p. [in Russian].
- Kotov P. A. and Kotova A. I., 1995. The Garsonui Deposit. In *Ore Deposits of Transbaikal Region, Russia* Geoinformmark, Moscow, Vol. 1, Book 2, pp. 179–184 [in Russian].
- Krylova T. L., Aleshin A. P., Lhomme T., et al., 2006. New data on the formation conditions of the uranium ores at the Streltsovsky and Antei deposits (Eastern Transbaikal region, Russia). In *Proceedings of IAGOD Symposium on Understanding the Genesis of Ore Deposits to Meet the Demands of the 21st Century* (Moscow, 2006), CD-ROM Version.
- Krylova T. L., Aleshin A. P., Velichkin V. I., et al., 2003. Physico-chemical conditions of uranium ore formation at the Streltsovsky and Antei deposits (Eastern Transbaikal region, Russia). In *Proceedings of the International Symposium on Uranium Geochemistry, 2003* (Nancy, France, 2003), pp. 205–208.
- Kuznetsov V. A., Andreeva I. A., Kovalenko V. I., et al., 2004. Abundance of water and trace elements in the ongonite melt of the Ary-Bulak massif, Eastern Baikal region: evidence from study of melt inclusions. *Dokl. Earth Sci.* 396 (4), 571–576.
- Malkovsky V. I. and Pek A. A., 1993. Computer Simulation of Radionuclide Transport through Thermal Convection of Groundwater from Borehole Repositories (Lawrence Berkeley Laboratory, Univ. California, 1993) Report LBL-36385, UC-603, RAC-3.
- Malkovsky V. I., Pek A. A., Omel'yanenko B. I., and Drozhko E. G., 1994. Numerical modeling of radionuclide transport through thermal convection of groundwater from high-level nuclear borehole repository. *Izv. Ross. Akad. Nauk, Energ.*, No. 3, 113–122.
- Mal'kovsky V.I., Pek A.A., Aleshin A.P., Velichkin V.I., 2007. Estimation of the time of magma chamber solidification beneath the Strel'tsovka caldera and its effect on the nonstationary temperature distribution in the upper crust, the eastern transbaikal region, Russia. *Geology of ore deposits*. Vol.50. No.3. P.192-198.
- Mel'nikov I. V., 1985. Specific mineralogical–geochemical features of the formation of uranium mineralization. In *Contributions to Geology of Uranium Deposits (VIMS, Moscow, 1985)*, Vol. 93, Book 2, pp. 74–82 [in Russian].

## Bibliography

---

- Menaker G.I., 1970. Disposal of ore deposits in relation to deep structure of the earth's crust of the south of Transbaikalia. In *Questions of the regional geology and metallogeny of the Transbaikalia*. Chita, Vol.V, P. 33-38 (in Russian)
- Menaker G.I., 1972. Earth's crust structure and regularities of ore deposits location in the Central and Eastern Transbaikalia. *Geology of ore deposits*. No. 6, P. 3-16 (in Russian)
- Menaker G.I., 1990. Tectonosphere and metallogeny of the Transbaikalia in the geohistoric aspect. *Geology of ore deposits*. Vol. 32, No. 1, P. 21-36 (in Russian)
- Mioduski T., 1997. The "regular" and "inverse" tetrad effect. *Comments Inorg. Chem.* 19, 93–119.
- Mironenko M. V., 1985. Physicochemical Model of Hydrothermal Mineral Formation at the Antei Deposit. *Contributions to Geology of Uranium Deposits (VIMS, Moscow, 1985)*, Vol. 93, Book 2, pp. 83–87 [in Russian].
- Modnikov I. S., Perets N. A., and Sychev I. V., 1984. Formation conditions of uranium mineralization in the basement of volcanic depressions. *Sov. Geol.*, No. 1, 24–33.
- Monecke T., Kempe U., Monecke J., et al., 2002. Tetrad effect in rare earth element distribution patterns: a method of quantification with application to rock and mineral samples from granite-related rare metal deposits. *Geochim. Cosmochim. Acta* 66 (7), 1185–1196.
- Naumov G. B., 1978. Principles of the physicochemical model of uranium mineralization. Atomizdat, Moscow [in Russian].
- Naumov V. B., Kovalenko V. I., and Dorofeeva V. A., 1998. Fluorine concentration in magmatic melts: evidence from inclusions in minerals. *Geochem. Int.* 36 (2), 117–127.
- Naumov G. B., Mironenko M. V., Salazkin A. N., et al., 1985. New data on the geochemical formation conditions of the Streltsovsky ore field and their applied implications. In *Contributions to Geology of Uranium Deposits (VIMS, Moscow, 1985)*, Vol. 93, Book 2, pp. 65–74 [in Russian].
- Naumov G.B., 1998. Uranium migration in hydrothermal solutions. *Geology of ore deposits*. Vol. 40, No.4, P.307-325 (in Russian)
- Peiffert C., Nguyen-Trung C., and Cuney M., 1996. Uranium in granitic magmas. Part 2. Experimental determination of uranium solubility and fluid–melt partition coefficients in the uranium oxide–haplogranite–H<sub>2</sub>O–NaX (X = Cl, F) system at 770°C, 2 Kb. *Geochim. Cosmochim. Acta* 60, 1515–1529.



## Bibliography

---

- Perez J. R., Banwart S. A., and Puigdomenech I., 2005. The kinetics of O<sub>2</sub>(Aq) reduction by structural ferrous iron in naturally occurring ferrous silicate minerals. *Appl. Geochem.* 20, 2003–2016.
- Reviews in Mineralogy, 1984. Vol. 13: Micas. BookCrafters, Chelsea.
- Romberger S. B., 1988. Uranium transformation and accumulation in hydrothermal systems at temperatures up to 300°C: geological implications. In *Geology, Geochemistry, Mineralogy, and Estimation Methods of Uranium Deposits*. Mir, Moscow, pp. 28–36.
- Rybalov B. L., 2000. Localization of Late Mesozoic Ore Deposits in the Eastern Transbaikalian Region (Russia). *Geol. Ore Deposits* 42 (4), 340–350.
- Sevigny J. H., 1993. Monazite controlled Sm/Nd fractionation: an ion microprobe study of garnet phenocrysts. *Geochim. Cosmochim. Acta* 57, 4095–4102.
- Shmulovich K., Heinrich W., Moller P., and Dulski P., 2002. Experimental determination of REE fractionation between liquid and vapour in the system NaCl–H<sub>2</sub>O and CaCl<sub>2</sub>–H<sub>2</sub>O up to 450°C. *Contrib. Mineral. Petrol.* 144, 257–273.
- Takahashi Y., Yoshida H., Sato N., et al., 2002. W- and M-type tetrad effects in REE patterns for water–rock systems in the Tono uranium deposit, Central Japan. *Chem. Geol.* 184, 311–335.
- Tröger W.E., 1959. Optische bestimmung der gesteinsbildenden minerale. Stuttgart.
- Uspensky V. A., Kochenov A. V., and Khaldei A. E., 1986. Coaly substance in a hydrothermal uranium deposit. *Litol. Polezn. Iskop.* 21 (1), 104–110.
- Veksler I. V., 2004. Liquid immiscibility and its role at the magmatic hydrothermal transition: a summary of experimental studies. *Chem. Geol.* 210, 7–31.
- Veksler I. V., Dorfman A. M., Kamenetsky M., et al., 2005. Partitioning of lanthanides and Y between immiscible silicate and fluoride melts, fluorite and cryolite and the origin of the lanthanide tetrad effect in igneous rocks. *Geochim. Cosmochim. Acta* 69 (11), 2847–2860.
- Vovk I. F., 1979. Radiolysis of underground water and its geochemical implications. Nedra, Moscow [in Russian].
- Yurimoto H., Duke E. F., Papoke J. J., and Shearer C. K., 1990. Are discontinuous chondrite-normalized REE patterns in pegmatitic granite systems the result of monazite fractionation? *Geochim. Cosmochim. Acta* 54, 2141–2145.
- Zharikov V. A., Ivanov I. P., Omel'yanenko B. I., et al., 1987. Experimental study of the solubility of uraninite in granitic melts and fluid solutions at high pressures and temperatures. *Int. Geol. Rev.* 29, 997–1004.

## Bibliography

---

Zonenshain L. P., Kuz'min M. I., and Natapov L. M., 1990. Plate Tectonics in the Territory of the USSR. Nedra, Moscow [in Russian].



## Annexes

### Annex I. Main statistical parameters of samplings on host rocks subjected to illitization with associated alteration of different intensity

Table I.1. Statistical parameters of the sampling on basalts subjected to weak alteration (oxides and S – in %, other elements – in ppm)

Var	Vol	Dstrb	Min	Max	Avr	Stand
Al <sub>2</sub> O <sub>3</sub>	17	logn.	12.24	18.51	15.00	1.37
CaO	17	norm.	1.40	11.86	7.94	2.59
Fe <sub>2</sub> O <sub>3</sub>	17	norm.	5.22	10.98	8.77	1.43
Fe	6	norm.	36959	72005	56346	14366
K <sub>2</sub> O	17	norm.	1.09	3.13	2.27	0.57
MgO	17	logn.	2.37	8.07	4.45	1.64
MnO	17	norm.	0.07	0.27	0.16	0.05
Mn	6	logn.	389.75	2116.17	909.98	648.01
Na <sub>2</sub> O	17	norm.?	0.43	3.79	2.91	0.95
P <sub>2</sub> O <sub>5</sub>	17	norm.	0.21	0.60	0.47	0.09
SiO <sub>2</sub>	17	logn.	43.58	64.73	48.81	4.79
S	8	logn.	0.00	0.03	0.00	0.01
TiO <sub>2</sub>	17	norm.	0.86	1.58	1.35	0.16
Ti	6	norm.	6217	8998	7790	1081
As	11	logn.	2.88	15.30	7.03	4.01
Ba	17	logn.	339.85	1361.74	670.73	331.11
Be	17	logn.	1.50	7.82	3.26	1.92
Bi	11	logn.	0.00	0.06	0.00	0.02
Cd	17	norm.	0.00	1.23	0.40	0.38
Ce	17	norm.	35.56	101.15	80.41	16.76
Co	17	norm.	18.33	48.03	31.93	7.17
Cr	17	logn.	230.69	975.00	438.66	219.28
Cs	17	logn.?	18.29	662.70	42.19	121.28
Cu	17	logn.	10.59	85.45	34.59	19.09
Dy	17	norm.	2.75	5.29	4.07	0.57
Er	17	logn.	1.49	2.64	1.93	0.25
Eu	17	norm.	1.06	2.11	1.85	0.24
Ga	17	logn.	16.81	24.26	19.74	2.17
Gd	17	norm.	3.16	7.22	5.65	0.93
Ge	9	norm.	0.86	1.86	1.39	0.28
Hf	17	norm.	2.91	5.93	4.54	0.67
Ho	17	logn.	0.52	1.00	0.73	0.10
In	9	logn.	0.06	0.08	0.07	0.01
La	17	norm.	16.21	45.16	37.44	7.99
Lu	17	logn.	0.19	0.38	0.26	0.05
Mo	17	norm.	0.48	2.53	1.63	0.54
Nb	17	norm.	3.77	24.82	14.39	4.75
Nd	17	norm.	18.50	46.00	37.68	7.19
Ni	17	logn.	45.19	295.29	131.16	73.24
Pb	17	logn.	7.28	17.24	11.24	2.13
Pr	17	norm.	4.51	11.41	9.44	1.88
Rb	17	norm.	12.07	161.27	86.24	52.42
Sb	11	norm.	0.00	5.70	1.22	1.79
Sc	8	logn.	18.48	34.66	23.31	4.77

## Annexes

Var	Vol	Dstrb	Min	Max	Avr	Stand
Sm	17	norm.	3.86	8.68	7.08	1.18
Sn	11	logn.	1.06	2.02	1.44	0.30
Sr	17	norm.	375.50	1308	871.35	245.06
Ta	17	norm.	0.28	1.74	0.99	0.32
Tb	17	norm.	0.47	0.96	0.75	0.10
Th	17	norm.	3.17	9.61	7.22	1.85
Tm	17	logn.	0.21	0.37	0.27	0.04
U	17	logn.?	0.75	47.50	2.58	8.69
V	17	norm.	112.59	215.60	184.80	25.13
W	17	norm.?	0.00	22.56	1.91	4.43
Y	17	logn.	15.20	27.92	21.08	3.54
Yb	17	logn.	1.42	2.35	1.75	0.22
Zn	17	logn.	87.03	146.48	108.13	13.95
Zr	17	norm.	115.00	245.74	195.67	29.87
LOI	15	norm.	3.68	12.68	8.15	2.99

Note: here and below: **Var** – variable (elements and Loss On Ignition), **Vol** – sampling volume, **Dstrb** – the most appropriate distribution law (norm. – normal, logn. – logarithmically normal), **Avr** – mean according to the distribution law (average for normal law and geometric mean for logarithmically normal law), **Stand** – standard deviation.

Table I.2. Statistical parameters of the sampling on basalts subjected to moderate and strong alteration (oxides and S – in %, other elements – in ppm)

Var	Vol	Dstrb	Min	Max	Avr	Stand
Al <sub>2</sub> O <sub>3</sub>	5	logn.	15.17	17.48	16.12	0.85
CaO	5	norm.	1.43	7.65	5.27	2.32
Fe <sub>2</sub> O <sub>3</sub>	5	logn.	4.88	7.47	5.95	1.05
Fe	4	norm.	$\frac{2644}{2}$	47552	37184	9492
K <sub>2</sub> O	5	logn.	2.32	3.15	2.65	0.41
MgO	5	norm.	1.85	2.81	2.41	0.39
MnO	5	logn.	0.03	0.20	0.08	0.06
Mn	4	logn.	146	1232	447	461
Na <sub>2</sub> O	5	norm.	1.17	4.20	3.20	1.18
P <sub>2</sub> O <sub>5</sub>	5	norm.	0.51	0.62	0.58	0.04
SiO <sub>2</sub>	5	norm.	48.54	58.46	53.75	4.02
S	4	norm.	0.11	0.32	0.23	0.09
TiO <sub>2</sub>	5	logn.	1.39	1.67	1.47	0.11
Ti	4	norm.	6654	9918	8487	1353
Ba	5	logn.	360	7440	1625	2815
Be	5	logn.	3.24	7.73	4.72	1.78
Cd	5	logn.	0.47	2.86	1.06	0.94
Ce	5	norm.	88.59	102.97	95.98	6.09
Co	5	logn.	28.39	211.94	58.77	76.03
Cr	5	logn.	245	358	291	43
Cs	5	norm.	24.33	39.36	32.52	5.92
Cu	5	logn.	46.42	82.94	59.28	17.36
Dy	5	logn.	3.70	4.43	4.01	0.27
Er	5	norm.	1.50	2.16	1.82	0.24
Eu	5	logn.	1.80	2.26	2.00	0.21
Ga	5	norm.	18.32	22.22	20.25	1.65
Gd	5	norm.	5.24	6.60	6.04	0.53
Hf	5	logn.	4.47	5.66	4.96	0.49



## Annexes

Var	Vol	Dstrb	Min	Max	Avr	Stand
Ho	5	norm.	0.60	0.83	0.71	0.08
La	5	logn.	43.52	48.68	45.85	2.25
Lu	5	logn.	0.19	0.27	0.21	0.03
Mo	5	norm.	1.05	2.41	1.99	0.55
Nb	5	logn.	12.91	25.48	16.59	5.20
Nd	5	logn.	40.61	47.93	43.65	3.36
Ni	5	logn.	92.06	482.96	167.76	162.66
Pb	5	logn.	12.54	35.60	16.56	9.88
Pr	5	logn.	10.18	12.29	11.22	0.85
Rb	5	norm.	67.52	142.39	106.90	30.10
Sc	4	norm.	20.60	23.84	22.28	1.43
Sm	5	logn.	7.14	8.48	7.78	0.56
Sr	5	norm.	534	1268	924	261
Ta	5	logn.	0.87	2.12	1.18	0.50
Tb	5	logn.	0.71	0.85	0.77	0.06
Th	5	norm.	8.05	9.76	8.96	0.67
Tm	5	logn.	0.24	0.31	0.25	0.03
U	5	norm.	3.23	5.79	4.47	0.98
V	5	norm.	147	179	164	13.91
W	5	logn.	0.42	6.44	1.12	2.55
Y	5	norm.	15.15	19.51	18.19	1.78
Yb	5	logn.	1.39	1.85	1.52	0.18
Zn	5	norm.	63.45	92.28	79.21	10.52
Zr	5	logn.	180	235	199	20.67
LOI	5	norm.	5.53	9.89	8.05	1.65

Table I.3. Statistical parameters of the sampling on dacites subjected to weak alteration (oxides and S – in %, other elements – in ppm)

Var	Vol	Dstrb	Min	Max	Avr	Stand
Al <sub>2</sub> O <sub>3</sub>	5	logn.	15.03	16.23	15.53	0.44
CaO	5	norm.	1.38	1.96	1.70	0.22
Fe <sub>2</sub> O <sub>3</sub>	5	logn.	3.01	4.96	3.90	0.72
Fe	4	logn.	21418	38078	27977	7757
K <sub>2</sub> O	5	norm.	4.02	5.13	4.78	0.44
MgO	5	logn.	0.31	0.36	0.34	0.02
MnO	5	norm.	0.00	0.03	0.02	0.01
Mn	4	logn.	103	217	149	61.49
Na <sub>2</sub> O	5	norm.	2.97	4.46	3.77	0.59
P <sub>2</sub> O <sub>5</sub>	5	logn.	0.12	0.16	0.13	0.02
SiO <sub>2</sub>	5	logn.	65.20	67.75	66.33	1.25
TiO <sub>2</sub>	5	logn.	0.58	0.66	0.61	0.03
Ti	4	norm.	3419	3822	3632	165
Ba	5	logn.	528	685	597	58.32
Be	5	norm.	2.96	3.90	3.48	0.43
Cd	5	norm.	0.17	0.37	0.30	0.08
Ce	5	logn.	107	118	112	4.47
Co	5	norm.	3.55	8.50	5.90	2.22
Cr	5	norm.	3.83	20.24	12.44	6.04
Cs	5	logn.	9.88	22.27	14.36	4.76
Cu	5	logn.	6.60	19.62	10.61	5.57
Dy	5	norm.	4.26	4.87	4.60	0.25

## Annexes

Var	Vol	Dstrb	Min	Max	Avr	Stand
Er	5	norm.	2.35	2.67	2.54	0.13
Eu	5	norm.	1.01	1.32	1.19	0.13
Ga	5	logn.	20.79	22.90	21.41	0.87
Gd	5	logn.	5.10	6.11	5.54	0.42
Hf	5	logn.	8.98	10.33	9.56	0.56
Ho	5	norm.	0.83	0.98	0.92	0.06
La	5	logn.	48.84	56.74	52.22	3.28
Lu	5	norm.	0.33	0.41	0.37	0.03
Mo	5	logn.	1.44	6.77	2.71	2.10
Nb	5	logn.	15.36	29.13	19.74	5.36
Nd	5	logn.	40.98	47.29	43.34	2.71
Ni	5	logn.	8.57	57.62	20.90	19.73
Pb	5	logn.	28.83	36.65	31.73	4.12
Pr	5	logn.	11.67	13.16	12.27	0.63
Rb	5	norm.	173	248	210	27.66
Sc	4	norm.	24.94	26.47	25.81	0.64
Sm	5	logn.	7.05	8.22	7.56	0.56
Sr	5	norm.	137	298	228	63.95
Ta	5	logn.	1.29	1.46	1.36	0.06
Tb	5	logn.	0.75	0.93	0.82	0.07
Th	5	logn.	26.72	33.03	28.55	2.52
Tm	5	norm.	0.35	0.40	0.38	0.02
U	5	logn.	4.51	11.86	6.58	2.96
V	5	logn.	42.28	49.78	45.43	3.02
W	5	logn.	2.68	3.65	3.08	0.45
Y	5	logn.	21.96	30.40	24.72	3.27
Yb	5	logn.	2.16	2.78	2.45	0.22
Zn	5	logn.	41.24	57.63	48.44	7.68
Zr	5	norm.	389	423	408	13.31
LOI	5	norm.	2.31	2.66	2.52	0.14

Table I.4. Statistical parameters of the sampling on dacites subjected to moderate and intensive alteration (oxides and S – in %, other elements – in ppm)

Var	vol	dstrb	min	max	avr	stand
Al <sub>2</sub> O <sub>3</sub>	8	norm.	14.63	16.58	15.63	0.60
CaO	8	norm.	0.18	2.50	1.35	0.86
Fe <sub>2</sub> O <sub>3</sub>	8	norm.	1.99	5.96	3.05	1.36
Fe	6	logn.	14370	33049	19624	8331
K <sub>2</sub> O	8	norm.	1.66	6.95	4.88	1.77
MgO	8	logn.	0.24	0.70	0.37	0.17
MnO	8	norm.	0.00	0.02	0.01	0.01
Mn	6	logn.	73.01	163	109	33.98
Na <sub>2</sub> O	8	logn.	1.82	5.76	3.09	1.37
P <sub>2</sub> O <sub>5</sub>	8	norm.	0.06	0.18	0.11	0.04
SiO <sub>2</sub>	8	norm.	64.15	70.34	67.60	2.03
S	6	norm.	0.00	0.44	0.11	0.17
TiO <sub>2</sub>	8	norm.	0.52	0.68	0.61	0.05
Ti	6	norm.	2273	3915	3484	614
Ba	8	logn.	220	1498	678	384
Be	8	logn.	3.10	14.16	4.50	3.72
Cd	8	norm.	0.16	0.52	0.37	0.13

## Annexes

Var	vol	dstrb	min	max	avr	stand
Ce	8	norm.	84.42	141	111	18.76
Co	8	logn.	2.56	21.64	6.17	6.39
Cr	8	logn.	7.98	105	20.73	34.16
Cs	8	logn.	10.79	31.30	16.80	6.87
Cu	8	logn.	4.36	57.91	14.09	17.93
Dy	8	logn.	3.65	5.13	4.30	0.52
Er	8	logn.	2.20	2.87	2.41	0.20
Eu	8	logn.	0.90	1.53	1.10	0.20
Ga	8	norm.	17.21	27.20	22.76	3.17
Gd	8	logn.	4.00	6.60	5.10	0.86
Hf	8	norm.	8.63	10.68	9.85	0.82
Ho	8	logn.	0.74	1.03	0.85	0.09
La	8	norm.	41.69	64.97	53.06	8.25
Lu	8	logn.	0.34	0.41	0.37	0.03
Mo	8	logn.	1.54	48.43	5.45	15.67
Nb	8	norm.	15.28	25.16	19.96	3.70
Nd	8	norm.	28.88	55.64	41.76	8.65
Ni	8	logn.	9.98	358	54.89	128
Pb	8	logn.	10.20	97.26	33.56	32.75
Pr	8	norm.	8.79	15.46	11.97	2.19
Rb	8	norm.	106.59	331	239	84.74
Sc	6	norm.	19.17	32.07	26.09	4.21
Sm	8	norm.	4.82	9.14	6.93	1.43
Sr	8	norm.	135	271	216	50.08
Ta	8	logn.	1.22	2.09	1.51	0.27
Tb	8	logn.	0.59	0.97	0.75	0.13
Th	8	norm.	20.53	35.88	28.26	5.47
Tm	8	logn.	0.34	0.45	0.37	0.03
U	8	logn.	4.33	396	22.26	139.76
V	8	logn.	32.25	87.94	46.40	16.89
W	8	logn.	3.01	13.64	4.65	3.51
Y	8	norm.	20.08	28.70	24.59	3.50
Yb	8	logn.	2.15	2.74	2.42	0.19
Zn	8	logn.	42.04	103	59.13	19.64
Zr	8	logn.	384	509	441	45.86
LOI	8	logn.	1.89	3.77	2.63	0.61

Table I.5. Statistical parameters of the sampling on granites subjected to weak alteration (oxides and S – in %, other elements – in ppm)

Var	Vol	Dstrb	Min	Max	Avr	Stand
Al <sub>2</sub> O <sub>3</sub>	15	norm.	11.73	16.27	14.37	1.22
CaO	15	norm.	0.34	2.49	1.50	0.62
Fe <sub>2</sub> O <sub>3</sub>	15	norm.	1.00	3.39	2.32	0.64
Fe	5	logn.	14915	19783	16744	2048
K <sub>2</sub> O	15	norm.	1.16	6.62	4.10	1.28
MgO	15	norm.	0.03	0.82	0.48	0.24
MnO	15	logn.	0.03	0.17	0.07	0.03
Mn	5	logn.	489	650	564	59.19
Na <sub>2</sub> O	15	logn.	3.62	5.65	4.10	0.53
P <sub>2</sub> O <sub>5</sub>	15	norm.	0.00	0.15	0.08	0.04
SiO <sub>2</sub>	15	logn.	68.37	78.31	71.81	2.63
S	11	logn.	0.00	0.05	0.00	0.02

## Annexes

<b>Var</b>	<b>Vol</b>	<b>Dstrb</b>	<b>Min</b>	<b>Max</b>	<b>Avr</b>	<b>Stand</b>
<b>TiO<sub>2</sub></b>	15	norm.	0.04	0.43	0.28	0.10
<b>Ti</b>	5	logn.	1520	1866	1677	156
<b>Ag</b>	6	logn.	0.00	9.87	0.04	3.95
<b>As</b>	12	logn.	0.00	17.15	0.25	4.61
<b>Ba</b>	17	norm.	45.17	860	524	226
<b>Be</b>	17	logn.	1.44	10.29	4.24	2.17
<b>Bi</b>	12	logn.	0.00	0.23	0.02	0.06
<b>Cd</b>	17	logn.	0.00	0.34	0.01	0.12
<b>Ce</b>	17	norm.	18.63	141	68.85	28.16
<b>Co</b>	17	norm.	0.49	3.85	2.38	1.07
<b>Cr</b>	17	norm.	4.21	40.27	18.08	10.90
<b>Cs</b>	17	logn.	2.40	18.00	7.92	5.17
<b>Cu</b>	17	logn.	0.00	49.47	0.22	12.21
<b>Dy</b>	17	logn.	3.47	14.50	5.47	2.92
<b>Er</b>	17	logn.	2.14	9.13	3.21	1.90
<b>Eu</b>	17	norm.	0.00	1.17	0.70	0.28
<b>Ga</b>	17	norm.	15.89	20.76	18.42	1.50
<b>Gd</b>	17	logn.	3.27	14.73	5.11	3.05
<b>Ge</b>	6	norm.	1.01	1.71	1.40	0.29
<b>Hf</b>	17	norm.	2.15	7.58	5.22	1.34
<b>Ho</b>	17	logn.	0.70	3.63	1.09	0.66
<b>In</b>	6	norm.	0.00	0.12	0.05	0.04
<b>La</b>	17	norm.	7.30	64.43	32.14	13.79
<b>Li</b>	6	norm.	4.17	59.06	31.27	17.53
<b>Lu</b>	17	logn.	0.35	1.11	0.54	0.21
<b>Mo</b>	17	norm.	0.33	5.61	2.14	1.38
<b>Nb</b>	17	logn.	8.41	28.82	16.01	4.86
<b>Nd</b>	17	logn.	14.33	55.29	28.37	10.42
<b>Ni</b>	17	norm.	0.00	62.21	14.37	21.82
<b>Pb</b>	17	norm.	13.39	31.92	22.03	4.48
<b>Pr</b>	17	logn.	2.86	15.71	7.35	2.94
<b>Rb</b>	17	norm.	37.86	231	171	51.58
<b>Sb</b>	12	norm.	0.00	1.65	0.72	0.60
<b>Sc</b>	11	logn.	1.47	30.80	8.59	13.59
<b>Se</b>	6	norm.	0.00	0.00	0.00	0.00
<b>Sm</b>	17	logn.	3.69	14.26	5.89	3.03
<b>Sn</b>	12	logn.	1.62	6.18	3.00	1.33
<b>Sr</b>	17	norm.	16.53	246	163	59.06
<b>Ta</b>	17	logn.	1.17	5.24	2.01	1.30
<b>Tb</b>	17	logn.	0.58	2.34	0.87	0.49
<b>Th</b>	17	logn.	9.06	66.51	23.45	11.71
<b>Tl</b>	8	logn.	1.04	3.56	1.82	0.93
<b>Tm</b>	17	logn.	0.35	1.27	0.51	0.27
<b>U</b>	17	logn.	2.07	21.88	4.70	4.45
<b>V</b>	17	norm.	2.90	35.32	18.46	8.65
<b>W</b>	17	logn.	0.17	5.00	0.75	1.35
<b>Y</b>	17	logn.	12.41	54.95	27.84	10.96
<b>Yb</b>	17	logn.	2.35	9.00	3.56	1.84
<b>Zn</b>	17	logn.	31.59	71.71	46.88	12.58
<b>Zr</b>	17	norm.	42.71	287	150	76.64
<b>LOI</b>	9	norm.	0.60	1.44	1.08	0.25

## Annexes

Table I.6. Statistical parameters of the sampling on granites subjected to moderate and intensive alteration  
(oxides and S – in %, other elements – in ppm)

Var	Vol	Dstrb	Min	Max	Avr	Stand
Al <sub>2</sub> O <sub>3</sub>	7	logn.	13.19	15.85	14.36	0.93
CaO	7	norm.	0.14	1.69	1.01	0.56
Fe <sub>2</sub> O <sub>3</sub>	7	logn.	1.19	3.37	2.12	0.80
K <sub>2</sub> O	7	norm.	3.66	4.97	4.35	0.51
MgO	7	norm.	0.20	0.73	0.45	0.17
MnO	7	norm.	0.01	0.13	0.07	0.04
Na <sub>2</sub> O	7	norm.	0.14	4.22	2.97	1.49
P <sub>2</sub> O <sub>5</sub>	7	logn.	0.05	0.17	0.09	0.04
SiO <sub>2</sub>	7	logn.	68.16	77.86	72.75	2.89
S	5	logn.	0.01	0.21	0.03	0.09
TiO <sub>2</sub>	7	logn.	0.16	0.49	0.28	0.11
Ag	4	norm.	0.00	0.20	0.05	0.10
As	7	norm.	0.00	13.85	4.71	4.71
Ba	8	norm.	234	789	550	191
Be	8	norm.	0.75	7.10	3.69	1.93
Bi	7	norm.	0.00	0.17	0.06	0.07
Cd	8	logn.	0.00	0.41	0.00	0.14
Ce	8	logn.	40.59	111	68.91	20.61
Co	8	logn.	1.50	8.81	2.52	2.40
Cr	8	logn.	7.51	48.05	19.99	12.68
Cs	8	logn.	4.06	35.52	12.62	10.57
Cu	8	logn.	0.00	66.06	0.10	22.69
Dy	8	logn.	3.08	7.28	4.91	1.54
Er	8	logn.	1.90	4.66	3.05	1.03
Eu	8	logn.	0.44	1.37	0.79	0.33
Ga	8	logn.	15.14	22.42	18.27	2.67
Gd	8	logn.	3.73	7.80	5.13	1.45
Ge	3	logn.	1.17	1.63	1.37	0.23
Hf	8	logn.	3.20	7.24	4.65	1.46
Ho	8	logn.	0.67	1.58	1.04	0.33
In	3	norm.	0.03	0.09	0.06	0.03
La	8	norm.	17.06	48.56	32.85	9.14
Li	4	norm.	7.72	39.09	22.95	13.55
Lu	8	logn.	0.35	0.81	0.55	0.18
Mo	8	logn.	1.02	38.27	4.83	16.28
Nb	8	logn.	11.99	25.07	16.48	5.07
Nd	8	logn.	22.49	54.23	29.54	10.32
Ni	8	logn.	1.42	123	5.15	41.98
Pb	8	norm.	11.42	26.68	20.64	5.09
Pr	8	logn.	4.81	12.43	7.56	2.27
Rb	8	logn.	111	244	194	44.96
Sb	7	logn.	0.91	6.45	2.46	1.99
Sc	5	logn.	0.97	29.93	3.67	12.35
Sm	8	logn.	4.11	9.82	5.83	1.77
Sn	7	logn.	1.83	6.59	3.20	1.56
Sr	8	logn.	63.12	202	112	45.22
Ta	8	logn.	1.52	7.93	2.53	2.15
Tb	8	logn.	0.49	1.20	0.80	0.24
Te	4	norm.	0.00	0.00	0.00	0.00
Th	8	logn.	17.31	44.14	25.62	8.39



## Annexes

---

<b>Var</b>	<b>Vol</b>	<b>Dstrb</b>	<b>Min</b>	<b>Max</b>	<b>Avr</b>	<b>Stand</b>
<b>TI</b>	5	norm.	1.19	2.62	1.96	0.52
<b>Tm</b>	8	norm.	0.26	0.77	0.52	0.19
<b>U</b>	8	logn.	2.51	37.53	7.81	12.29
<b>V</b>	8	logn.	11.81	25.96	17.43	6.07
<b>W</b>	8	logn.	1.13	8.98	2.25	2.61
<b>Y</b>	8	norm.	12.98	47.11	28.74	10.24
<b>Yb</b>	8	norm.	1.92	4.86	3.56	1.22
<b>Zn</b>	8	logn.	32.07	80.99	48.21	16.76
<b>Zr</b>	8	logn.	55	282	117	75.86
<b>LOI</b>	3	logn.	1.08	4.52	1.81	1.95

## **Electronic annexes**

**E-annex I. 3D GIS model of the central part of the Oktyabrsky deposit, with the installation of Acrobat Reader 3D**

**E-annex II. Results of microprobe analyses**

**E-annex III. Results of ICP-MS analyses of mineral separations of fluorite and carbonate**

**E-annex IV. Results of whole-rock analyses (ICP-AES, -MS, XRF, INAA)**





